

Dissertation
submitted to the
Combined Faculties for the Natural Sciences and for Mathematics
of the Ruperto-Carola University of Heidelberg, Germany
for the degree of
Doctor of Natural Sciences

Put forward by
Diplom-Phys.: Stefan M. Kallenberger
Born in: Frankfurt am Main

Oral examination: 23.01.2014

für meine Eltern

Variability in cellular signal transduction networks

Referees:

Prof. Dr. Roland Eils

Prof. Dr. Motomu Tanaka

Zusammenfassung

Zelluläre Variabilität entspricht der physiologischen Realität aber bleibt in Modellen üblicherweise unbeachtet. Im Rahmen der Doktorarbeit wurde eine neue Vorgehensweise entwickelt, biochemische Signaltransduktionsnetzwerke in sich verschiedenartig verhaltenden Zellen durch zelluläre Ensemble-Modelle zu beschreiben. Zelluläre Ensemble-Modelle enthalten Netzwerke gekoppelter gewöhnlicher Differentialgleichungen zur Beschreibung der Trajektorien von Proteinkonzentrationen in verschiedenen Zellen, welche durch bestimmte Randbedingungen gekoppelt sind, um den Bezug zu physiologischen Gegebenheiten zu gewährleisten. Durch die Beschreibung experimenteller Einzelzell- und Populationsdaten im selben Modell konnte die Modelldiskrimination erleichtert und die Genauigkeit der Parameterschätzung verbessert werden.

Die Vorgehensweise wurde in zwei biochemischen Systemen, dem programmierten Zelltod und dem intrazellulären Transport von Erythropoietinrezeptoren, angewandt. Eine experimentelle Technik wurde entwickelt, um die Aktivität des Enzyms Caspase-8, welches den Zelltod initiiert, in einzelnen Zellen zu quantifizieren. Die analytische Lösung eines Modells zur Oligomerisation von Zelltodrezeptoren wurde mit einem zellulären Ensemble-Modell der Caspase-8 Aktivierung verknüpft. Ein Aktivierungsmechanismus, welcher positives Feedback impliziert, konnte vorhergesagt und experimentell bestätigt werden. Vorhergesagte multivariate logarithmische Normalverteilungen initialer Proteinkonzentrationen ermöglichten Simulationen, um funktionelle Rollen involvierter Signaltransduktionsproteine zu analysieren. In ähnlicher Weise konnte durch ein zelluläres Ensemble-Modell die Variabilität der intrazellulären Transportkinetik von Erythropoietinrezeptoren charakterisiert werden.

Die neue Vorgehensweise kann zur Optimierung therapeutischer Anwendungen beitragen, die auf eine heterogene Population von Krebszellen gerichtet sind.

Summary

Cellular variability is fundamental to physiological reality but usually unattended in signaling models. This thesis introduces the new approach of cell ensemble models, which describe biochemical signal transduction networks in heterogeneously behaving cells. Cell ensemble models comprise sets of coupled ordinary differential equations describing protein concentration trajectories in different cells, which are linked

by boundary conditions restricting models to physiological limitations. Simultaneous description of single-cell and population data facilitated model discrimination and improved the accuracy of parameter estimations.

The approach was applied in two biochemical systems, programmed cell death and the intracellular traffic of erythropoietin receptors. An experimental method was developed to quantify the enzymatic activity of caspase-8, which initializes programmed cell death, in single cells. The analytic solution of a death receptor oligomerization model was combined with cell ensemble models of caspase-8 activation. An activation mechanism, which implies positive feedback, was predicted and experimentally validated. Simulations based on estimated multivariate log-normal distributions of initial cellular protein concentrations clarified the functional roles of involved signaling proteins. In a similar manner, a cell ensemble model was applied to characterize cell-to-cell variability in intracellular erythropoietin receptor transport.

The new approach might support optimization of therapeutic applications targeting heterogeneous populations of cancer cells.

Contents

1. General Introduction	1
1.1. Biochemical basics of apoptosis	1
1.2. Mathematical models of apoptosis	2
1.2.1. Overview of formalisms applied in apoptosis models	2
1.2.2. Mechanistic ODE models describing apoptosis networks	7
1.3. Biochemical basics of erythropoietin receptor signaling	21
1.4. Mathematical models of erythropoietin receptor signaling	23
2. Methods	25
2.1. Confocal fluorescence microscopy	25
2.2. Biochemical experimental methods	30
2.3. Mathematical modeling with systems of ODEs	33
I Cellular heterogeneity determined by variable protein levels: cell ensemble model of apoptosis	39
3. Introduction	41
4. Quantifying enzyme activities by a confocal imaging based method	45
5. Integrating single cell and population data in a cell ensemble model	55
6. Explaining the inverse bell-shape of cell death kinetics by receptor oligomer- ization models	63
7. Modeling shows a combined cis/trans cleavage mechanism of caspase-8 activation	71
7.1. Alternative mechanisms of caspase-8 activation	71
7.2. Model implementation	72
7.3. Model fitting, model selection and experimental validation	75
7.4. Monte Carlo modeling reveals qualitative differences in 'cis/cis' and 'cis/trans' topologies	86
7.5. Caspase-8 operates as a molecular timer	91

8. Simulating the variability of apoptosis in heterogeneous cell populations	93
8.1. Simulating cell-to-cell variability by a multivariate lognormal joint distribution	93
8.2. Testing the predictive capability of a model of cell death induction .	95
8.3. Ligand, receptor and FADD control timing and variability while p55 and BID control survival	96
9. Discussion	101
II Cellular heterogeneity determined by variable kinetic parameters: cell ensemble model of Epo receptor traffic	105
10. Modeling EpoR receptor traffic in single cells	107
10.1. Quantification of EpoR traffic in single cells	108
10.2. Model of EpoR traffic	110
10.3. Cell-to-cell variability in EpoR traffic	122
III Conclusions	127
IV Appendix	131
A. Additional material on the cell ensemble model of apoptosis	133
A.1. Additional figures	133
A.2. Model equations and kinetic parameters	138
A.3. Flux analysis in caspase-8 cleavage model variants	141
A.4. Quantification of total signaling protein numbers	143
A.5. Using flow cytometry to estimate receptor levels and set upper and lower boundaries for initial concentrations	148
B. Additional material on the cell ensemble model of Epo receptor traffic	151
Bibliography	155
Acknowledgements	173

1. General Introduction

In this thesis, mathematical models of programmed cell death initiation and intracellular erythropoietin receptor transport were studied. This chapter outlines basic principles of these systems, and gives an overview of different modeling approaches and successful applications of ODE models of apoptosis (sections 1.1 and 1.2) and of Erythropoietin signaling (sections 1.3 and 1.4). This section contains parts of two book chapters by Kallenberger et al. in 'Systems Biology of Apoptosis' [1] and in 'Computational Systems Biology' [2].

1.1. Biochemical basics of apoptosis

Apoptosis is an intensively regulated signal transduction process leading to self-destruction of cells. While apoptosis is essential for embryogenesis and regulation of the immune system, its dysregulation can be the cause for cancer, immune system diseases and neurodegenerative disorders [3]. Two signaling cascades initiate apoptosis, namely extrinsic and intrinsic apoptosis, which combine in a common final path. Extrinsic apoptosis is initiated by cell death ligands binding to their specific receptors. Important members of the death receptor (DR) family that belongs to the TNF-R superfamily are the receptors TNFR1 (DR1), CD95 (DR2, Fas, APO-1) and DR 4/5 (TRAILR1/2), which specifically initiate extrinsic cell death [4]. Upon ligand binding to death receptors, death inducing signaling complexes (DISCs) are formed that serve as a platform for the activation of caspase-8 and -10 [5–7]. Caspase enzymes are aspartate-specific cysteine proteases and act as main executioners of apoptosis by cleaving specific target proteins [8]. The initiator caspases caspase-8 and -10 cleave and activate effector caspases-3 and -7 as well as the pro-apoptotic Bcl-2 family member Bid to tBid, which leads to mitochondria outer membrane permeabilization (MOMP) after stimulating pore formation by the proteins Bax or Bak [9,10]. MOMP irreversibly triggers activation of effector caspases: the pro-apoptotic proteins Smac and cytochrome c are released from mitochondria. Together with the cytosolic protein Apaf-1, cytochrome c forms apoptosomes, serving as platform for the activation of procaspase-9 which then cleaves and activates effector caspases, while Smac blocks the inhibition of caspase-9 and effector caspases by XIAP [11–17]. Active effector caspases cleave a variety of proteins including components of the cytoskeleton, and cause activation of the nuclease CAD (caspase-activated DNase) thus leading to chromosome fragmentation [8,18]. Dependent on the requirement of effector caspases activation, two types of extrinsic apoptosis are distinguished: In type I cells initiator caspases are sufficiently active to directly activate effector caspases. In type II cells, amplification of the cell death signal through Bid cleavage and

MOMP is required for undergoing apoptosis [19, 20]. Intrinsic apoptosis is directly initiated at the level of mitochondria. Different influences such as cellular stress, accumulation of reactive oxygen species (ROS) or DNA damage change the ratios between pro- and anti-apoptotic Bcl-2 family member proteins which leads to pore formation and MOMP, again leading to apoptosome formation and the activation of caspase-3 and -7 [21, 22].

Even though individual steps of the apoptotic signal transduction cascades are well understood, we lack insights into the system properties and the dynamics of the death decision. Questions to be addressed in apoptosis by systems biology approaches include:

- (i) How do cells ensure that apoptosis robustly occurs in all-or-none manner? What is the "point-of-no-return" representing irreversibility in apoptosis? Which signaling motifs are responsible for such digital and context-specific behavior?
- (ii) How is specificity in the apoptosis vs. survival responses ensured? A topic of particular interest for apoptosis modeling is that apoptotic stimuli trigger survival or death signaling depending on initial conditions and the stimulus strength. At least in some cases, the inhibitory crosstalk between survival and cell death signaling pathways appears to be mutually exclusive at the single-cell level [23], implying that death and survival represent different attractor states for the cell.
- (iii) What are the principles underlying cell-to-cell variability in the apoptosis response of a cell population? Why do cell types differ widely in their sensitivity to death-inducing stimuli? Currently, several new therapeutic agents are tested to stimulate apoptosis in cancer cells, to decelerate tumor growth, or to prevent cells, preferentially neurons or cardiomyocytes, from undergoing programmed cell death. Modeling approaches could help to plan therapies and to predict the outcome on a population of cells.
- (iv) How can models be used to predict the responsiveness of cancer cell populations towards cancer therapy? Starting from a certain model topology and measured numbers of pro- or anti-apoptotic signaling species, predictions of cell fates resulting from concentration trajectories at given input stimulus, represented e.g. by a drug concentration, can be obtained.

1.2. Mathematical models of apoptosis

1.2.1. Overview of formalisms applied in apoptosis models

Analyzing the cell on a systems view can be done by top-down and bottom-up approaches. Detailed mechanistic mathematical models constructed from the molec-

1.2. *Mathematical models of apoptosis*

ular characteristics of individual proteins (“bottom-up models”) have so far only been developed for metabolic and signaling networks. In contrast, transcriptional regulatory networks, and the link between signaling networks and ultimate cellular decisions are best tackled by statistical methods which integrate huge amounts of data but are mostly phenomenological (“top-down modeling”).

Top-down approaches examine the cell on a global level, treating individual regulatory modules as black boxes that are not analyzed mechanistically but only characterized with respect to input-output behavior. Thus, top-down methods typically do not require much prior knowledge about the system, so that many signaling and/or metabolic pathways can be studied at once. Most top-down approaches are solely data-driven and rely on high throughput screens of cellular behavior (gene expression profiling, proteomics, siRNA screening, sequencing, and affinity assays). Typically, the ultimate goal of top-down approaches is to identify biologically relevant patterns and correlations to the data (e.g. disease marker gene identification) or to predict new molecular interactions (e.g. reverse engineering algorithms).

Bottom-up approaches focus on well-characterized parts of the biochemical regulatory network, and are typically based on the assumption that the properties of these subnetworks (or “modules”) can be studied in isolation. Based on prior knowledge and on time-resolved experimental data, mechanistic mathematical models describing the interactions of individual proteins in the module are constructed (e.g. by using sets of coupled differential equations). The goal of bottom-up modeling is to identify physiologically relevant systems-level properties emerging from complex interactions within the network (e.g. feedback).

Apoptosis-inducing signaling cascades, especially those induced by death ligands, were mainly studied using bottom-up modeling approaches, since: (i) the molecular events are well characterized; (ii) transcriptional events can be neglected; (iii) the ultimate death decision often closely correlates with all-or-none activation of effector caspases, implying that statistical methods are not required to link signaling to cellular phenotypes. However, bottom-up approaches to apoptosis are diverse and the methodology of choice depends on the complexity of the signaling network under study, the available experimental data, and the question to be addressed by modeling. Boolean approaches are typically employed to qualitatively analyze the (quasi-)static behavior of large apoptosis-survival crosstalk networks which comprise many molecular species. Ordinary differential equation (ODE) models allow for the quantitative description of network dynamics but typically require knowledge about many kinetic parameters which either limits the network size and/or requires huge amounts of experimental data. Standard ODE modeling may even not be sufficient if spatiotemporally resolved single-cell data is available: (i) spatial gradients within the cell can be modeled using subcellular compartment ODE models or partial differential equations (PDEs). (ii) Cell-to-cell variability may arise due to stochastic dynamics of the apoptotic signaling cascade (‘intrinsic noise’) or due to cell-to-cell variability in the expression of pathway components (‘extrinsic noise’). While ODE models with randomly sampled initial protein concentrations can be employed to simulate extrinsic noise, stochastic simulation algorithms are required to understand

intrinsic noise. In the following, an overview of top-down and bottom-up modeling approaches is given that were applied to apoptosis signaling, before discussing applications of ODE models in more detail.

Linear regression models

To systematically analyze how the pro- and anti-apoptotic cytokines TNF, EGF and insulin impinge on the cellular apoptosis decision, Janes et al. [24] generated a compendium of co-stimulation measurements. Based on the assumption that simple linear combinations of signaling activity profiles account for apoptosis initiation, they employed a top-down modeling approach known as partial least-squares regression (PLSR) which does not require prior knowledge. PLS modeling calculates super axes as an orthogonal set of "principal components", which contain linear combinations of the original signaling protein activities weighted by their contribution to the apoptotic outputs. Thereby, the dimension of the data matrix is reduced to a small set of informative super axes, which can be used to predict apoptosis initiation for any experimental condition provided that measurements of signaling species used for model training are available. PLSR has been successfully applied to large-scale apoptosis datasets, and provided insights into complex phenomena such as autocrine amplification loops [24] or cytokine-modulated inter-relationships between different signaling pathways following DNA damage [25]. A major drawback of PLSR is the lack of mechanistic insights into (i) how signaling activity patterns are generated and (ii) how signaling activities are integrated, e.g., at the level of caspases, to control the death decision. Therefore, the next section will be devoted to bottom-up approaches applied to apoptosis which take into account mechanisms of apoptosis initiation.

Boolean models

Recent biomedical research revealed a plethora of protein-protein and enzymatic interactions, and thus extensively characterized the topology of the intracellular signaling network. However, quantitative information characterizing the affinity of protein-protein interactions or enzyme kinetic parameters is still scarce. Moreover, quantitative characterization is often performed using recombinant proteins in vitro, with questionable relevance to the in vivo situation. Simulations of large-scale networks is therefore often performed using Boolean or logic modeling, a qualitative approach that is based on network topology, but does not take into account quantitative features of individual reactions. Instead protein activities are represented by nodes which can either be on or off (activity 0 or 1), depending on the activities of upstream input nodes. Logic rules are applied at each iteration: For example, in a so-called AND-gate, the node Z will be activated if and only if both input nodes X and Y are active. In contrast, an OR-gate simply requires either X or Y to be active. Thus, Boolean rules can be used to qualitatively represent real biochemical mechanisms such as functional redundancy (OR-gate) or coincidence detection (AND-gate), the latter, arising from sequential processing by two distinct

1.2. Mathematical models of apoptosis

enzymes. Since logical rules are applied iteratively, the approach can be used to study temporal phenomena such as adaptation. Moreover, Boolean networks can exhibit nonlinear dynamic phenomena such as oscillations, and stable vs. unstable attractors.

A number of Boolean modeling studies have been presented in the context of apoptosis [26–30]. All these studies analyzed the crosstalk of apoptosis signaling via caspases and survival pathways such as NF- κ B signaling. The main goal was the identification of stable states in the systems, representing cell fates such as apoptosis, necrosis, and survival. Calzone et al. [26] and Mai and Liu [27] focused on signaling upon death receptor engagement. They showed that the stable states of the apoptosis network are robust and investigated the requirements for irreversibility in the apoptosis decision. Schlatter et al. [29] and Philippi et al. [28] took into account co-stimulation with pro-death and pro-survival ligands, and experimentally confirmed key model predictions. Zhang et al. [30] analyzed antigen-induced survival signaling network in T cell large granular lymphocyte (T-LGL) leukemia cells including transcriptional induction of cytokines and autocrine stimulation events. Model predictions could be confirmed in leukemic cells isolated from patients, thus contributing to our understanding of signaling deregulation in the disease. Taken together, Boolean modeling approaches provided valuable insights into apoptosis at multiple timescales and for various experimental settings.

Quantitative modeling approaches

Although helpful to understand principles of network topologies, Boolean models are inherently limited in their capability of quantitatively describing the temporal dynamics of biochemical networks. In the context of perturbation analysis, Boolean approaches are restricted to the simulation of complete elimination of network nodes and/or reactions; thus, gradual phenomena such as dosage compensation cannot be studied. Moreover, the qualitative effects of perturbations as revealed by Boolean modeling are often intuitively clear. Thus, in many cases, nontrivial and experimentally testable predictions require quantitative modeling approaches such as ODE and PDE modeling, as well as stochastic simulations.

An ODE model comprises a network of coupled rate equations for every involved signaling species. The kinetics of each involved reaction is described with reaction rates dependent on the concentrations of educts and products. Specifically, one typically assumes that the number of product molecules synthesized in a certain time interval is linearly dependent on the concentrations of educt molecules (law of mass action). The net influx or efflux arising from all participating reactions determines the rate of change in each molecular species. Thus, ODE modeling is based on the assumption that the temporal derivatives of molecule concentrations equal the sum of all relevant reaction rates. Larger biochemical signal transduction networks are therefore reflected using coupled ODEs (for further details see section 2.3). ODE approaches assume that large numbers of signaling molecules are present within the cell, so that random fluctuations in reaction events can be neglected by averaging over the

whole molecule population. Moreover, in ODE modeling it is assumed that the cell represents a well-stirred reactor, implying that diffusion effects do not matter and that spatial gradients, which are described in PDEs, can be neglected. In apoptosis networks, these assumptions are likely to be fulfilled, as caspases and their regulators are typically expressed at the number of several hundred thousand molecules per cell [31]. Furthermore, the time scale of apoptosis induction (hours) is slow relative to the time scale of protein diffusion within a cell (milliseconds to seconds); therefore, spatial gradients of apoptosis signaling molecules are unlikely to play a decisive role in apoptosis initiation. Nonetheless, reaction-diffusion models allowed investigating molecular mechanisms of apoptosis induction: Using live-cell imaging with high temporal resolution, Rehm and colleagues observed that cytochrome *c* release from mitochondria during apoptosis occurs in spatial waves that propagate from a subcellular mitochondrial pool to the remainder of the mitochondrial population [32]. Partial differential equation (PDE) modeling was employed to investigate the dynamics of non-steady state diffusion. This approach revealed that localized release and diffusion of inducers of mitochondrial outer membrane permeabilization (MOMP) alone was insufficient to explain the data. However, then the authors took into account that MOMP inducers bind to mitochondria, and modeling indicated that this absorption shapes the dynamics of cytochrome *c* release, thus providing insights into molecular mechanisms controlling apoptosis induction.

Owing to low molecule numbers of Bcl-2 family members, stochastic simulations using cellular automaton approaches were performed by Chen et al. [33], Siehs et al. [34], and Düsselmann et al. [35] to describe the dynamics of mitochondrial outer membrane permeabilization (MOMP). Chen et al. [33] focused on bistability and concluded that the stochastic system attained two distinct stable states much like the deterministic case; thus robustness of switching towards molecular noise could be confirmed. Düsselmann et al. [35] compared their model to measurements in cells expressing Bax-FRET probes monitoring Bax oligomerization. Their model could provide an explanation for pore formation upon Bax accumulation and oligomerization in the outer mitochondria membrane. A further study making use of cellular automaton approaches explained the stoichiometry of DISC components that was observed in mass spectrometry experiments [36]. These experiments showed that in immunoprecipitates of DISCs, the number of procaspase-8 and *c*-FLIP molecules exceeds the number of FADD molecules several-fold, suggesting that chains of procaspase-8 and *c*-FLIP are formed on DISC-bound FADD molecules. A cellular automaton model was used to reproduce the observed protein ratios, and to test further hypotheses on chain lengths and chain formation kinetics. This approach facilitated handling the large combinatorial complexity arising from possible compositions of larger protein chains of FADD, *c*-FLIP and procaspase-8, in comparison to an ODE model that would require a large number of equations for each possible oligomer state.

Live cell imaging tools are increasingly important and allow the analysis of apoptosis at the single cell level or even with subcellular resolution. Thus, stochastic and reaction-diffusion modeling are likely to become central to apoptosis modeling. For example, death receptors are frequently expressed at low levels and form

1.2. Mathematical models of apoptosis

localized (nano-) clusters on the cell membrane [37], implying that deterministic ODE approaches will fail, especially upon weak stimulation. Stochastic and reaction-diffusion modeling will reveal underlying mechanisms and, more importantly, predict strategies for intervention for testing the functional relevance of such phenomena.

1.2.2. Mechanistic ODE models describing apoptosis networks

The first mechanistic apoptosis model of coupled differential equations, presented by Fussenegger et al. [38], described sequential activation of caspase-8, caspase-9 and caspase-3 by intrinsic or extrinsic stimuli. The model accounted for a positive feedback from caspase-3 promoting the release of cytochrome c from mitochondria and thus promoting the additional activation of caspase-9 in apoptosomes. As this model was not trained against quantitative data, it provided only predictions on activated fractions of initiator and executioner caspases dependent on initial concentrations of apoptosis promoting or inhibiting proteins. A lot of progress has been made since this first apoptosis model, and different aspects have been studied in detail.

In the following, current literature on ODE-based apoptosis modeling will be reviewed. Figure 1.1 shows an overview about subareas of the apoptotic signaling network that were investigated by current models. First, models, which understand apoptosis as a bistable process, will be described. Second, studies investigating the temporal dynamics of apoptosis will be summarized. Third, crosstalk models describing apoptosis and survival networks will be discussed. The final focus of this review part will be cell-to-cell variability.

Origins of a robust all-or-none behavior - models characterized by bistability and feedback mechanisms Bistability may play an important role for all-or-none and irreversible decision making, thus allowing the suppression of noise and prevention from accidental apoptotic stimuli. In the following, models will be reviewed that exhibit bistability due to positive feedback in the intrinsic or extrinsic apoptosis pathways.

Extrinsic apoptosis pathway Understanding bistability in the process of apoptosis initiation was the focus of the study of Eissing et al. [45]. Their model described the bistability in extrinsic apoptosis within the context of caspase-mediated positive feedback. Caspase-8 activated by receptor-induced apoptosis in type I cells activates caspase-3, while caspase-3 promotes positive feedback by caspase-8 activation. A stability analysis showed, which kinetic parameter values allowed bistability, and therefore a stable steady state for survival. It could be shown that bistability was only possible at parameter values far off the experimentally measured kinetic parameters. By extending the model topology, the authors concluded that bistable caspase activation within the physiologically reasonable parameter range required the consideration of inhibitors of activated caspase-8. Specifically, it was suggested that caspase-8 inhibitory proteins such as the bifunctional apoptosis regulator pro-

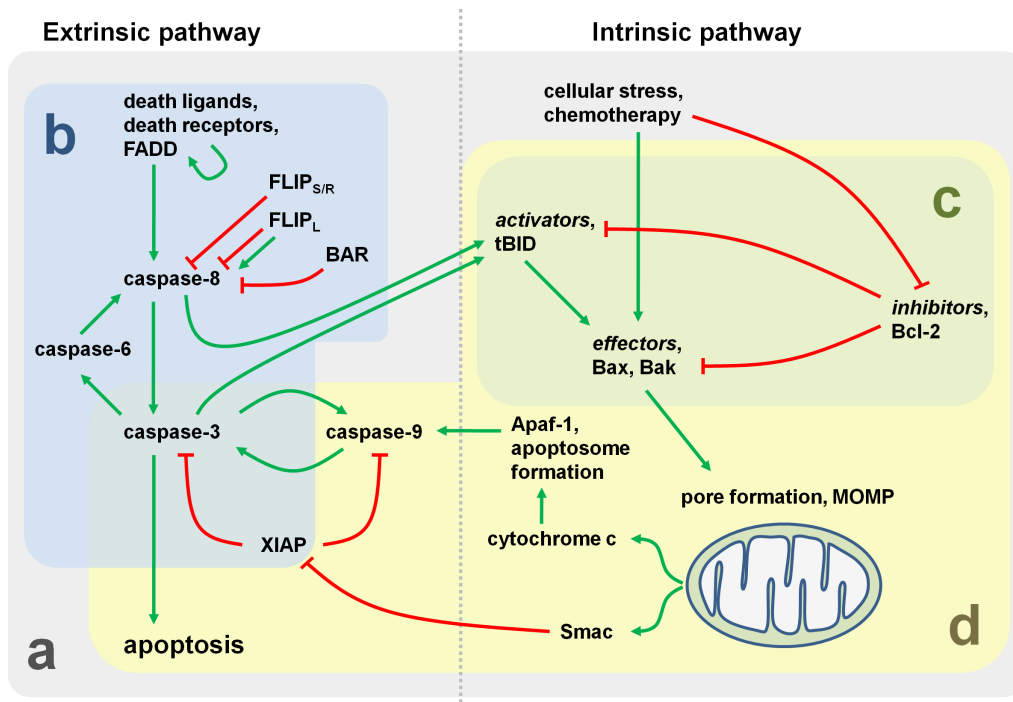


Figure 1.1. Overview of the extrinsic and intrinsic parts of the apoptotic signaling network. Subareas are indicated that were investigated by current modeling studies. (a) Modeling studies that captured extrinsic and intrinsic pathways [38–44]. (b) Modeling studies with main focus on the level of death receptors, DISC assembly and caspase activation processes [45–50]. (c) Modeling studies that described interactions between members of the Bcl-2 family prior to mitochondria outer membrane permeabilization (MOMP) [33–35, 51–53]. (d) Modeling studies with main focus on intrinsic apoptosis and caspase inhibition [54–58].

1.2. Mathematical models of apoptosis

tein (BAR) [59], and caspase-8 and -10-associated RING proteins (CARPs) [60] play a central role for establishing bistability.

Bistability on the ligand/receptor level was proposed upon theoretical considerations of a positive feedback in receptor oligomerization reactions [47]. These were motivated by new insights into the structure and function of CD95 (APO-1/Fas) molecules [61]. Protein crystallization experiments on receptor/FADD-clusters had shown that receptors in the absence of ligands favor a closed form where FADD cannot bind. Upon ligand binding an open form is favored, allowing FADD binding, DISC formation and signal progression. The conformation of open receptors leads to the mutual stabilization of the receptors in their open state, which may cause receptor oligomerization and positive feedback amplification. An ODE model was formulated in a continuum approximation where molecule numbers were treated as local protein concentrations [47]. At high receptor densities, which could be potentially induced locally inside lipid rafts, reactions can take place where several open receptors stabilize each other. In the model these events could be approximated by higher order reactions. Rate equations for reactions that contain terms with an order of three or larger can have two stable steady states and one unstable steady state in between, which causes bistable behavior. Therefore, depending on the local receptor densities, reversible or irreversible bistability can result. This leads to an all-or-none response on the level of DISCs, resulting in a gradual response, integrated over all clusters on the cell level.

Intrinsic apoptosis pathway The theoretical study by Bagci et al. [40] addressed origins of bistability on the level of mitochondrial outer membrane permeabilization (MOMP) and apoptosome formation. Two positive feedback mechanisms contribute to bistability: First, caspase-3 cleaves and inactivates the MOMP inhibitor Bcl-2, and thereby amplifies its own production. A second feedback arises from the cleavage of the MOMP inducer Bid by caspase-3; thus Bid cleavage, initially triggered by caspase-8, can be enhanced by caspase-3. Their mass-action model describes oligomerization of Apaf-1 bound to cytochrome c to the heptameric complexes of apoptosomes. As this cooperative oligomerization process leads to higher order terms in the corresponding rate equation, the positive feedback interactions can result in bistable regimes corresponding to either survival or apoptosis. As the model of Bagci et al. [40] does not consider reactions upstream of initiator caspases, initial doses of caspase-8 and caspase-3 serve as stimulus. Their considerations were motivated by experimental studies that had shown a survival mechanism of cancer cells based on elevated Bax degradation [62], decreased Bax expression in human breast cancers [63] or overexpression of Bcl-2 [64]. In the model of Bagci et al., bifurcation points in the caspase-3 activity were investigated, that are dependent on the production or degradation of Bax and their relation to inhibitory Bcl-2 proteins. Above a certain threshold for the degradation rate of Bax or below a certain threshold for the Bax production rate, the bistable behavior is changed into a monostable survival state. In this state an initiator caspase stimulus cannot trigger the apoptosome-mediated feedback anymore.

Current studies on Bcl-2 family members show even more complicated relations on the level of mitochondria among proteins that act as sensitizers (as Bad, Noxa or Puma), activators (Bid, Bim) or effectors (Bax, Bak). To characterize the vulnerability of tumors to apoptosis effectors, the impacts of different Bcl-2 family members on mitochondria isolated from tumor samples were investigated [65, 66]. For more detailed reviews see [67–69].

Recently, models of intrinsic cell death were applied to predict the responsiveness of patient tumors to chemotherapies [53, 70, 71]. Two studies applied a model describing activation of caspase-9 and caspase-3 after MOMP, cytochrome c and Smac release and inhibition of XIAP, which was originally developed based on experiments in common lab cell lines [55]. Measurements of Apaf-1, XIAP, Smac, procaspase-3 and -9 levels in patient tumor samples of colorectal cancers [70] and glioblastoma multiforme brain tumors [71] were used as initial concentrations for model simulations. In the study on colon cancer samples, model simulations were used to predict if effector caspases activity could be effectively evoked by applying chemotherapy, and model predictions were significantly correlated with observed clinical outcomes [70]. Similarly, the study on brain tumor samples showed that model simulations were correlated with progression free survival durations in patients [71]. A model describing interactions between pro- and anti-apoptotic Bcl-2 family members was developed by Lindner et al. to predict responses of colon cancers to chemotherapy with 5-FU and oxaliplatin, based on the quantification of Bak, Bax, Bcl-2, Bcl-xL and Mcl-1 in tumor samples compared to normal tissue [53]. Similar to the study focused on signaling species downstream of MOMP, knowledge of Bcl-2 family member levels facilitated model predictions of responses to chemotherapy that were highly correlated with observed clinical outcomes. Furthermore, their model enabled predictions, which patients may be successfully co-treated with BH3-mimetic drugs as ABT-263, ABT-737 or ApoG2 that mimic natural inhibitors of anti-apoptotic Bcl-2 family members [72].

Taken together, models of intrinsic cell death could successfully reveal mechanisms of interactions between pro- and anti-apoptotic Bcl-2 family members and show promising results with regard to chemotherapy optimization.

Implicit feedback mechanisms in the intrinsic apoptosis pathway In the modeling studies summarized so far, the positive feedback mechanisms known from the biomedical literature and their contribution to bistability were analyzed. Additionally, mathematical modeling can provide valuable insights into non-obvious, hidden feedback loops that arise from the topology of the apoptosis network. This phenomenon has been referred to as implicit positive feedback regulation. The interplay of caspase-3, caspase-9 and inhibitors of apoptosis (IAPs) in the mitochondrial pro-apoptotic pathway was investigated in a model by Legewie et al. [54]: Cytochrome c released from mitochondria, triggers activation of caspase-9, which in turn cleaves procaspase-3 into active caspase-3. Both caspase-3 and caspase-9 are inhibited by XIAPs to prevent auto-reactive activation. Interestingly, an implicit positive feedback loop arises from the dual inhibition of both caspases by XIAPs: Once active

1.2. Mathematical models of apoptosis

caspase-3 is generated, it can bind to XIAPs, thus sequestering XIAPs away from caspase-9. This sequestration effect enhances caspase-9 activation, resulting in auto-amplification of caspase-3 cleavage. In the model by Legewie et al., the dependency of the concentration of active caspase-3 as the response to an Apaf-1 concentration shows different characteristics of either monostable, bistable reversible or bistable irreversible behavior. The authors concluded that implicit positive feedback alone brings a very small range of bistability; however, implicit feedback synergizes with other feedback mechanisms to establish a broad bistable range and irreversibility in the life-death decision.

The studies of Chen et al. [33, 51] combined ODE, stochastic and cellular automaton modeling to further understand signaling processes that potentially lead to MOMP. In these studies interactions between pore forming effectors (Bax, Bak), activators and enablers (tBid and several others), and inhibitors (Bcl-2 amongst others) that lead to or prevent mitochondria outer membrane permeabilization are analyzed. After translocation to mitochondria, inactive Bax and Bak are catalyzed to their active form by an activator. Subsequently, activated Bax and Bak lead to membrane pore formation and cell death. In the study of Cui et al. [52] models involved in the bistability of MOMP were further developed. Questions on the possible model topology led to hierarchical considerations in the studies of Chen et al. [33, 51] as well as Cui et al. [52]: Do activators and enablers indirectly induce apoptosis by sequestering Bcl-2 away from Bax, or are activators directly pro-apoptotic by catalyzing the reaction of Bax to its active form that can cause pore formation and cytochrome c release? This question led to an indirect model recapturing the inhibition of Bcl-2 by activators and topologies describing direct Bax activation. Inhibitors as Bcl-2 in the indirect topology interfere by inhibiting Bax and thereby preventing its oligomerization at the pores. In direct topologies they inhibit activators from catalyzing Bax activation. Direct topologies were favored in this study, as they involve two possible feedback mechanisms that could contribute to a bistability in Bax activation. These considerations were motivated by experimental studies that showed a bimodal distribution of cells that had low or high amounts of activated Bax and Bak monitored by flow cytometry [73–75]. The first described feedback mechanism is facilitated by activated Bax that can sequester Bcl-2, leading to an increase of free activators and thereby providing increased Bax activation. This mechanism is similar to the role of XIAP as discussed in the study of Legewie et al. [54], since Bcl-2 acts as a dual inhibitor of upstream activators and their downstream effector Bax. Furthermore, the model of Cui et al. [52] considers a feedback mechanism, in which activated Bax itself provides further Bax activation. In their study the signal response behavior is characterized by the dependency of active Bax and Bcl-2 steady state levels as dependent on the production rate of activators. In a model containing both feedback mechanisms the interval of activator production rates that lead to bistability of active Bax and Bcl-2 concentrations is significantly enlarged compared to a variant with only one feedback mechanism. Therefore, the combination of both feedback mechanisms would provide a higher robustness for the bistable behavior of Bax activation and mitochondria pore formation.

Origins of a robust all-or-none behavior - Switching and threshold mechanisms other than bistability

Biochemical signaling networks may exhibit switching mechanisms other than bistability arising from positive feedback. In such cases, the system exhibits a single steady state which increases in a steep, non-linear manner with increasing input concentration. Such sigmoidal, all-or-none dose-response behavior has been termed ultrasensitivity. One ultrasensitivity mechanism with particular relevance to apoptosis is inhibitor ultrasensitivity: here, a protein inhibitor strongly binds to its target, implying that the target remains completely inactive unless the total concentration exceeds the total inhibitor concentration [76]. Thus, the stoichiometry between inhibitor and target determines the system behavior, explaining why the mechanism is also known as stoichiometric switch.

The critical roles of c-FLIP_L and c-FLIP_S, which potentially act as stoichiometric inhibitors in the death-inducing signaling complex, were investigated in a model of Bentele et al. [41]. The dependence of the ligand concentration threshold on the concentrations of both splicing variants of c-FLIP was characterized, and it was concluded that c-FLIPs establish a stoichiometric switch. A large scale model comprising DISC assembly, caspase activation, MOMP, interference from caspase inhibitors, and degradation processes was derived. The model could be fitted to quantitative western blot data (caspase-8, -2, -7, -3, -9, Bid, PARP) representing population measures of protein concentrations under different ligand concentrations using hierarchical parameter estimation. By a global sensitivity analysis clusters of modeled signaling proteins with high mutual sensitivities of protein concentrations were defined, which lead to functional subsystems. By disregarding parameters that had low sensitivities to parameters in one cluster the dimensionality of the parameter estimation problem could be decreased. Predictions of the reduced model were subsequently verified experimentally. Most importantly, it could be shown that the threshold ligand concentration was highly sensitive to the c-FLIP concentration which is consistent with a stoichiometric switch mechanism. A refined version of the Bentele model was presented in the theoretical study of Toivonen et al. [77] which took into account fast turnover of c-FLIP variants that could be relevant for their anti-apoptotic effect. It could be shown that the concentration of c-FLIP at the time of ligand addition is central to apoptosis timing. Recently, accumulation of c-FLIP due to proteasome inhibition was investigated in a study by Laussmann et al. [50]. As a direct effect, c-FLIP overexpression delays caspase-8 activation. Changes in apoptosis kinetics, however, were not intuitive as proteasome inhibition simultaneously caused TRAIL receptor 2 accumulation. Therefore, pro- and anti-apoptotic effects of proteasome inhibition were investigated by a kinetic model.

Another ultrasensitivity mechanism with potential relevance to apoptosis is protein dimerization. For protein dimerization the steady state of the active dimer depends on the total protein concentration in a quadratic manner. Thus, weak input signals controlling the concentration of the monomer species can be suppressed, while stronger inputs are transmitted. This phenomenon, known as multistep ultrasensitivity, was analyzed by Würstle et al. [49] as described in the following.

In the absence of death receptor ligands, the amplification loop from active

1.2. Mathematical models of apoptosis

caspase-8 to caspase-3, from activated caspase-8 to caspase-6 and back to caspase-8, has to be silenced to prevent apoptosis induction at low levels of active caspase-8. Würstle et al. compared different model variants to understand how efficient suppression of the amplification loop can be achieved [49]. First, they analyzed the role of well-known caspase inhibitors such as the caspase-8 inhibitor BAR and the caspase-3 inhibitor XIAP. Second, they took into account that only caspase-8 dimers are catalytically active, and considered de-dimerization of caspase-8 complexes released from the DISC. In this context, it had been shown experimentally that the caspase-8 dimerization equilibrium favors the formation of caspase-8 monomers [78]. A core model describing the activation loop only was extended by either one of these three inhibiting mechanisms. Time series of caspase activation and substrate cleavage by caspase-3 caused by mild initial stimuli of caspase-8, -3 or -6, were calculated for each model variant, using experimentally measured kinetic constants for caspase activities and caspase-8 dimerization. Subsequently, time courses of the model variables were calculated under various initial concentrations of procaspases-3, -6 and -8, BAR and XIAP to assess the sensitivity of the system towards each inhibitory mechanism in a time interval of 24 hours, respectively. Each parameter constellation leading to less than 20% substrate cleavage was classified as non-apoptotic, while more than 80% substrate cleavage was considered as effective apoptosis. Thereby model variants could be compared regarding their potential to prevent apoptosis. A model was considered as more preventive if it caused weak cleavage in a larger fraction of the randomly chosen parameter sets than other model variants. As a result of an initial stimulus of caspase-8 the numbers of parameter constellations leading to hypothetical survival were slightly higher in the XIAP model than for the de-dimerization model, while the number was highest for the de-dimerization model in response to stimuli of caspase-3 or caspase-6. The apoptosis-preventing effect of the low affinity in a caspase-8 dimer becomes evident when considering that caspase-6 can only cleave monomers of procaspase-8 in absence of a dimerization inducer as the DISC. Because of the low affinity in the caspase-8 dimer the system is especially stable against a stimulus of caspase-8 monomers. Consequently, all three inhibitory mechanisms were included into one model to assess thresholds of the maximal caspase-8 stimulus strength that could be compensated. Threshold changes upon removal of one of the mechanisms were determined that showed again the strong perturbation resistance by caspase-8 dimerization and dissociation [49]. Thus, it was concluded that the caspase-8 dimerization equilibrium efficiently prevents accidental cell death initiation.

Another monostable model of the apoptosis threshold was introduced in the theoretical study of Stucki and Simon [56]. However, these authors did not focus on the mechanism of ultrasensitivity, but represented all-or-none caspase-3 activation phenomenologically using a Heaviside function in the caspase-3 production term. The major focus of the study was to analyze how the caspase-3 activation threshold could be modulated by the caspase-3 inhibitory XIAPs, the XIAP antagonist Smac, and Smac binding anti-apoptotic proteins such as survivin [79]. The potentially limiting role of caspase-3 degradation was addressed, and it was concluded that XI-

APs efficiently suppress apoptosis by triggering the degradation of caspase-3 in a non-linear manner.

Models characterized by a timing switch Steady states, bistable switches and ultrasensitivity govern long-term decision making within biochemical signaling networks. However, in the context of apoptosis, it is also important that the time course of effector caspase activation is abrupt. Such temporal switching ensures complete and coherent initiation of cellular demise. Single cell measurements using GFP-tagged cytochrome *c* and caspase FRET probes confirmed that mitochondrial permeabilization and subsequent effector caspase activation indeed occur in a temporally abrupt manner [80, 81]. Accordingly, a more recent study concluded that the apoptosis timing in single cells consists of a variable lag time followed by the sudden switch-like effector caspase activation [82]. While the lag time varies within the range of one to several hours, dependent on the stimulus strength, the sudden switching time was shown to be relatively invariant around 30 minutes. This robustness of sudden switching can be interpreted as necessary to prevent from states of partial destruction that could cause genomic instability. The lag time is lengthened by proteins upstream of activated Bax, as c-FLIP, BAR or cytosolic Bcl-2, and shortened by TRAIL receptors, caspase-8, Bid and Bax. Moreover, the robustness of the switching time is determined on the level of Bax-Bcl-2 interaction leading to mitochondria pore formation [82]. Thus, most modeling studies characterizing the temporal dynamics of apoptosis initiation in type II cells employing the mitochondrial pathway were focused on regulation at the level of caspase-8 or Bcl-2. In the following the systems biological literature on the temporal dynamics of apoptosis initiation will be reviewed.

In the study of Hua et al. [43] different topologies reflecting possible interactions of Bcl-2 with Bid, tBid or Bax were compared regarding their role in controlling the kinetics of caspase-3 activation and preventing apoptosis. Four topologies, including Bcl-2 binding to Bid, tBid or Bax only, or to tBid and Bax, were implemented into a large scale model describing extrinsic apoptosis from ligand binding to caspase-3 activation. Specifically, their model describes DISC assembly, caspase-8 activation, Bid cleavage and subsequent mitochondrial reactions (i.e. binding reactions of Bcl-2, Bax oligomerization, Smac release, cytochrome *c* release and apoptosome formation). By comparing experimental data from wild type and Bcl-2 overexpressing cells with simulated trajectories of the model variants, model discrimination was possible: Their experimental data supported a mechanism where the caspase-3 time course reacts very sensitively to Bcl-2 overexpression, and the model suggested that this can only be realized if Bcl-2 can simultaneously inhibit both tBid and Bax. A global sensitivity analysis on initial concentrations of the model variables gave insight into effects of overexpression or suppression. In this context it was interesting that in the model of Hua et al. suppression of Bcl-2 under its basal level did not accelerate apoptosis, which could be experimentally verified [43]. This indicates that Bcl-2 inhibitors could selectively sensitize Bcl-2 overexpressing tumor cells to apoptosis [83], while not affecting non-transformed cells expressing Bcl-2 at moderate levels. The sensi-

1.2. Mathematical models of apoptosis

tivity analysis by Hua et al. showed further asymmetric effects of overexpression or suppression: In some proteins an overexpression does not affect apoptosis timing, while their suppression causes significant changes (e.g. death receptors). Taken together, the model was able to predict dynamics of caspase-3 activation with high accuracy and provided insights into mechanisms of Bcl-2 action.

Albeck et al. [39] presented a refined model which exhibits similar complexity as the Hua et al. [43] model, but was based on a large body of data, mostly at the single-cell level. Specifically, the model was trained against population data acquired with flow cytometry and western blotting as well as single cell imaging data. These were measured at various TRAIL concentrations and under several conditions of overexpression or depletion of signaling proteins. In the study of Albeck et al. [39] it was shown experimentally that MOMP timing and the kinetics of Smac/cytochrome c release were only dependent on the upstream signaling network controlling caspase-8 activation, while the contribution of positive feedback was negligible. Specifically, a role of three putative positive feedback mechanisms from caspase-3, caspase-6 or caspase-9 could be excluded. This suggests that some of the bistability mechanisms discussed above do not account for the temporal dynamics of apoptosis initiation at least in HeLa cells. In contrast to other apoptosis models the cell death decision was not dependent on bistability but explained apoptosis by the monostable trans-critical process of MOMP. The interaction of Bcl-2 family members with tBid and Bax, the process of Smac release followed by the reduction of effector caspase inhibition by XIAP, and the mitochondria membrane pore formation dynamics were identified as critical stages of the all-or-none behavior of effector caspase activation. Signal transduction from MOMP to effector caspases apparently proceeds in a redundant manner through Smac inactivating XIAP and apoptosome formation causing XIAP sequestration and activation of caspase-3. In conclusion, the study by Albeck et al. currently represents the most comprehensive and realistic large-scale model of apoptosis.

In a combined experimental and theoretical study, Rehm et al. analyzed the kinetics of temporally switch-like effector caspase activation downstream of mitochondria [55]. In particular, they focused on the control of effector caspase activation by XIAP. Their model described apoptosis signaling following MOMP induced by the drug staurosporine. The agent tetramethylrhodamine methylester (TMRM) was used to experimentally measure changes of the mitochondria membrane potential to monitor the occurrence of MOMP. In their model, Smac and cytochrome c released from mitochondria served as stimuli. Subsequent events in the model include apoptosome formation, caspase-9 as well as caspase-3 activation and caspase inhibition by XIAP. Their modeling analyses focused on the inhibition of caspase-9 and caspase-3 auto-amplification loops by XIAP, and model predictions were confirmed using single cell experiments with cells stably expressing FRET probes that contained a cleavage site for caspase-3. Specifically, their model prediction, that a reduction of XIAP levels would not affect apoptosis timing, while an XIAP overexpression would significantly delay effector caspase activation, could be experimentally verified in HeLa cells and in MCF7 cells which are completely devoid of caspase-3. Similarly,

another prediction that interference on the level of Smac has only weak influences on apoptosis timing was verified. In conclusion, the study of Rehm et al. provided detailed insights into the regulative function of XIAP on the timing of effector caspase activation [55]. Recently, the model was successfully applied to explain lack of effector caspase activation after MOMP in different cancer cell lines as a result from cell death impairing combinations of Apaf-1, procaspase-9, XIAP and procaspase-3 levels [84]. Huber et al. combined approaches from metabolic engineering with the model of Rehm et al. to study the crosstalk between reactions of the respiration chain and the intrinsic apoptosis pathway [58]. Their model quantitatively characterized how an increased glucose level that increases cytosolic ATP production can stabilize the transmembrane potential, a mechanism that may support the cell death evasion of cancer cells.

It can be expected that future research will provide much more detailed insights into the kinetics of apoptosis initiation, since various tools are now available to monitor apoptosis on several signaling levels at the single-cell level: FRET reporters consisting of two fluorescent proteins linked with a cleavage sequence for caspase-8 or caspase-3 were used to monitor the activity of initiator and effector caspases [55, 81, 82, 85]. In the study of Albeck et al. a GFP-tagged form of Bax was used to measure the translocation of Bax into mitochondria upon Bid activation [82]. Furthermore, a reporter protein that contains the mitochondria import sequence of Smac and thus accumulates in the mitochondria inter-membrane space (IMS-RP) was used to indicate MOMP in single cells. Simultaneous and quantitative description of multiple signaling levels will be a major challenge for future modeling studies.

Modeling the ambiguity between cell death and survival Experimental studies by Nair et al. suggested that the mechanisms of cell death and survival can be mutually exclusive [23]. The behavior of a population of cells upon an oxidative stress (H_2O_2) stimulus was observed. While some cells underwent apoptosis, others clearly showed a successful overcoming of the stress stimulus and a proliferative response. However, the paradigm of mutually exclusive cell death or survival processes was challenged in the subsequent experimental and theoretical studies described in this section.

To understand the double-edged role of CD95 (APO-1/Fas) activation in apoptosis as well as in NF- κ B activation, models describing the role of c-FLIP on both cell fates were established [46, 48]. A focus of the models is the balance between caspase activation and inhibitory processes at the DISC. Cleavage of homodimers of the two main procaspase-8 isoforms, procaspase-8a and b (p55 and p53), bound to FADD can result in two forms that possess catalytic activity: an intermediate form p43/p41 that remains bound to the DISC as a homodimer, and the completely processed form p18 that dissociates from the DISC as p18₂-p10₂ heterotetramers [86, 87] (Figure 1.2). Three splicing variants of the cellular FADD-like interleukin-1 β -converting enzyme inhibitory protein (c-FLIP), c-FLIP short (c-FLIP_S), c-FLIP long (c-FLIP_L) and c-FLIP Raji (c-FLIP_R) can heterodimerize with a monomer of procaspase-8 bound

1.2. Mathematical models of apoptosis

to a FADD molecule at the DISC and interfere with caspase-8 activation. The two variants $c\text{-FLIP}_S$ and $c\text{-FLIP}_R$ block procaspase-8 autoprocessing in a heterodimer and therefore inhibit propagation of the apoptosis signal. In contrast, $c\text{-FLIP}_L$ can facilitate procaspase-8 cleavage to p43/p41 but not to p18. Therefore, $c\text{-FLIP}_L$ leads to heterodimers with p43/p41 at the DISC, and these complexes have a certain catalytic activity. While the two forms $c\text{-FLIP}_S$ and $c\text{-FLIP}_R$ clearly inhibit signal propagation, it was not obvious if $c\text{-FLIP}_L$ promotes or also inhibits apoptosis [88–90].

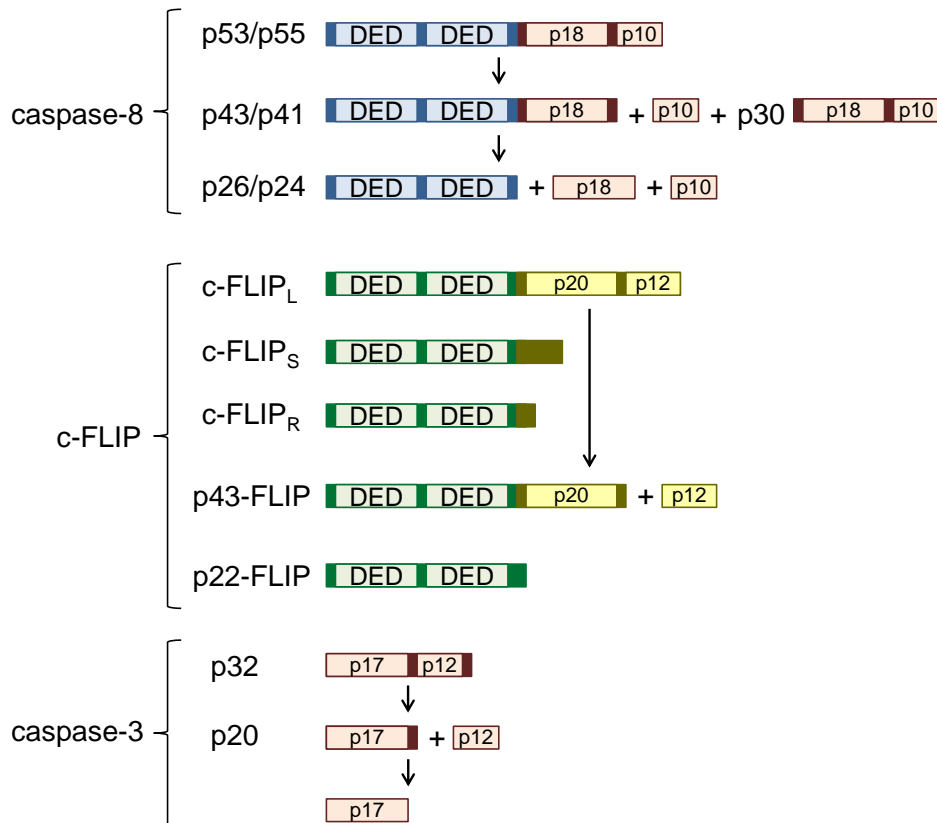


Figure 1.2. Forms of caspase-8, c-FLIP and caspase-3. For caspase-8 activation the two isoforms of procaspase-8, p55 and p53, are cleaved to p43/p41 plus p18 or p26/p24 plus p30. The death effector domains (DEDs) of procaspase-8 can bind to FADD, to other procaspase-8 monomers or to the similar DEDs of c-FLIP proteins. These are $c\text{-FLIP}_L$, $c\text{-FLIP}_S$, $c\text{-FLIP}_R$, and the two cleaved forms p43-FLIP and p22-FLIP, containing catalytically inactive caspase-like domains p20 and p12 [46,91]. Caspase-3 exists as a pre-formed dimer and is activated by cleavage to p17 and p12.

To resolve this question, a study of Fricker et al. on the signaling function of $c\text{-FLIP}_L$ combined experiments and modeling, and showed an ambiguous function of the protein as dependent on the stimulus strength [46]. Their model considered the formation of homodimers of procaspase-8 or heterodimers of procaspase-8 and

c-FLIP variants at the DISC and either termination of further reactions or processing to caspase-8 or p43-FLIP by other active homo- or heterodimers. The model was trained against immunoblot data of procaspase-8 (p55), the intermediate form p43/p41 and caspase-8 (p18 in p18₂-p10₂) at a given ligand concentration. The model predicted that at a low ligand concentration a twenty-fold overexpression of c-FLIPL would lead to a significant reduction of caspase-8 activity. Contrarily it was predicted, that at high ligand concentration, the same overexpression would lead to an acceleration of cell death. The authors could confirm these predictions with time lapse imaging of cells moderately overexpressing c-FLIPL. As the processing of procaspase-8 is relatively fast, and c-FLIPL overexpression therefore can only cause small accelerating effects, Fricker et al. tested their model subsequently in conditions of c-FLIPS or c-FLIPR overexpression. As these c-FLIP variants inhibit caspase-8 activation, an even stronger activating effect of c-FLIPL was predicted. Again the predictions were verified, confirming the predicted ambiguous effect of c-FLIPL being anti-apoptotic at low and pro-apoptotic at high stimulus strengths. The study by Neumann et al. investigated in detail how NF- κ B is activated by CD95L, and how this process is modulated by c-FLIP and caspase-8 [48]. The different possibilities of DISC formation of activated receptors, FADD, procaspase-8, c-FLIPL and c-FLIPS and their processed forms were described in their model: (i) DISCs containing at least two procaspase-8 molecules give rise to p43/p41 dimers and subsequently mature caspase-8. (ii) At DISCs that contain at least one procaspase-8 and one c-FLIPL molecule a heterodimer of p43/p41 and c-FLIPL is created. Besides, several other DISC constitutions preventing further processing were considered. By immunoprecipitation experiments, it was shown that interaction of p43-FLIP with IKK α leads to the phosphorylation of I κ B (NF- κ B·I κ B·P). Phosphorylation of I κ B was previously shown to trigger degradation, thereby promoting NF- κ B activation. The subsequent translocation of NF- κ B into the nucleus after I κ B·P degradation was monitored in live cell experiments. The model matched the dynamics of these processes and the model complexity was iteratively reduced by summarizing or disregarding variables and modeled reactions. The simplification was supervised by means of the fitting accuracy in iterative parameter estimations. The balance between c-FLIPL and procaspase-8 was shown to be responsible for proliferative or apoptotic effects of CD95 stimulation. Regimes of predominant NF- κ B activation or caspase-3 or of both processes could be predicted.

Systems biological studies on the ambiguity towards cell death or survival pathways revealed close interlinks between both processes. A more complicated overall image results when considering connections to other cellular signaling processes. Within the process of cell growth and mitosis, cell cycle regulatory mechanisms can determine pro- or anti-apoptotic conditioning as investigated in the cell cycle model of Pfeuty et al. [92]. Further interlinks exist between cell cycle repair mechanisms leading to cell cycle arrest or apoptosis execution [57]. Additionally, the apoptosis sensitivity is modulated by other cellular stress responses as theoretically analyzed in recent modeling studies [77, 93].

1.2. Mathematical models of apoptosis

Understanding cell-to-cell variability Several new experimental techniques and theoretical approaches were developed to investigate the origins and the role of cellular variability in cell death signaling. In several modeling studies, the effects of randomly choosing initial protein concentration sets from probability distributions to estimate consequences of variable initial protein concentrations were investigated [39, 45, 49, 77].

In general, it is not clear whether cell-to-cell variability in cell signaling mainly arises from stochastic dynamics in biochemical reactions (intrinsic noise) or from the variability of initial protein levels (extrinsic noise). Combining modeling and single cell experiments, it could be shown that heterogeneous apoptosis timing in a population of cells has its origin in the variable initial levels of apoptotic proteins [94]. In single cell experiments using FRET reporters for initiator and effector caspase activity and the MOMP reporter protein IMS-RP, after cell divisions pairs of cells were observed. While the time of apoptosis was highly correlated in the first hours after cell division, correlation in cell death timing ceased in pairs of older sister cells. This correlation was sustained over a longer period of time by inhibition of protein synthesis. Thereby it was demonstrated that the variability of protein levels arising from noise in gene expression is responsible for cell-to-cell variability in apoptosis timing rather than genetic mutations or epigenetic differences that occur on a larger time scale. By combining single cell experiments with the model of Albeck et al. it was verified that the time of apoptosis is dependent on the concentrations of several signaling proteins upstream of MOMP [39]. Thus, the control of apoptosis timing appears to be distributed over many protein expression levels. Only when overexpressing single signaling proteins as Bid, the dependency of single protein concentration increases. Based on the same model, Gaudet et al. simulated the effects of protein level changes on the variability of cell fates. Their study characterized to which degree variability in cell fate decisions depends on the levels of involved signaling proteins, and how variances of initial protein levels and covariances between protein levels impact on the variability of characteristic features as the time of MOMP or the time when half of the effector caspase substrate PARP is cleaved [95]. In particular, it was pointed out that altering the initial level of a certain model species can strongly change the influence of the variability of involved signaling species on cell death kinetics, termed contextual sensitivity.

As an alternative approach to link the possible behavior of heterogeneous single cells to their population level measures at certain time points of a dynamic process, Hasenauer et al. developed methods based on parameter probability densities [96]. These were demonstrated on a synthetic data set for a simple model of tumor necrosis factor (TNF) signaling [97]. The original parameter densities could successfully be estimated from simulated flow cytometric data.

Taken together, cell-to-cell variability is an inherently complex phenomenon that can only be tackled by quantitative approaches. ODE modeling combined with sensitivity analysis and stochastic modeling became valuable tools in this field of apoptosis research.

Conclusions and future perspective of cell death modeling Apoptosis is a well-characterized biological process amenable to mathematical modeling. Mechanistic models provided valuable insights into nonlinear phenomena such as all-or-none switching and irreversible decision making. Modeling reconciled apparently contradictory observations at the single-cell and population level, and was employed to identify molecular mechanisms controlling whether a cell enters death via the type I or type II pathway of apoptosis [42–44,98]. In particular, the study by Hua et al. verified corresponding model predictions experimentally, and showed that the anti-apoptotic influence of Bcl-2 is completely lost in type II cells in the case of procaspase-8 overexpression [43]. Lyapunov coefficients served as a tool to predict under which conditions changes in initial protein concentrations cells shift from a type I to a type II apoptosis behavior. Specifically, this method showed that the ratio between caspase-3 and XIAP determines the type of cell death [98]. Non-intuitive feedback loops arising implicitly from the apoptosis network structure could be identified by simulation analysis [52,54]. The crosstalk between cell death and survival signaling is much less understood; here, modeling was mostly restricted to top-down and qualitative approaches owing to crosstalk complexity. However, quantitative modeling and sensitivity analysis are required to predict effective co-treatment strategies for cancer cells that often harbor combined mutations in interdependent growth factor and apoptosis networks. Currently, a major limitation is our incomplete understanding of autophagy ('self eating') which shares many molecular components with the apoptosis machinery (e.g. Bcl-2 family members) [99,100]. Depending on the cell type, autophagy protects cells from death by removing damaged organelles or it triggers another form of cell death, further complicating the apoptosis survival network. Another limitation of current models is that they mainly focus on extrinsic apoptosis induced by death ligands. However, most pharmacologically relevant responses, e.g., during chemotherapy, proceed via the intrinsic mitochondrial pathway. The intrinsic pathway includes another layer of complexity, as it requires transcriptional regulation, e.g., of Bcl-2 protein family regulators (Puma, Noxa). Quantitative gene expression profiling and chromatin immunoprecipitation (ChIP) studies combined with systematic molecular perturbations are required to quantitatively model gene regulatory networks controlling intrinsic apoptosis. Antagonists inhibiting the Inhibitor of Apoptosis (IAP) proteins appear to be promising therapeutics, as they selectively kill cancer cells in the absence of further stimulation. Apoptosis models taking into account basal state signaling are required to understand and to optimize such therapeutic approaches. Live-cell imaging and flow cytometric approaches led to insights into apoptosis at the single cell level, and revealed principles of cell-to-cell variability [55,94]. Further experimental and theoretical analyses are required to understand how complete eradication of tumor cell populations can be achieved. In principle, it might be possible that nonlinear phenomena such as bistability give rise to tumor cell sub-populations that are completely insensitive to therapy. Moreover, single cells may differ in the apoptosis pathways they employ, implying that combinatorial inhibition of multiple pathways is required for elimination of the whole tumor. This requires the development of new parameter estimation tools which

1.3. Biochemical basics of erythropoietin receptor signaling

take into account cell-to-cell variability, and integrate population-based as well as single-cell measurements.

1.3. Biochemical basics of erythropoietin receptor signaling

The glycoprotein hormone erythropoietin (Epo) regulates the production of red blood cells by binding to the Erythropoietin receptor (EpoR) at the plasma membrane of hematopoietic precursor cells in the bone marrow [101]. It is used to treat renal anemia, tumor anemia, and is applied as an adjuvant therapeutic agent in anemia resulting from chemotherapy induced bone marrow depression [102]. Non-erythropoietic effects of Epo, as protection of neurons after stroke or cardiomyocytes after cardiac infarction, are the subject of current research [103].

The signal transduction mechanism of EpoR is similar to other cytokine receptors, in which a ligand stimulus is translated to a response on the level of gene transcription. After binding to dimeric EpoR, associated Janus kinase 2 (JAK2) enzymes are brought into proximity and can phosphorylate each other (Figure 1.3). Auto-activated JAK2 then phosphorylates tyrosyl residues at EpoR, which allows binding of STAT5 monomers that are subsequently phosphorylated by JAK2 [104]. Phosphorylated STAT5, after being released from EpoR, dimerizes and is then actively transported to the nucleus where it binds to its consensus sequences and induces the transcription of specific genes [105]. After dephosphorylation, STAT5 re-enters the signaling cycle [106]. On the level of transcription, STAT5 activation stimulates the differentiation of erythroid progenitor cells and inhibits their apoptotic demise [107–109].

The signal transduction cascade from an Epo stimulus to a transcriptional response is an example for the general physiological principle of receptor signaling in cells. General questions in research on ligand-receptor signaling address mechanisms, by which cells shape the response towards a certain ligand stimulus that can be translated to a specific cellular fate:

- (i) How does receptor shuttling between the intracellular pool and the membrane, the internalization of active receptors and receptor recycling influence the signal response dynamics of a cytokine? Cells can adapt to a certain stimulus and translate a continuous stimulus to a transient response by negative feedback, a mechanism termed “perfect adaptation” [110], as it is the case for cytokine receptors of the immune system [111]. Contrarily, a pulse stimulus can be translated to a constant response due to a bistable switch, which can result from the combination of positive feedback and cooperativity, as it is the case for $TGF\beta$ [112] or progesterone signaling [113]. The cellular response towards epidermal growth factor (EGF) is a classic example for adaptation to a cytokine stimulus by internalization and subsequent degradation of activated receptors, which effectively reduces the fraction of receptors contributing to signal trans-

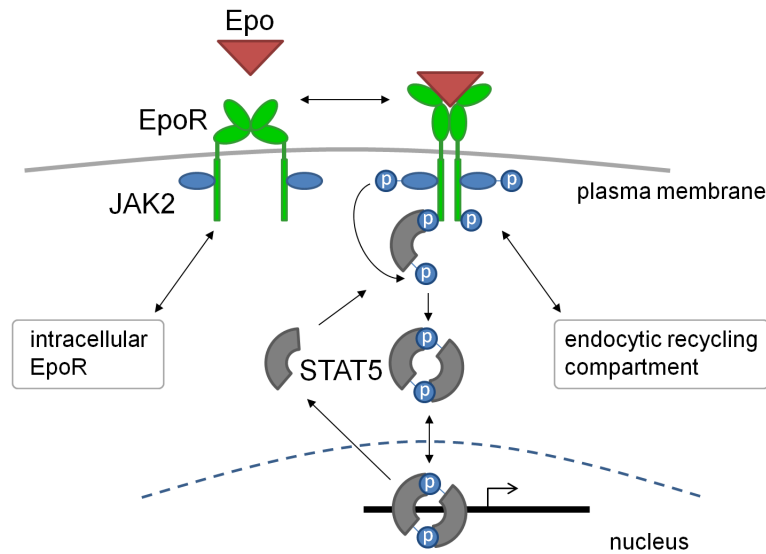


Figure 1.3. EpoR activated JAK-STAT signaling. Upon Epo binding, JAK2 is autophosphorylated and phosphorylates tyrosyl residues at EpoR, thus enabling STAT5 activation and a specific transcriptional response.

duction [114]. In this example, receptor trafficking effectively modulates signal transduction [115, 116].

- (ii) How is receptor signaling regulated by mechanisms involving post-translational modifications? In the example of EpoR, besides the direct involvement of kinases and phosphatases in signaling, other modifications were found to take influence on signal transduction. EpoR phosphorylation was found to be responsible for receptor internalization mediated by the PI3K subunit p85, which is impaired in patients with primary familial and congenital polycythemia [117]. Ubiquitylation was shown to trigger internalization and degradation of EpoR, dependent on which lysyl residues of the EpoR are targeted [118].
- (iii) Which receptor traffic processes should be targeted by modifying the properties of an Epo mimetic drug in order to optimize the therapeutic effect towards a heterogeneous population of target cells? Due to variability, in some cells adaptation mechanisms could lead to a weak response, while only in a fraction of cells a therapeutic effect will be achieved. In this context, understanding sources of cell-to-cell variability might help to optimize therapeutic applications with respect to heterogeneity in the dynamics of receptor traffic.

1.4. Mathematical models of erythropoietin receptor signaling

Studies on EpoR signaling that were based on mathematical models mainly focused two processes, either the dynamics of EpoR traffic or the STAT induced transcriptional responses. The JAK-STAT signaling pathway, which links receptor activation of several cytokine receptors at the plasma membrane to transcriptional responses, was extensively characterized by ODE models [119, 120]. Because of the high relevance of Epo for clinical applications, Epo models were motivated by the development of new strategies for optimizing its efficiency, and by defining a therapeutic window for stimulating hematopoiesis but not tumor growth [121].

Several Epo mimetic drugs were developed to enhance the therapeutic effect of stimulating erythropoiesis [122]. Amongst them, NESP is a hyperglycosylated Epo variant, which has, compared to Epo, a lower affinity to the EpoR and a higher dissociation rate. Nevertheless, NESP can more efficiently stimulate erythropoiesis. A modeling study by Gross and Lodish, based on surface bound and internalized amounts of radioactively labeled ligand in a population of cells, showed that only differences in NESP and Epo with regard to receptor binding and unbinding were responsible for the higher efficiency of NESP [123]. However, other processes as internalization, resecretion or degradation of the ligand, were equally fast for both ligands. Compared to Epo, NESP yielded higher efficiency, as a smaller fraction is internalized and degraded due to its faster unbinding. An important aspect of EpoR signaling is the large intracellular receptor pool compared to a small receptor fraction at the membrane. The study of Becker et al. showed that the fast cycling between the plasma membrane and the intracellular pool in combination with an accelerated internalization of active membrane bound EpoR, facilitates signaling over a broad dynamic range of ligand concentrations [124]. As a result, the time integral of active EpoR after ligand addition is linearly dependent on the ligand concentration in the medium. Therefore, the EpoR system functions as a linear integrator over a large interval of Epo concentrations. The kinetic behavior of the induced STAT5 activation and its nuclear translocation was addressed in the study by Swameye et al., which showed that the steps of nuclear import and export are the most sensitive processes in the Epo system towards external perturbations [106]. A further modeling study addressed regulatory mechanisms that modulate the induced STAT5 response, which was based on western blot measurements of STAT5 and JAK-STAT signaling regulators [125]. Inhibitory effects from the two relevant JAK-STAT regulators CIS and SOCS3 were quantitatively characterized and linked to the cellular survival supporting effect of STAT5 activation. While CIS provided an effective negative feedback at low Epo concentrations, due to direct interference with STAT binding to active EpoR, negative feedback from SOCS3, which inhibits both STAT5 dimerization and interference with STAT5 binding to EpoR, became predominant at high Epo concentrations.

In summary, the dynamics of EpoR traffic and Epo induced transcriptional re-

sponses were accurately characterized by ODE modeling studies on the level of cellular populations. So far, no study addressed cell-to-cell variability in Epo signaling, which motivated for the project described in part II.

2. Methods

The cell ensemble models of apoptosis initiation and Epo receptor traffic described in this thesis were calibrated with experimental data at the single-cell and cell population level. The single-cell behavior was characterized using confocal microscopy. Population-based assays included western blotting and fluorescence activated cell sorting (FACS). This chapter describes basic principles underlying these experimental techniques, and explains the experimental procedures in detail (sections 2.1 and 2.2). Section 2.3 describes how mathematical models were fitted to experimental data and how the model parameters were estimated. Section 2.3 contains parts of the book chapter by Kallenberger et al. in *Computational Systems Biology* [2], and section 2.2 contains parts of a submitted manuscript by Kallenberger et al. [126].

2.1. Confocal fluorescence microscopy

Confocal microscopy

The basic principle of confocal microscopy is that the excitation source and the detector system are focused on the same optical plane, while a pinhole allows only light from a small region of the optical plane to be passed to the detector (Figure 2.1) [127]. For this purpose, contrary to conventional widefield microscopy, not the whole sample but only a small focus spot is illuminated. To record an image from a fluorescent object the microscopic sample is illuminated point-wise, typically by employing the collimated light of a laser. The principle of confocal microscopy was originally developed by the mathematician and neuroscientist M. Minsky to optimize imaging of neurons [128]. As the pinhole prevents that light from other regions than the focus spot reaches the detector, planes at defined depths can be imaged, and the signal-to-noise ratio is significantly improved compared to conventional widefield microscopy.

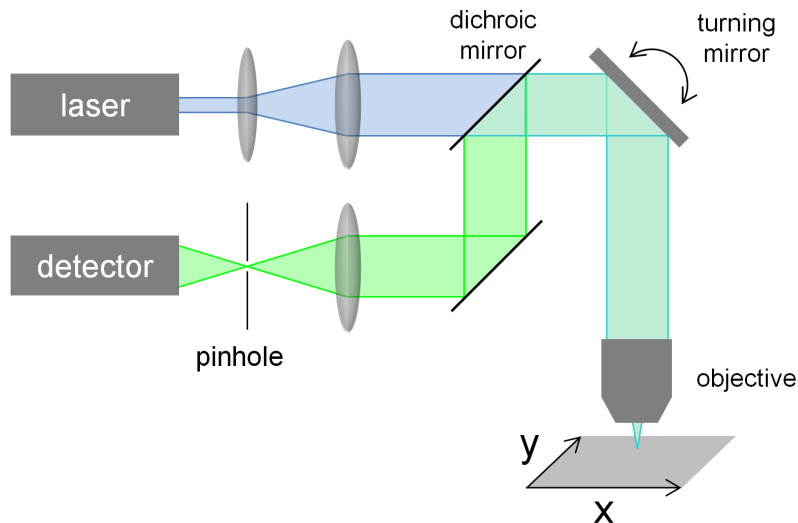


Figure 2.1. Principle of a confocal microscope. A laser beam is expanded, passes a dichroic mirror and is focused by the microscope objective to a point at the fluorescent sample. On the same optical path, light from the sample is reflected by the dichroic mirror and passes the pinhole, which excludes light from other locations than the focal spot. An image is recorded by iteratively moving the focal spot with the turning mirror to an array of positions in the focal plane. The figure was modified after [129, 130].

The resolution of a microscope objective is limited by the wavelength λ and the optical properties of the objective due to diffraction. A point in the plane of an object in the distance d_{obj} from the lens with radius R is imaged to an Airy pattern in the distance d_{im} from the lens. The first minimum of the Airy pattern is located at the angle θ from the center of the diffraction pattern, with $\sin \theta = 0.61\lambda/R$, according to the first zero of the intensity distribution that contains a first-order Bessel function. This results in the radius

$$r_{diff} \approx 0.61\lambda d_{im}/R \quad (2.1)$$

of the inner disk-shaped area of the diffraction pattern. To be able to distinguish two nearby diffraction disks from two image points, they have to be in a distance larger than the diffraction disk radius r_{diff} , which can be translated to a minimal distance Δx of two points in the plane of the imaged object that can still be resolved. Using the relation between the object and image sizes for a lens and Equation 2.1, the minimal resolvable distance reads $\Delta x = r_{diff} d_{obj}/d_{im} = 0.61\lambda d_{obj}/R \approx 0.61\lambda f/R$, assuming $d_{obj} \approx f$ as the object is close to the focus plane in the distance f from the lens. For the object the maximal angle of aperture is 2α , with $2 \sin \alpha = 2R/f$. Using this relation the minimal resolvable distance, i.e. the lateral resolution $r_{lateral}$, reads $r_{lateral} \equiv \Delta x = 0.61 \frac{\lambda}{\sin \alpha}$. To increase the resolution, immersion oil between the object and the lens is used to decrease the wavelength according to the diffraction index $n \approx 1.5$ to $\lambda_0 = \lambda/n$. The product $n \sin \alpha$, termed numerical aperture NA , describes the optical properties of an objective and had a value of $NA = 1.4$ in the used setup. The lateral resolution then reads

2.1. Confocal fluorescence microscopy

$$r_{lateral} = 0.61 \frac{\lambda_0}{n \sin \alpha} = 0.61 \frac{\lambda_0}{NA}. \quad (2.2)$$

In a confocal microscope the pinhole size is measured in Airy units AU . A size of $1AU$ accords to the size of the diameter of the central Airy disk in the plane of the pinhole. The intensity distribution of the diffraction pattern in the image of a point is termed point spread function (PSF). In a simple microscope consisting of two lenses the PSF is given by an Airy pattern. At small pinhole sizes, as described in [127], the total PSF can be approximated by the product of the PSFs for the excitation light path and for the detection light path,

$$PSF_{confocal} \approx PSF_{excitation} \cdot PSF_{detection}. \quad (2.3)$$

In an epi-fluorescence microscope, as shown in Figure 2.1, the total PSF is equal to the squared PSF of the objective, as it is simultaneously used for excitation and detection. The inner disk between the maximum and the first minimum of an Airy pattern can be well approximated by a Gaussian function $I(r) = I_0 \exp(-(r-r_0)^2/2\sigma^2)$. Therefore, the total PSF for an epi-fluorescence confocal microscope can be approximated by a Gaussian with the smaller standard deviation $\tilde{\sigma} = \sigma/\sqrt{2}$. For this reason, the lateral resolution in a confocal microscope is decreased, compared to a widefield microscope, by a factor of approximately $\sqrt{2}$, which results in an improved lateral resolution of

$$r_{lat,confocal} = 0.43 \frac{\lambda_0}{NA}. \quad (2.4)$$

The axial resolution is equivalent to the full width at half maximum (FWHM) of the PSF, and can be approximated by the term

$$r_{axial} \equiv \text{FWHM}_{axial} \approx \frac{0.88\lambda_0}{n - \sqrt{n^2 - NA^2}}, \quad (2.5)$$

which is valid for pinhole sizes around $1AU$ [127, 131]. In the microscope that was used for live-cell imaging experiments the lateral resolution was about $r_{lateral} \approx 144nm$ and the axial resolution $r_{axial} \approx 0.5\mu m$. Single cell measurements were conducted with a spinning disk confocal microscope that was optimized for fast image recording, weak photobleaching and low phototoxicity for cells.

Spinning disc microscopy

To improve the velocity of image acquisition, microscopy techniques were invented, in which larger areas of an object can be imaged simultaneously. A widened laser beam is subdivided by an array of holes and is focused on an array of spots the object plane. The pattern of focus spots is arranged in a way that the magnified image of the spot pattern accords to the pixel array of a CCD camera for recording the fluorescence intensity from each spot. A spinning disk microscope uses a *Nipkow disk*, which is a rotating disk with spirals of equally sized holes that has been used for displaying

images on early cathode ray screens [132]. Each hole of one spiral covers a radial interval Δr to record the image of a sector part between two circles $(r_{max} - r_{min})\Delta\varphi$ in one disk rotation. The employed setup makes use of the Yokogawa technique, in which a first disk of 20.000 microlenses focuses laser light on the corresponding pinholes in the second disk (Figure 2.2) [133].

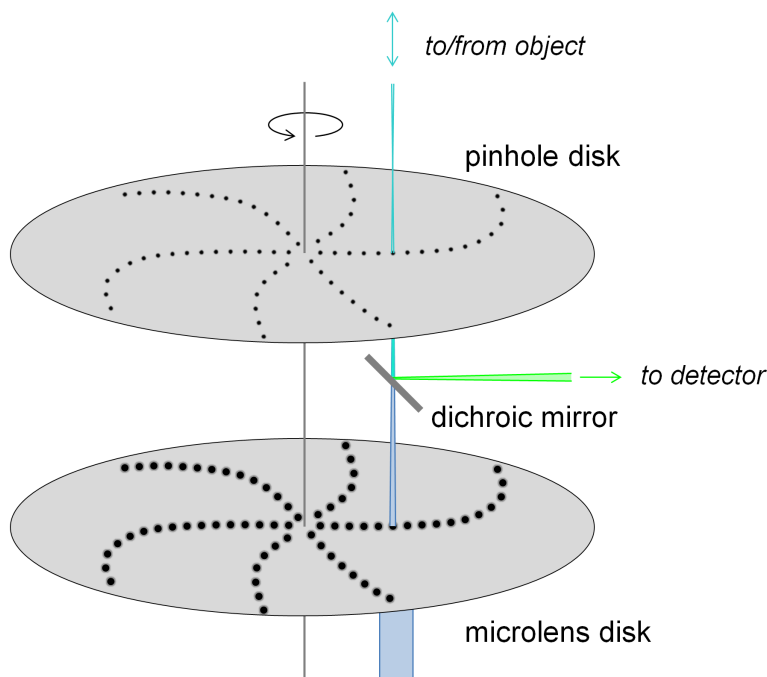


Figure 2.2. Principle of a spinning disk confocal microscope. A rotating microlens disk focuses coherent blue light (in the case of imaging GFP) to an equally oriented pinhole disk that simultaneously collimates green light from focus spots in the object plane, which is transmitted by a dichroic mirror to the detector, modified after [127].

The disk contains 12 spirals, which means that rotation by 30° is required to record one image, resulting in a typical speed of one frame per millisecond at 5000 rotations per minute. The image is projected on a CCD camera that is synchronized with disk rotation.

In the absence of a microlens disk the pinhole disk blocks a large amount of laser light. The transmission factor $T = (D/S)^2$, calculated from the pinhole diameter D and the distance S between adjacent pinholes, quantifies the fraction of the excitation light that is used for imaging [127]. For conventional confocal microscopes the transmission factor is around 50%, while spinning disk microscopes without a microlens disk would have a transmission factor of around 5% only. Using a microlens disk, a transmission factor of about 40% can be achieved [133].

2.1. Confocal fluorescence microscopy

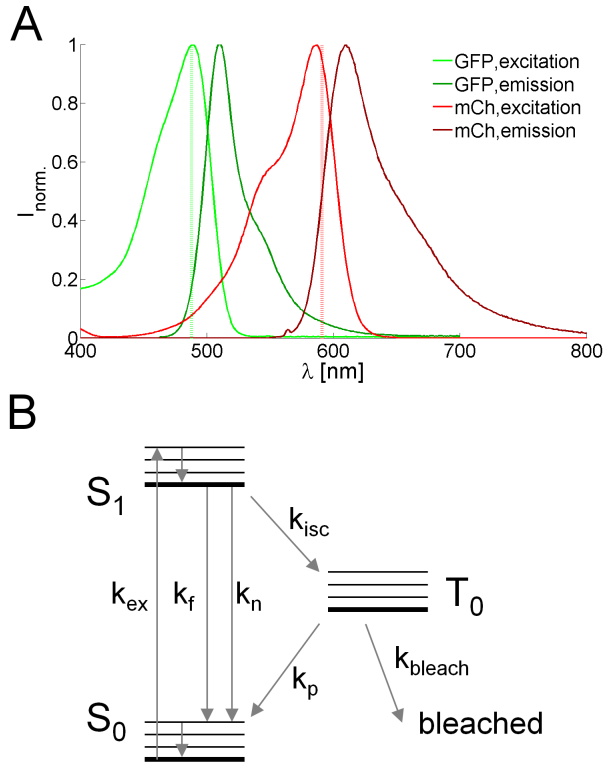


Figure 2.3. Employing fluorescent proteins for microscopy. (A) Emission and excitation spectra for eGFP and mCherry (mCh) (data were taken from <http://spectra.arizona.edu>). For live-cell experiments GFP was excited at 488nm and mCherry at 591nm (dotted vertical lines). (B) Jablonski diagram indicating electronic excited states (thick lines) with vibrational modes (thin lines) and transition rates in an ensemble of molecules (k_{ex} : excitation rate, k_f : fluorescence rate, k_n : rate of non-radiative relaxation, k_{isc} : interstate conversion rate, k_p : phosphorescence rate, k_{bleach} : bleaching rate, relaxation from vibrationally excited to ground states are fast and can be seen in equilibrium compared to other transitions), modified after [134].

Basics of fluorescence

Fluorescent molecules as GFP or mCherry that are used for confocal microscopy of cells can be excited by absorbing a photon with the energy $h\nu_{\text{exc}}$ according to their excitation spectra (Figure 2.3A). Then, the molecule switches to an excited electronic state implicating the transition of an electron to an unoccupied orbital that is separated by the absorbed energy amount. This transition can be visualized in a *Jablonski diagram*, in which the rotational, vibrational and electronic energies of a molecule are added in order to simultaneously show the different energetic states.

Figure 2.3B shows three electronic states, which are two singlet states S_0 and S_1 with equal antiparallel spins and a triplet state T_0 with parallel spins. Electronic states are visualized as thick horizontal lines, while nuclear vibrational levels for each state are symbolized by thin lines. When a molecule in the state S_0 absorbs a photon with $h\nu_{\text{exc}}$ the molecule changes to a vibrationally excited state S_1 and rapidly relaxates to the vibrational ground state of S_1 . Then, the molecule can change back either by fluorescence or non-radiative internal conversion. Fluorescence implicates that a photon with the energy $h\nu_{\text{em}}$ is emitted, and the molecule typically changes to a vibrationally excited S_0 mode, which can relaxate to its ground state. As the molecule quickly relaxates from vibrationally excited to ground modes in S_1 before fluorescence, and in S_0 after fluorescence, the frequency of the emitted photon $\nu_{\text{em}} = (\nu_{\text{exc}} - E_{\text{rel}}/h)$ is red-shifted due to possible energy losses E_{rel} in these non-

radiative transitions, termed *Stokes shift*, which results in the red-shifted emission spectrum (Figure 2.3A). Besides fluorescence, the molecule can change from S_1 to S_0 by internal conversion, without emitting a photon, due to distributing the absorbed energy by other processes. The third possibility, termed intersystem conversion, implies a non-radiative transition occurring with a spin-flip of the electron to a triplet state T_0 . For the transition from this state back to S_0 the spin multiplicity has to be changed as it requires a spin-flip, and is therefore kinetically unfavored, which leads to a long half-life of the state T_0 . Such a metastable state is the requirement for phosphorescence, which denotes the delayed relaxation to S_0 and the emission of a photon with a larger wavelength compared to the exciting photon. Due to the long half-life of T_0 , which can be in the range of milliseconds to hours, the chance for photochemical destruction of the molecule, termed photobleaching, is increased in this state. When describing an ensemble of fluorescent molecules, the transitions between different states can be described with rates that are proportional to the transition probabilities for single molecules (Figure 2.3B). From the rates for fluorescence (k_f), non-radiative internal conversion (k_n) and interstate conversion (k_{isc}), the quantum efficiency

$$QE = \frac{k_f}{k_f + k_n + k_{isc}} \quad (2.6)$$

can be calculated, which is proportional to the number of photons emitted by fluorescence divided by the number of absorbed photons [134]. For variants of the fluorescent protein GFP, the quantum efficiency is in the range between 0.65 and 0.72 [135].

2.2. Biochemical experimental methods

Cell lines and cell culture

For apoptosis modeling (part I) stable cell lines were generated from wild type HeLa cells. CD95R-HeLa and the HeLa cell lines stably expressing procaspase-8-mGFP were described in [136]. From HeLa wt and CD95R-HeLa cells, probe or GFP fusion expressing cell lines were selected with 0.8mg/ml G418 (Sigma-Aldrich, Taufkirchen, Germany).

For erythropoietin receptor modeling (part II) stable cell lines were generated from EpoR-GFP-H838 cells, stably expressing EpoR-GFP, which were obtained from the group of Prof. Ursula Klingmüller at the German Cancer Research Center in Heidelberg. A cell line that stably expressed fusions of the myristoylation-palmitoylation (MyrPalm) with mCherry (MyrPalm-mCh) was generated by transfection of EpoR-GFP-H838 cells and selection with 0.8mg/ml G418.

Cell lines were maintained in DMEM (Invitrogen, Darmstadt, Germany) containing 10% fetal calf serum (Biocrom AG, Berlin, Germany), 100µg/ml penicillin and streptomycin (Invitrogen), stably transfected cell lines additionally with 0.2 mg/ml G418 or 0.2µg/ml puromycin (Sigma-Aldrich). Cells were transfected with Fugene

2.2. Biochemical experimental methods

6 (Roche, Basel, Switzerland). For microscopy, cells were maintained in 8-well Lab-Tek chambers (Thermo Scientific, Asheville, NC, USA) with a density of 40.000/well, for western blot experiments in 2-well Lab-Tek chambers at the same density as for single cell experiments (204.000/well).

Antibodies and reagents

For apoptosis modeling (part I), caspase-8 was detected by C-15 antibody [137], which was a kind gift of Peter Krammer. Furthermore, anti-FADD (Cell Signaling), anti-BID (Cell Signaling, Danvers, MA, USA), anti-5F8 (Chromotek) and anti-GFP (Roche Diagnostics) antibodies were used. Horseradish peroxidase-conjugated secondary antibodies (Southern Biotech, Birmingham, AL, USA) were used for detection. For flow cytometry secondary antibodies coupled to Alexa Fluor 488, goat anti rabbit or goat anti mouse (Invitrogen) were used. Cell death was induced with T4-CD95 ligand (Apogenix, Heidelberg, Germany) in all experiments, except for the combined FRET and NES probe cleavage experiment (Figure 4.4), and prodomain probe cleavage experiments (Figures 7.11 and 7.12), where LZ-sCD95 ligand [138] was used that was expressed in 293T cells as described in [136].

For erythropoietin receptor modeling (part II), Cy5.5 stained Epo was obtained from Roche Diagnostics GmbH (Penzberg, Germany).

DNA constructs

The ER-anchored probe from the calnexin-LQTDG-YFP was built as described in [136] by replacing the ELQTDG cleavage sequence by GIETDS and by shortening the luminal domain of Calnexin by removing residues 25 to 462. For the NES probe used in live-cell experiments to generate single cell observables for model fitting, the NES sequence MNLVDLQKKLEELDEQQ was fused to the cleavage sequence GIETDS (caspase-3), followed by a linker and mCherry (NES-GIETDS-mCh) as described in [136]. Furthermore, NES probes containing the part C164 to K231 of the caspase-8 prodomain linker with cleavage sites D210, D216 and D223 as cleavage sequence, or containing the not cleavable sequence DEVA were created. The Calnexin construct was cloned in the pEGFP N1 vector (BD Biosciences, Franklin Lakes, NJ, USA) and the NES sequence, its promoter region and its polyadenylation signal were cloned into the Calnexin construct on the other side of the enhancer region of the CMV to generate a bidirectional CMV promoter.

FADD was fused to mGFP [139] with the linker PRARDPTSGGGGGPVAT and cloned in the pIRES-Neo3 vector (BD Biosciences). BID was fused to mGFP C-terminally and mCherry N-terminally with the linkers GSIAT and RSRG respectively and cloned in the PEGFP N1 vector. Myristoylation-palmitoylation (Myr-Palm) probes were constructed as described in [136]. The MyrPalm domain was fused to a spacer of snap tags, alternative cleavage sequences and either mCherry or mGFP. Cleavage sequences were either MTISDS (caspase-8 prodomain, D210), PREQDS (caspase-8 prodomain, D216), PVETDS (caspase-8 enzymatic subdomain linker, D374) or ELQTDG (BID).

Analysis of total cellular lysates and protein quantifications

Western blot samples were lysed with lysis buffer (20mM Tris/HCl, pH 7.5, 150mM NaCl, 1mM phenylmethylsulfonyl fluoride (Sigma-Aldrich), protease inhibitor cocktail, 1% Triton X-100 (Serva, Mannheim, Germany), and 10% glycerol). Lysates were analyzed using SDS PAGE gels (Invitrogen). The different time points were loaded in a random manner to avoid quantification bias (Figures A.8 and A.9). Proteins were transferred to PVDF membrane (Millipore, Billerica, MA, USA) using wet blotting. Detection was performed using the Pico Chemiluminescent Substrate from Thermo Scientific and a CCD camera (Intas, Göttingen, Germany).

In probe expressing CD95-HeLa and HeLa wt cell lines that were used for time series experiments we quantified endogenous FADD, p55 and BID levels with help of calibrated GFP fusion proteins (Figures A.10-A.12). First, GFP fusion protein lysates were calibrated to recombinant eGFP (BioVision, Mountain View, CA, USA). Therefore, we loaded different amounts between 0.1 and 30ng of GFP mixed with equal amounts of cell lysate of non-transfected cells together with lysates of fusion protein expressing cells to western blot gels. Then calibrated fusion protein lysates were loaded at different amounts to western blot gels together with lysates from the cleavage probe expressing cell lines that were used for time series experiments.

Flow cytometry

To estimate the numbers of surface CD95 receptors and parameters μ and σ for log-normal distributions $\mathcal{LN}(\mu, \sigma)$ of initial protein concentrations by flow cytometry, we used QIFIKIT calibration beads (Dako, Glostrup, Denmark) with five different antibody epitope numbers per bead, according to the manufacturers' protocol (Figure A.13). To obtain parameters σ for lognormal distributions of initial protein concentrations for FADD, p55 and BID, we used a protocol for intracellular immunostaining of fixed permeabilized cells (Figure A.14). For each experiment, 5×10^5 cells were washed in blocking buffer (0.04M sucrose, 1x PBS, 1% BSA), fixated with 4% PFA before primary and secondary antibody staining in 1x PBS with 1% BSA. Between each step, cells were washed three times with 0.04M sucrose in 1x PBS, respectively. Samples were measured on a modified flow cytometer, FC500/MPL (Beckman Coulter, Brea, CA, USA) at 488nm with a 20mW solid state laser (Coherent Inc., Santa Clara, CA, USA). For estimations of distribution parameters the FACS events were gated for narrow forward scatter and side scatter intensity intervals to include cells with similar volumes.

Live-cell imaging and simultaneous western blot sample preparation

Live-cell experiments were performed in a 37°C, 5% CO₂ incubation chamber on a Yokogawa spinning disk confocal on a Nikon Ti inverted microscope equipped with 63x Plan Apo NA 1.4 objective lens and the Perfect Focus System for continuous maintenance of the focus, using MetaMorph 7 software (Nikon, Tokyo, Japan). GFP (Calnsh-GIETDS-mGFP) fluorescence was excited at 491nm with a 100mW solid state laser and collected with a 525/50 emission filter (Chroma Technology Corp,

2.3. Mathematical modeling with systems of ODEs

Bellows Falls, VT, USA) and an exposure time of 70ms. Cherry (NES-GIETDS-mCh) fluorescence was excited at 561nm with a 200mW solid state laser and collected with a 620/60 emission filter (Chroma Technology Corp). A binning of 4x4 pixels was used. At the beginning of each experiment a z-Stack with 20 slides at 0.7 μ m step size was recorded, followed by recording single slides in the stack center every two minutes (CD95-HeLa cells) or three minutes (HeLa wt cells).

Western blot samples were obtained from $2 \cdot 10^5$ cells in two well Lab-Tek chambers for each time point, kept inside a microscope incubation chamber to obtain equivalent experimental conditions as for the imaged single cells. For every time point Lab-Teks were instantly transferred on an ice-cooled metal block, washed in ice-cooled $1 \times$ PBS before treatment with ice-cooled lysis buffer, and harvested with cell scrapers (BD Biosciences).

2.3. Mathematical modeling with systems of ODEs

Parameter estimation in ODE models

In a biochemical system, knowledge on interactions between signaling species can be translated to a system of coupled ordinary differential equations

$$\frac{d\vec{x}}{dt} = f(\vec{x}, \vec{p}, u) \quad (2.7)$$

that describe the dynamics of concentrations \vec{x} of n model species, kinetic parameters \vec{p} and an external stimulus u . The observables

$$\vec{y} = g(\vec{s}, \vec{x}) + \vec{\varepsilon}, \quad (2.8)$$

which link the model variables to time series of experimental measurements, are functions of concentrations \vec{x} , scaling factors \vec{s} , and a noise term $\vec{\varepsilon}$. Usually, observables y_j with $j = 1, \dots, m$ are linearly dependent on single variables x_i or linear combinations of variables. To then estimate the parameters \vec{p} , \vec{x}_0 and \vec{s} , the distance between experimental data \tilde{y}_{jk} for d_j time points with $k = 1, \dots, d_j$ and corresponding observable values $y_{jk}(\vec{p}, \vec{x}_0, \vec{s})$ for a given set of parameters is minimized. For this purpose, usually the weighted sum of residuals

$$\chi^2(\vec{p}, \vec{x}_0, \vec{s}) = \sum_{j=1}^m \sum_{k=1}^{d_j} \left(\frac{\tilde{y}_{jk} - y_{jk}(\vec{p}, \vec{x}_0, \vec{s})}{\sigma_{j,k}} \right)^2, \quad (2.9)$$

with measurement errors $\sigma_{j,k}$ for each time point serves as objective function, which is iteratively minimized [140–142]. Therein, the errors $\sigma_{j,k}$ are assumed to be normally distributed. Minimizing χ^2 is equivalent to maximizing the logarithmic likelihood that the data set \tilde{y}_{jk} plus or minus a certain deviation Δy occurs for the observables $y_{jk}(\vec{p}, \vec{x}_0, \vec{s})$ of a certain model [140]. The likelihood function for the data set of with normally distributed measurement errors reads

$$L(\tilde{y}_{jk}) = \prod_{j=1}^m \prod_{k=1}^{d_j} \exp \left[-\frac{1}{2} \left(\frac{\tilde{y}_{jk} - y_{jk}}{\sigma_{j,k}} \right)^2 \Delta y \right]. \quad (2.10)$$

Accordingly, the log-likelihood for the total number of data points $N = \sum_{j=1}^m d_j$, with Equation 2.9 reads

$$\ln L = N \ln \Delta y - \frac{1}{2} \chi^2. \quad (2.11)$$

Therefore, minimizing $\chi^2 = \text{const.} - 2 \ln L$ maximizes the corresponding log-likelihood. The following paragraphs describe strategies that are employed to minimize χ^2 .

Strategies for parameter fitting

To minimize the residual function and find an optimal set of parameters, gradient based optimization algorithms are employed that either directly follow gradients of the residual function (line search algorithms) or employ a model that approximates the residual function in a certain region of the parameter space (trustregion algorithms).

In general, for a function $f(\vec{r})$ of $\vec{r} \in \mathbb{R}^n$, which in the case of χ^2 minimization contains the set of parameters $(\vec{p}, \vec{x}_0, \vec{s})$, the problem

$$f(\vec{r}) = \min!$$

has to be solved.

Line search methods

In line search methods a series of points

$$\vec{r}_{k+1} = \vec{r}_k + \alpha_k \vec{d}_k$$

is calculated, moving to the iteratively updated directions \vec{d}_k by the step width α_k , such that $f(\vec{r}_{k+1}) < f(\vec{r}_k)$ until a certain criterion as $\nabla f(\vec{r}) < c$ with a small $c \in \mathbb{R}$ is fulfilled, as described in [143]. A simple approach is the steepest gradient method, in which the direction accords to the steepest gradient $\vec{d}_k = -\nabla f(\vec{r}_k)$ and the series to $\vec{r}_{k+1} = \vec{r}_k - \alpha_k \nabla f(\vec{r}_k)$. A faster converging approach is the Newton method. At a point \vec{r}_k the function $f(\vec{r})$ is approximated by the second order Taylor series

$$m(\vec{r}) = f(\vec{r}_k) + (\vec{r} - \vec{r}_k)^T \nabla f(\vec{r}_k) + \frac{1}{2} (\vec{r} - \vec{r}_k)^T \mathbf{H}(\vec{r}_k) (\vec{r} - \vec{r}_k), \quad (2.12)$$

in which $\mathbf{H}(\vec{r}_k)$ is the Hessian matrix containing second partial derivatives $\frac{\partial^2 f(\vec{r}_k)}{\partial r_i \partial r_j}$. The direction of an optimization step is defined by the minimum of $m(\vec{r})$ at $\nabla m(\vec{r}) = 0$, which exists if $\mathbf{H}(\vec{r}_k)$ is positive definite. Then, the direction $\vec{d}_k = \vec{r}_{k+1} - \vec{r}_k$ for $m(\vec{r}_{k+1})$ becomes $\vec{d}_k = -\mathbf{H}^{-1}(\vec{r}_k) \nabla f(\vec{r}_k)$, according to

2.3. Mathematical modeling with systems of ODEs

$$0 = \nabla m(\vec{r}_{k+1}) = \nabla f(\vec{r}_k) + \mathbf{H}(\vec{r}_k)\vec{d}_k.$$

As the calculation of \mathbf{H} is computationally extensive, common variants of the Newton method use approximated Hessians [143].

Trust region strategy

In trust region approaches, instead of directly minimizing $f(\vec{r})$, a model $m_k(\vec{r})$ is approximated to a certain region of $f(\vec{r})$ and iteratively minimized [144]. Usually, again, a quadratic approximation of $f(\vec{r})$ in \vec{r}_k is defined by

$$m_k(\vec{d}) = f(\vec{r}_k) + \vec{d}^T \nabla f(\vec{r}_k) + \frac{1}{2} \vec{d}^T \mathbf{B}(\vec{r}_k) \vec{d},$$

in which $\mathbf{B}(\vec{r}_k)$ is an approximation of the Hessian at \vec{r}_k [145]. The problem $m_k(\vec{d}) = \min!$ is now solved to obtain the step \vec{d}_k for each iteration within a subregion of $f(\vec{r})$, which is limited by the radius $\Delta_k > 0$. The radius defines the trust region by $\{\vec{d} \mid |\vec{d}| \leq \Delta_k\}$. In this region the model $m_k(\vec{d})$ can be trusted, as it approximates, at least in small regions around \vec{r}_k , $f(\vec{r})$ sufficiently well. Now, the predicted reduction of by $\xi = m_k(0) - m_k(\vec{d}_k)$ can be compared with the actual reduction $\zeta = f(\vec{r}_k) - f(\vec{r}_{k+1})$. Certain parameters c_l with $l = 0..4$ are chosen in the ranges $0 < c_3 < c_4 < 1 < c_1$, $0 \leq c_0 \leq c_2 < 1$, with $c_2 > 0$, to decide if the position will be changed to $\vec{r}_{k+1} = \vec{r}_k + \vec{d}_k$ or stays at $\vec{r}_{k+1} = \vec{r}_k$. Furthermore it is decided according to these parameters if the radius Δ_k will be reduced or enlarged [145]. If the criterion $\xi/\zeta < c_1$ is fulfilled, the next step starts from $\vec{r}_k + \vec{d}_k$, otherwise from the old position \vec{r}_k . The radius for the next step is chosen according to

$$\Delta_{k+1} \in \begin{cases} [c_3 |\vec{d}_k|, c_4 \Delta_k] & \text{if } \xi/\zeta \leq c_0 \\ [\Delta_k, c_1 \Delta_k] & \text{if } \xi/\zeta > c_0 \end{cases}$$

before the optimization problem $m_{k+1}(\vec{d}) = \min!$ is solved for the following iteration step. The step-wise optimization proceeds until a stop criterion $|\nabla f(\vec{r}_k)| \leq \varepsilon$ with a small $\varepsilon > 0$ is fulfilled. When using $\mathbf{B} = \mathbf{H}$ the optimization strategy is denoted as trust region Newton method.

ODE models of biochemical signal transduction networks

Applying ODE models in biochemical signaling networks often consists of a sequence of work steps, in which biochemical hypotheses are translated to ODE models and tested by experimental data. After having experimentally validated a certain model topology, the model can be further analyzed to quantitatively investigate characteristic properties of the system and to plan strategies for therapeutic interventions.

Figure 2.4 illustrates the process of working with ODE models that are calibrated with experimental data, as it is typically applied in studies on biochemical signaling networks. Conflicting hypotheses on biochemical mechanisms that are translated to

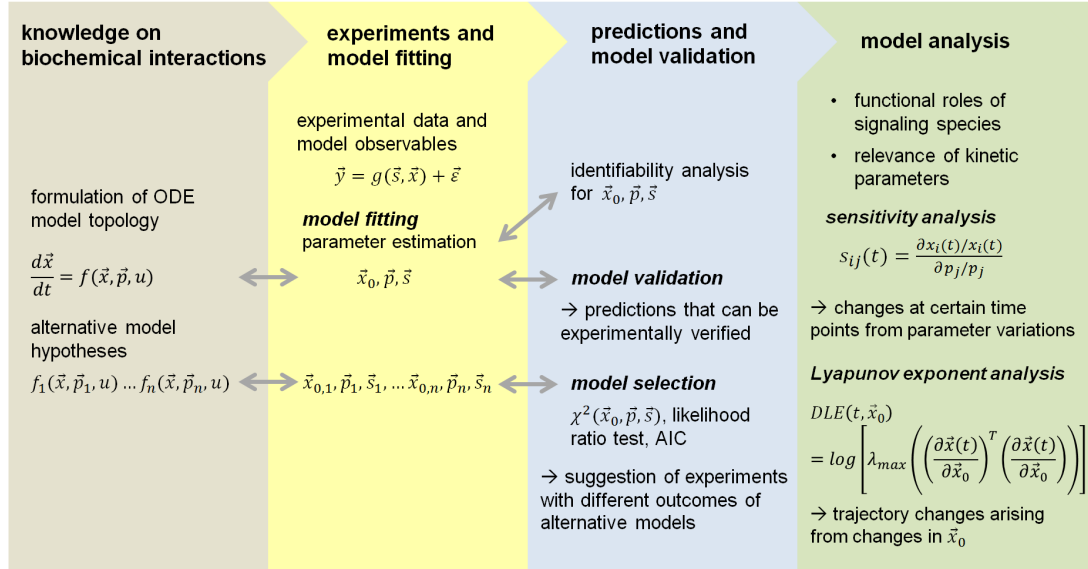


Figure 2.4. Overview of ODE modeling used in several apoptosis modeling studies. Biochemical knowledge on a signal transduction network can be translated to a system of coupled ODEs with variables \vec{x} , parameters \vec{p} and an external stimulus u , which could be a cell death ligand or drug concentration. Conflicting mechanistic hypotheses can be translated to alternative model topologies. By model fitting to experimental data represented by observables \vec{y} with experimental errors $\vec{\epsilon}$ initial concentrations x_0 , parameters \vec{p} and scaling factors \vec{s} are estimated. After fitting of model variants, a model selection can be carried out based on methods as the likelihood ratio test or the Akaike information criterion (AIC). Identifiability of estimated parameters can be analyzed and experiments can be predicted for model validation or further model discrimination. To characterize kinetic properties of the underlying biochemical signal transduction network a sensitivity analysis can be conducted. Direct Lyapunov exponents (DLE), calculated from the maximum eigenvalue λ_{max} of a matrix containing derivatives of the variables \vec{x} against initial values \vec{x}_0 , can be used to characterize the dependency of model trajectories on initial concentrations [98, 146].

2.3. Mathematical modeling with systems of ODEs

alternative model topologies can be tested by assessing, which model variant can explain a set of experimental data sufficiently well. Kinetic parameters and initial protein concentrations are estimated, as well as scaling factors between model variables and experimental data, by fitting an ODE model to experimental data. An identifiability analysis can show if estimated parameters can be successfully determined from the given set of experimental data or are unidentifiable [141,142,147]. An unidentifiable parameter can have different values without reducing the fit quality, eventually being correlated with another unidentifiable parameter, which decreases the predictive power of the model. For model validation, observable trajectories under different starting conditions as in the experimental data set (e.g. changed protein levels by knock-down or overexpression), can be predicted and tested by recording further experimental data under these conditions. After fitting alternative model variants, the most likely model can be determined by comparing values of the log-likelihood estimator χ^2 , using methods as the likelihood ratio test or the Akaike information criterion (AIC) [148,149]. It might be that a model variant, in which a reaction was omitted, can explain the experimental data equally well as a larger model, indicating that a certain reaction is irrelevant. For this purpose, the AIC accounts for the model size and penalizes the number of parameters, so that a more parsimonious model will be preferred. It is a practical estimator of the expected relative Kullback-Leibler information [150], as it simply depends on the difference between the number of parameters k and the logarithmic likelihood $\ln L$,

$$\text{AIC}^* = 2k - 2 \ln L = 2k - 2 \left(c - \frac{\chi^2}{2} \right) = 2k - 2c + \chi^2, \quad (2.13)$$

using Equation 2.11 with $c = N \ln \Delta y$. In this context, the Kullback-Leibler information

$$I(f, g) = \int f(x) \ln \left(\frac{f(x)}{g(x | p)} \right) dx \quad (2.14)$$

denotes the loss of information by approximating the function f by the model g with parameters p [151]. Minimization of $I(f, g)$ can be directly related to maximizing the likelihood of the model $g(x | p)$ as described in [150]. While the nominator of the logarithmic term in Equation 2.14 is a constant

$$C = \int f(x) \ln f(x) dx,$$

the denominator, which corresponds to an expectation value for the relative loss of information

$$E_f [\ln g(x | p)] = \int f(x) \ln g(x | p) dx = C - I(f, g), \quad (2.15)$$

has to be optimized by model fitting. To obtain a model selection criterion based on the Kullback-Leibler information, Akaike showed that the expectation value $E_y E_x [\ln (g(x | \hat{p}(y)))]$, which contains the expectation value described in Equation 2.15 with the maximum likelihood estimate $\hat{p}(y)$ of parameters p for the data y , can

be well approximated by the difference $\ln L - k$, as detailed in [148]. To obtain a direct relation to χ^2 , the AIC was defined with the additional factor -2 as in Equation 2.13. As the differences of AIC values for model variants are relevant, rather than exact values, the expression

$$\text{AIC} = \chi^2 + 2k \quad (2.16)$$

is normally used, omitting the constant c in Equation 2.13. At large values of k compared to N , in particular if $n/k \leq 40$, the corrected Akaike information criterion

$$\text{AIC}_{\text{corr}} = \text{AIC} + \frac{2k(k+1)}{N-k-1} \quad (2.17)$$

is preferred [152].

Using this criterion, a preferred model variant can be selected, which explains the experimental data sufficiently well with the smallest possible number of parameters. If clear discrimination between alternative models is not possible, experimental conditions can be chosen, in which predictions from different candidate models differ the most. After having validated a model, its kinetic properties can be analyzed by a sensitivity analysis. The relevance of model reactions on the concentration of a model species at a certain time point can be determined by calculating derivatives to kinetic parameters, as applied in different apoptosis modeling studies [41, 47, 48]. Furthermore, direct Lyapunov exponent (DLE) analysis has been used in apoptosis models to characterize functional roles of signaling species. By this method, trajectory changes of model species due to changes in initial concentrations of involved signaling proteins can be determined to analyze consequences for cellular fates [98, 146].

**Cellular heterogeneity determined by variable
protein levels: cell ensemble model of apoptosis**

A manuscript based on the content of this part has been submitted to the journal 'Science Signaling' [126]. The study described in this part was supervised by Dr. Stefan Legewie (IMB, Mainz) and Dr. Joel Beaudouin (German Cancer Research Center, Heidelberg). Basic ideas of this part had their origin in the master thesis of Juliane Claus that was supervised by Dr. Stefan Legewie [153]. Parts of the project were accomplished during the stay of Stefan Kallenberger in the lab of Prof. Peter Sorger at Harvard Medical School.

3. Introduction

A fundamental problem of cancer chemotherapies is fractional killing. After applying a cell death inducing chemotherapy protocol, a small fraction of the tumor cell population survives, in which apoptosis could not be induced. Fractional killing can be explained by variability of apoptotic signaling protein concentrations. The question arises, which combinations of protein levels are decisive for survival and the variability of cell death timing. Extrinsic apoptosis, which is targeted by therapeutically used cell death ligands, is initiated by the activation of caspase-8, which subsequently causes the activation of effector caspases that dismantle the cell. A part of the tumor cell population might, for example, survive due to a too low number of cell death receptors in combination with a certain too low level of caspase-8 at a given cell death stimulus. This part describes an approach that links the variability of apoptotic signaling protein levels with the variable cell death kinetics in a heterogeneous cancer cell population.

For this purpose, a technique was developed to record time series of caspase activities, resulting from a cell death stimulus, in single cells that is described in chapter 4. Then, a novel modeling approach was developed in order to describe a heterogeneous cancer cell population with a cell ensemble model that combines time series from single cells with population data (chapter 5). Based on the current biochemical knowledge on apoptosis, ODE model variants were developed, which are described in chapters 6 and 7, in order to investigate the mechanism of apoptosis initiation, its temporal control and to simulate cell populations. A minimal model variant was found and experimentally validated, in which prodomain cleavage sites are cleaved within dimers and enzymatic domain sites are cleaved between dimers. The model of caspase-8 activation indicates mechanistic similarities to caspase-9 activation at apoptosomes, and that caspase-8 acts as molecular timer, which terminates its own cleavage activity after a certain active period. Obtaining a valid model to simulate cell death of heterogeneous cancer cell populations is motivated by the optimization of chemotherapeutic treatments: Conditions can be predicted that maximize the fraction of apoptotic cells. To this end, a multivariate log-normal joint distribution was estimated by fitting a model simultaneously to a heterogeneous population of

cells (chapter 8). This multivariate joint distribution was used for further simulations of “random cells” and effects of taking influence on the start concentrations of involved signaling proteins. As discussed in chapter 9, a model topology was found that effectively contributes to pathway branching between non-apoptotic signaling pathways at weak cell death stimulus strengths and an efficient induction of apoptosis at higher stimulus strengths.

Initiation of extrinsic apoptosis by caspase-8 activation

Extrinsic apoptosis is initiated by extracellular death ligand and by formation of the Death Inducing Signaling Complex (DISC) [6] that serves as a platform for the activation of initiator caspases, caspase-8 and -10. These enzymes cleave and activate effector caspases, caspase-3 and -7, and cleave the pro-apoptotic Bcl2 family member BID to tBID, which induces mitochondria outer membrane permeabilization (MOMP). MOMP irreversibly triggers effector caspases activation by releasing further pro-apoptotic proteins. In so-called type I cells, initiator caspases activity is sufficient for direct activation of effector caspases, while type II cells require indirect activation via BID cleavage and MOMP [98,154]. Despite extensive characterization of caspase-8/10 activation, cleavage and other posttranslational modifications, little is known on how their cellular activity is effectively generated and controlled over time, and how it allows cells to decide between death and survival.

DISCs contain clustered CD95/Fas death receptors bound to the adaptor protein FADD on their cytosolic domain, on which dimers of procaspase-8 are assembled [5,155]. The two main procaspase-8 isoforms, procaspase-8a and b (p55 and p53), consist of a prodomain (p26/24), which interacts with FADD, and an enzymatic domain with two subunits, p18 and p10. The prodomain and the enzymatic subdomains are connected with linkers that can be cleaved by caspase-8 itself. Cleavage at D374 and D384 between the catalytic subunits generates p43/41 and p10, which typically appear first after activation [7,156]. Cleavage at D210 and D216, between the prodomain and the catalytic subunits, leads to the formation of p26/24 and p30 if cleavage occurs on p55/53, or to the formation of p26/24, p18 and p10 if cleavage occurs on p43/41 [86]. Fully cleaved caspase-8 is released from the DISC to the cytosol as the hetero-tetramer p18₂-p10₂.

Uncleaved procaspase-8 dimers can cleave themselves and a restricted group of local DISC bound proteins [157,158], while cleavage to p43/41 leads to a “substrate switch” allowing the cleavage of downstream effectors of apoptosis as BID or procaspase-3 [87]. Proximity induced activation of caspase-8 is attributed to dimerization, while cleavage of the inter-subunit linker in procaspase-8 dimers is thought to stabilize the dimeric conformation [159,160] and is required for caspase-8 cleavage activity towards downstream substrates, as it is the case for p43/41 [87,161]. Two active caspase-8 pools are constituted from this activation process, a membrane pool represented by p43/41, and a cytosolic pool of p18/caspase-8.

As procaspase-8 is at the same time enzyme and substrate its cleavages can occur in three ways: by an intramolecular process, an intermolecular process within dimers,

or an interdimeric process. Contradictory results have been obtained concerning the intra- vs. intermolecular cleavage of caspase-8: Chen et al. proposed that the first cleavage event in caspase-8 auto-processing is intramolecular [162]. Moreover, structural studies proposed that the cleavage sites in the catalytic subunits may access the active site inside the same molecule and favored intra-dimer processing [163, 164]. However, active, processed caspase-8 and other proteases can cleave dimeric procaspase-8 via an interdimeric process [78, 156].

4. Quantifying enzyme activities by a confocal imaging based method

This chapter describes a new method to quantitatively observe compartmentalized caspase-8 cleavage activity in single cells. Cleavage probes containing fluorescent proteins were expressed in cells. While uncleaved probes are kept in the cytosol, after cleavage, the fluorescent proteins can enter the nucleus. Time series of nuclear fluorescence intensities were recorded by confocal microscopy under various experimental conditions. From these intensity time series, enzyme activities, which are proportional to single cell concentrations of active forms of caspase-8, were calculated that can be used to calibrate ODE models of extrinsic cell death as it will be described in the subsequent chapters. Finally, the method was compared with a previous approach that employs fluorescence resonance energy transfer (FRET) cleavage probes.

Caspase-8 substrates such as caspase-3 and BID can be cleaved by the caspase-8 intermediate p43/p41 (later referred to as p43) at the plasma membrane and its final product p18₂-p10₂ (later referred to as p18), which is released to the cytosol, but not by p55/p53 (later referred to as p55) or p30 [87, 161]. Here, two compartmentalized caspase-8 specific cleavage probes were used, to distinguish the cleavage activities of the p43 and p18 intermediates. These cleavage probes are targeted to different cellular compartments by fusing fluorescence proteins to localization domains through a short cleavage sequence of amino acid residues IETD (Isoleucine - Glutamic Acid - Threonine - Aspartic Acid), recognized specifically by caspase-8. Upon caspase-8 activation, the linker is cleaved and the fluorescent protein released from its localization domain allowing the fluorescent proteins to equilibrate over the entire cell [136]. Dynamic changes in nuclear intensity measured by time-resolved confocal microscopy imaging, served as readout for enzymatic activity. To distinguish the cleavage activity of caspase-8 at the plasma membrane and within the cytosol Calnexin, which localizes at the surface of the endoplasmic reticulum (ER) [165], was fused to mGFP through the cleavage sequence IETD. This probe monitors the activity of the cytosolic form of caspase-8 (p18) away from the plasma membrane. The other cleavage probe employs a nuclear export signal (NES), which causes its active transport out of the nucleus [166] and restricts its localization to the complete cytosol. Therefore, the NES probe can be used for reporting cleavage activity of caspase-8 at both the plasma membrane (p43) and within the cytosol (p18, Figure 4.1).

The degree of probe cleavage reflects the integrated activity of caspase-8 over

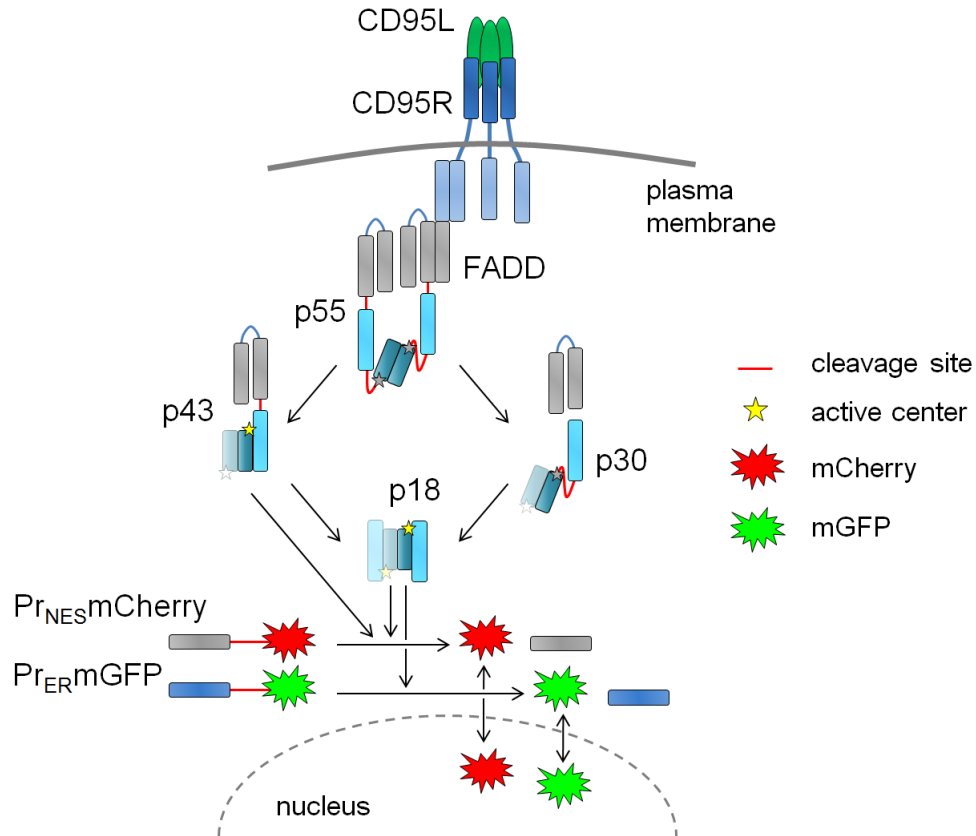


Figure 4.1. Observation of single cell caspase-8 trajectories with cleavage probes. Schematic representation of CD95 signaling: Subsequently to CD95 ligand binding to CD95 death receptors and FADD binding, dimers of procaspase-8 (p55) are assembled that can be cut at two cleavage sites (drawn in red). Cleavage in the catalytic domain generates p43, which is further processed in the prodomain to p18 that enters the cytosol. Prodomain linker cleavage in p55 produces catalytically inactive p30. While the cytoplasmic probe can be cleaved by p43 and p18, the ER probe is cleaved by p18 only.

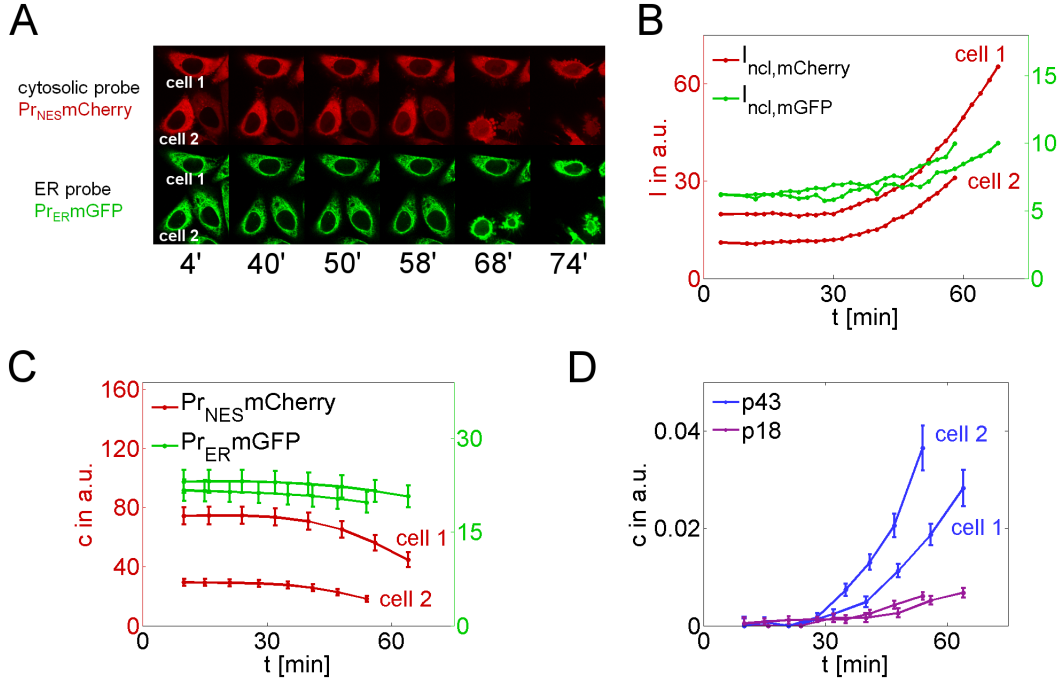


Figure 4.2. Quantification of caspase-8 enzyme activities. (A) Live-cell imaging of probe cleavage (red channel – mCherry/cytosolic probe, green channel – mGFP/ER probe). In two marked cells time series of nuclear fluorescence intensities (C) were measured and transformed to concentrations of uncleaved probes (D) or p43 and p18 (E) using equations 4.5 and 4.6.

time, but not the caspase-8 activity at a certain time point. A mathematical model was developed to derive the enzymatic activities of p18 and p43 from the imaging based cleavage data (Figure 4.2).

The model assumes that enzyme saturation in caspase-8 mediated probe cleavage can be neglected. The cleavage rate of a probe $[Pr]$ is then proportional to the concentration of the uncleaved probe $[PrF]$ and of caspase-8 $[C8]$ multiplied by the kinetic constant k_{probe}

$$[\dot{Pr}] = k_{probe}[C8][PrF] \Leftrightarrow k_{probe}[C8] = \frac{[\dot{Pr}]}{[PrF]}. \quad (4.1)$$

The caspase-8 activity profile can thus be calculated by extracting $[\dot{Pr}]$ and $[PrF]$ from the data. To this end $[\dot{Pr}]$ and $[PrF]$ will be expressed as functions of average probe intensities in the nucleus I_{ncl} and in the total cell I_{tot} because these intensities can be extracted most reliably from single-cell measurements. Alternatively, the averaged probe intensities in the nucleus I_{ncl} and in the cytosol I_{cpl} could be used as described in the following.

Upon stimulation, the number of uncleaved probes N_{PrF} reacts to N_{Pr} cleaved probe molecules and $N_F = N_{Pr}$ fluorescent protein molecules. The fluorescence

intensity in the nucleus $I_{ncl} = cN_F/V_c$, reflects the number of fluorescent protein molecules N_F in the cell volume V_c , multiplied by a scaling factor c . The total concentration of cleaved probes $[Pr]$ is higher than the concentration of fluorescent protein molecules by the ratio of the cytoplasmic volume V_{cpl} and the total cellular volume

$$[Pr] = \frac{N_{Pr}}{V_{cpl}} = \frac{N_F}{V_{cpl}} = \frac{V_c}{cV_{cpl}} I_{ncl}. \quad (4.2)$$

The concentration of the uncleaved probes $[PrF]$ can be either determined by additionally measuring the average intensity inside the whole cell $I_{tot} = c(N_{PrF} + N_F)/V_c$ or the fluorescence intensity inside the cytosol $I_{cpl} = c(N_{PrF}/V_{cpl} + N_F/V_c)$ as

$$[PrF] = \frac{N_{Pr}}{V_{cpl}} = \frac{1}{c}(I_{cpl} - I_{ncl}) = \frac{V_c}{cV_{cpl}}(I_{tot} - I_{ncl}). \quad (4.3)$$

Thereby, estimates of the amount of active caspase-8 multiplied by the cleavage constant

$$k_{probe}[C8] = \frac{V_c}{V_{cpl}} \frac{\dot{I}_{ncl}}{I_{cpl} - I_{ncl}} = \frac{\dot{I}_{ncl}}{I_{tot} - I_{ncl}} \quad (4.4)$$

are obtained, eliminating the scaling factor.

The ER-anchored cleavage probe $Pr_{ER}F_1$ can only be accessed by the soluble, cytoplasmic form p18. Based on the approach described in Equations 4.1-4.4, the activity from cytoplasmic [p18]

$$[Pr_{ER}] = k_{probe}[p18][Pr_{ER}F_1] \Leftrightarrow k_{probe}[p18] = \frac{\dot{I}_{1,ncl}}{I_{1,tot} - I_{1,ncl}} \quad (4.5)$$

can be calculated using $I_{1,tot}$ the trajectories for $I_{1,ncl}$. The activity of the active membrane bound intermediate p43 cannot be calculated directly, because no membrane-specific cleavage probe is available. The total concentration of active casepase-8 equals the sum of soluble and membrane-bound forms ($[C8_{tot}] = [p18] + [p43]$). For simplicity, it was assumed that probe cleavage by p43 and p18 is of similar magnitude, and can be described with the same kinetic constant k_{probe} . Then, the membrane-bound activity can be calculated based on the difference between terms for cytosolic and ER probe cleavage ($Pr_{cpl}F_2$ and $Pr_{ER}F_1$, respectively)

$$[Pr_{cpl}] = k_{probe} ([p43] + [p18]) [Pr_{cpl}F_2] \Leftrightarrow$$

$$k_{probe}[p43] = \frac{\dot{I}_{2,ncl}}{I_{2,tot} - I_{2,ncl}} - \frac{\dot{I}_{1,ncl}}{I_{1,tot} - I_{1,ncl}}. \quad (4.6)$$

In the case of this study F_1 is mGFP and F_2 is mCherry. Automated image analysis was employed to estimate amounts of cleaved and uncleaved probes. The total cellular and the nuclear fluorescence intensities were extracted by segmentation.

MatLab scripts (The Mathworks, Natick, MA, USA) and the software ImageJ (NIH, Bethesda, MD, USA) were used for segmentation and analysis of cell shapes and intensities from stack data and of nuclear intensities from slide data for every time point. NES-probe signals were used to segment inner and outer cytoplasm and nucleus borders. Volumes were calculated by voxel numbers and voxel volumes of $0.427 \times 0.427 \times 0.7 \mu m^3$ while cell surface areas were calculated by adding faces areas of polygon meshes (Table A.4).

Equations 4.1-4.6 require that slopes of probe cleavage can be estimated from time course data with limited sampling rate. To improve the robustness of slope estimation, temporal derivatives in equations 4.5 and 4.6 were calculated over longer time intervals, in which several intensity measurements were averaged. For each single cell quantity, values were calculated in eight equidistant time intervals. This relatively small number was chosen to obtain a reasonable signal-to-noise ratio in p43 and p18 activities, which limited the propagated error from noisy intensity measurements. Optimizing model fitting performance was a further reason to keep the number of data points for each cell low.

Smoothing splines were fit to the nuclear intensity trajectories. The errors $\Delta I_{1,ncl}$ and $\Delta I_{2,ncl}$ were estimated as standard deviation of the difference between the smoothing spline and experimental data. For $I_{1,tot}$ and $I_{2,tot}$ an error of 10 percent was assumed. Figure 4.3 shows trajectories of estimated total caspase-8 activities in single CD95-HeLa and HeLa wt cells at different death ligand concentrations. CD95-HeLa cells underwent apoptosis in the range between 40 minutes and around two hours. In these cells, at a ligand concentration of 10000 ng/ml caspase-8 trajectories and cell deaths are slightly delayed compared to the trajectories at 5000 ng/ml. Caspase-8 trajectories for HeLa wt cells that undergo apoptosis in the range of one to twelve hours show a more pronounced saturation behavior of caspase-8 activity and cell death kinetics at increasing ligand concentrations. While highest caspase-8 activities are obtained at 2000 ng/ml, caspase-8 activity decreases and cell death is delayed at higher concentrations.

In few cells, almost the total amount of cytoplasmic cleavage probes was cleaved before apoptosis. Then nuclear fluorescence intensity that indicates the concentration of cleaved off fluorescent protein approximates the cytosolic fluorescence intensity representing the sum of uncleaved and cleaved probe concentrations. As soon as the nuclear intensity I_{ncl} was equal or larger than 90% of the average intensity of the whole cell $I_{ncl} \geq 0.9 \cdot I_{tot}$ further calculating of caspase-8 observables was stopped. When further calculating caspase-8 observables, flattening of observable trajectories can be observed due to probe depletion.

Caspase-8 activation is known to be significantly enhanced by caspase-3 mediated feedback cleavage, which is activated after MOMP in the last six to eight minutes before apoptosis [82, 167]. Recently it was shown that before MOMP, most caspase activity seen from the probes indeed comes from caspase-8 [136]. As this study was focused on the primary dynamics of caspase-8 autoprocessing, the last 10 minutes prior to bleb appearance from analysis were excluded. The kinetics of probe cleavage was recorded in HeLa wt and in CD95-HeLa cells, which stably overexpressed CD95

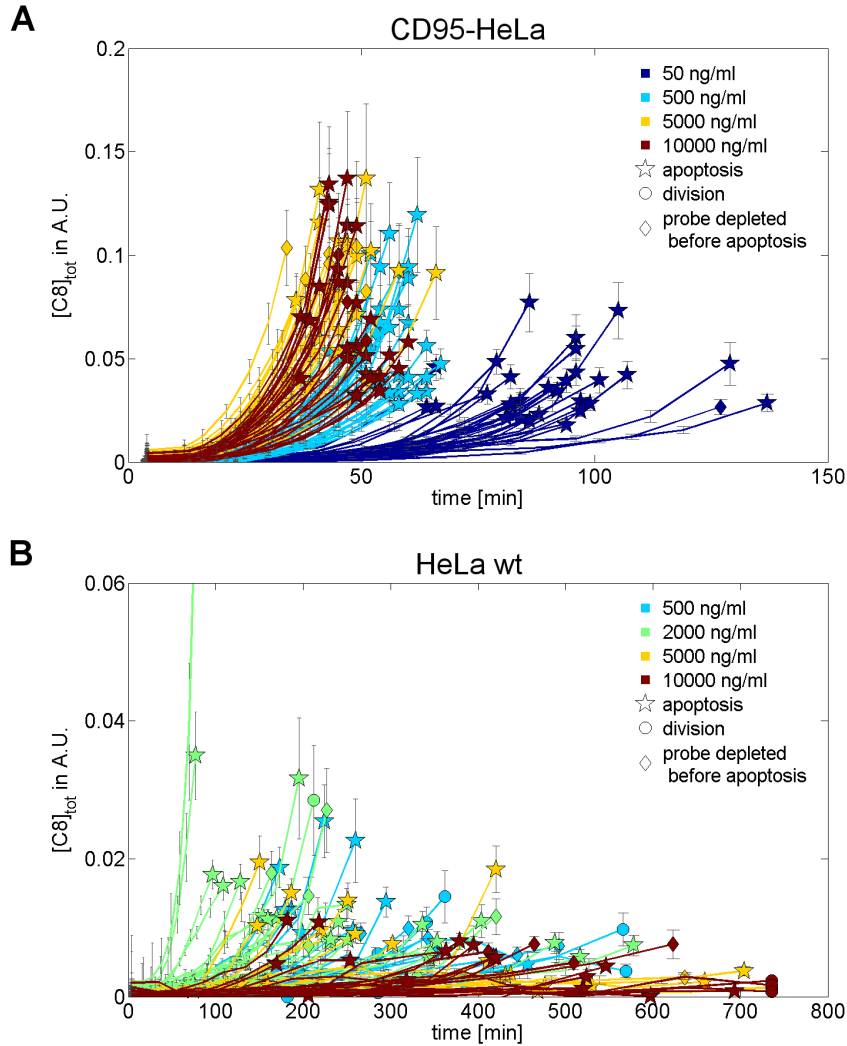


Figure 4.3. Single cell caspase-8 trajectories. Observable trajectories for $C8_{tot}$ (sum of p43 and p18 observables) in CD95-HeLa (A) and HeLa wt (B) cells at indicated CD95 ligand concentrations show decreased caspase-8 activity and delayed cell death at high ligand concentrations (error bars: propagated errors in observable calculations). Cell fates are indicated by symbols at the trajectory ends: In most cells apoptosis (stars) could be monitored. When starting cell division (circles), the compartmentalization of the NES probes was lost, and no further data could be obtained in mitotic cells undergoing apoptosis. In few cells, almost the total amount of cytoplasmic cleavage probes was cleaved before apoptosis (diamonds) and caspase-8 trajectories could not be further determined.

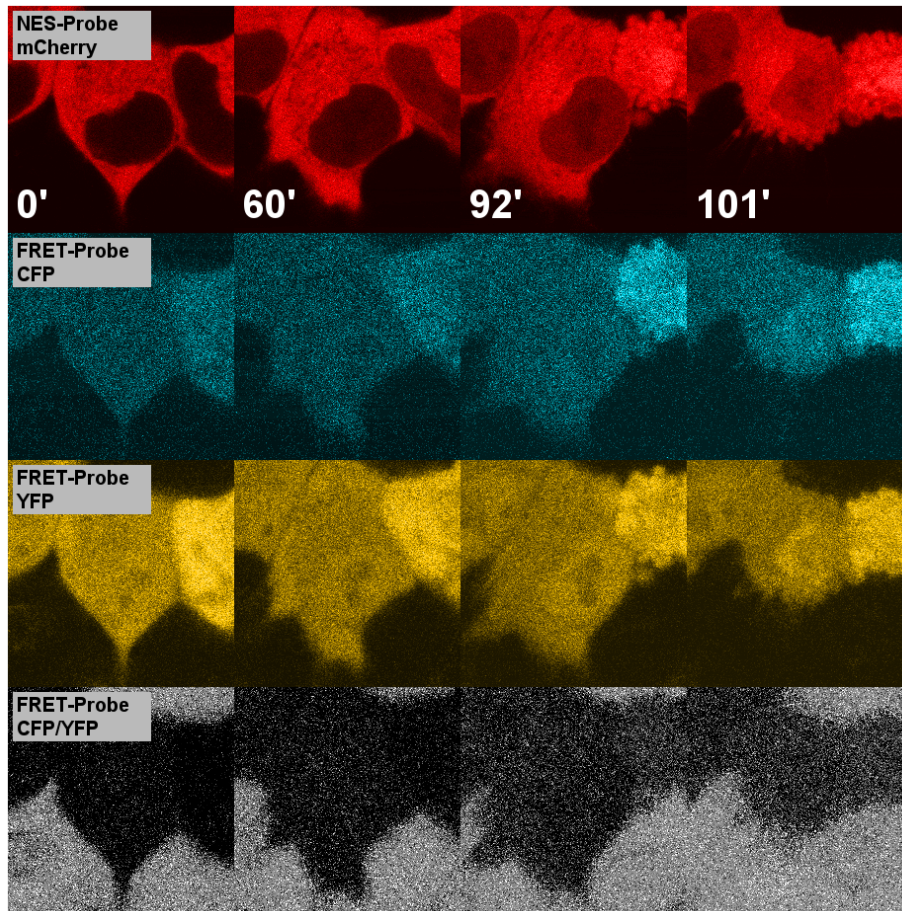


Figure 4.4. Live-cell confocal microscopic images for an exemplary cell that expresses NES- and FRET-cleavage probes. After cleavage of the nuclear export signal (NES) probe, the fluorescent protein mCherry enters the nucleus (top row). Cleavage of the FRET-probe separates the two fluorescent proteins CFP and YFP. The loss of FRET is measured in the quotient of the intensities I_{CFP}/I_{YFP} (bottom row).

by 10-fold. At different ligand concentrations more than 100 cells were analyzed in each cell line. Time of death, visually estimated as the time of apoptotic membrane blebbing, was between 1 and more than 12 hours for HeLa wt and between 40 to 120 minutes for CD95-HeLa cells. A representative result for quantitative estimation of model-based caspase-8 activity is shown in Figure 4.2. Activity of probe cleavage is low in the beginning, and is strongly enhanced in the second half of the time course (Figures 4.2A and 4.2B). Temporal profiles were experimentally confirmed with fluorescence resonance energy transfer (FRET) cleavage probes simultaneously expressed with NES cleavage probes as described in the following paragraph.

Comparison of caspase-8 activity profiles in FRET- and NES-probe measurements Currently two methods are available to monitor caspase-8 activity in single

cells. Several studies used FRET-reporters that consist of a pair of fluorescent proteins, usually CFP and YFP, connected with a cleavage sequence that is specific for caspase-8 [81, 82, 85]. Probe cleavage is indicated by loss of FRET effect, which resembles an energy transfer from the donor fluorophore CFP to the acceptor fluorophore YFP [168]. The energy transfer underlies the dipole-dipole coupling between donor and acceptor. The alternative excited-state relaxation competes with photon emission of the donor. Small changes between donor and acceptor molecule distance R can be detected as decay of the FRET efficiency

$$E_{FRET} = \frac{R_0^6}{R_0^6 + R^6},$$

in which the Förster radius R_0 denotes the molecule distance at a FRET efficiency of 50% [169].

Here, both methods were compared and their equivalence was shown. Figure 4.4 shows microscopic image data from exemplary cells that after transient transfection simultaneously express FRET and NES cleavage probes and were stimulated with CD95L. Cleavage of the NES-probe containing the cleavage site for BID (top panel, NES-ELQTDG-mCherry) can be measured by an increase of the nuclear fluorescence intensity $I_{mCherry,ncl}$, while FRET probe (CFP-ELQTDG-YFP) cleavage is indicated by an increase of the ratio

$$\frac{I_{CFP}}{I_{YFP}} = \frac{\tilde{I}_{CFP} - I_{CFP,bg}}{\tilde{I}_{YFP} - I_{YFP,bg}}$$

of background subtracted intensities of CFP and YFP (bottom panel).

The single cell trajectories (Figures 4.5A and 4.5B) of cells that simultaneously express both probes show high correlation coefficients (Figure 4.5C).

Fluorophore intensities were processed such that uncleaved probe levels are directly comparable (Figure 4.2C). Calculated enzyme activity trajectories (Figure 4.2D) were very similar between individual cells, confirming the robustness of the method. Membrane cleavage activities (p43) showing a steep increase after the certain latency period largely exceeded the cytosolic cleavage activities (p18), which showed a delayed set off and a more gradual increase.

Taken together, employing cleavage probes for calculating caspase activities in single cells has proven to be a robust and reproducible method to obtain insights to variable cell death kinetics in an ensemble of single cells. The approach of generating quantitative protease activity trajectories could be transferred to similar systems of intracellular proteases as cathepsins, serine proteases, secretases or HIV-protease to obtain mechanistic insights to involved signaling pathways.

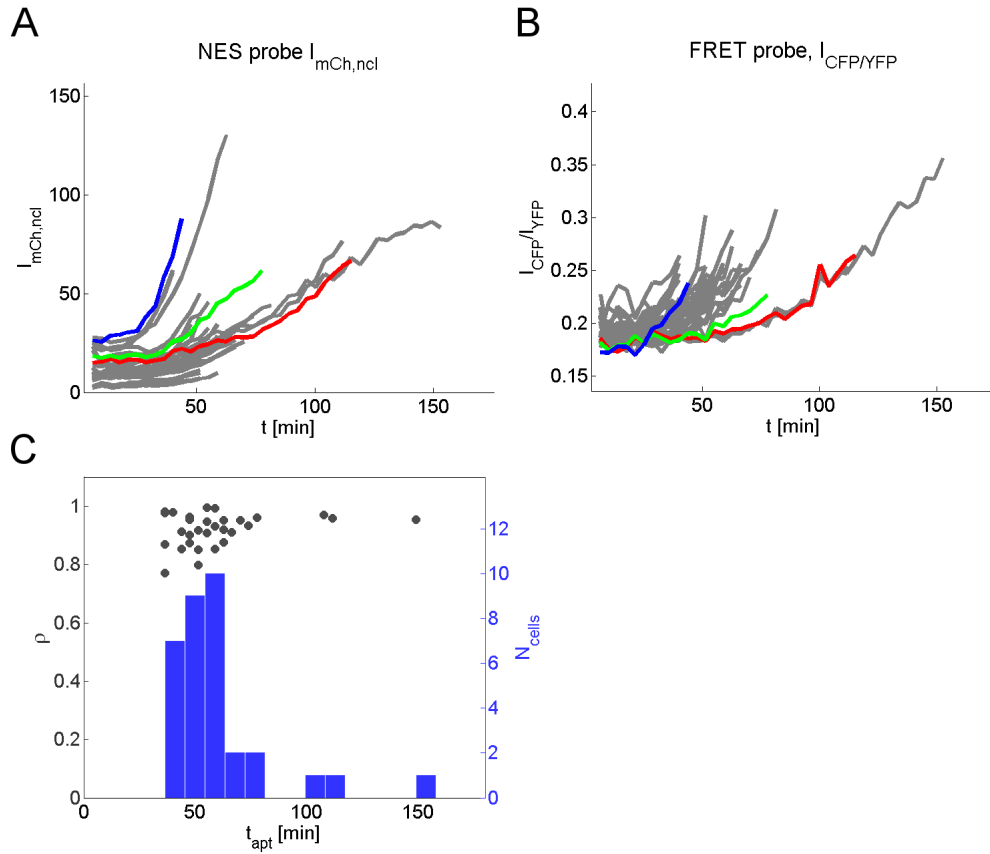


Figure 4.5. Single cell trajectories for NES- and FRET-probe cleavage related to caspase-8 activity. (A) Fluorescence intensity trajectories of all measured cells ($n=33$) were determined in ROIs within cross sections of the nuclei. (B) FRET signal trajectories of all measured cells. The quotients of the fluorescence intensities for CFP and YFP were measured in ROIs of whole cell cross sections, respectively. The NES probe and FRET probe trajectories of three representative cells are highlighted in green, blue or red. (C) Correlation coefficients ρ between FRET- and NES-probe signal trajectories for each cell dependent on the time of cell death t_{apt} . The blue bars represent the numbers of cells that underwent cell death in a certain time interval. Correlation coefficients ρ (indicated by gray dots) are lower for cells with smaller t_{apt} , which can be explained by a lower number of data points at equal noise levels.

5. Integrating single cell and population data in a cell ensemble model

Mathematical models of signal transduction are typically fitted to cell population data that have two main disadvantages: they hide cell-to-cell variability and smoothen, as they represent population averages, the kinetics that would be seen in individual cells. In a situation, where single cells show steep and switch-like trajectories with variable temporal delay population observable trajectories will show a gradual response, which hides the kinetics of the underlying biochemical process. This chapter describes how different experimental data were simultaneously described by cell ensemble models, which combine the advantages of different experimental techniques, integrate information of different qualities and describe heterogeneous populations of cells. The subsequent chapters 6 and 7 will describe the model components that are based on this approach.

Single cell observables that were obtained with help of cleavage probes as described in chapter 4 were restricted to catalytically active caspase-8 forms. In contrast, also inactive enzyme intermediates and other cleavage products can be quantified by the conventional population based method of western blotting. The dataset of single cell observables was enriched by population-based western blot measurements of p55, p43, p30, p18, as well as BID and tBID in CD95-HeLa cells at 50 and 500ng/ml (Figures 7.6, A.8 and A.9). Flow cytometric measurements further allowed restricting the cell-to-cell variability of signaling protein concentrations to a physiologically relevant range (Table 5.3, Figures A.13 and A.14). Experimental data obtained by several techniques, providing information of different qualities, were integrated in a multi-scale modeling approach (Figure 5.1). To simultaneously describe a heterogeneous cell population an ensemble of single cell models was created, in which each cell is described with equal sets of ODEs and the same kinetic parameters, but by different initial protein concentrations, thus introducing cell-to-cell variability. The ensemble of single cell models was fitted to single cell observables for uncleaved probes, $y_{Pr_{ER}F_1}$ and $y_{Pr_{cpl}F_2}$, as well as y_{p43} and y_{p18} , from an ensemble of cells. Simultaneous to fitting of individual parameters, ensemble averages were fitted to western blot data (Figure 5.1).

Setting boundary conditions for model fitting by quantifying mean protein levels and variances In order to define appropriate starting conditions for the estimation

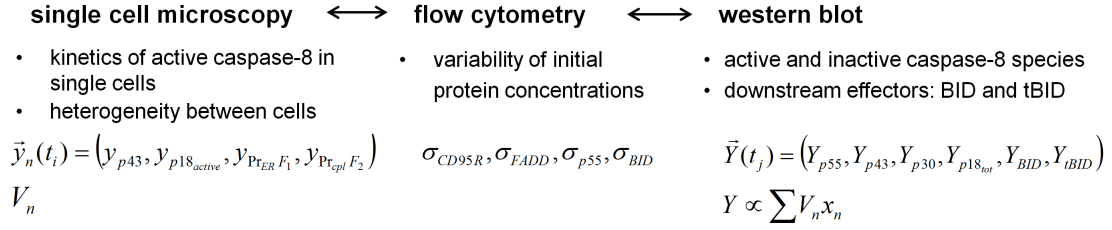


Figure 5.1. Representation of data from different experimental techniques in the model. Single cell models were fitted to single cell measurements \vec{y}_n . Population based measurements \vec{Y} for caspase-8 intermediates, BID and tBID are represented by sums of single cell variables x_n weighted by cellular volumes V_n . Distribution parameters σ from flow cytometry and mean initial protein levels from western blot were not directly fitted but used to constrain parameter limits.

of initial protein concentrations of involved signaling species in single cells, mean protein levels were measured with calibrated western blots and by fluorescence activated cell sorting (FACS) using calibration beads. Furthermore, FACS was applied to measure variances of protein levels and thereby define lower and upper allowed boundaries for estimated protein levels in single cells to constrain the mathematical model of caspase-8 processing.

To determine average protein levels, in the first step GFP fusions to FADD, p55, and BID were calibrated with recombinant GFP of known concentration by western blot. In the second step, these calibrated GFP fusions were blotted simultaneously with cell lysates of cleavage probe expressing HeLa wt and CD95-HeLa cells (Tables 5.1, Figures A.10-A.12). For this purpose, cell lines stably expressing FADD-GFP or p55-GFP were generated from HeLa wt cells. The same cell line was used to transiently express BID-GFP-mCherry. The concentrations of FADD-GFP, p55-GFP and BID-GFP-mCherry in fusion protein lysates were estimated by a calibration curve that was obtained by simultaneously blotting fusion protein lysates together with different doses of recombinant GFP, and immunostaining of GFP. Endogenous levels of FADD, p55, BID and cytosolic cleavage probes (NES-GIETDS-mCherry) were determined by blotting different doses of fusion protein lysates together with lysates of probe expressing CD95-HeLa and HeLa wt cells, and immunostaining with antibodies against FADD, p55, BID and mCherry (Figures A.10-A.12). Average levels of the ER probe (Calnexin-GIETDS-mGFP) could be directly measured by blotting lysates of probe expressing cell lines together with known doses of recombinant GFP (Figure A.12). The order of samples was shuffled to avoid biases from gel and blotting inhomogeneities [170]. Employing the method of calibrated western blots to determine average protein concentrations yielded relatively large standard deviations but served to estimate the orders of magnitude of protein levels and were sufficient for defining start values in the parameter fitting procedures. Estimates of FADD and p55 had the same magnitude order as in the study of Fricker et al. [46] ($N_{FADD} \approx 200.000/cell$ compared to $130.000/cell$, and $N_{FADD} \approx 320.000/cell$ com-

	CD95R-HeLa (mean \pm SD)	HeLa wt (mean \pm SD)
FADD	200843 \pm 31549	229583 \pm 31073
procaspase-8	334075 \pm 143428	324431 \pm 164643
BID	509926 \pm 48462	571555 \pm 108848
cytosolic probe	2093323 \pm 759296	4852343 \pm 1514532
ER probe	11137085 \pm 4103493	8428324 \pm 4495411

Table 5.1. Estimates of protein numbers in CD95R-HeLa and HeLa wt cells from calibrated western blots (means \pm SD, $n_{samples} = 4$).

	N (c. i.)
HeLa wt	12085 (11807, 12363)
CD95R-HeLa	157087 (155607, 158580)
HeLa wt, with probe expression	63425 (53014, 73892)
CD95R-HeLa, with probe expression	330269 (322410, 338155)

Table 5.2. Estimates of receptor numbers in probe expressing and native CD95R-HeLa and HeLa wt cells by calibrated FACS measurements.

pared to 250.000/*cell*). In this study, FADD and p55 levels of similar magnitude in probe expressing CD95-HeLa and HeLa wt cells were measured.

Mean levels of CD95 receptors and variability of CD95 receptors, FADD, p55 and BID were determined in probe expressing or not probe expressing HeLa wt and CD95-HeLa cells by immunostaining followed by flow cytometry (Table 5.2, Figures A.13 and A.14). The absolute concentration of CD95 receptors was estimated with help of calibration beads carrying defined epitope numbers for secondary antibodies (Figure A.13). CD95 receptors on the surface of cells are bound by primary antibodies under saturation conditions, i.e. where it can be assumed that all receptors are bound to primary antibodies. Then, beads and cells with bound primary antibodies were stained with fluorescently labeled secondary antibodies. Cells that were incubated with the secondary but without the primary antibody served to measure the background fluorescence intensities. The measured intensities were at the upper limit of the intensity range of the calibration beads. Therefore the calibration error was rather large in the probe expressing cells. To initialize the parameter estimation a receptor concentration start value was used, which lay between measures for the native and the probe expressing cells according to $N \approx 30000$ receptors for probe expressing HeLa wt cells and $N \approx 250000$ receptors for probe expressing CD95R-HeLa cells (see Table 5.3) that were as well consistent with earlier studies on these cell lines [46, 48].

FACS distributions were used to restrict the variability of initial protein concentrations for CD95R, FADD, p55 and BID in the model to physiologically reasonable levels. To measure variability of protein levels independent from cell size, FACS events were filtered for cells of similar volumes by gating for narrow front scat-

ter and side scatter intervals. To correct intensity measurements for background fluorescence, medians of normal distribution function fits to intensities of control measurements were subtracted. The lognormal distribution parameters μ and σ for initial concentration distributions were determined by fitting the probability density function

$$f(\zeta) = \frac{1}{\zeta\sigma\sqrt{2\pi}} \exp\left(\frac{-(\ln \zeta - \mu)^2}{2\sigma^2}\right)$$

to rescaled and background corrected FACS signal ζ . Compared to the immunostaining of membrane bound receptors, intracellular staining of FADD, p55 and BID cannot be assumed to achieve saturation with primary antibodies and mean levels will be underestimated by FACS. Therefore, the variance measured in FACS experiments was combined with mean levels from the more accurate calibrated western blots to obtain lognormal probability density functions of initial protein concentrations. In order to restrict initial protein concentrations in the model, 5% and 95% percentiles were calculated and combined with mean signals from western blots to set lower and upper limit for parameter fitting, respectively (Table 5.3).

Coefficients of variation in the range of $VarK = \sqrt{\exp(\sigma^2) - 1} = 0.8 \dots 1.1$ were obtained, which are rather large compared to studies on the variability of protein levels [171, 172], probably due to additional variability from intracellular antibody staining and FACS measurements. For this reason, the obtained 5% percentiles were used as lower and 95% percentiles as upper allowed boundaries for estimations of initial protein concentrations in each cell. Cellular volumes that were used to calculate average protein concentrations in Table 5.3 from protein numbers per cell as well as surface areas were determined by segmentation from confocal microscopic image stacks (Table A.4). For the ER-anchored and cytosolic probes the initial values were directly determined in individual cells by combining single cell observables $y_{Pr_{ER}F_1}$ and $y_{Pr_{cpl}F_2}$ from live-cell experiments with the average value from western blot measurements. Therefore, it was not required to define upper and lower limits for initial cleave probe concentrations.

Combining single cell with population observables The experimental data set comprised measurements at the single-cell and population levels. Single-cell models were directly fitted to single-cell measurements, and variability was introduced by allowing the initial signaling protein concentrations to vary between individual cells. Population-based measurements were represented in the model by ensemble averages of multiple single-cell models. In the following, it shall be described in detail how model variables were fitted to observables from single cell and population based experiments.

Single cell observables \vec{y}_n of cells for the uncleaved probe concentrations, $y_{Pr_{ER}F_1,n}$ and $y_{Pr_{cpl}F_2,n}$, as well as observables for effective caspase-8 concentrations $y_{p43,n}$ and $y_{p18,n}$ were used for model fitting. The model variables were linked to observables by using scaling factors s that were estimated from the data. At four different ligand concentrations, ten cells were included respectively. In total data from 80 cells was

	CD95R-HeLa			HeLa wt		
	\hat{c}	$u_{5\%}$	$u_{95\%}$	\hat{c}	$u_{5\%}$	$u_{95\%}$
CD95R	116	34	396	12	2,4	58
FADD	93	21	405	90	22	372
procaspase-8	155	36	671	127	37	434
BID	236	59	943	224	47	1060
	\hat{c}	c_{min}	c_{max}	\hat{c}	c_{min}	c_{max}
cytosolic probe	973	n.d.	n.d.	1909	n.d.	n.d.
ER probe	5178	n.d.	n.d.	3316	n.d.	n.d.

Table 5.3. Initial values, lower and upper limits for estimations of initial concentration. The values for CD95R correspond to estimates from calibrated FACS measurements, whereas the values for FADD, procaspase-8 and BID correspond to the median protein numbers obtained from calibrated western blots and FACS experiments. For CD95R, FADD, procaspase-8 and BID, 5% and the 95% percentiles $u_{5\%}$ and $u_{95\%}$ were estimated by fitting lognormal probability density functions to FACS signals. Lower and upper limits were not defined for the cytosolic and the ER probes as probe concentrations were directly determined by combining single cell observables from individual cells with the mean values from western blot experiments.

included. When fitting a model topology to data from 80 cells, more than 2560 residuals were minimized (80 cells \times 4 observables \times 8 time points).

To include population data into the parameter fitting procedure and link population observables with model variables for single cells population observables Y were introduced. A population observable was assumed to be proportional to the sum of the corresponding single cell variables x_n , weighted by the cellular volumes V_n that were segmented from microscopic data. The total amount of caspase-8 and BID, estimated from the band intensities, did not significantly change over time. Single cell observables

$$\vec{y}_n(t_i) = \begin{pmatrix} y_{p43} \\ y_{p18} \\ y_{Pr_{ER}F_1} \\ y_{Pr_{cpl}F_2} \end{pmatrix} = \begin{pmatrix} s_{C8}[p43]_n(t_i) + \epsilon_{p43} \\ s_{C8}[p18]_n(t_i) + \epsilon_{p18} \\ s_{F1}[Pr_{ER}F_1]_n(t_i) + \epsilon_{Pr_{ER}F_1} \\ s_{F2}[Pr_{cpl}F_2]_n(t_i) + \epsilon_{Pr_{cpl}F_2} \end{pmatrix} = \vec{s}\vec{x}_n(t_i) + \vec{\epsilon} \quad (5.1)$$

of each cell n included in the model were related to the model variables \vec{x} with entries $[p43]_n$ to $[Pr_{cpl}F_2]_n$ multiplied by scaling factors \vec{s} with entries s_{C8} for caspase-8 species, as well as s_{F1} and s_{F2} for the two fluorescent proteins F_1 and F_2 with experimental errors $\vec{\epsilon}$ for each species. Population observables Y were related to normalized ensemble averages of corresponding single cell variables that were weighted with cell volumes V_n , respectively. The absolute values for western blot intensities and variables for each caspase-8 species (p55, p43, p30 and p18) and the two forms of BID (BID and tBID) were normalized by the respective sums of intensities caspase-8 or BID intensities

$$I_{C8,tot} = I_{p55} + I_{p43} + I_{p30} + I_{p18} \quad (5.2)$$

or

$$I_{BID,tot} = I_{BID} + I_{tBID} \quad (5.3)$$

and sums of concentrations

$$S_{C8} = \sum_n V_n ([p55]_n + [DISCp55]_n + [p43]_n + [p18]_n + [p18_i]_n) \quad (5.4)$$

or

$$S_{BID} = \sum_n V_n ([BID]_n + [tBID]_n). \quad (5.5)$$

The expression for the population observables at time points t_k reads

$$\vec{Y}(t_k) = \begin{pmatrix} I_{p55}(t_k)/I_{C8,tot}(t_k) \\ I_{p43}(t_k)/I_{C8,tot}(t_k) \\ I_{p30}(t_k)/I_{C8,tot}(t_k) \\ I_{p18}(t_k)/I_{C8,tot}(t_k) \\ I_{BID}(t_k)/I_{BID,tot}(t_k) \\ I_{tBID}(t_k)/I_{BID,tot}(t_k) \end{pmatrix} = \begin{pmatrix} \sum_n V_n ([p55]_n(t_k) + [DISCp55]_n(t_k)) / S_{C8} + \Delta_{p55} \\ \sum_n V_n [p43]_n(t_k) / S_{C8} + \Delta_{p43} \\ \sum_n V_n [p30]_n(t_k) / S_{C8} + \Delta_{p30} \\ \sum_n V_n ([p18]_n(t_k) + [p18_i]_n(t_k)) / S_{C8} + \Delta_{p18} \\ \sum_n V_n [BID]_n(t_k) / S_{BID} + \Delta_{BID} \\ \sum_n V_n [tBID]_n(t_k) / S_{BID} + \Delta_{tBID} \end{pmatrix} = \vec{X}_p(t_k) + \vec{\Delta}. \quad (5.6)$$

Therein, \vec{X}_p denotes derived population variables with errors $\vec{\Delta}$. By using western blot band intensity fractions instead of absolute intensities the introduction of another scaling factor was avoided. Furthermore, fractions of western blot intensities were used in order to avoid errors from small differences in total protein amounts within western blot samples for different time points that result from the experimental procedure of sample preparation.

While the single cell observable $y_{p18,n}$ for p18 reflected the corresponding single cell variable $[p18]_n$ of active p18, the western blot observable Y_{p18} derived from the western blot intensity I_{p18} reflected the sum of active p18 as well as the inactive species $p18_i$ and was related to the sum of single cell variables $[p18]_n$ and $[p18_i]_n$. Thereby, combining single cell and western blot data facilitated estimating the stability of p18.

By parameter fitting, the kinetic model parameters were globally estimated, i.e. they were assumed to be equal for each cell. Furthermore, initial concentrations

for CD95R, FADD, p55, BID and the two cleavage probes were locally estimated for each included cell. The function of residuals R , which was minimized during parameter estimations, comprised three parts: a weighted sum of single cell residuals R_{sc} , a residual term for the population observables R_p and another residual term $R_{\bar{x}_0}$ to minimize the distance of initial concentration averages and experimentally determined mean protein concentrations

$$R = R_{sc} + R_p + R_{\bar{x}_0} \quad (5.7)$$

with

$$R_{sc} = \sum_{i,j,n} \frac{s_j x_{jn}(t_i) - y_{jn}(t_i)}{\epsilon_{ijn}}, \quad (5.8)$$

$$R_p = N \sum_{k,l} (Y_l(t_k) - X_l(t_k)) \quad (5.9)$$

and

$$R_{\bar{x}_0} = \sum_s \left| \frac{1}{N_s} \begin{pmatrix} \sum_{n_s} V_{n_s} [CD95R]_{n_s}(t_0) \\ \sum_{n_s} V_{n_s} [FADD]_{n_s}(t_0) \\ \sum_{n_s} V_{n_s} [p55]_{n_s}(t_0) \\ \sum_{n_s} V_{n_s} [BID]_{n_s}(t_0) \end{pmatrix} - \begin{pmatrix} \overline{CD95R}_{FACS} \\ \overline{FADD}_{WB} \\ \overline{p55}_{WB} \\ \overline{BID}_{WB} \end{pmatrix} \right|. \quad (5.10)$$

Equation 5.8 weights the difference between model observables $s_j x_{jn}(t_i)$ for cell n and single cell data $y_{jn}(t_i)$ by the experimental errors ϵ_{ijn} for each time point i that was obtained by error propagation for single cell observable calculations as described in chapter 4. In Equation 5.9 the residuals R_p for population observables Y_j were weighted by the number of cells N included in the model rather than weighting by the experimental error of each western blot sample. This procedure is equivalent to choosing an error model with a certain relative error, and had turned out to be more robust for parameter fitting. In Equation 5.10 the single cell model averages for initial CD95R, FADD, p55 and BID concentrations in HeLa wt or CD95-HeLa cells were compared with experimentally determined averages, from FACS or western blot experiments, respectively. This penalty term should assure that single cell models, which were fitted to data of cells at different ligand concentrations, had the same mean initial concentrations. Therefore, differences were calculated for experimental sets of data s that comprised a group of $n_s = 1 \dots N_s$ cells with $N = \sum_s N_s$ treated at the same ligand concentration, respectively. Single cell data of two cell lines were recorded at four ligand concentrations, respectively, which results in a total number of eight datasets. It was tested, if further penalty terms that represent additional boundary conditions are beneficial for parameter estimations and accelerate the convergence of model fits. Tentatively, a penalty term was included in R for deviations between of lognormal distributions of estimated initial concentrations

and the corresponding distributions from FACS experiments. However, as experimentally determined variability was unrealistically large, distribution penalty terms were not further employed.

For parameter estimations, the squared residuals in Equation 5.7 were minimized, employing a trustregion algorithm. While the squared single cell residuals correspond to a χ^2 estimator, the two additional residual terms represent artificial boundary conditions to comply with physiological circumstances.

Taken together, the described procedure represents a substantial extension of previous apoptosis models that took into account cell-to-cell variability. So far, no other model of cellular signal transduction networks was calibrated with the combination of time resolved single cell and population observables. The study of Albeck et al. [39] that was applied in further studies on cell-to-cell variability [94,95] combined population observables from western blot and FACS experiments with distributions of time points of certain cellular events as the time when mitochondria outer membrane permeabilization or apoptosis occurred. Kinetic parameters were manually adjusted until model simulations from randomly sampled initial conditions reflected experimentally measured distributions. It will be the aim of further work to optimize model calibration with combined single cell and population data regarding the convergence behavior of fitting procedures, and to characterize the value of different boundary conditions for parameter identifiability [141,142,147]. Within this context it will be of interest, which advantages can be gained by including further boundary conditions as probability density functions of initial protein concentrations. The following chapters 6 and 7 address the implementation of two separate parts of the model that was fitted to the combination of single cell and population observables.

6. Explaining the inverse bell-shape of cell death kinetics by receptor oligomerization models

To investigate the quantitative dynamics of caspase-8 activation, kinetic models were developed that comprise two parts, one describing receptor oligomerization and one describing subsequent caspase-8 activation mechanisms. In this chapter, the first part of the model will be described.

To characterize caspase-8 processing and identify potential non-linearities, a dose response analysis was performed with soluble CD95 ligand fused to the T4 domain (T4-CD95L), which stabilizes the ligand in its trimeric form [173], ranging from 50ng/ml to 10 μ g/ml. Interestingly, it was discovered that at high CD95 ligand concentrations cell death is decelerated relative to intermediate levels (Figure 6.1). This inverse bell-shaped dose-response profile was found in HeLa wt, and to a weaker extent as tendency in CD95-HeLa cells. As a similar inverse bell-shaped dose-response behavior was observed for probe cleavage kinetics (Figures 7.5B and 4.3, decreasing caspase-8 activity and delayed apoptosis at high CD95 concentration in HeLa wt, and with less extent in CD95-HeLa cells), it was hypothesized that this characteristic behavior emerges early in the signaling cascade, upstream of caspase-8 activation, possibly at the receptor level.

In the following, mathematical models of ordinary differential equations (ODEs) based on known features of CD95 receptor-ligand binding will be described, which reflect mechanisms underlying the inverse bell-shaped dose-response profile of cell

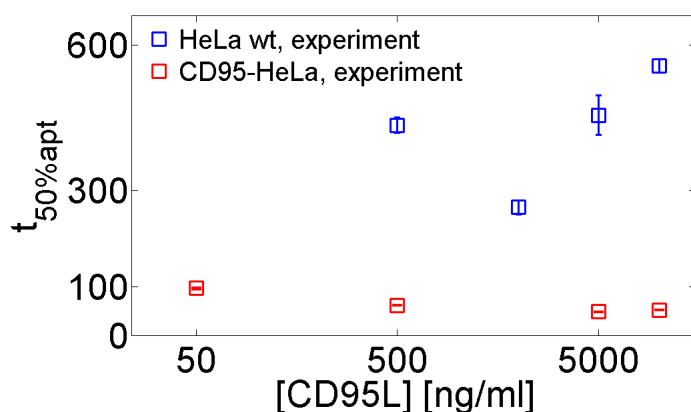


Figure 6.1. Median cell death times (squares) for HeLa wt and CD95-HeLa cells. Error bars represent standard deviations from medians in different microscopic fields.

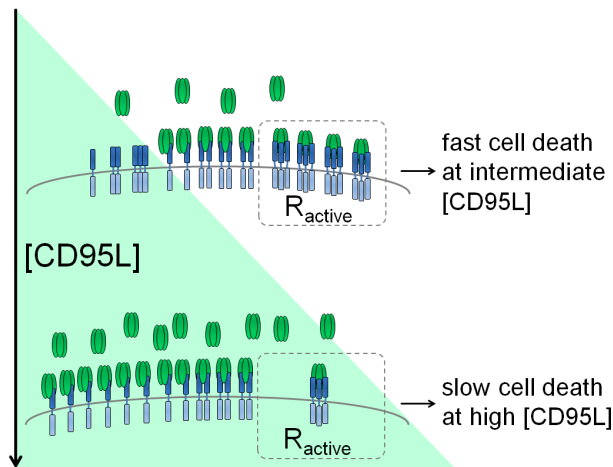


Figure 6.2. Illustration of the mechanism of inverse bell-shaped behavior. At high ligand concentrations most bound ligands are connected to receptors in a 1:1 stoichiometry, resulting in a low number of oligomerized receptors capable of caspase-8 activation.

death. Possible model topologies shall be based on the following premises: (i) CD95 receptors oligomerize and may exist as pre-formed oligomers in the absence of stimulation [174–176]. (ii) Only oligomerized receptors bound to extracellular ligand are biologically active and serve as a platform for procaspase-8 activation. (iii) The T4-CD95 ligand used in this study is a highly pure and stable trimer [173] that efficiently induces receptor oligomerization by simultaneously binding to three receptor monomers [177–180].

These features of receptor signaling can explain the inverse bell-shaped dose-response profile: Each monomeric receptor binds with 1:1 stoichiometry to a trimeric ligand if the ligand is in large excess over the receptors, which represents the state of maximal entropy. The system is thus shifted towards biologically inactive one-to-one complexes of receptors and ligands upon strong stimulation, whereas intermediate concentrations of the trimeric ligand efficiently oligomerize and activate the receptor (Figure 6.2).

Two possible models of multivalent ligand binding to oligomerizing receptors will be discussed, a simple model of dimerization and a more complex trimer model. Using further assumptions, a steady state solution based on a simplified trimerization model will be derived that facilitated parameter fitting, and provided an explanation of the observed cell death kinetics with a similar dose response relation. The assembly of active death receptor complexes has been shown to take place within a few minutes after ligand addition [6], and is a rapid process compared to caspase-8 activation. Therefore time scale separation of both processes was applied, and it was assumed that the receptor-ligand binding was at steady state for mathematical modeling.

Model of receptor dimerization A key assumption is that only oligomerized receptors bound to a multimeric ligand are active receptor species that can bind FADD and form death inducing signaling complexes. This assumption alone, independent from the required number of oligomerized receptors in an active receptor complex,

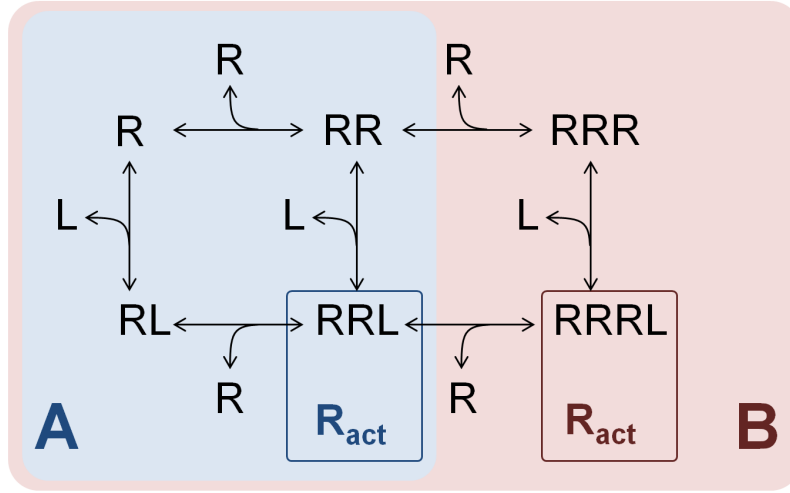


Figure 6.3. Receptor oligomerization models. (A) Model of receptor dimerization, in which receptors R reversibly dimerize, and complexes of two receptors bound to a ligand L represent the active receptor species R_{act} . (B) Model of receptor trimerization, in which three receptors bound to one ligand represent active receptors R_{act} .

can explain the observed inverse bell-shaped cell death kinetics. Therefore, a sufficient minimal model is a model of receptor dimerization, in which receptors reversibly dimerize and a ligand molecule can bind up to two receptors (Figure 6.3A). In the following equations, r and r_2 denote concentrations of monomeric receptors $[R]$ and receptor dimers $[RR]$, while c_1 and c_2 denote concentrations of ligand bound monomeric receptors $[RL]$ and ligand bound receptor dimers $[RRL] \equiv 1/2[R_{active}]$. The ligand concentration $[L]$, denoted as l , is assumed to be constant, representing the experimental condition where ligand is in large excess. Kinetic constants for receptor binding and unbinding are k_{r+} and k_{r-} , for ligand binding and unbinding k_{l+} and k_{l-} , respectively.

$$\dot{r} = -k_{r+}r(2r + c_1) + k_{r-}(2r_2 + c_2) - k_{l+}lr + k_{l-}c_1 \quad (6.1)$$

$$\dot{r}_2 = k_{r+}r^2 - k_{r-}r_2 - k_{l+}lr_2 + k_{l-}c_2 \quad (6.2)$$

$$\dot{c}_1 = -k_{r+}rc_1 + k_{r-}c_2 + k_{l+}lr - k_{l-}c_1 \quad (6.3)$$

$$\dot{c}_2 = k_{r+}rc_1 - k_{r-}c_2 + k_{l+}lr_2 - k_{l-}c_2. \quad (6.4)$$

Equations 6.1 to 6.4 contain the simplification that binding of the second receptor to LR (“crosslinking”) has the same kinetic parameters k_{r+} and k_{r-} as binding of the first receptor. The set of non-linear ordinary differential equations can be solved in a steady state where $\dot{r} = \dot{r}_2 = \dot{c}_1 = \dot{c}_2 = 0$. The polynomial that results from combining the equations and denoting the total receptor pool with $r_0 = r + c_1 + 2(r_2 + c_2)$ has one experimentally reasonable zero. After collecting the kinetic

parameters for binding and unbinding in the dissociation constants $K_{DR} = k_{r-}/k_{r+}$ and $K_{DL} = k_{l-}/k_{l+}$ the solution for active receptor concentration reads

$$\frac{1}{2}[R_{active}] \equiv c_2 = \frac{l}{8K_{DL}(K_{DL} + l)} \left[K_{DR}l + K_{DL}(K_{DR} + 4r_0) - \sqrt{K_{DR}(K_{DL} + l)(K_{DL}K_{DR} + K_{DR}l + 8K_{DL}r_0)} \right]. \quad (6.5)$$

It is plotted for comparison together with other model solutions in Figure 6.4.

Model of receptor trimerization Using the more realistic assumption that ligands can bind up to three receptors, and that ligand bound receptor trimers represent the active receptor species, an analogous set of rate equations can be formulated. Two further species, receptor trimers and ligands bound to three receptors, have to be considered. Here, r_3 denotes the concentration of receptor trimers $[RRR]$, and c_3 the concentration of ligands bound to three receptors $[RRRL] \equiv 1/3[R_{active}]$ (Figure 6.3B).

$$\dot{r} = -k_{r+}r(2r + r_2 + c_1 + c_2) + k_{r-}(2r_2 + r_3 + c_2 + c_3) - k_{l+}lr + k_{l-}c_1 \quad (6.6)$$

$$\dot{r}_2 = k_{r+}r(r - r_2) + k_{r-}(r_3 - r_2) - k_{l+}lr_2 + k_{l-}c_2 \quad (6.7)$$

$$\dot{r}_3 = k_{r+}rr_2 - k_{r-}r_3 - k_{l+}lr_3 + k_{l-}c_3 \quad (6.8)$$

$$\dot{c}_1 = -k_{r+}rc_1 + k_{r-}c_2 + k_{l+}lr - k_{l-}c_1 \quad (6.9)$$

$$\dot{c}_2 = k_{r+}r(c_1 - c_2) + k_{r-}(c_3 - c_2) + k_{l+}lr_2 - k_{l-}c_2 \quad (6.10)$$

$$\dot{c}_3 = k_{r+}rc_2 - k_{r-}c_3 + k_{l+}lr_3 - k_{l-}c_3 \quad (6.11)$$

Solving the equation system according to the dimer model would lead to a complex cubic equation. Below, an alternative expression for active receptor levels will be derived based on further simplifying assumptions in order to avoid terms as the square root in Equation 6.5 that strongly increase the numerical effort for each step of an optimization process. The steady state solutions of this simplified model will be compared to the more exact dimer (Eqs. 6.1 to 6.4) or trimer model (Eqs. 6.6 to 6.11).

Simplified model of receptor trimerization summarizing different oligomeric states The solution of a simplified trimerization model was derived in order to decrease the computational effort of parameter fitting. Therein, ligand bound oligomer forms will be summarized in $r_{l,tot}$ and free receptor forms in $r_{f,tot}$, assuming the same binding kinetics for different receptor oligomerization states.

The overall concentration of receptors consists is

$$r_{tot} = r_{f,tot} + r_{l,tot}. \quad (6.12)$$

The steady state concentration of receptor/ligand complexes depends on the ligand concentration l and the ligand dissociation constant K_{DL}

$$K_{DL} = \frac{k_{l-}}{k_{l+}} = \frac{r_{f,tot}l}{r_{l,tot}}. \quad (6.13)$$

Including Equation 6.12 yields

$$r_{l,tot} = r_{tot} \frac{l}{l + K_{DL}}. \quad (6.14)$$

Now it shall be further assumed that active receptors R_{act} with the concentration r_{act} are a subspecies of ligated and not ligated receptors, independent from steady states of ligand binding, and result from the reaction of one ligand bound with two free receptor species, leading to the steady state equation

$$(r_{l,tot} - r_{act})(r_{f,tot} - r_{act})^2 = K_{DR}r_{act} \quad (6.15)$$

with the dissociation constant K_{DR} for active receptors. To avoid a cubic term in r_{act} and simplify Equation 6.15, it is further assumed that the concentration of free receptors $r_{f,tot}$ is little influenced by the amount of active receptors. However, the concentration of ligated receptor is assumed to be dependent on the amount of active receptors. The simplified form

$$(r_{l,tot} - r_{act})r_{f,tot}^2 - K_{DR}r_{act} = 0 \quad (6.16)$$

can be combined with Equations 6.12 and 6.14 to

$$\left(\frac{r_{tot}l}{l + K_{DL}} - r_{act} \right) \left(1 - \frac{l}{l + K_{DL}} \right)^2 r_{tot}^2 - K_{DR}r_{act} = 0. \quad (6.17)$$

The solution of this polynomial equation reads

$$r_{act} = \frac{K_{DL}^2 r_{tot}^3 l}{(K_{DL} + l)(K_{DR}K_{DL}^2 + r_{tot}^2 K_{DL}^2 + 2K_{DR}K_{DL}l + K_{DL}l^2)}. \quad (6.18)$$

The cell death kinetics observed in experimental data could be sufficiently well explained by using this equation as shown in the subsequent chapters. The characteristics of the simplified trimer model were compared with the more exact dimer and trimer models. Figure 6.4 shows active receptor fractions R_{active}/R_{tot} that were calculated using the exact trimer model. Solutions of the exact dimer model (Eq. 6.5) and the simplified trimer model (Eq. 6.18) were fit to these trajectories. The bell shape of active receptors is more pronounced in the simplified trimer model and very similar in exact dimer and trimer oligomerization models. However, as experimental data were only recorded at four different ligand concentrations, all model versions could be used to explain the experimentally observed death kinetics

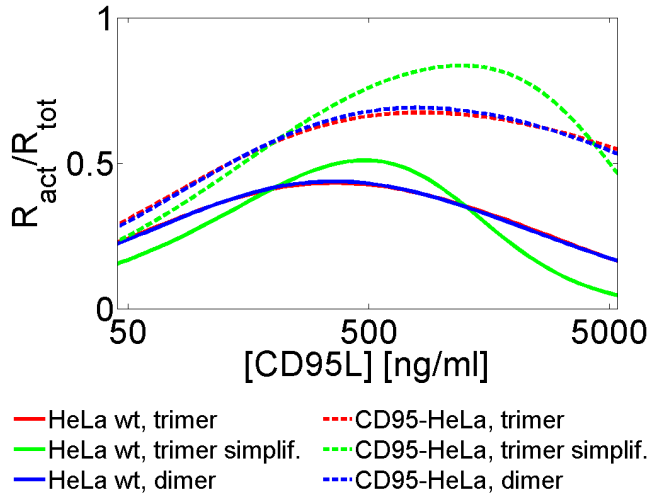


Figure 6.4. Active receptor fractions in different oligomerization models. Fits of the solutions of the simplified trimer model (Eq. 6.18, green lines) and the dimer model (Eq. 6.5, blue lines) to numeric solutions of the exact trimer model for CD95-HeLa (dotted lines) and HeLa wt cells (solid lines) that were calculated the exemplary values $K_{DR} = 0.5nM$ and $K_{DL} = 5nM$.

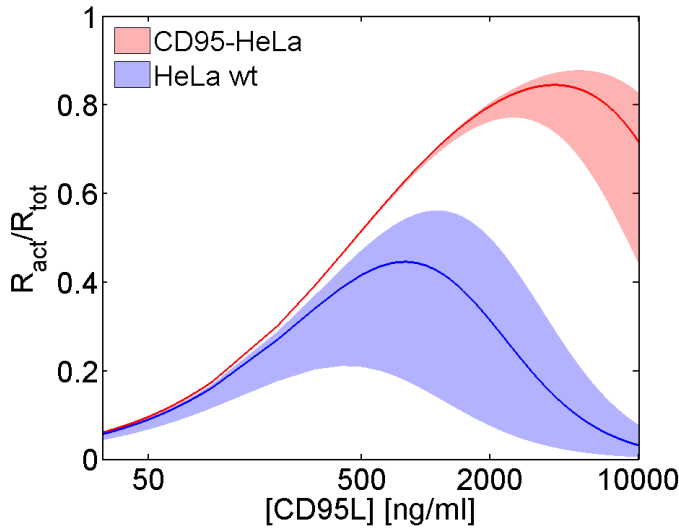


Figure 6.5. Variability of active receptor fractions for CD95-HeLa, and HeLa wt cells. Mean fractions (lines) and areas for 1σ confidence intervals for single cells with different receptor levels (shaded areas). Simulations were calculated with Equation 6.18 using kinetic parameters from model fitting and model estimations of receptor numbers in a cell population.

sufficiently well. Obtaining one fit of the whole cell ensemble model on a cluster node using the simplified trimer model solution opposed including the trimer model ODEs (Eqs. 6.6 to 6.11) reduced the time compared to the from about three hours to twenty minutes. More detailed insights into the oligomerization dynamics and a better discrimination between possible models could be facilitated by recording data at more densely sampled ligand concentrations.

Equation 6.18 was implemented to calculate the amount of active receptors at the beginning of each parameter optimization step in the full model that takes into account caspase-8 autoprocessing (see chapter 7). The initial concentrations of receptors r_{tot} in an ensemble of cells, the constants K_{DL} and K_{DR} were then estimated by model fitting to experimental data. Corresponding model simulations show peaks of the active receptor fractions at intermediate ligand concentrations

(Figure 6.5), which corresponds to the fast apoptosis kinetics at intermediate ligand concentrations in cell death measurements.

The model furthermore explains the observed phenomenon that CD95-HeLa cells show saturated cell death kinetics at higher ligand concentrations than HeLa wt cells, as these have about ten times less CD95 receptors. Variability in receptor levels causes variable inverse bell-shaped active receptor profiles and saturation levels. This variability can have a pro-survival effect and increases apoptosis time variability in a cellular population with variable receptor levels: At low receptor numbers the oligomerization mechanism prevents DISC formation. Increasing ligand levels towards the saturation levels in cells with low receptor numbers enlarges cell death variability: In cells with small receptor numbers death kinetics is decelerated, while in cells with higher receptor levels cell death is further accelerated.

To conclude, the observed inverse bell-shape in caspase-8 activity can be explained based on the dynamics of receptor oligomerization. The association of active receptors and subsequent reaction steps were assumed to be slow compared to receptor-ligand binding, and thus implemented as ODEs as described in the following chapter.

7. Modeling shows a combined cis/trans cleavage mechanism of caspase-8 activation

7.1. Alternative mechanisms of caspase-8 activation

Activation of caspase-8 at death inducing signaling complexes, which are assembled after activation of death receptors at the plasma membrane of cells, is an initial event of the signaling cascade that leads to apoptosis. Several mechanisms have been proposed for caspase-8 autocleavage [8]. From the perspective of information processing, two classes of mechanisms are of particular interest: the ones that result in apparent intradimeric ('cis') mechanisms and the ones that cause apparent interdimeric ('trans') mechanisms (Figure 7.1). Both would potentially lead to different response characteristics: cis mechanisms can be seen as unimolecular reactions with kinetics independent from input strength, while trans mechanisms introduce bimolecular reactions, implying accelerated activation with increased input strength.

In this chapter, section 7.2 describes the formulation of alternative caspase-8 activation model variants, which include the above described receptor activation model. By fitting these models to experimental data, discrimination between intra- and interdimeric processing modes was possible, and a minimal model variant could be selected and experimentally validated (section 7.3). Model selection showed that interdimeric cleavage is essential for caspase-8 activation, which implies that death receptor clustering at the plasma membrane is mechanistically required. In section 7.4, a Monte Carlo method is applied to intuitively understand consequences of different cleavage mechanisms on cleavage kinetics. Section 7.5 addresses the finding that caspase-8 acts as a 'molecular timer' similar to caspase-9 activation in apoptosomes. Expressions for reaction rates and ODEs of two model versions, which were implemented as described in the following, are listed in Tables A.1 and A.2.

Modeling shows a combined *cis/trans* cleavage mechanism of caspase-8 activation

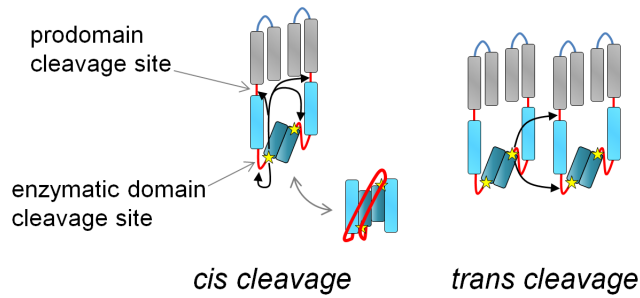


Figure 7.1. Intra- vs. inter-dimeric cleavage mechanisms: active centers (stars) in procaspase-8 can cleave domain linkers (red lines) within procaspase-8 dimers ('cis'), or between neighboring dimers ('trans').

7.2. Model implementation

Mass-action based ODEs were employed to describe DISC formation, p55 binding, the activation, release and deactivation of caspase-8, as well as substrate cleavage (Figure 7.2). The steady state solution of the receptor activation model that was described in chapter 6 served as the input for the caspase-8 auto processing model. In the following, several assumptions are described that were made to limit the complexity of the model but can be assumed to be sufficiently realistic with regard to biochemical processes.

DISC formation: In the model, DISC formation involved ligand, receptor, FADD and procaspase-8. C-FLIP proteins can influence caspase-8 activity [46, 48], but as their level was not perturbed in our experiments and was low, in the range of a few hundred compared to 3×10^5 procaspase-8 molecules per cell [46, 48], they were not explicitly included in the model, and likely appeared implicitly in some kinetic parameters. Procaspase-8 autoprocessing can only occur in a dimer configuration where two (pro)caspase-8 molecules are in close vicinity. The trimeric CD95 receptor must therefore recruit two or more FADD and procaspase-8 molecules, which then need to remain bound until autoprocessing is completed.

Single monomer binding: To avoid combinatorial complexity, several assumptions were made for describing the dimer dynamics by a simplified reaction scheme with monomeric reaction steps (Figure 7.2). It was assumed that FADD and p55 binding are highly cooperative processes. Cooperativity implies that a second p55 or FADD monomer rapidly binds to the receptor complex, once the first monomer has been recruited. Then, binding of two monomers is mechanistically equivalent to one bimolecular reaction, and can be described by a single reaction step.

Effectively monomeric reactions: Procaspase-8 needs to be bound to the DISC in a dimeric configuration to death receptors to be capable of auto-processing. Procaspase-8 auto-cleavage is to some extent a random-ordered process and may thus proceed in two alternative routes: In processing of p55 via p43 to p18 cleavage between the enzymatic subdomains precedes cleavage between prodomain and enzymatic domain. The inverse order of cleavage events results in the reactions from p55 via p30 to p18. It was not explicitly distinguished between different homo- and heterodimeric configurations of caspase-8 at the DISC, and instead, the behavior of

7.2. Model implementation

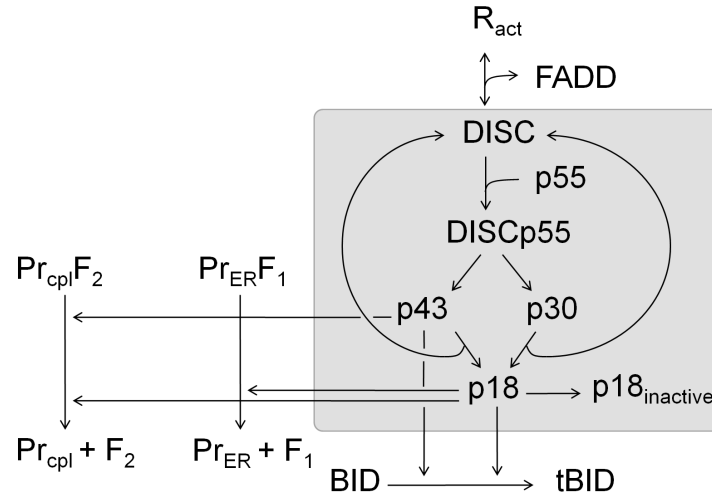


Figure 7.2. Graph of the caspase-8 activation model. Arrows represent reaction fluxes that were described in ODEs. A steady state solution for the receptor oligomerization model was combined with the visualized model, in which active receptors R_{act} serve as platform for DISC formation and procaspase-8 cleavage reactions. Here, the 'cis/cis' variant is represented, where cleavages of the prodomain and enzymatic domain sites are described as unimolecular reactions. In other variants shown in Figures 7.3 and A.1 the part in the grey area is replaced by an alternative set of reactions.

p55, p43, p30 and p18 within dimers was described as monomers. This is justified when assuming that the cleavage activity of a procaspase-8 dimer is independent of the respective dimer partner molecule. This implies for example that the activity of p43 in p43-p43 homodimers contributes to the catalytic activity of the model species p43 to the same extent as p43 in the heterodimers (p55-p43, p30-p43).

Cleavage reactions: The subsequent caspase-8 auto-processing occurs at five cleavage sites, two of which are located in the enzymatic domain of procaspase-8 (D374 and D384), whereas the remaining ones lie between the prodomain and the enzymatic domain (D210, D216 and E201) [8,87] (Figure 1.2). These groups of neighboring cleavage sites are located in close vicinity, suggesting that the corresponding cleavage products show very similar biological activity. It was therefore assumed in the model that caspase-8 autoprocessing involves only two cleavage events, one between the prodomain and the enzymatic domain (p55→p30 and p43→p18), and one between the enzymatic subdomains (p55→p43 and p30→p18). The kinetic parameters for each cleavage reaction can be regarded as collective parameters for any prodomain site or enzymatic site cleavage, respectively. The active center of caspase-8 is reversibly open in the forms p55 and p30, while it is permanently open and accessible for substrates in p43, due to cleavage of the intersubunit linker that otherwise could cover the active center [8]. Therefore, different trans cleavage activities were assumed for p55 and p30 than for p43.

Binding and unbinding: The prodomain of procaspase-8 allows for high-affinity

Modeling shows a combined cis/trans cleavage mechanism of caspase-8 activation

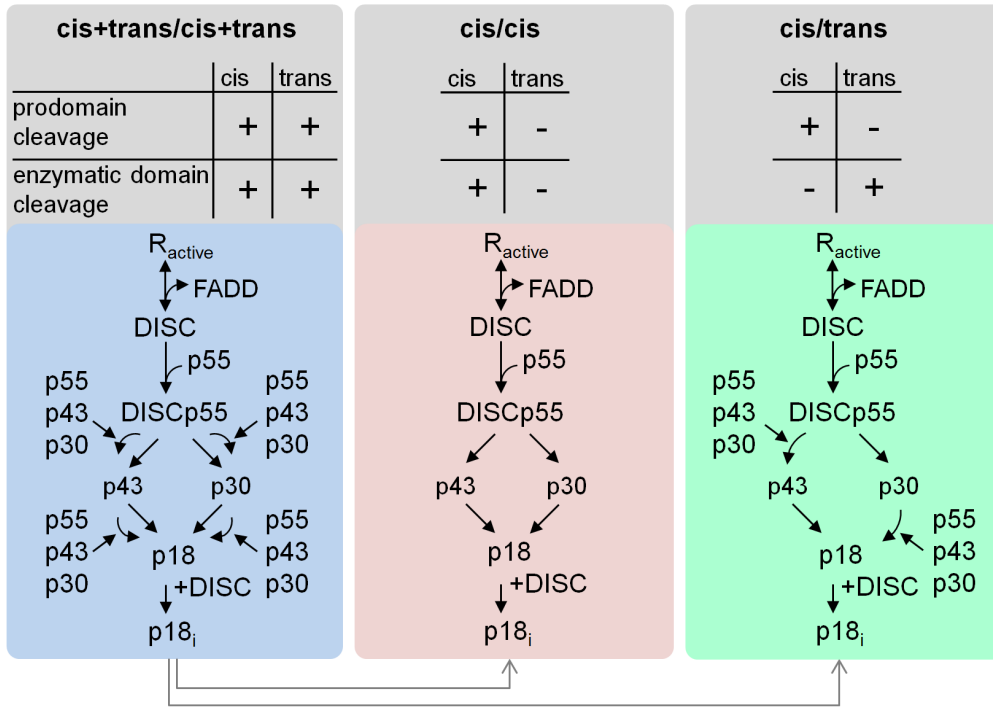


Figure 7.3. Schematic representation of model variants. The enzymatic domain sites and the prodomain sites are potentially cleaved in cis, in trans or both in cis and trans. Here, the maximal variant ‘cis+trans/cis+trans’ and two minimal variants are symbolized: a pure cis and the ‘cis/trans’ topology.

binding to the FADD-receptor complex. The species p55 and p43 contain the prodomain, and are therefore assumed to be located to the receptor complex [87]. Unbinding of these species was neglected, assuming that unbinding is slow compared to the subsequent cleavage reactions. The prodomain is cleaved off in p18 and p30, suggesting that these species can dissociate into the cytosol. It was assumed in the model that p18 is immediately released from the DISC, as only weak traces of p18 are measured in DISC immunoprecipitates [87]. The p30 intermediate is assumed to be retained at the DISC in the model, as it is only transiently formed in little amounts: The vast majority of p30 is thus expected to form heterodimers with p55 or p43, and therefore remains bound to the DISC via the dimer interface. Probe cleavage was implemented as described above and BID cleavage was modeled like the NES probe cleavage.

Intra- and interdimeric modes of caspase-8 autoprocessing could be discriminated by fitting different model variants (Figures 7.3 and A.1) to experimental data. The model variants differ in the cleavage kinetics of the caspase-8 auto-processing reactions: cis cleavage reactions are reflected by a unimolecular reaction, whereas trans cleavage reactions are reflected by a bimolecular reaction.

7.3. Model fitting, model selection and experimental validation

In the following, model variants are abbreviated by the cleavage modes, cis, trans or cis+trans, of the two linkers. For example, 'cis/trans' means that the prodomain linker cleavage can be described as unimolecular and the catalytic linker can be described as bimolecular trans reaction. As cis and trans mechanisms of each linker cleavage are not mutually exclusive, three topologies are possible for each linker, generating a total of nine different topologies (Figure 7.3 shows three of them, all are illustrated in Figure A.1). Expressions for reaction fluxes and ODEs of the complete 'cis+trans/cis+trans' model and the 'cis/trans' variant are shown in Tables A.1 and A.2. Model parameters were unknown and determined by fitting to experimental data. The MatLab toolbox PottersWheel was used for parameter estimations for each model variant [181] employing the trustregion method. Model analysis and simulations were performed with custom MatLab scripts.

Together with cleavage reactions for the cytosolic probe, the ER-anchored probe and BID, the models contain 11 species, between 14 and 26 reactions, and 12 to 16 kinetic parameters. The maximum single cell dataset that was used for model fitting comprised ten cells at four different ligand concentrations, for HeLa wt and CD95-HeLa cells. This leads to a total number of $N_{cells} \cdot N_{concentrations} \cdot N_{cell\ lines} \cdot N_{species} = 10 \cdot 4 \cdot 2 \cdot 11 = 880$ ODEs in each model variant, and a total number of 493 to 497 estimated parameters. Using the maximum dataset, 2560 single cell residuals and 80 population residuals, as defined in Equations 5.8 to 5.10, were minimized. Under these conditions, one fit that started from a random choice of values for initial concentrations \vec{x}_0 for each cell, kinetic parameters \vec{p} and scaling factors \vec{s} took around twenty minutes on a cluster node. The following section will describe the model fitting results.

7.3. Model fitting, model selection and experimental validation

Ensemble models of different caspase-8 auto-processing scenarios were fitted to experimental data to discriminate between alternative hypotheses on cis or trans mechanisms. First, the capacity of the four smallest models, 'cis/trans', 'cis/cis', 'trans/cis' and 'trans/trans', to fit the data was compared with the model that contains the highest degrees of freedom, namely 'cis+trans/cis+trans'. As a measure for the goodness of fit, the quotient χ_{sc}^2/N was used, i.e. the sum of weighted model-data differences for single cell observables, divided by the number of single cell observable data points N . Therein, the term χ_{sc}^2 of the residual function was the dominant remaining part in the residual function at the end of a model fit, and the only component that could be clearly defined as χ^2 -estimator. A value of χ_{sc}^2/N smaller than one indicates that a model topology fits the experimental data well as the distance between model and data is smaller than the experimental standard error. Strikingly, the two minimal models that constrain the cleavage in the catalytic domain to a cis mechanism could not reproduce the data (Figure 7.4).

In contrast, the minimal model variants 'cis/trans' and 'trans/trans' could ex-

Modeling shows a combined cis/trans cleavage mechanism of caspase-8 activation

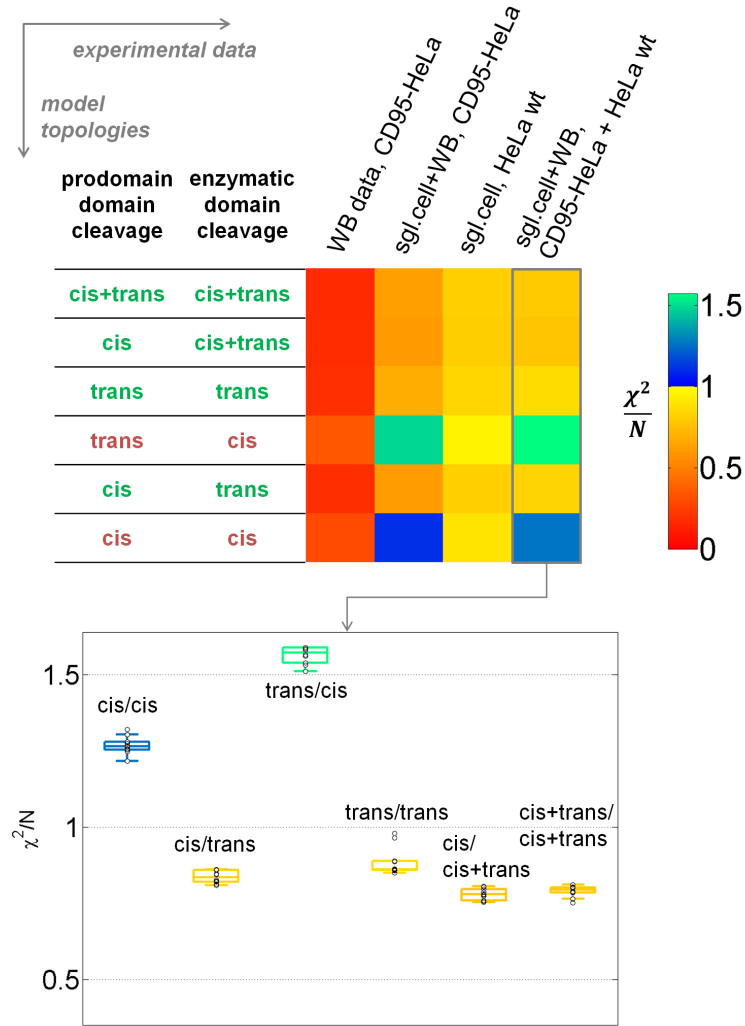


Figure 7.4. Model discrimination between cis and trans cleavage variants. Color coded χ^2/N values, indicating goodness of fit, for the 1% best of $n = 1000$ fits are shown for model topologies that were fit to experimental data of increasing complexity, and box plots for fits to the full experimental dataset, in which box colors indicate median χ^2/N values. Models with $\chi^2/N > 1$ were regarded as not being able to explain experimental data.

7.3. Model fitting, model selection and experimental validation

plain the data well ($\min(\chi_{sc,cis/trans}^2/N)=0.81$, $\min(\chi_{sc,trans/trans}^2/N)=0.85$). Moreover, extended model variants did not significantly improve the fit quality (Figure A.2) demonstrating that the minimal models 'cis/trans' (Figures 7.5 and 7.6) and 'trans/trans' are sufficient to explain the data.

One might ask, if other common indicators as the corrected Akaike information criterion (AIC_{corr}) that take into account the numbers of estimated model parameters could improve model selection: Here, differences in parameter numbers k of different model variants ($k_{cis/cis} = 493$, $k_{cis+trans/cis+trans} = 497$) contribute much less to AIC_{corr} values than differences in log-likelihood after model fitting to data ($LL_{1\%best\ fits,cis/cis} = -4093 \dots -3868$, $LL_{1\%best\ fits,cis+trans/cis+trans} = -3419 \dots -3277$), i.e. all evaluated models are about equally parsimonious with regard to parameter numbers. In this case, AIC_{corr} values are approximately proportional to χ^2 , justifying the use of χ^2/N as criterion for comparisons between model variants. Kinetic parameter estimates can be found in Table A.3.

Figure 7.7 shows two exemplary cells that were marked in Figure 7.5A to clarify why a pure cis mechanism is insufficient for explaining the single cell observables: The accelerated increase in p43 activity after a phase of low activity can be explained by the 'cis/trans' model but not by the 'cis/cis' variant that would require a rather gradual increase of enzyme activities.

To test whether the combination of single cell and population data was required for model discrimination, it was tested if reduced amounts of experimental data would have been sufficient. To this end, model variants were calibrated with western blot data only. In this case, a single set of ODEs for each model variant was used instead of the ensemble of single cell models, in accordance to previous models that were based on population data [41, 48]. As population data was not recorded at extremely high ligand concentrations, in this case, the receptor oligomerization model defined by Equation 6.18 was replaced with a simple equation for receptor binding $R_{act} = R \cdot L / (K_{DL} + L)$. As the population models were not based on probe cleavage data, they were reduced by the two ODEs describing probe cleavage, compared to the single cell models. Therefore, the population data based model variants comprised 9 ODEs and 10 to 14 kinetic parameters, which results in a total number of 16 to 20 estimated parameters. The population model variants were fitted to 60 western blot data points.

Interestingly, neither the western blot data alone nor the single cell data for HeLa wt cells alone were sufficient for model discrimination (Figure 7.4, left column). As expected, model fits to western blot data alone did not show clear differences between model variants as the western blot trajectories showed rather gradual increases of active caspase-8 compared to the corresponding single cell data. Therefore, the combination of single-cell and population data from CD95-HeLa, or from both HeLa-wt and CD95-HeLa, was required for model discrimination.

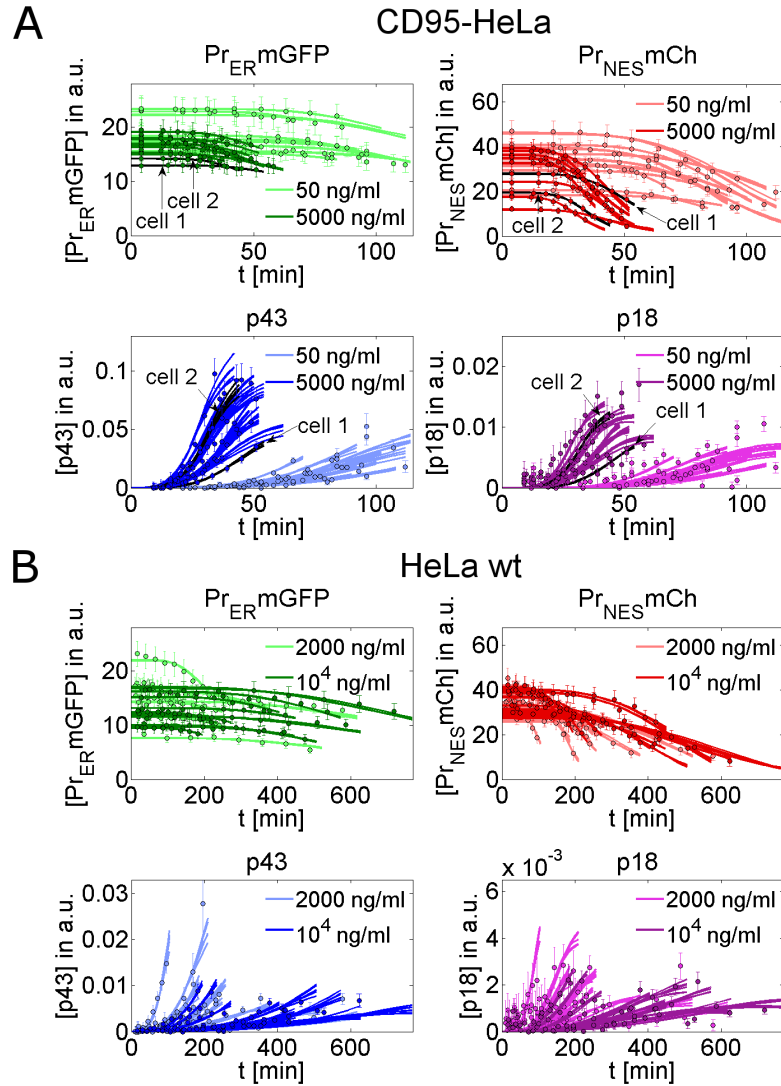


Figure 7.5. Fits of the ensemble of single cell 'cis/trans' models after calibrating with single cell data of 80 cells (2 cell lines \times 4 ligand concentrations \times 10 cells per condition) and western blot data (best 0.5% of $n = 10^3$ fits). For clarity, only fits and data at two of four concentrations are shown. Experimental data (points) and model fits (lines) for cleavage probes, p43 and p18 for CD95-HeLa (A) and HeLa wt (B) cells.

7.3. Model fitting, model selection and experimental validation

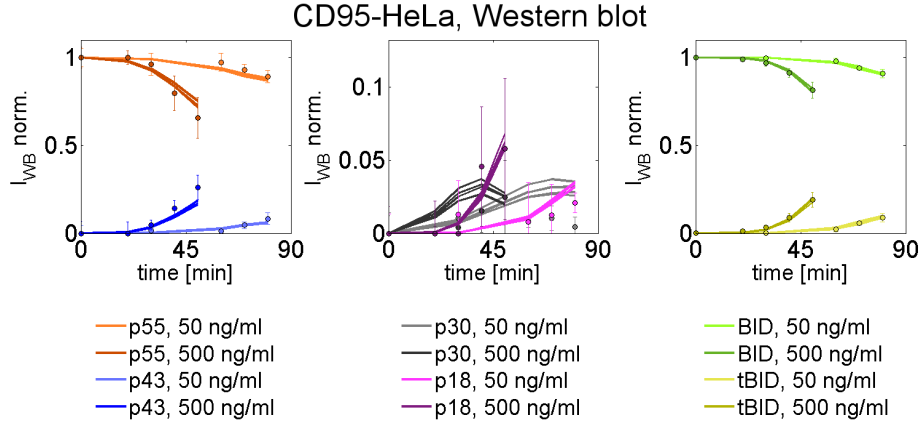


Figure 7.6. Western blot data for CD95R-HeLa cells for caspase-8 intermediates, BID and tBID and model fits.

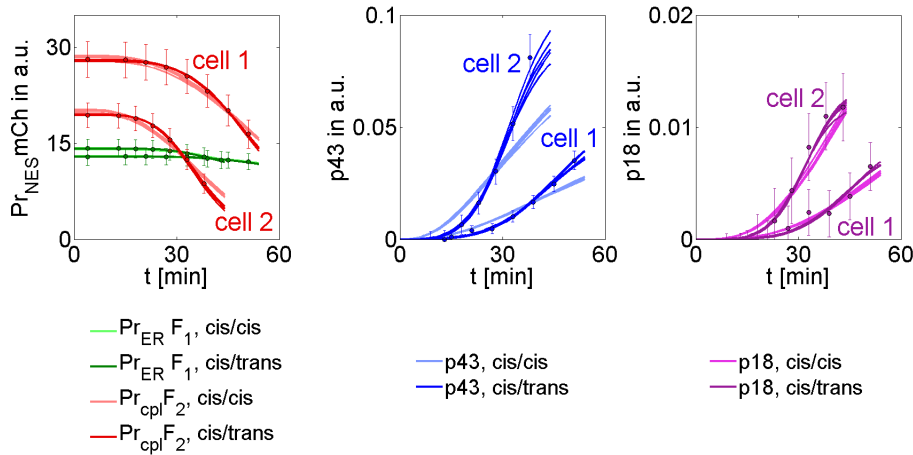


Figure 7.7. Model fits to trajectories from two exemplary CD95-HeLa cells, indicated in (A) at $[L] = 5000 \text{ ng/ml}$. The 'cis/cis' version fails to fit the data, especially for p43 and p18, while the 'cis/trans' model explains the switch like increase with delay seen in single cell trajectories.

Flux analysis shows transition from 'cis+trans/cis+trans' to 'cis/trans'

The largest model variant essentially behaved like the minimal 'cis/trans' variant indicating that the 'cis+trans/cis+trans' version over-fitted the experimental data, which could be learned from analyzing fluxes in cleavage reactions.

Fluxes were calculated by multiplying caspase-8 intermediate concentrations with the kinetic parameters of involved cleavage reactions. To distinguish between relevant and irrelevant cleavage reactions, fluxes were integrated until median apoptosis times \hat{t}_{apt} . In the full 'cis+trans/cis+trans' model each of the four reactions from p55 to p43 or p30, and from p43 or p30 to p18, is described with unimolecular ('cis') or bimolecular ('trans') kinetics, which results in eight model reactions (model equations are listed in Table A.2). For example, the equation for integrated fluxes in the reactions p55→p43, which depends on the kinetic parameters for enzymatic domain site cleavage, reads

$$\begin{aligned}
 I_{p55 \rightarrow p43} = & I_{p55 \rightarrow p43, tr, p43} + I_{p55 \rightarrow p43, tr, p55+p30} + I_{p55 \rightarrow p43, cis} = \\
 & k_{tr, D374, p43} \int_{t_0}^t [p55][p43] dt + k_{tr, D374, p55/p30} \int_{t_0}^t [p55]([p55] + [p30]) dt \\
 & + k_{cis, D374} \int_{t_0}^t [p55] dt.
 \end{aligned} \tag{7.1}$$

Therein, the two first terms describe trans cleavage of p55 either by p43 or by the sum of p55 and p30 while the third term reflects the contribution from the cis cleavage reaction. In Equation 7.1, the integrated fluxes, as well as concentration trajectories are functions of death ligand concentrations, respectively. In the same manner, reaction flux integrals for reactions were calculated for the other cleavage reactions.

Figure 7.8 shows integrated fluxes in the 'cis+trans/cis+trans' model for reactions of caspase-8 intermediates in CD95-HeLa and HeLa wt cells at different ligand concentrations, which were calculated starting from the median estimated initial concentrations in the cell ensemble model until median cell death times, respectively.

Furthermore, fractions of initial p55 levels that were processed by a certain cleavage reaction between ligand addition and the median time of apoptosis were calculated (Figure 7.9). Following the example in Equation 7.1, the left bar graphs in Figure 7.9 visualize the fractions

$$\frac{I_{p55 \rightarrow p43, cis}(\hat{t}_{apt})}{[p55](t_0)}, \frac{I_{p55 \rightarrow p43, tr, p43}(\hat{t}_{apt})}{[p55](t_0)} \text{ and } \frac{I_{p55 \rightarrow p43, tr, p55+p30}(\hat{t}_{apt})}{[p55](t_0)}.$$

Analyzing processed p55 fractions shows that certain cleavage reactions have small contributions, which can be neglected. Strikingly, the largest amount of p55 is processed in trans by p43 to p43, whereas trans cleavage by p55 plays a minor role. Contributions from cis reactions for the enzymatic domain cleavage reactions (p55→p43, p30→p18) are negligibly small. However, in prodomain cleavage reactions (p43→p18, p55→p30), fluxes for cis reactions are significantly larger than

7.3. Model fitting, model selection and experimental validation

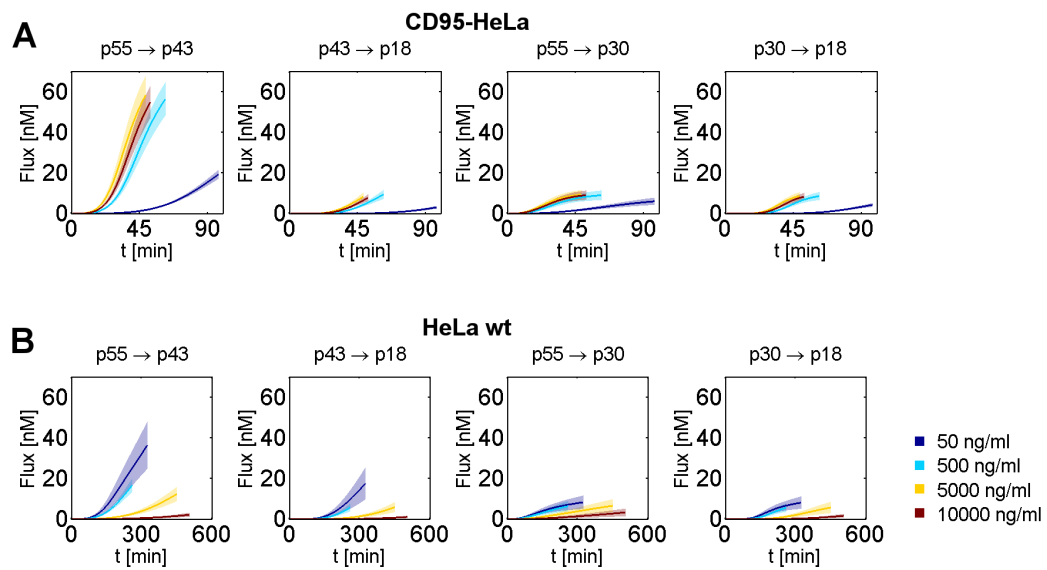


Figure 7.8. Integrated fluxes for caspase-8 cleavage reactions in the 'cis+trans/cis+trans' variant. (A, B) Solid lines represent mean trajectories and shaded areas standard deviations for the 1% best of $n = 10^3$ fits. (A) In CD95-HeLa cells, the largest amount of initial p55 is processed in the reaction $p55 \rightarrow p43$, whereas minor amounts are processed from p43 to p18 and from p55 via p30 to p18. Changing ligand concentrations has the strongest effect on the reaction from p55 to p43, due to weaker positive feedback from trans cleavage by p43. (B) Integrated fluxes for HeLa wt cells as in (A). As in CD95-HeLa cells, the reaction from p55 to p43 has the largest fluxes, whereas the relative difference to the other cleavage reactions is smaller. Compared to reactions in CD95-HeLa cells, larger amounts of p18 relative to p43 are generated before undergoing apoptosis.

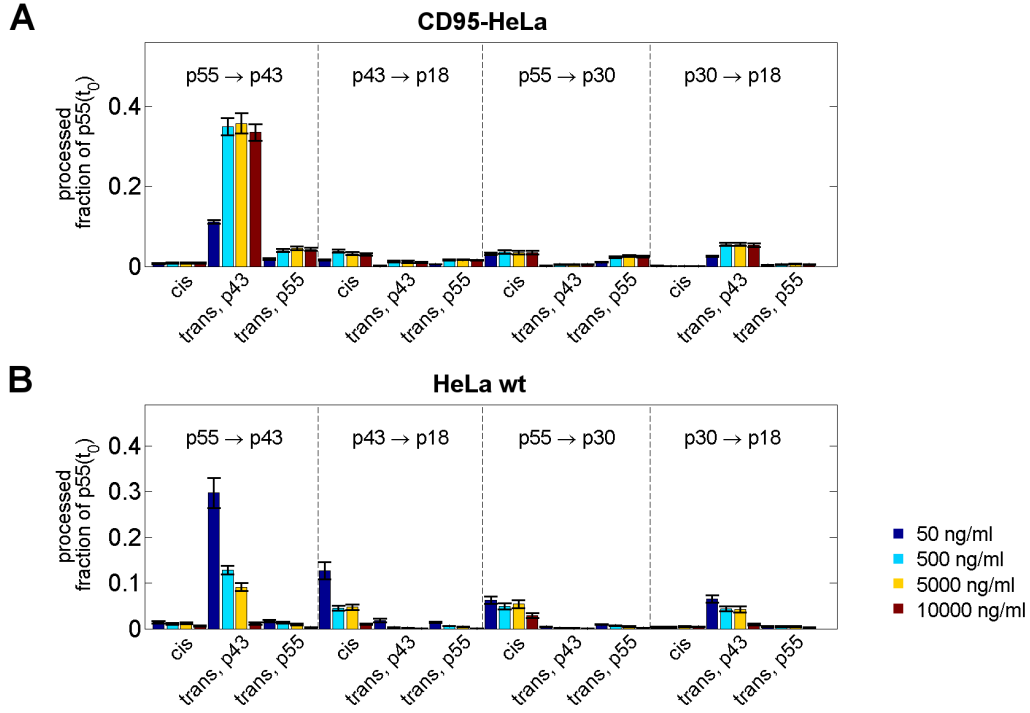


Figure 7.9. Fractions of initial p55 levels processed in cleavage reactions of the 'cis+trans/cis+trans' model. (A) Processed p55 fractions in CD95-HeLa cells. Error bars represent standard deviations for the best 1% of $n = 10^3$ model fits. (B) Processed fractions of initial p55 levels in HeLa wt cells as in (A). Similar to CD95-HeLa cells, trans cleavage of p55 by p43 is the strongest contributing reaction. Again, fluxes for cis cleavage of the enzymatic domain and for trans cleavage of the prodomain are negligible, which supports model simplifications to the 'cis/trans' topology.

trans reactions. Therefore, model simplification by rejecting enzymatic domain cis cleavage and prodomain trans cleavage is justified, which results in the 'cis/trans' model.

For the less contributing prodomain trans cleavage reactions larger fluxes are estimated for trans cleavage by p55 than by p43, opposite to the trans cleavage reactions of the enzymatic site, where p43 has larger trans cleavage activity. In this reaction, kinetics of trans cleavage by p55 is rather similar to the kinetics of p55 cis cleavage than p55 trans cleavage by p43. Therefore it is made more difficult to discriminate between cis cleavage of p55 with a reaction rate proportional to $[p55]$ and trans cleavage of p55 by p55 where the reaction rate is proportional to $[p55]^2$. Additional experiments supported further discrimination between model variants as described in the following section.

To obtain intuitive insights in the timing of caspase-8, momentary half-life times of caspase-8 intermediates were calculated for parameter estimates of different model variants. For example, momentary half-lives of p55 and of p43 were calculated for

7.3. Model fitting, model selection and experimental validation

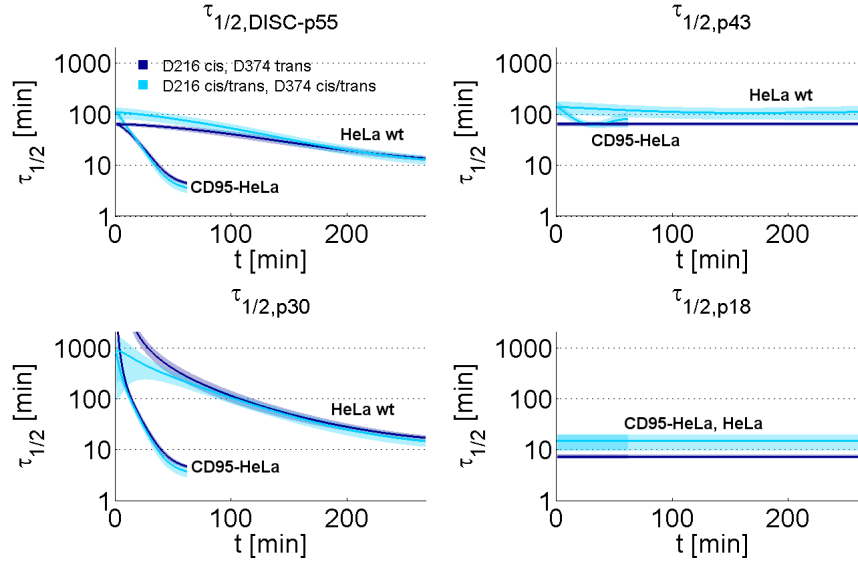


Figure 7.10. Predicted half-life times of caspase-8 intermediates for the 'cis/trans' (blue) and the 'cis+trans/cis+trans' (cyan) models in CD95-HeLa and HeLa wt cells. Both variants show very similar half-life estimates for caspase-8 intermediates, in particular for p18 and p43 ($\tau_{1/2,p18} \approx 10'$ and $\tau_{1/2,p43} \approx 100'$, solid lines: means, shaded areas: standard deviations for the best 1% of $n = 1000$ fits).

the 'cis+trans/cis+trans' model by

$$\tau_{1/2,p55,'cis+trans/cis+trans'} = \ln 2 [(k_{tr,D216,p43} + k_{tr,D374,p43})[p43] +$$

$$(k_{tr,D216,p55/p30} + k_{tr,D374,p55/p30})([p55] + [p30]) + k_{cis,D216} + k_{cis,D374}]^{-1}$$

and

$$\tau_{1/2,p43,'cis+trans/cis+trans'} = \frac{\ln 2}{k_{tr,D216,p43}[p43] + k_{tr,D216,p55/p30}([p55] + [p30]) + k_{cis,D216}}.$$

For the 'cis/trans' model, half-lives were analogously calculated by

$$\tau_{1/2,p55,'cis/trans'} = \frac{\ln 2}{k_{tr,D374,p43}[p43] + k_{tr,D374,p55/p30}([p55] + [p30]) + k_{cis,D216}}$$

and

$$\tau_{1/2,p43,'cis/trans'} = \frac{\ln 2}{k_{cis,D216}}.$$

Half-lives of p30 and p18 were calculated in the same manner. Figure 7.10 shows that estimated half-lives of caspase-8 intermediates for the 'cis+trans/cis+trans' and the 'cis/trans' topologies are in an equivalent range.

Modeling shows a combined cis/trans cleavage mechanism of caspase-8 activation

In comparison to the 'cis/trans' topology, fit quality to experimental data was slightly worse for the 'trans/trans' model variant, which describes prodomain site and the enzymatic domain site are cleaved by interdimeric cleavage reactions (Figure 7.4). Clear discrimination between these two variants was not possible by model fitting. However, model analysis for the best fits of the 'trans/trans' model showed clear deviations from predictions of the complete 'cis+trans/cis+trans' model (Figures A.5, A.6 and A.7). The 'trans/trans' model could be finally excluded by additional experiments, which will be described in the following paragraph.

Taken together, analyzing reaction fluxes in caspase-8 cleavage reactions and half-lives of caspase-8 intermediates shows that simplifying the complete 'cis+trans/cis+trans' topology leads to the 'cis/trans' variant rather than other minimal model topologies. Trans cleavage reactions potentially cause positive feedback or feedforward: in the 'cis+trans/cis+trans' variant, p55, p43 and p30 catalyze their own processing in a feedforward manner. Furthermore, p43 and p30 amplify their own production by positive feedback to p55 cleavage. The flux analysis shows that trans cleavage reactions rather establish a positive feedback than a feed forward activation, especially for the reaction catalyzed by p43. The most important positive feedback is involved in trans cleavage of p55 by p43 to p43 while other trans reactions only have minor contributions. This feedback of p43 on its own generation is mechanistically important, as estimated parameters showed about eight times higher trans-cleavage activity for p43 than for DISC-bound p55 or p30 (Table A.3). Half-lives indicate that the active intermediate p43 is relatively stable compared to the short-lived final product p18. This principle, which was denoted as 'molecular timer', will be further addressed in section 7.5.

Experimental validation: cleavage probes containing caspase-8 autoprocessing sites support a 'cis/trans' mechanism

The experimental data described in this paragraph were obtained from Dr. Joel Beaudouin (German Cancer Research Center, Heidelberg).

Model fitting to single cell and population data favored trans kinetics for cleavage of the enzymatic domain site and a cis reaction for prodomain site cleavage (Figure 7.4). However, the 'trans/trans' variant, in which both sites are cleaved with trans mechanisms, could not unequivocally be rejected by model fitting to experimental data. In order to provide independent experimental support for 'cis/trans' cleavage reactions, cleavage probes containing caspase-8 auto-processing sites were designed and their cleavage kinetics was analyzed. A cleavage probe containing the prodomain linker sequence requires a bimolecular reaction step to be cleaved by caspase-8. By localizing this probe with a myristoylation-palmitoylation (Myr-Palm) domain on the plasma membrane a caspase-8 trans auto-cleavage scenario could be mimicked.

Cleavage probes contained cleavage sequences of amino acid residues MTISDS (caspase-8 prodomain, D210), PREQDS (caspase-8 prodomain, D216), PVETDS

7.3. Model fitting, model selection and experimental validation

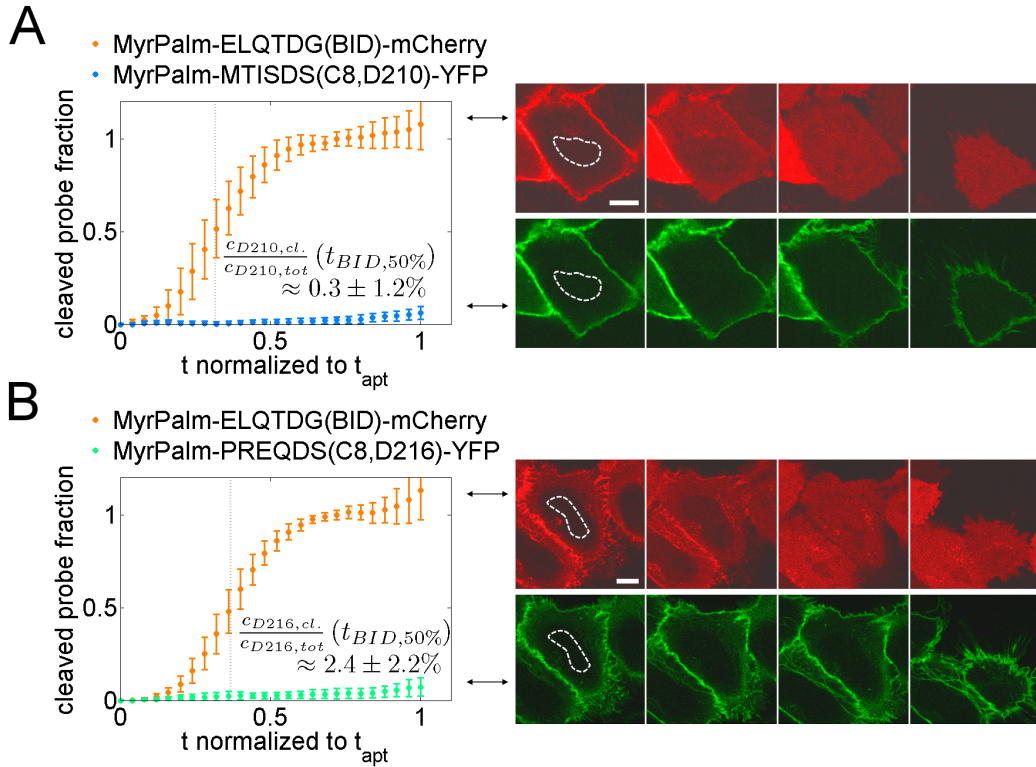


Figure 7.11. Discrimination experiments with cleavage probes. (A) Averaged normalized intensities from nuclear ROIs (white dotted lines) recorded in $n = 21$ HeLa wt cells expressing MyrPalm-(BID site)-mCherry (top row, red channel) and MyrPalm-(D210 site)-YFP (bottom row, green channel) probes. (B) Averaged nuclear intensities from $n = 16$ HeLa wt cells expressing MyrPalm-(BID site)-mCherry (top row, red channel) and MyrPalm-(D216 site)-YFP (bottom row, green channel) probes. Trajectories in panels (A) and (B) indicate that at half-times $t_{BID,50\%}$ only small amounts of prodomain site probes are processed (error bars: standard deviations, scale bars: $10\mu m$).

(caspase-8 enzymatic subdomain linker, D374) or ELQTDG (BID) and a fluorescent protein. Furthermore, cleavage probes linked to a nuclear export signal (NES) were used that either contain all prodomain cleavage sites (D210, D216 and D223), the sequence DEVA (non-cleavable for caspase-8), or ELQTDG (BID) and a fluorescent protein. Cells simultaneously expressed probes with the BID cleavage sequence bound to mCherry and probes containing one of the other cleavage sequences bound to YFP, to use BID probe cleavage kinetics as reference, respectively.

After probe cleavage the, fluorescent protein entered the nucleus whereas un-cleaved probes were exclusively localized at the plasma membrane. After ligand addition, fluorescence intensity in nuclear regions of interest was measured to monitor probe cleavage, similar as for probe cleavage experiments to generate single cell observables for active caspase-8 as described in chapter 4. Here, the leucine zipper-soluble CD95 ligand (LZ-sCD95L) [138] was used as described in [136] to

stimulate apoptosis. To compare between groups of signal trajectories, nuclear intensity trajectories were normalized to the time of apoptosis, which was indicated by membrane blebbing, and to the average signal of the complete cell (Figures 7.11A, 7.11B and 7.12A) or to the saturation limit indicating cleavage of the total amount of probes (Figure 7.12B). Average trajectories therefore approximate the value one if the nuclear intensity is equal to the average intensity of the cell.

In line with the predicted cis mechanism, it was found that probes using the aminoacid sequences REQD (prodomain cleavage site D210) and TISD (prodomain cleavage site D216) as cleavage linkers showed no significant cleavage before cell death (Figures 7.11A and 7.11B). Similar results were obtained with probes containing a more complete caspase-8 prodomain linker (Figure 7.12A). In contrast, the model clearly predicted trans cleavage of the enzymatic domain linker. Therefore, it was expected that a probe with the aminoacid sequence VETD, corresponding to the enzymatic domain cleavage site D374, is efficiently cleaved. According to this prediction, it could be observed that the VETD probe is fully cleaved at the time of cell death, comparable to an LQTD probe containing the cleavage sequence of BID (Figure 7.12B). Furthermore, cytosolic NES probes showed that trajectories of probes with all prodomain cleavage sites were similar to trajectories of probes with non-cleavable sites (Figure 7.12A). This validates the hypothesis that prodomain site cleavage is a cis mechanism within procaspase-8 dimers rather than a trans reaction between neighbored dimers.

Taken together, these data provide independent support for the model-predicted 'cis/trans' cleavage mechanism of caspase-8 autoprocessing. Next, it was investigated why a trans cleavage of the enzymatic domain was required in the model to explain the experimental data. As can be seen in Figure 7.7, a cis mechanism for the cleavage of the catalytic domain linker fails to reproduce the switch-like increase in the p43 trajectories after a certain delay of low enzymatic activity. A similar conclusion could be drawn by analyzing the qualitative features of 'cis/cis' and 'cis/trans' models using simulations with randomly chosen kinetic parameters in a Monte Carlo approach, as described in the following.

7.4. Monte Carlo modeling reveals qualitative differences in 'cis/cis' and 'cis/trans' topologies

Model fitting suggested that trans-cleavage is required for caspase-8 activation, but did not provide intuitive explanations why the pure cis mechanism fails to fit the data. Fits of the 'cis/cis' and 'cis/trans' models were systematically compared to understand how the two mechanisms differ. It could be observed that the 'cis/cis' mechanism fails to explain the switch-like accumulation of the catalytically active p43 intermediate observed in single-cell measurements (Figure 7.7). This indicated the requirement of trans cleavage, which results in a positive feedback loop that amplifies the signal and thereby induces a more rapid caspase-8 activation and cell

7.4. Monte Carlo modeling reveals qualitative differences in 'cis/cis' and 'cis/trans' topologies

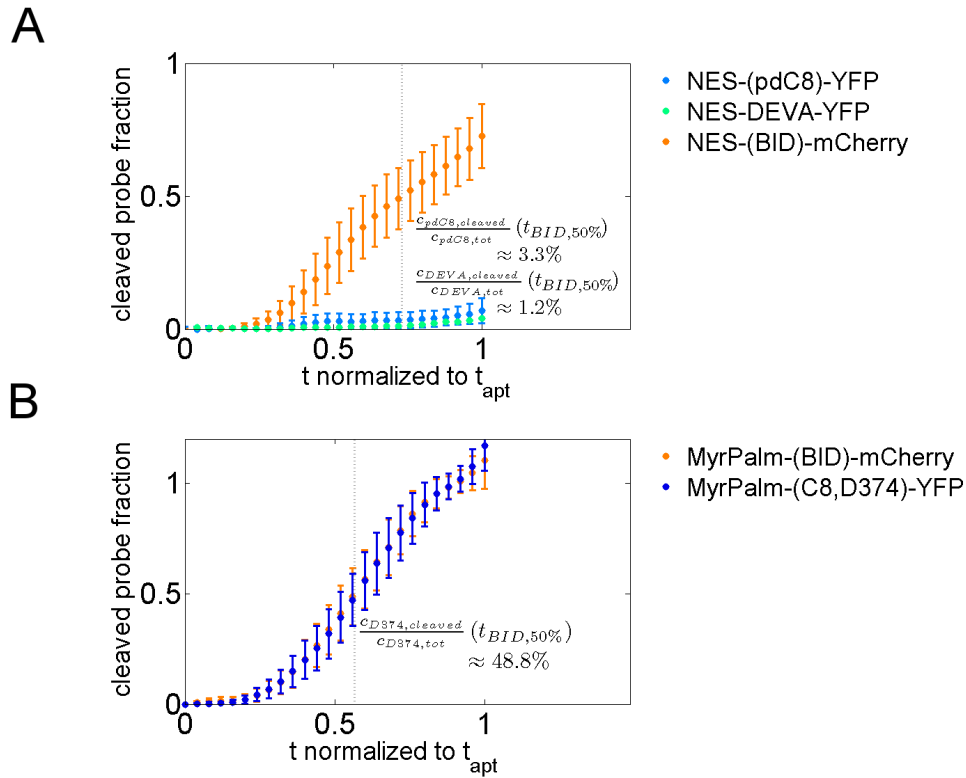


Figure 7.12. The enzymatic domain cleavage site, but not the prodomain site, is cleaved in *trans*. (A) Averaged nuclear intensities from $n = 16$ HeLa wt cells expressing NES-(caspase-8 prodomain sites)-YFP, $n = 23$ cells expressing MyrPalm-DEVA-YFP, and $n = 39$ cells expressing MyrPalm-(BID site)-mCherry probes. Probes with caspase-8 prodomain sites are not efficiently cleaved compared to probes with the cleavage sequence of BID. Trajectories with prodomain sites show only slightly higher cleavage for the probe with prodomain sites than for the DEVA probe, which cannot be cleaved by caspase-8. (B) Averaged normalized intensities from nuclear ROIs recorded in $n = 20$ HeLa wt cells expressing the two probes MyrPalm-(BID site)-mCherry and MyrPalm-(D374 site)-YFP. At $t_{BID,50\%}$ when half of BID probes was cleaved, about the same amount of enzymatic domain probes was processed.

Modeling shows a combined cis/trans cleavage mechanism of caspase-8 activation

	fast reactions, $k \in [10, 10^4]$	slow reactions, $k \in [10^{-3}, 1]$
parameters in both variants	$k_{on,CD95L}, k_{off,CD95L},$ $k_{on,FADD}, k_{off,FADD}, k_{on,p55}$	$k_{p18,inactive}, k_{cl,probe}$
'cis/cis'		$k_{cis,D216}$ (prodomain cleavage), $k_{cis,D374}$ (enz. domain cl.)
'cis/trans'		$k_{cis,D216}$ (prodomain cl.), $k_{tr,D374,p55/p30}$ (enz. domain cl.), $k_{tr,D374,p43}$

Table 7.1. Kinetic model parameters and sampling intervals.

death.

An exhaustive analysis of the whole parameter space for 'cis/cis' and 'cis/trans' models was performed based on a Monte Carlo approach to show more rigorously that switch-like caspase-8 activation can only be observed in a 'cis/trans' mechanism. The kinetic parameters of the models were 10^4 times randomly sampled, and simulations were performed for each parameter set. Kinetic parameters were sampled from uniform distributions within two interval sizes, one for fast binding reactions of CD95L, FADD and p55 ($k \in [10, 10^4]$), and one for slow reactions ($k \in [10^{-3}, 1]$). For simplicity, the receptor oligomerization model component was replaced by a simple bimolecular reaction describing monomeric ligand binding to monomeric receptors. This was sufficient in this case, as it was intended to simply obtain a wide range of active receptor amounts for simulating caspase-8 activation kinetics under variable conditions. The ligand concentration values $[CD95L] \in [10^{-2}, 3 \cdot 10^{-2}, 0.1, 0.3, 1, 3, 10, 10^2] \cdot K_{DL}$ and experimentally measured average initial protein concentrations were used as initial conditions for simulations with each randomly chosen set of kinetic parameters.

The simulation results were systematically analyzed to show that 'cis/cis' and 'cis/trans' models differ in the switch-like behavior of the time courses. Trajectories resulting from different parameter sets were temporally normalized by the time $t_{5\%}$ when 5% of the probes are cleaved, and normalized in amplitude by the total probe concentrations $[Pr_{cpl}F_2]$, respectively. In general, 'cis/trans' trajectories can show a steeper time course for cytosolic probe cleavage than 'cis/cis' trajectories, especially in CD95-HeLa cells (Figure 7.13): In these, cytosolic probe cleavage switched from 5% to 50% during a less than two-fold increase in time for the 'cis/trans' mechanism (blue trajectories), while trajectories were shallower for the 'cis/cis' model simulations (red trajectories).

This complementary approach can further support discrimination between 'cis/cis' and 'cis/trans' topologies by trajectory shape attributes. To this end, the times

7.4. Monte Carlo modeling reveals qualitative differences in 'cis/cis' and 'cis/trans' topologies

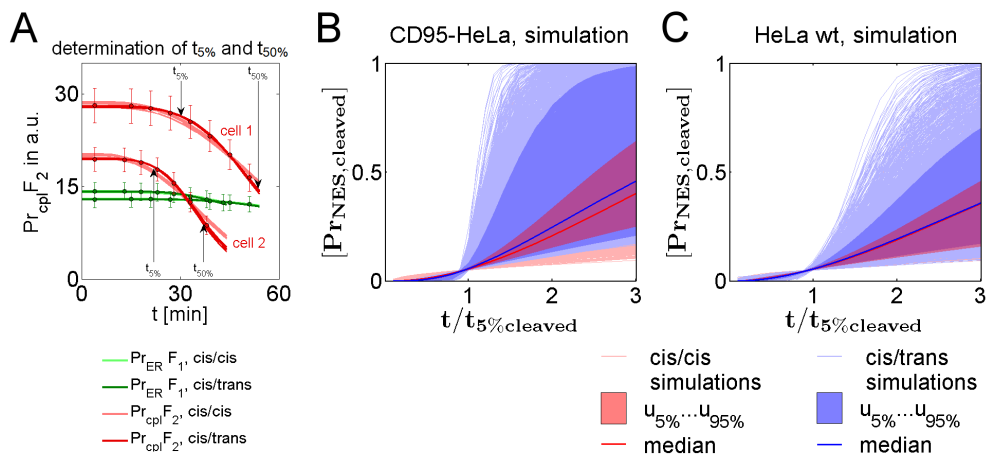


Figure 7.13. Monte Carlo simulations of cytosolic probe cleavage kinetics support discrimination between 'cis/cis' and 'cis/trans' topologies. (A) Model fits of 'cis/cis' and 'cis/trans' versions to data of two exemplary cells as in Figure 7.7. In the left plot, times until 5% or 50% cytosolic probe cleavage, $t_{5\%}$ and $t_{50\%}$, are indicated. (B, C) Cytosolic probe cleavage trajectories from random parameter simulations illustrate that the 'cis/trans' variant can explain steeper and switch-like probe cleavage trajectories than the 'cis/cis' topology for CD95-HeLa (B) and HeLa wt cells (C). Trajectories were obtained by randomly sampling kinetic rate constants ($N_{\text{samples}} = 10^4$) from large parameter intervals (shaded areas: space between 5% and 95% percentiles, solid lines: medians).

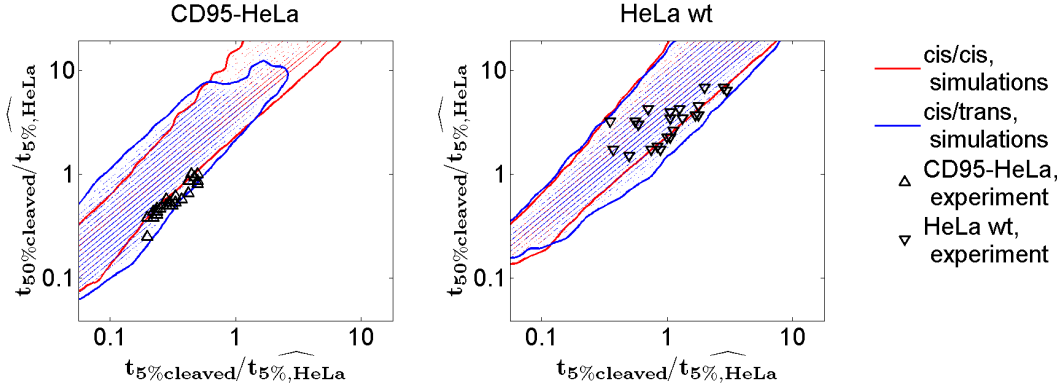


Figure 7.14. Monte Carlo modeling of cytosolic probe cleavage supports discrimination between 'cis/cis' and 'cis/trans' topologies. Combinations of normalized $t_{5\%}$ and $t_{50\%}$ experimental values for CD95-HeLa cells fit into the space for $t_{5\%}$ - $t_{50\%}$ combinations of simulated 'cis/trans' trajectories but not into the space of simulated 'cis/cis' trajectories. However, for HeLa wt cells a direct discrimination by the $t_{5\%}$ and $t_{50\%}$ measures is not possible as most of the experimental values are compatible with simulated values from the 'cis/trans' as well as the 'cis/cis' versions. Time points extracted from simulated trajectories are shown as dots. Solid lines mark borders of dot densities that include 99% of simulated values. To obtain a collective timescale, time points were normalized by the mean of $t_{5\%}$ values for HeLa wt cells ($\hat{t}_{5\%,HeLa}$)

until 5% or 50% cytosolic probe cleavage were determined to describe two major trajectory characteristics, a delay period of low cleavage activity ($t_{5\%}$) and a period of accelerated cleavage between $t_{5\%}$ and $t_{50\%}$, which is indicated in Figure 7.13A. Figure 7.14 shows combinations of the cytosolic probe cleavage times $t_{5\%}$ and $t_{50\%}$ for simulations and experiments that were normalized by mean $t_{5\%}$ of HeLa cells, respectively.

To display areas of possible $t_{5\%}$ and $t_{50\%}$ combinations for 'cis/cis' and 'cis/trans' models, dot densities $\rho = 1/N_{samples}N_{ij}$, in which N_{ij} is the number of $t_{5\%}$ and $t_{50\%}$ combinations in the area $i\Delta t_{5\%}j\Delta t_{50\%}$ in a grid defined by coordinates i and j , were calculated. Areas that contain 99% of the integrated density of simulation results are surrounded by solid lines for the two model variants. Experimental combinations ($t_{5\%}, t_{50\%}$) for CD95-HeLa cells (Figure 7.14, left plot) lie within the valid area for the 'cis/trans', but outside the area for the 'cis/cis' model, which does not support relatively low ratios of $t_{50\%}$ to $t_{5\%}$. Contrarily, most of the experimental measures for HeLa wt cells (Figure 7.14, right plot) lie within valid areas of both topologies. Here, in accordance to the model fitting results, again CD95-HeLa cells support mechanistic discrimination, while both topologies are tolerable for data from HeLa wt cells. By decreasing the level of death receptors, the trajectories become less switch-like: Comparing between the mean $t_{5\%}$ and $t_{50\%}$ for CD95-HeLa and HeLa wt cells shows, that tenfold less receptors cause a stronger decrease in $t_{50\%}$ than for $t_{5\%}$.

7.5. Caspase-8 operates as a molecular timer

In conclusion, simulating trajectories by a Monte Carlo approach confirmed that 'cis/trans' models were able to generate switch like trajectories, especially in CD95-HeLa cells, in contrast to 'cis/cis' models. A trans mechanism is required to explain the experimental data on the kinetics of cytosolic probe cleavage and to establish a switch-like initiation of apoptosis.

7.5. Caspase-8 operates as a molecular timer

Combining single cell and western blot data, it could be concluded that caspase-8 is activated by a combined 'cis/trans' mechanism. This section addresses an interesting finding with regard to the deactivation kinetics of caspase-8 that shows a parallel to the kinetics of caspase-9 activation at apoptosomes.

Effective half-lives of the different caspase-8 cleavage products during the time course of apoptosis were calculated to shed light on the timing of caspase-8 activation at the DISC and compare different model variants (Figure 7.10). Figure 7.15 shows half-lives of the different caspase-8 intermediates for the validated 'cis/trans' model variant. The half-lives of p55 and p30 decrease over time as more p43 is generated, which catalyzes the processing of these intermediates. p43 is processed to p18 via an apparent cis mechanism, implying a constant half-life of p43. According to the best fits of the model, this half-life was around 1 hour. In contrast, the model predicted that p18 is active for 7 minutes only, which indicates that mostly p43 contributes to caspase-8 activity in the cell. However, the final product p18 never accumulates. Therefore, caspase-8 can be regarded as a molecular timer that determines the duration of its activity by the combination of the low cleavage constant for prodomain site cleavage and the rapid inactivation of p18. As p43 is restricted to the DISC, this also indicates that the activity is spatially restricted to the plasma membrane and is not significantly propagated to the cytosol.

The term 'molecular timer' describes the mechanism for the activation of the related enzyme caspase-9 [182,183]: After the event of mitochondria outer membrane permeabilization (MOMP), apoptosomes are assembled from the proteins Apaf-1 and cytochrome c that serve as a platform for procaspase-9 binding. When binding to apoptosomes, procaspase-9 becomes active, cleaves downstream substrates and processes itself to caspase-9. While procaspase-9 has a high binding affinity to apoptosomes, caspase-9 has a low binding affinity and becomes inactive after being released from apoptosomes [183]. Therefore, procaspase-9 is a stable intermediate enzyme form that generates most of the cleavage activity, while the final product caspase-9 is quickly inactivated. Here, model analysis indicated that caspase-8 activation at the DISC is mechanistically equivalent to procaspase-9 activation at apoptosomes: p43 is a stable intermediate form that processes itself to the unstable form p18, which is quickly inactivated after being released from the DISC.

Taken together, the model is consistent with the idea that p43 is the main active form of caspase-8 during apoptosis. It maintains its activity through a molecular clock to eventually switch off caspase-8 activity after p18 formation.

Modeling shows a combined cis/trans cleavage mechanism of caspase-8 activation

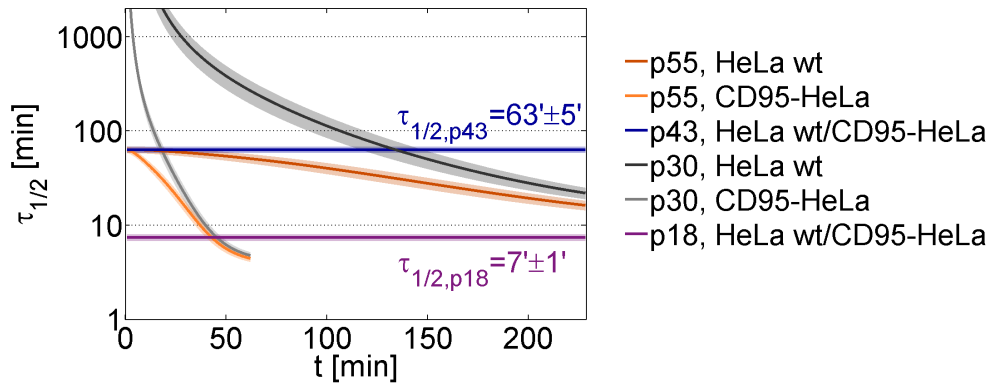


Figure 7.15. Half-lives for caspase-8 intermediates. Lines show means and areas indicate standard deviations for the best 1% best of $n = 1000$ 'cis/trans' model fits, simulated at $[CD95L] = 500ng/ml$. While p43 accumulates at the DISC, due to a higher half-life than p55, p18 has a low stability and does not accumulate.

8. Simulating the variability of apoptosis in heterogeneous cell populations

In the cell ensemble model on caspase-8 activation, cell-to-cell variability in probe cleavage, single cell caspase-8 activities and apoptosis times was explained by different levels of initial protein concentrations. From estimated initial protein levels, a multivariate lognormal joint distribution was derived to randomly sample vectors of initial concentrations and simulate the behavior of a heterogeneous population of cells. Originating at random sets of initial protein concentrations the model was integrated until certain tBID levels were reached that were sufficient to induce mitochondria outer membrane permeabilization (MOMP) and thereby irreversibly lead to cell death.

First, this procedure was applied, as described in section 8.1, to validate the model of caspase-8 activation. For this purpose the model was calibrated to a training data set and then validated with a test data set as described in section 8.2. Then, the model calibrated to the entire data set was used to simulate a variety of overexpression or knock-down conditions in order to study functional roles of the involved signaling protein species (section 8.3).

8.1. Simulating cell-to-cell variability by a multivariate lognormal joint distribution

It is known that protein concentrations in cells commonly follow lognormal distributions as they result from a sequence of processes with stochastic influences, which depend on each other in a multiplicative manner [184,185]. A fundamental origin of lognormal distributions of protein concentrations is the intrinsic noise at the level of the transcription of genes, which leads to lognormally distributed mRNA levels [186]. Therefore, it was assumed that a lognormal joint distribution of initial protein levels is sufficient to explain cell-to-cell variability in the caspase-8 activation model. While initial concentrations were allowed to be variable the kinetic parameters were assumed to be equal for each cell. This assumption is justified as the model reactions exactly describe the reactions of molecular species rather than collective processes, in which the interactions of several proteins are involved, as it is the case for the model described in part II.

By model fitting, the initial concentrations for CD95R, FADD, p55 and BID were

estimated for each cell included in the cell ensemble model. To link the model of caspase-8 activation to cell death, the arrival at a certain tBID threshold level was regarded as sufficient trigger for apoptosis [39, 167], which happens a few minutes after MOMP [81, 82]. In the cells, which were used to extract observables for probe cleavage and caspase-8 activities, these critical tBID levels were estimated from integrating the model with estimated kinetic parameters until their apoptosis time.

The multivariate lognormal density for a vector of concentrations \vec{x}_0 with n dimensions is defined by the vector of parameters $\vec{\mu}$ and the covariance matrix D and reads

$$p(\vec{x}_0) = \frac{1}{(2\pi)^{n/2} \det(D)^{1/2} \prod_{i=1}^n x_{0,i}} \exp\left(-\frac{1}{2}(\ln \vec{x}_0 - \vec{\mu})^T D^{-1}(\ln \vec{x}_0 - \vec{\mu})\right)$$

as described in [187]. In order to estimate the parameters μ and σ , one-dimensional lognormal distributions were fitted to the estimated initial single cell concentrations for CD95R, FADD, p55, and BID. Estimated initial levels of BID and estimated tBID levels at apoptosis times were slightly correlated, despite the fixation of the mean BID and tBID levels to population observables for BID and tBID. To eliminate the bias of this correlation from the parameter estimation process, tBID threshold fractions $[tBID](t_{apt})/[BID]$ were used instead of absolute tBID concentrations. Then, correlation coefficients and covariances were calculated between estimated initial concentrations and critical tBID fractions to define the covariance matrix D of a combined multivariate lognormal joint distribution. To randomly sample from the multivariate lognormal distribution using a random number generator for multivariate normal distributions, the covariance matrix $D \equiv cov(x_{0,i}, x_{0,j})$ of variables $x_{0,i}$ and $x_{0,j}$ had to be transformed to the covariance matrix $cov(y_i, y_j)$ of the corresponding normal distribution of variables $y_i = \ln x_{0,i}$ and $y_j = \ln x_{0,j}$. The correlation coefficient $\rho_{x_{0,i}x_{0,j}}$ of a lognormal distribution is related to the correlation coefficient $\rho_{y_i y_j}$ of normally distributed variables by the relation

$$\rho_{x_{0,i}x_{0,j}} = \frac{cov(x_{0,i}, x_{0,j})}{\sigma_i \sigma_j} = \frac{\exp(\rho_{y_i y_j} \sigma_i \sigma_j) - 1}{\sqrt{(e^{\sigma_i^2} - 1)(e^{\sigma_j^2} - 1)}}.$$

Therefore, in order to generate random vectors from the corresponding multivariate normal distribution, the corresponding covariance matrix

$$cov(y_i, y_j) = \rho_{y_i y_j} \sigma_i \sigma_j = \ln \left(\rho_{x_{0,i}x_{0,j}} \sqrt{(e^{\sigma_i^2} - 1)(e^{\sigma_j^2} - 1)} + 1 \right)$$

was calculated from lognormal correlation coefficients $\rho_{x_{0,i}x_{0,j}}$. Using the covariance matrix $cov(y_i, y_j)$ multiple random vectors \vec{y} were sampled to use $\vec{x}_0 = \exp(\vec{y})$ as input of initial concentrations and critical tBID fractions for model integration. The time points when the sampled fractions $[tBID](t_{apt})/[BID]$ were reached were regarded as apoptosis times.

8.2. Testing the predictive capability of a model of cell death induction

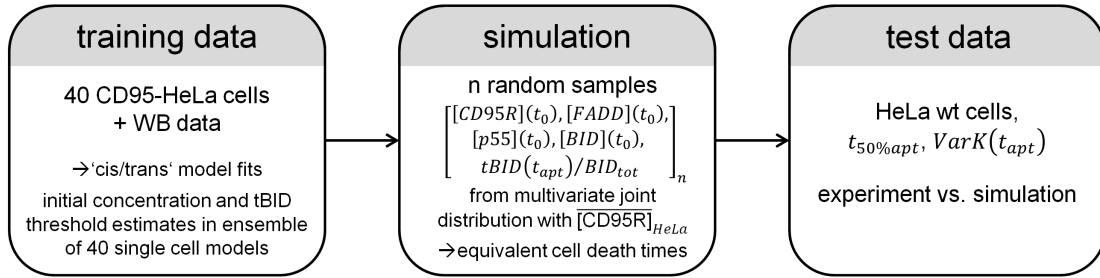


Figure 8.1. For validation, fits of the 'cis/trans' model to CD95-HeLa cells and the experimentally determined average receptor number of HeLa wt cells were used to generate a lognormal multivariate joint distribution. Random vectors of initial concentrations and tBID threshold fractions were drawn from this distribution to calculate equivalent cell death times for HeLa wt cells and compare simulated with experimental kinetics and variability.

Employing this procedure the determinants of cell death timing, variability and survival in a heterogeneous population of cells were studied as described in the following sections.

8.2. Testing the predictive capability of a model of cell death induction

To further validate the 'cis/trans' model, its capacity to predict cell death kinetics and the variability in cell death time was tested. For this purpose, the 'cis/trans' model was fitted to a test data set from CD95-HeLa cells to predict cell death kinetics and variability of cell death times in HeLa wt cells expressing about ten times less CD95 death receptors.

In order to predict required conditions for cell death, an ensemble of 40 single cell models was fitted to a training data set of 40 CD95-HeLa single cell datasets (10 cells per ligand concentration) combined with western blot data for caspase-8 intermediates, BID and tBID (Figure 8.1). The trained model was then used to predict individual fractions of tBID in total BID levels at death times, regarded as tBID thresholds that are sufficient for apoptosis, in combination with initial protein levels for each cell in the training data set.

Then, to simulate kinetics of HeLa wt cells, it was assumed that all levels of all involved signaling proteins are lognormally distributed and equal, except the CD95 receptor, between CD95-HeLa and HeLa wt cells. A lognormal multivariate distribution was defined from median FADD, p55 and BID level and median tBID threshold estimates, and the experimentally determined mean CD95 receptor level of HeLa wt cells. Therein, covariances of initial concentration estimates and tBID thresholds in the training data set were taken into account, according to the procedure of previous studies [95], except for CD95 receptor. Covariances with CD95 receptor levels

were neglected as it was likely that they were unequal for CD95-HeLa and HeLa wt cells. Random vectors of initial concentrations and tBID thresholds were sampled from this distribution, representing simulated conditions of HeLa wt cells. For different ligand concentrations, the model was integrated for 100 randomly chosen sets of initial concentrations and tBID fractions, respectively, until the respective tBID threshold was reached, which was regarded as time of cell death. This procedure was executed for each of the 1% best of 10^3 model fits. Cells, in which tBID thresholds were not reached, were hypothetically regarded as survivors. It was distinguished between simulated cells, in which tBID thresholds were not reached within the time of the experiment (13 hours) or within the maximal integration time (10^4 minutes).

Predicted median cell death times in HeLa wt cells were in good accordance with experimental measurements, except for one data point for the ligand concentration of 500ng/ml (Figure 8.2A). Furthermore, the model predicted a much larger coefficient of variation of cell death times for HeLa wt than for CD95-HeLa cells, which is in good agreement with experimental data (Figure 8.2B).

In summary, CD95-HeLa observables could be successfully used as training data set in order to predict death kinetics and variability in HeLa wt cells for model validation.

8.3. Ligand, receptor and FADD control timing and variability while p55 and BID control survival

Regulatory control in signaling networks is often distributed unequally, implying that different signaling species control different aspects of the signaling response. To this end, a systematic sensitivity analysis was conducted to analyze how the total cellular concentrations of CD95L, CD95R, FADD, procaspase-8/p55 and BID control the cell death kinetics and variability.

To study functional roles of involved signaling proteins, cell death was simulated at different fold-changes of initial protein concentrations, now using the 'cis/trans' model fitted to the complete set of CD95-HeLa and HeLa wt data (Figure 8.3). From initial protein concentration and tBID threshold estimates, separate lognormal multivariate joint distributions were determined for CD95-HeLa and HeLa wt cells, now including all variances and covariances. Random vectors were sampled from these distributions and the model was integrated with different fold-changes between 0.1 and 10 times the original concentration, separately for each protein. Again, equivalent death times were determined by integrating the model until tBID levels arrived at required thresholds. Cells, in which tBID thresholds were not reached within the maximum integration time, were considered as survivors.

From simulations of 100 random samples for each condition and each of the 1% best of 10^3 fits, median cell death times, coefficients of variation of cell death times and surviving fractions were determined. Additionally, trajectories of surviving fractions of cells with an apoptosis time smaller than the experimental duration of 13

8.3. Ligand, receptor and FADD control timing and variability while p55 and BID control survival

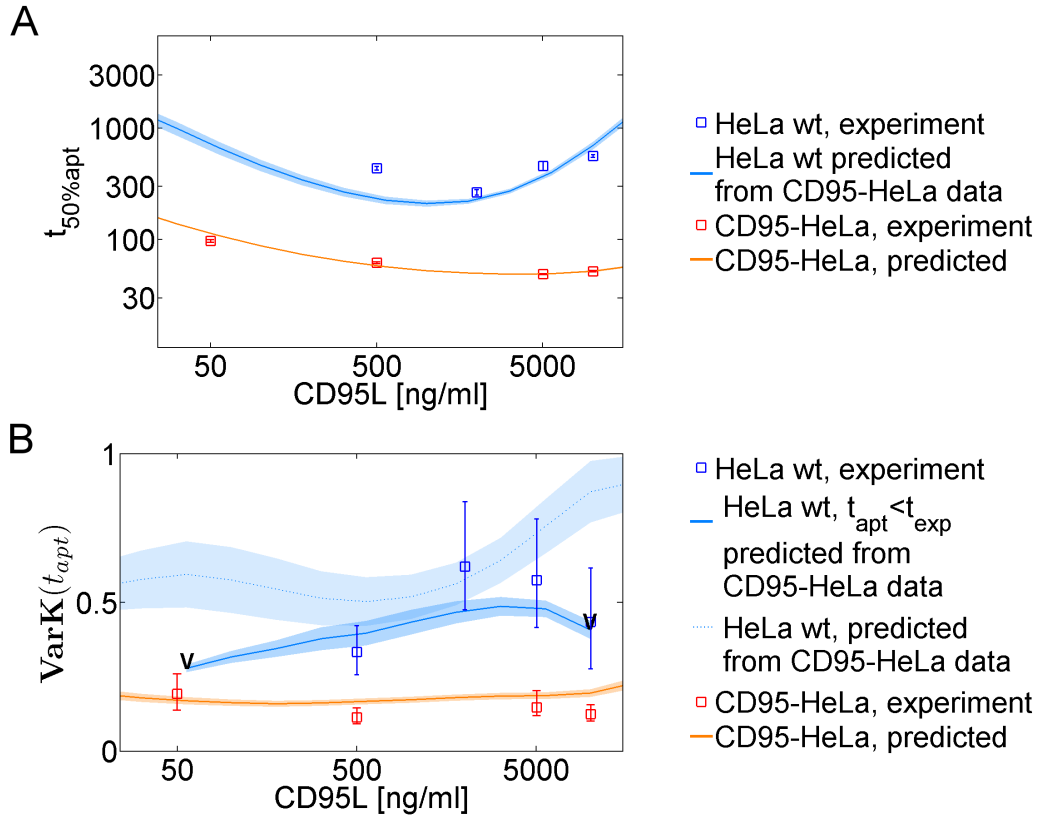


Figure 8.2. Validation of the 'cis/trans' model. (A) Experimental values (squares) and predictions (lines and shaded areas) of median cell death times for HeLa wt and CD95-HeLa cells. For validation, model fits to CD95-HeLa cells were used to predict HeLa wt death kinetics. Error bars represent standard deviations between medians in different fields of view on the object carrier (solid lines: means, shaded areas: standard deviations, best 1% of $n = 10^3$ fits). (B) Coefficients of variation for cell death times had values in the range of 0.5 to 0.6 for HeLa wt and in the range of 0.1 to 0.2 for CD95-HeLa cells (squares with error bars estimated by bootstrapping) and from 'cis/trans' model simulations, based on fits to CD95-HeLa data. Lines and shaded areas correspond to standard deviations as in panel (A). Predicted coefficients of variation ($VarK$) were calculated at ligand concentrations, at which at least 50% of the simulated cells underwent apoptosis during t_{exp} (limits marked by 'V'). $VarK$ estimates including cells undergoing apoptosis later than t_{exp} are shown as dotted line.

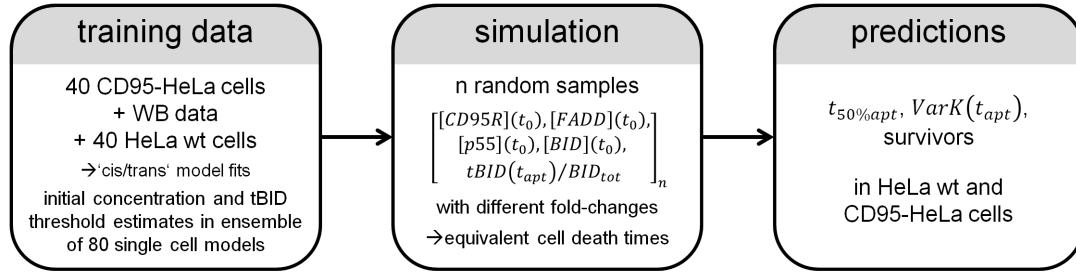


Figure 8.3. Procedure for predicting the behavior of a heterogeneous cell population. To study functional roles of involved signaling proteins, fits of the 'cis/trans' model to CD95-HeLa cells and HeLa wt cells were used to generate lognormal multivariate joint distributions for the two cell lines, and sample random vectors of initial concentrations and tBID threshold fractions with different fold-changes of initial concentrations.

hours ($t_{apt} < t_{exp}$) were calculated, representing fractions of cells that survive the duration of the experiment. Predictions originating at the ligand concentration of $500ng/ml$, are shown in Figure 8.4, while predictions originating from the other experimentally used ligand concentrations, which mostly lead to similar characteristic observations, are shown in Figures A.3 and A.4.

Simulations showed that cell-to-cell variability and the cell death times are strongly dependent on levels of the upstream signaling species CD95L, CD95 and FADD. These species determine the number of active DISCs, which represent the bottleneck in caspase-8 activation, especially in HeLa wt cells. In CD95-HeLa cells, overexpression of proteins does not influence cell death variability, and reduction only weakly does so (Figures 8.4B and A.4). In contrast to upstream species, the downstream species procaspase-8 and BID levels have minor influence on cell death timing and variability.

Cellular survival, however, is strongly regulated by the downstream signaling proteins procaspase-8 and BID. Below a certain level of procaspase-8 or BID the required apoptosis inducing tBID thresholds are not reached anymore (Figures 8.4A and 8.4B, lower rows). Procaspase-8 can restrict tBID production because of its limited life time. During the turnover of p55 to p18 only a limited number of substrate molecules can be cleaved before p18 becomes inactive. Therefore, reducing p55 levels increases the amount of surviving cells, in which not enough tBID is processed by the available pool of procaspase-8. Similarly, but with much weaker influence, the upstream receptor and FADD levels have influence on survival fraction. Especially in CD95-HeLa cells survival is independent from ligand, receptor and FADD levels. From simulations, further experiments can be predicted: pulse-wash experiments, in which caspase-8 activation is induced for a limited time, should show transient cleavage activity of p43 and the decay of caspase-8 activity after CD95L removal.

It can be concluded that upstream and downstream signaling species inversely control the dynamics of cells death: upstream species control speed of cell death

8.3. Ligand, receptor and FADD control timing and variability while p55 and BID control survival

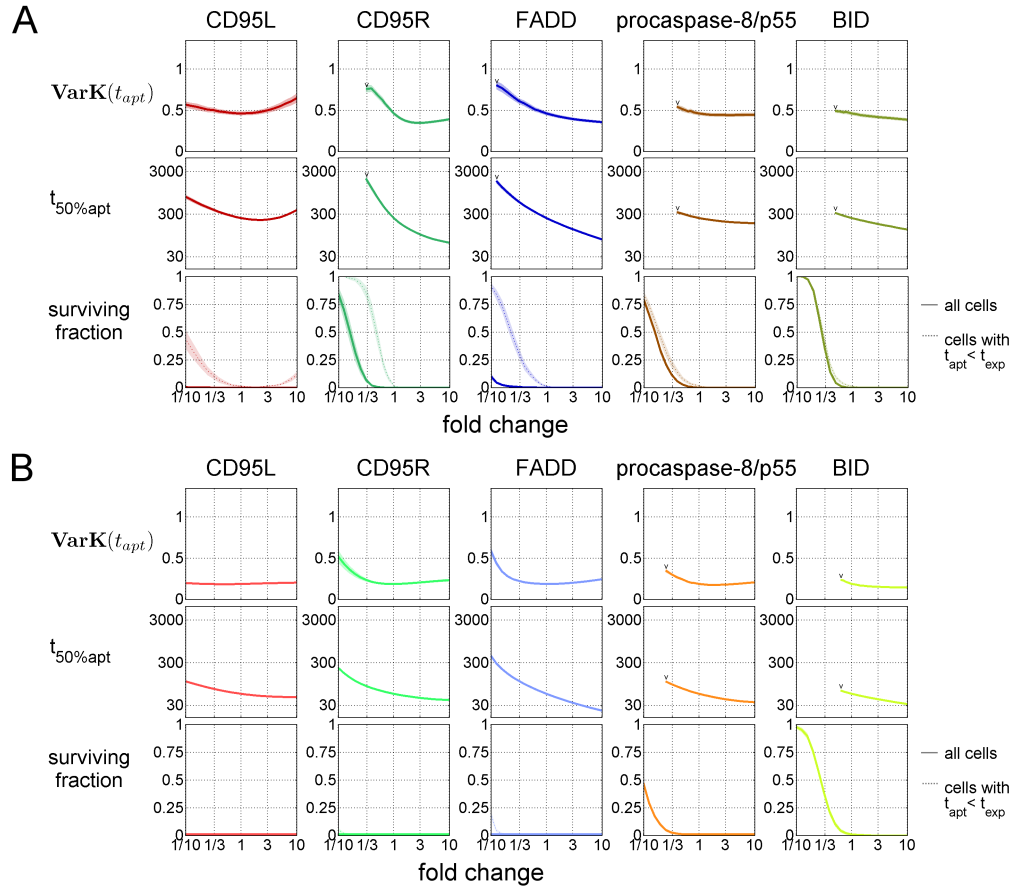


Figure 8.4. Determinants of cell death kinetics and variability. (A) Predicted coefficients of variation for cell death times, median cell death times and fractions of surviving cells at different fold changes of initial protein concentrations for CD95 ligands, receptors, FADD, p55 and BID for HeLa wt cells. The origins represent conditions at ligand stimulation with a concentration of 500ng/ml . In the subplots for surviving fractions, dotted lines represent the surviving fractions within the duration of the single cell experiments (13 hours), while solid lines represent surviving fractions within the total integration time interval. $VarK(t_{apt})$ and $t_{50\%apt}$ are only calculated in situations, where $\geq 90\%$ of the cells die (limits marked by 'V'). (B) Predictions for CD95-HeLa cells as in panel (A) (dotted or solid lines: means from 1% best of $n = 10^3$ fits, shaded areas around lines: standard deviations).

Simulating the variability of apoptosis in heterogeneous cell populations

and its variability, while the downstream species control fraction of cells killed.

9. Discussion

To study the initiation of extrinsic apoptosis, a model-based method to estimate caspase-8 activity in single cells and a multi-scale modeling approach combining single cell with cell population measurements were developed. The approach extends previous apoptosis models, which were trained on cell population measurements only and thereby may not fully capture the detailed kinetics at the single cell level.

The developed caspase-8 activation model complements previous apoptosis models, which were more focused on MOMP dynamics [35, 39] or downstream effector caspases activation [40, 45, 49, 54, 55]. Models that included details of DISC assembly [41, 46, 48] did not discriminate between putative molecular mechanisms of caspase-8 activation, and were primarily focused on the role of c-FLIP proteins in the life/death decision.

Using a model selection approach, intradimeric ('cis') processing of procaspase-8 dimers was excluded and an interdimeric cleavage ('trans') mechanism could be revealed, in which DISCs need to be assembled at least transiently into higher-order clusters at the plasma membrane. Experimental data was best explained by the 'cis/trans' model variant, in which the prodomain site in pro-caspase-8 is cleaved in cis and the enzymatic domain site in trans. Interdimeric trans cleavage mechanism establishes a positive feedback loop with important functional implications for signaling: Auto-amplification of p43 allows a more pronounced switch between low and high activity states. As a consequence, the caspase-8 network may promote survival upon weak transient cell death ligand expositions, while prolonged stimulation efficiently triggers cell death. A delay in caspase-8 activation as a consequence of a positive feedback may help to separate the apoptosis signal from the dynamics of other CD95 dependent pathways involved in proliferation or cellular differentiation (Figure 9.1) [173, 188].

Recently, a study employing mass spectrometry of CD95 receptor immune-precipitates showed that after stimulation with LZ-CD95 the number of procaspase-8 molecules exceeds the number of FADD molecules several-fold, interpreted as chain formation of several procaspase-8 at single FADD molecules [36, 189]. In this study the formation of such protein conglomerates was not explicitly included. This simplification was introduced as this modeling study was mainly focused on effective mechanisms of caspase-8 activation while neglecting the stoichiometric details of the complexes. The simplified model of the DISC is justified, as DISC formation occurs on a shorter time scale than the subsequent procaspase-8 autoprocessing [6].

Based on model fitting to a complex dataset, the kinetic parameters describing caspase-8 autoprocessing could be reliably estimated, revealing that p43 efficiently accumulates at the DISC, whereas p18 is highly unstable. Caspase-8 processing

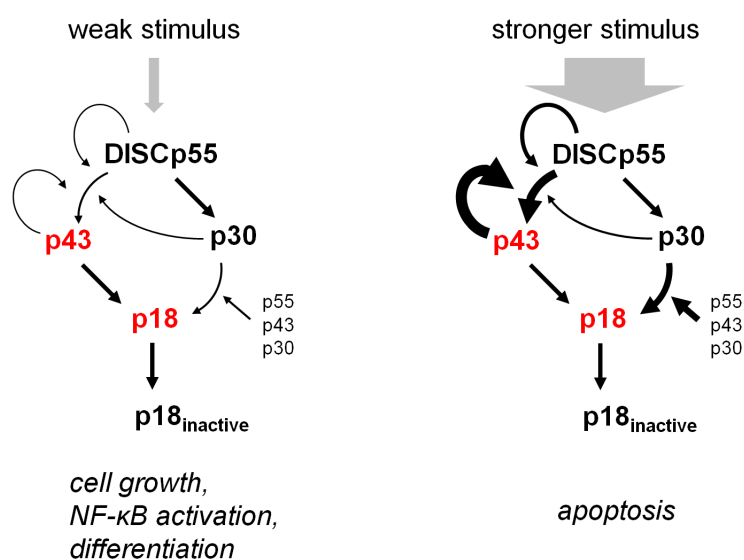


Figure 9.1. The 'cis/trans' cleavage mechanism facilitates pathway branching. A weak cell death stimulus generates low caspase-8 cleavage activity: Low numbers of active DISCs generate low levels of p43 during weak feedback from p43. In this situation, p55 is rather processed via the inactive intermediate p30. Therefore, rather non-apoptotic pathways can be activated by caspase-8, stimulating cell growth, activation of the transcription factor NF- κ B and cellular differentiation. A stronger stimulus enhances production of the active intermediate p43 by causing stronger feedback therefore increasing the *efficiency* of procaspase-8 usage to generate an apoptosis inducing cleavage activity.

is thus mechanistically similar to procaspase-9 auto-activation at the apoptosome. Apoptosome-bound procaspase-9 cleaves downstream substrates and cleaves itself to caspase-9. After dissociation of caspase-9 the cleavage activity is lost, implying the function as a 'molecular timer', in which the cleavage probabilities control the active time or the extent of cleavage activity [182,183]. Here, procaspase-8 processing at the DISC shows the same phenomenon of the stable intermediate enzyme p43 and the unstable product p18. Accordingly, a previous study showed that the catalytic activity of caspase-8 can be increased by mutating the prodomain cleavage sites [87]: this prevents the conversion of the stable p43 intermediate into unstable p18, alleviating the timer effect.

By systematic sensitivity analysis it could be demonstrated that signaling components upstream of procaspase-8 such as cell death ligand, receptor and the adaptor protein FADD primarily shape the cell death kinetics and variability. In contrast, downstream species like procaspase-8 and BID rather influence the fraction of cells surviving the cell death stimulus. Furthermore, survival by lacking caspase-8 activity underlines that an 'efficient' use of procaspase-8, employing p43 for cleaving downstream substrates, is a requirement for apoptosis, as caspase-8 cleavage capacity is limited due to rapid p18 inactivation. In summary, the multi-scale model presented in this study, calibrating an ensemble of single cell models to observables of a heterogeneous population of cells, represents an important conceptual advance in the understanding of mechanisms involved in variable response of individual cells to cell death stimuli.

**Cellular heterogeneity determined by variable
kinetic parameters: cell ensemble model of Epo
receptor traffic**

This part describes a modeling study of Epo receptor traffic in single cells that was based on experimental data recorded by confocal microscopy. The experiments that were conducted for this purpose were carried out in collaboration with Anne-Lucia Unger from the group of Prof. Dirk-Peter Herten (Institute for Physical Chemistry, Heidelberg University).

10. Modeling EpoR receptor traffic in single cells

In cells, external signals from ligands are transmitted by receptors to intracellular signaling cascades. Receptor signaling is typically regulated by receptor internalization and transport processes between the plasma membrane and other cellular compartments [190]. Internalization not only weakens the signal but was also shown to enhance the accuracy of signaling [191]. The signal transduction by erythropoietin receptors (EpoR) was shown to be strongly dependent on receptor internalization kinetics [123]. A characteristic property of the EpoR system is that only a small fraction of the total receptor amount is present at the membrane and can be activated by external ligands. The receptor signal is attenuated by rapid internalization of active EpoR, which is followed by receptor inactivation [124]. While the traffic and signaling of EpoR has been described in models that were based on population data [123, 124], no study has quantified EpoR transport kinetics in single cells yet. This part addresses an approach to characterize cell-to-cell variability in EpoR traffic based on cell ensemble models that are calibrated with quantitative single cell data.

In the model of caspase-8 activation (part I), the underlying biochemical reactions could be explicitly described. Therefore, reaction kinetics was assumed to be equal in different cells. Single cell models in the cell ensemble model were linked by the boundary condition of equal kinetic parameters. Cellular variability was explained by variable initial protein concentrations. In current models of Epo receptor signaling, the receptor transport processes were described by unimolecular reactions, which are in fact dependent on several biochemical processes. Unimolecular reactions masked several processes involved in vesicle formation, the activation of kinases and phosphatases [117], ubiquitinylation reactions [118], cargo protein and cytoskeleton dependent processes, as the assembly of actin oligomers [192]. In the current study, direct measures of EpoR concentrations in different cellular compartments were recorded, and the heterogeneous behavior of different cells was described by variable kinetic parameters.

In order to test several model hypotheses, an experimental setup was developed to extract quantitative information of EpoR traffic in single cells by using confocal

microscopy of GFP fused EpoR and Epo that was labeled with the fluorescent inorganic dye Cy5.5 (section 10.1). To quantify receptor synthesis and degradation, auxiliary experiments were performed to record GFP-EpoR synthesis after bleaching and GFP-EpoR degradation after blocking its synthesis. In order to learn, which processes are relevant for EpoR traffic in single cells, cell ensemble models were constructed and calibrated with single cell data (section 10.2). An optimal model could be selected, in which internalized active EpoR are directly recycled to the plasma membrane and unbound Epo is accumulated inside the endocytic recycling compartment. Analyzing the variability of kinetic parameters between cells showed that cell-to-cell variability mostly originates from the processes of active receptor internalization and receptor recycling (section 10.3).

10.1. Quantification of EpoR traffic in single cells

An experimental setup was developed to quantify internalization and intracellular transport of EpoR in single cells by confocal live cell imaging. These quantitative single cell data were required to calibrate kinetic models of intracellular EpoR traffic. The fusion protein of EpoR with the fluorescent protein GFP was used to image receptors. Epo labeled with the inorganic dye Cy5.5 was used to quantify the amount of internalized ligand. Furthermore, a membrane marker protein fused to the fluorescent protein mCherry was used to quantify the amount of EpoR at the plasma membrane or near the plasma membrane.

Live-cell experiments For live-cell experiments, a cell line stably expressing EpoR-GFP was used, which was derived from H838 lung adenocarcinoma cells. The cell line was stably transfected with a plasmid encoding for a fusion protein consisting of a myristoylation-palmitoylation domain and the fluorescent protein mCherry (MyrPalm-mCh). This membrane marker was similar to the caspase-8 cleavage probe described in chapter 7 (Figure 7.11) but without a cleavage site. In a similar setup as described in part I, microscopic stack images were recorded (Figure 10.1). After the first time point was recorded, cells were treated with Epo-Cy5.5 at a concentration of $4.2nM$ corresponding to $10U/ml$ in enzyme activity units. While EpoR was labeled with the fluorescent protein GFP, which is degraded together with EpoR, Epo was labeled with the inorganic dye Cy5.5, which cannot be degraded by the cell. This combination of a degradable EpoR label with a non-degradable label of Epo was chosen to improve estimates of intracellularly degraded EpoR. Data was recorded for a total period of 6 hours. For each time point, an image stack with 26 slices and a slice thickness of $\Delta z = 0.7\mu m$ was recorded to enclose the whole cell volumes. In the first 30 minutes, a time interval of 5 minutes and afterwards of 10 minutes was chosen, which resulted in 40 time points. To obtain quantitative measurements of EpoR-GFP synthesis and degradation, further live-cell experiments were conducted, which employed photobleaching and blocking protein synthesis by the drug cycloheximide (CHX). A microscope appliance that was orig-

10.1. Quantification of EpoR traffic in single cells

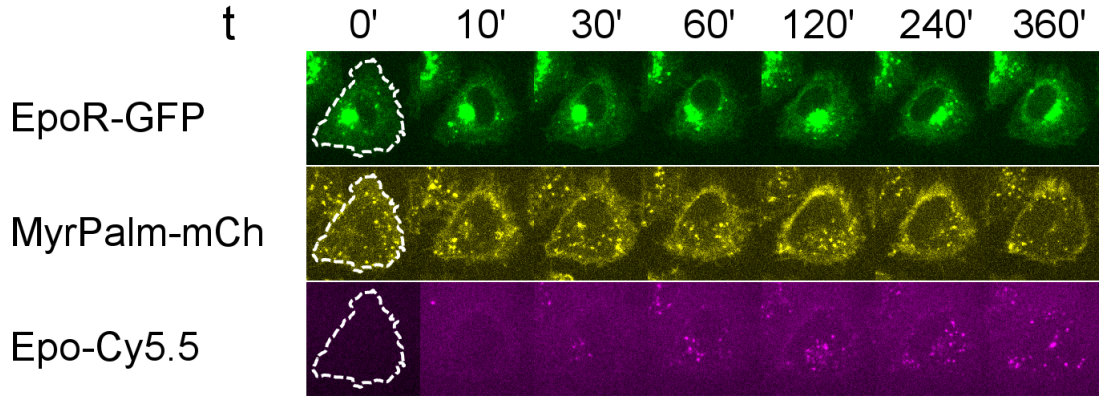


Figure 10.1. Measurements of EpoR-GFP and Epo-Cy5.5 internalization in H838 cells. Single planes of 3D stack images are shown for different time points. Epo-Cy5.5 was added after the first recorded stack. The membrane ROI was defined from the outer cell borders in MyrPalm-mCherry images as indicated by the white dotted line at $t = 0'$.

inally designed for FRAP experiments (fluorescence recovery after photobleaching) was used to bleach GFP in complete volumes of single cells. After recording the first image stack, the laser pulse for photobleaching was applied. Then, new synthesis and recovery of the fluorescent Epo-GFP signals was recorded for 6 hours as for Epo treated cells.

Image segmentation A simple segmentation software was developed to semiautomatically define regions of interest (ROIs) for subcellular compartments of the cells within each image stack (Figure B.1), according to intensity threshold values $I_{th,GFP}$, $I_{th,Cy5.5}$ and $I_{th,mCh}$. In each image with intensities $I_c = I_c(x_i, y_j, z_k)$ of a cell at the height z_k within an image stack of channel c , ROIs were defined for the plasma membrane, the enclosed cytoplasmic volume and vesicles therein. Intensity threshold values were manually determined by classifying multiple small image regions as membrane, vesicle or background voxels, and choosing average intensity values that separate between these regions. The outer border line of the area with $I_{mCh} \geq I_{th,mCh}$, having a line width of three pixels, which corresponds to a width of $\approx 1\mu m$, was segmented to define the membrane ROI. In the plane of the contact area between the plasma membrane and the specimen slide, the whole bottom area of the cell with $I_{mCh} \geq I_{th,mCh}$ was included to the membrane ROI. In the volume enclosed by the membrane ROI, further ROIs were defined for EpoR-GFP vesicles ($I_{GFP} \geq I_{th,GFP}$), Epo-Cy5.5 vesicles ($I_{Cy5.5} \geq I_{th,Cy5.5}$) and vesicles, which contained EpoR-GFP and Epo-Cy5.5 ($I_{GFP} \geq I_{th,GFP}$ and $I_{mCh} \geq I_{th,mCh}$). Figure 10.2 shows a visualization of exemplary membrane and vesicle ROIs. For each subregion, mean I_{GFP} and $I_{Cy5.5}$ values were multiplied with ROI volumes and divided by the total cell volumes to obtain measures that correspond to cellular concentrations.

The available set of single cell data comprised time-resolved measurements in

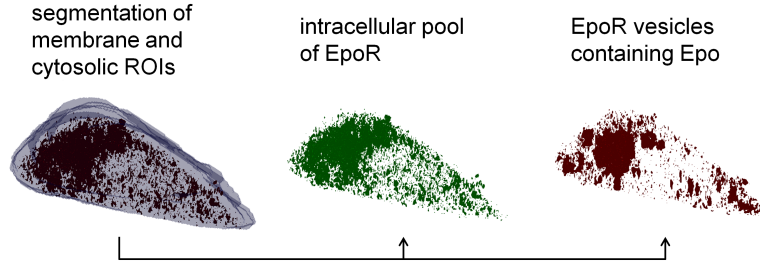


Figure 10.2. Segmentation of ROIs for the plasma membrane (left), EpoR-GFP vesicles (center) and vesicles containing EpoR-GFP and Epo-Cy5.5 (right).

10 Epo treated, 10 photobleached and 2 CHX treated cells. The complete set of single cell data is shown together with model trajectories (Figure 10.6). Intensity trajectories were linked to model variables describing cellular concentrations of EpoR and Epo as described in the following section.

10.2. Model of EpoR traffic

To study the internalization of Epo and EpoR, the transport of Epo and EpoR to endocytic recycling compartment and the intracellular traffic of EpoR in single cells, different ODE models were developed and calibrated with single cell measurements from confocal microscopic experiments. Model variants comprised ODEs for different sets of intracellular transport reactions to determine, which reaction fluxes effectively contribute to EpoR traffic. By model selection, a minimal model variant was identified, which contains components for EpoR recycling and intracellular accumulation of internalized Epo.

The EpoR model variants, consisting of a basic model and variable extensions, describe the two observed species, free EpoR and EpoR bound to Epo, in different cellular compartments or at the plasma membrane. The basic model describes reversible binding of Epo to EpoR at the plasma membrane ($EpoR_m$) and formation of active EpoR ($EpoR_m^*$) (Figure 10.3). In model reactions, free Epo is not depleted by binding or increased by unbinding, as the amount of Epo in the medium largely exceeds the total amount of EpoR and can therefore be assumed to be constant. Epo receptors permanently cycle between the membrane pool ($EpoR_m$) and the intracellular pool ($EpoR_i$). The intracellular pool of EpoR is subject to degradation and refilled by synthesis. Active EpoR at the membrane $EpoR_m^*$ are internalized to the endocytic recycling compartment ($EpoR_{RE}^*$). The so far described reactions of the basic model, visualized as black arrows in Figure 10.3, were extended by variable parts A to D, which were formulated under the following premises: Internalized Epo is unbound from EpoR and either released back into the cytosol (A and C) or degraded and accumulated inside the cell (B and D) [123,124]. After the internalization of active EpoR, receptors can recycle back to the plasma membrane (A and B) or are degraded (C and D) [124,193]. From the endocytic recycling compartment,

10.2. Model of EpoR traffic

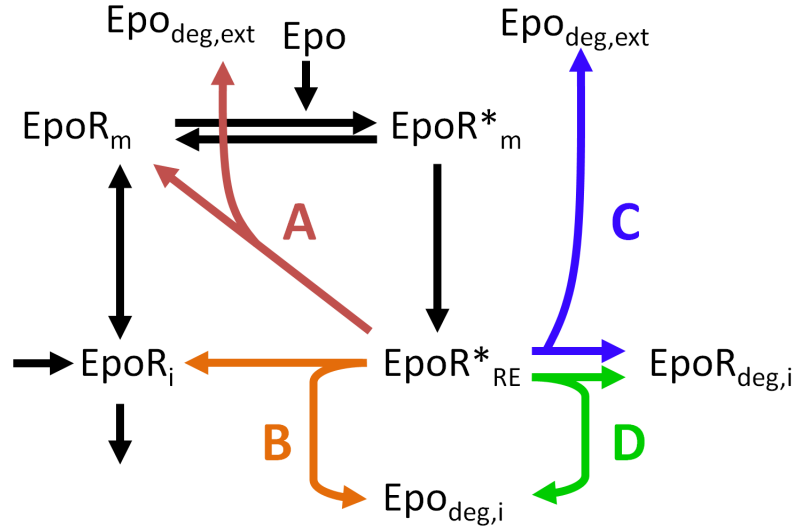


Figure 10.3. Model of EpoR traffic. A basic model (black arrows) can be extended by variable parts A to D.

receptors can be recycled via path A directly to the membrane ($EpoR_m$) or via B to the intracellular pool ($EpoR_i$). Following path A, 'consumed' Epo is released to the plasma membrane with EpoR and leaves the cell, while path B leads to accumulation of inactivated Epo ($Epo_{deg,i}$) inside the cell. By appending variable combinations of parts A to D to the basic model, the 16 possible model variants were formulated.

For all model variants, cell ensemble models were constructed, similar as in the caspase-8 activation model (part I), which consisted of independent sets of ODEs for each described cell, and were linked by certain boundary conditions. An ensemble model consisted of single cell models for Epo internalizing cells, and auxiliary models for photobleached and CHX treated cells. One single cell model describing an Epo treated cell contained 6 ODEs and between 7 and 11 parameters (Tables 10.1 and 10.2). Auxiliary models of photobleached cells contained a subset of reactions describing only synthesis, degradation, shuttling of EpoR between the plasma membrane and the intracellular pool and an additional reaction on the effect of photobleaching (Table B.1). The auxiliary model for CHX treated cells, in which synthesis was inhibited, consisted of ODEs describing EpoR degradation and shuttling between the plasma membrane and the intracellular pool of EpoR (Table B.1). Models of photobleached cells consisted of 3 ODEs with 5 kinetic parameters, models of CHX treated cells contained 3 ODEs with 3 kinetic parameters.

The parameters for Epo binding and unbinding, $k_{Epo,on}$ and $k_{Epo,off}$ were defined as being equal for each single cell model. All other kinetic parameters were allowed to vary between cells. Therefore, an ensemble model containing the complete available dataset of 10 Epo treated, 10 photobleached, and 2 CHX treated cells comprised between 106 and 146 kinetic parameters, scaling factors for the GFP and Cy5.5 microscope channels, and initial concentrations $[EpoR_m](t_0)$ and $[EpoR_i](t_0)$ resulting

reaction rates	
$v_1 = k_{on,Epo}[EpoR_m][Epo]$	
$v_2 = k_{off,Epo}[EpoR_m^*]$	
$v_3 = k_{EpoR,ItoM}[EpoR_i]$	
$v_4 = k_{EpoR,MtoI}[EpoR_m]$	
$v_5 = k_{EpoR_{RE}^*,MtoRE}[EpoR_m^*]$	
$v_7 = k_{syn}$	
$v_8 = k_{deg}[EpoR_i]$	
	$v_A = k_{EpoR_{RE}^*,REtoM}[EpoR_{RE}^*]$
	$v_B = k_{EpoR_{RE}^*,REtoI}[EpoR_{RE}^*]$
	$v_C = k_{EpoR_{RE}^*,deg,REtoEx}[EpoR_{RE}^*]$
	$v_D = k_{EpoR_{RE}^*,deg,REtoI}[EpoR_{RE}^*]$

Table 10.1. Reaction rates for variants of the EpoR traffic model with variable parts A to D.

differential equations				
<i>basic model</i>	<i>A</i>	<i>B</i>	<i>C</i>	<i>D</i>
$\frac{d[EpoR_m]}{dt} = -v_1 + v_2 + v_3 - v_4$	$+v_A$			
$\frac{d[EpoR_m^*]}{dt} = v_1 - v_2 - v_5$				
$\frac{d[EpoR_{RE}^*]}{dt} = v_5$	$-v_A$	$-v_B$	$-v_C$	$-v_D$
$\frac{d[EpoR_i]}{dt} = -v_3 + v_4 + v_7 - v_8$		$+v_B$		
$\frac{d[EpoR_{deg}]}{dt} = v_8$			$+v_C$	$+v_D$
$\frac{d[Epo_{deg}]}{dt} = 0$		$+v_B$		$+v_D$

Table 10.2. Equations of the EpoR traffic model variants. The variable terms for A to D can be included or set to zero.

10.2. Model of EpoR traffic

$$\begin{aligned}
 I_{GFP,mem} &\sim s_{GFP} ([EpoR_m] + [EpoR_m^*]) \\
 I_{GFP,ves} &\sim s_{GFP} [EpoR_i] \\
 I_{GFP\&Cy5.5,ves} &\sim s_{GFP} [EpoR_{RE}^*] \\
 I_{Cy5.5,mem} &\sim s_{Cy5.5} [EpoR_m^*] \\
 I_{Cy5.5,ves} &\sim s_{Cy5.5} ([EpoR_{RE}^*] + [Epo_{deg}])
 \end{aligned}$$

Table 10.3. Links between experimental quantities and model variables

in a total number of 152 to 192 parameters, which were estimated by model fitting. To exactly estimate the scaling factor between normalized fluorescence intensities in cellular compartment ROIs and absolute receptor amounts, average EpoR levels were determined by a calibrated western blot. Cell lysates of certain numbers of cells were blotted together with known amounts of recombinant GFP. The calibrated western blot and image stack segmentations showed that each cell contained on average 145.000 receptors and had a mean volume of about 6.97pl, which resulted in an average cellular concentration of $[EpoR]_{tot} = 34.5nM$.

Variability between cells was introduced by differences in kinetic parameters. In the EpoR model, these parameter variability reflected differences in initial concentrations of not observable signaling species, which are involved in vesicle formation and transport processes, different degrees of posttranslational modifications of signaling proteins and differences in spatial distributions of cellular compartments due to the individual cellular architecture. It was assumed that processes involving a low number of unknown processes, show less variability, and complex processes, which involve several reactions and a high degree of spatial organization, are highly variable between cells. Section 10.3 will describe an attempt to obtain insights into the complexity of not observable processes, which can be mechanistically described as 'bundled' uni-molecular reactions but cause cell-to-cell variability.

Model fitting

For model fitting, the experimental quantities were linked to model variable for free and Epo bound EpoR at different cellular compartments, thus defining single cell residuals that were minimized by the parameter estimation procedure. Furthermore, the residual function was extended by penalty terms to assure the same means and variabilities of kinetic parameters for groups of cells that underwent different experimental treatments.

Table 10.3 shows the relations between experimental quantities I_{GFP} and $I_{Cy5.5}$, the fluorescence intensities of EpoR-GFP and Epo-Cy5.5, in different cellular compartments and the corresponding model variables, multiplied by scaling factors s_{GFP} or $s_{Cy5.5}$, respectively.

To improve the accuracy of parameter estimations, and restrict the model to physiologically reasonable parameter ranges, single cell models of Epo internalizing

cells were combined with auxiliary single cell models. These comprised models of cells, in which EpoR synthesis could be observed after photobleaching, and models of cells, in which EpoR degradation could be quantified after inhibiting synthesis by CHX treatment. As the cells from the same cell line were treated with Epo, photobleaching or CHX, the single cell models for each experimental setting had to account for the same means and variabilities of kinetic parameters. To implement this physiological boundary condition in the parameter fitting procedure, the residual function, which contained the single cell residuals R_{sc} , had to be extended by two penalty terms for deviations between distributions of kinetic parameters k_i in cell populations from different experiments.

$$R = R_{sc} + R_m + R_{VarK} \quad (10.1)$$

The first term in Equation 10.1

$$R_{sc} = \sum_{i,j,n} \frac{\tilde{y}_{jn}(t_i) - y_{jn}(\vec{k}, \vec{x}_0, \vec{s}, t_i)}{\epsilon_{ijn}}$$

contains deviations between experimental data $\tilde{y}_{jn}(t_i)$ of cell n and experimental quantity j , and the corresponding model observables $y_{jn}(\vec{k}, \vec{x}_0, \vec{s}, t_i)$, which are functions of the estimated kinetic parameters \vec{k} , initial concentrations \vec{x}_0 and scaling factors \vec{s} , weighted by experimental errors ϵ_{ijn} . The next term

$$R_m = \sum_s N_s \sum_{i,s} \frac{\bar{k}_i - \bar{k}_{is}}{\bar{k}_i} \quad (10.2)$$

penalizes for differences between mean kinetic parameter values \bar{k}_{is} in cells of experimental set s , and the overall mean kinetic parameter value \bar{k}_i . The deviations were weighted by the total number of cells $\sum_s N_s$ in all included experimental subsets in accordance to the number of cells contributing to the term for single cell residuals R_{sc} . This penalty term contained contributions for parameters k_{ItoM} , k_{MtoI} and k_{deg} for all three included experimental subsets, and additionally the contribution for k_{syn} between the subset for Epo treated and photobleached cells. Another term

$$R_{VarK} = \sum_s N_s \sum_{i,s} \frac{\overline{VarK}(k_i) - VarK(k_{is})}{\overline{VarK}(k_i)} \quad (10.3)$$

was introduced to penalize deviations of coefficients of variation $\overline{VarK}(k_i)$ in subsets s from mean coefficients of variation $\overline{VarK}(k_i)$ for all involved subsets. As the subset of CHX treated cells was too small, only deviations of $VarK(k_{is})$ between Epo and photobleaching treated cells were taken into account for parameter estimations. Again, the term R_{VarK} was multiplied by the number of cells $\sum_s N_s$. The squared residual function was minimized for parameter estimations.

This procedure could successfully adjust the means and variabilities of kinetic parameters in the experimental subsets of cells and improved parameter estimations as described in the following paragraphs.

10.2. Model of EpoR traffic

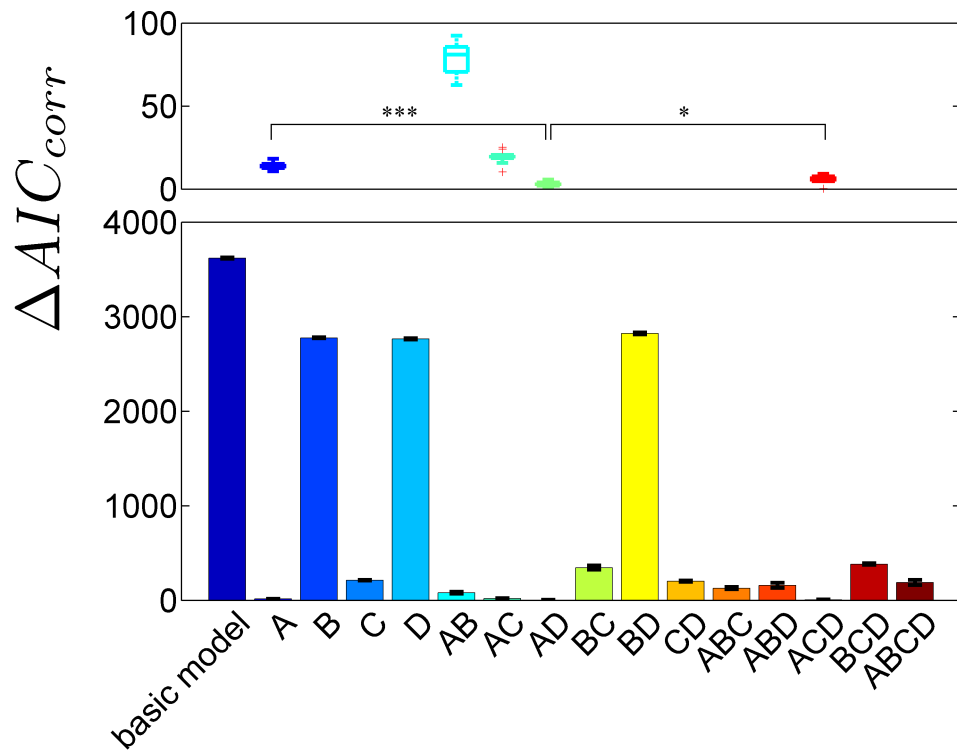


Figure 10.4. Selection of the optimal model variant 'AD'. The basic model with components A and D had the lowest AIC_{corr} value. ΔAIC_{corr} values calculated relative to the the 'AD' variant indicate that the second- and third-best variants, 'A' and 'ACD', have significantly higher AIC_{corr} values ('AD' vs. 'A' with $p = 6.61 \cdot 10^{-8}$, 'AD' vs. 'ACD' with $p = 0.013$).

Model selection

The cell ensemble model variants were fitted to experimental data to select the minimal topology that explains the data sufficiently well and to exclude irrelevant reactions. The corrected Akaike information criterion (AIC_{corr} , Equation 2.17) was used for this purpose. The AIC penalizes for the number of model parameters in order to prefer a model variant if it can explain the experimental data equally well compared to a larger model with additional reactions. Figure 10.4 shows differences ΔAIC_{corr} for all model variants relative to the optimal variant 'AD' that contained components A for recycling and D for EpoR degradation. Further extending the variant 'AD' did not increase the fit quality and can therefore be neglected. Figures 10.5 and 10.6 show model fits of the variant 'AD' to the complete set of experimental data. Model predictions of single cell concentrations of $EpoR_m$, $EpoR_i$, $EpoR_m^*$ and $EpoR_{RE}^*$ are shown in Figure 10.7.

The model variant confirms assumptions of earlier population based models, which similarly described the direct EpoR recycling to the plasma membrane together with exocytosis of degraded Epo [123,124]. In contrast, reactions for receptor degradation inside the cell together with exocytosis of intracellular Epo, which were included in the study of Becker et al. [124], did not substantially contribute to EpoR traffic in single cells. After degradation of $EpoR_{RE}^*$, the internalized Epo-Cy5.5 was rather accumulated inside cells. Analyzing reaction fluxes, however, showed that the flux for intracellular EpoR degradation and Epo-Cy5.5 accumulation was relatively small compared to the flux of recycling reactions (Figure 10.8). Flux analysis furthermore shows that about half of the internalized receptors were recycled to the plasma membrane, while only a small receptor fraction was degraded. Reaction fluxes in different cells varied approximately by a factor of ten implying that the consumption of Epo and the signal strength strongly differs between cells. After adding Epo, nearly all EpoR at the plasma membrane are quickly bound to Epo. The transport from the intracellular pool of EpoR ($EpoR_i$) to the plasma membrane can compensate for the internalization of Epo-bound EpoR ($EpoR_m^*$), which results in approximately constant total EpoR levels in the membrane ROI. Fluxes for EpoR recycling ($F_{EpoR^*,REtoM}$ in Figure 10.8) reach similar magnitudes as fluxes of unoccupied EpoR from the intracellular pool to the plasma membrane (F_{ItoM}). The cell-to-cell variability of kinetic parameters will be addressed in section 10.3.

Consequences of the boundary conditions for parameter estimations It was tested to which extent estimates of the kinetic parameters k_{syn} and k_{deg} were influenced by merging single cell models of Epo treated cells with single cell models of photobleached and CHX treated cells, which were included to obtain more accurate insights into EpoR synthesis and degradation. To this end, model fits of the 'AD' variant, using the modified residual function described in Equation 10.1, were compared with model fits without using additional penalty terms that adjust for differences in kinetic parameter means and variabilities between cells of different experimental settings. It was found that without additional penalty terms, k_{syn} es-

10.2. Model of EpoR traffic

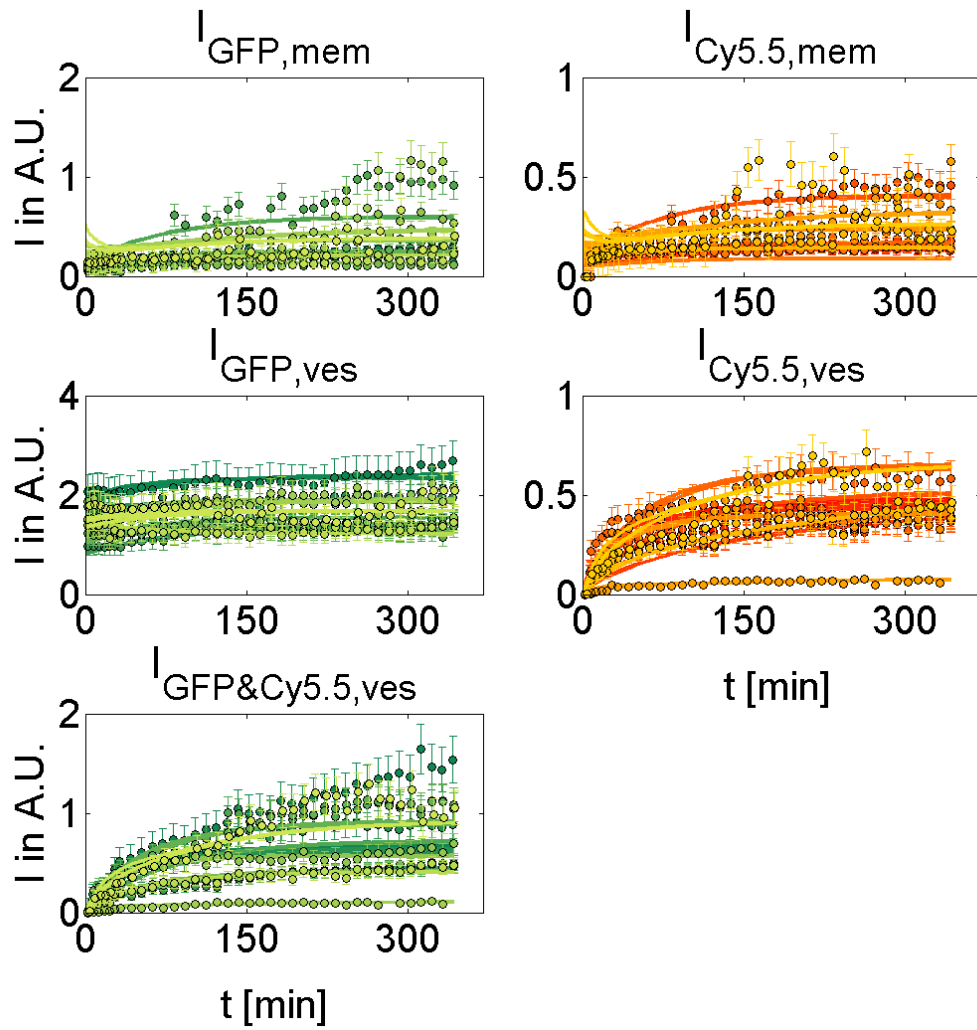


Figure 10.5. Fits of the basic model with components A and D to data from Epo internalizing cells ($n = 10$).

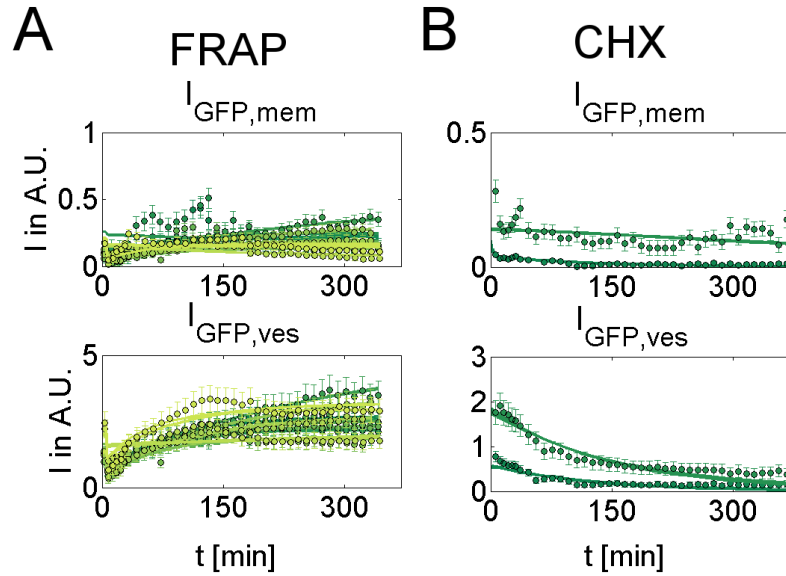


Figure 10.6. Fits of the basic model with components A and D to data from $n = 10$ FRAP treated cells (A), and $n = 2$ cycloheximide (CHX) treated cells (B).

estimates are changed on average by 29% and k_{deg} estimates by 57%, which indicates that the modified residual function successfully adjusts estimates of these parameters between different experimental settings.

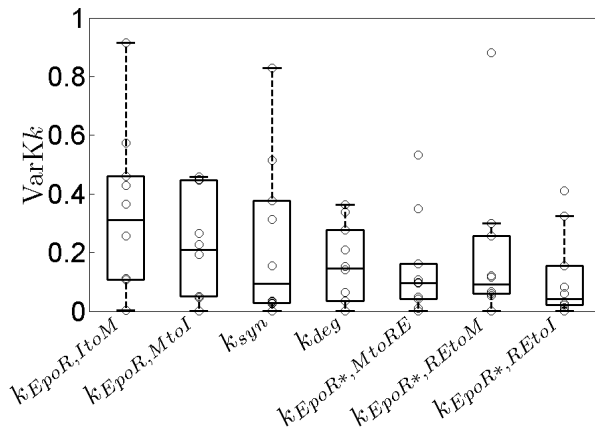


Figure 10.9. Coefficients of variation for parameter estimates. Small circles indicate VarKs for Epo treated model cells.

In order to evaluate the accuracy of kinetic parameter estimates in single cells, coefficients of variation for kinetic parameters in Epo internalizing cells were calculated from the best 2% of $n = 500$ model fits of the variant 'AD' to the complete set of experimental data (Figure 10.9). In most of the parameters the coefficients of

10.2. Model of EpoR traffic

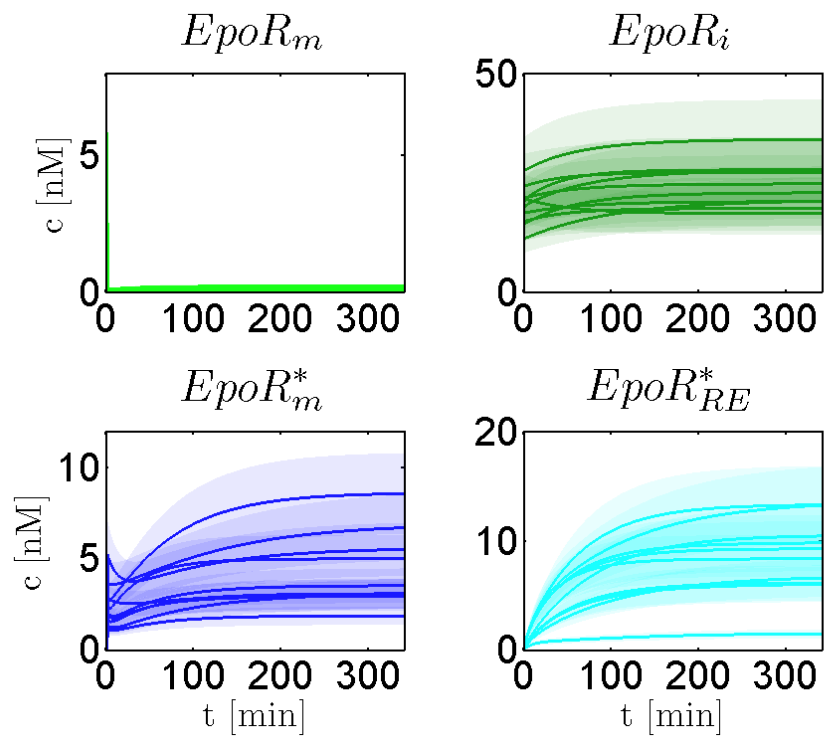


Figure 10.7. Predictions in Epo internalizing model cells of the 'AD' variant. Lines represent the means and shaded areas standard deviations of 1% best of $n = 500$ fits ($EpoR_m$: membrane bound EpoR, $EpoR_i$: intracellular EpoR, $EpoR_m^*$: Epo bound EpoR at the plasma membrane, $EpoR_{RE}^*$: Epo bound EpoR in the endocytic recycling compartment).

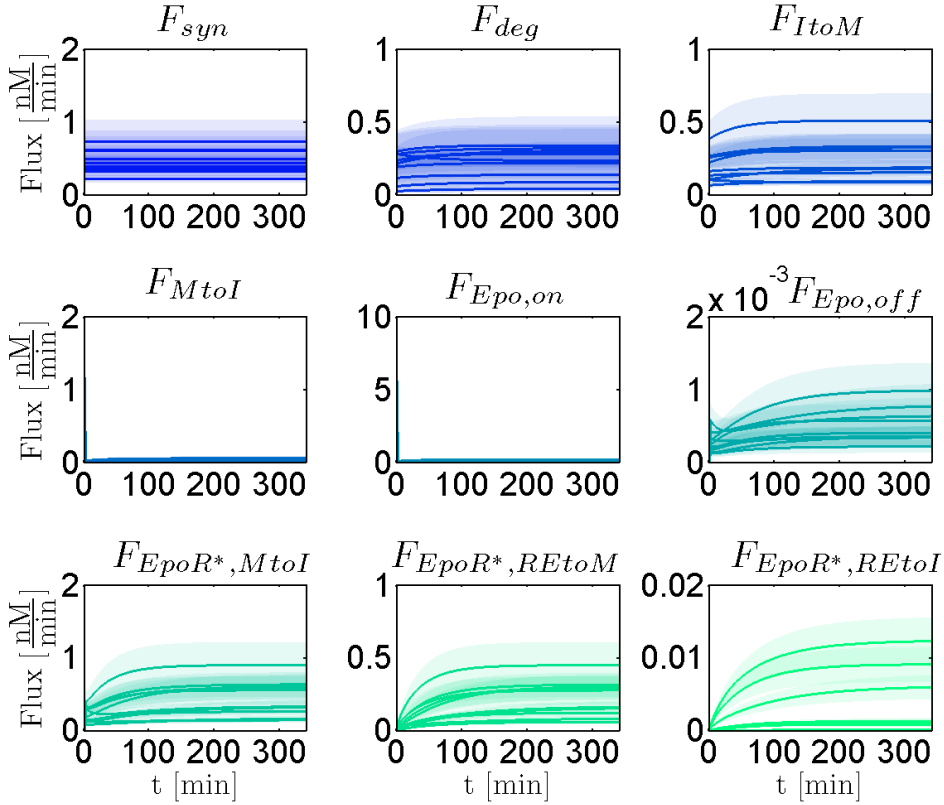


Figure 10.8. Predictions of EpoR fluxes in Epo internalizing model cells of the 'AD' variant. Half of the internalized $EpoR^*$ is recycled while only small fractions are degraded (lines: means, shaded areas: standard deviations of 1% best of $n = 500$ fits, F_{syn} : EpoR synthesis, F_{deg} : degradation, F_{ItoM}, F_{MtoI} : from intracellular pool to plasma membrane and reverse, $F_{Epo,on}, F_{Epo,off}$: Epo binding and unbinding, $F_{EpoR^*,MtoI}$: internalization of Epo bound EpoR, $F_{EpoR^*,REtoM}$: recycling, $F_{EpoR^*,REtoI}$: degradation from endocytic recycling compartment).

10.2. Model of EpoR traffic

variation were smaller than 0.3, indicating that the 1σ confidence intervals deviated less than 30% from the mean parameter values. Similarly, coefficients of variation were calculated for kinetic parameter estimates of 'AD' model that was fitted to a reduced set of experimental data. Thereby, it should be tested to which extent the combination of data from Epo internalizing cells with auxiliary data from photobleached and CHX treated cells can improve parameter estimations. To this end, differences between the coefficients of variation $\Delta VarK(k_{in})$ for the parameters k_i in cells n were calculated to compare model fits to the complete dataset with model fits to the reduced set of experimental data. As shown in Figure 10.10, reducing the ensemble model by leaving out single cell models of photobleached and CHX treated cells increases the confidence intervals for parameter estimates in most cells, which is indicated by positive $\Delta VarK$ values (red dots). Furthermore, coefficients of variation were calculated for the same kinetic parameters estimated with the largest model variant 'ABCD'. Figure 10.10 shows $VarK(k_{in})$ differences between the 'AD' and the 'ABCD' variants (blue dots), which indicate that using the smaller model variant clearly improves the accuracy of kinetic parameter estimates.

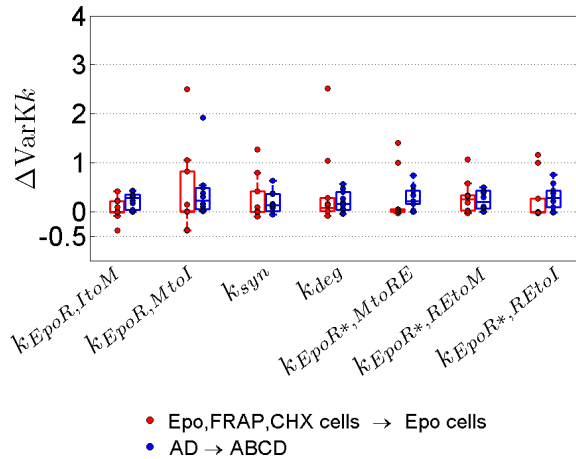


Figure 10.10. VarK changes in Epo treated model cells dependent on the training dataset and model size. Parameters can be estimated more accurately by combining data from Epo treated with data from FRAP or CHX treated cells (red dots), and by model simplification from 'ABCD' to 'AD' (blue dots). The 2% best of $n = 500$ fits were taken into account, respectively.

In summary, a minimal model variant could be selected, which includes reactions for direct recycling of internalized Epo-bound EpoR ($EpoR_{RE}^*$) from the endocytic recycling compartment to the plasma membrane, and intracellular accumulation of Epo-Cy5.5 after degradation of internalized Epo-bound EpoR. In general, intracellular EpoR traffic in single cells can be sufficiently well described implying similar model assumptions as in studies that were based on population data but varies by an order of magnitude between cells (Figures 10.7 and 10.8). Combining single cell models of Epo internalizing cells with auxiliary models based on experiments focused on EpoR synthesis and degradation increased the accuracy of parameter estimations. Using a modified residual function to adjust means and variabilities of kinetic parameters between single cell models that were based on different experiments adapted the cell ensemble model to physiologically reasonable conditions.

10.3. Cell-to-cell variability in EpoR traffic

A central motivation of this study was to test if the kinetics observed on the level of population average data can be transferred to the single cell level, and to which degree EpoR transport kinetics varies between cells. It was found that Epo-bound EpoR at the membrane ($EpoR_m^*$) and in the endosomal recycling compartment ($EpoR_{RE}^*$) approximate constant levels after the first two hours and that these constant levels strongly vary between cells.

After having assured that kinetic parameters could be determined with reasonable accuracy, the variability of kinetic parameters between different cells was analyzed. Interestingly, coefficients of variation of all single cell kinetic parameters had values around 0.5 besides the parameter $k_{EpoR_{RE}^*,deg,REtoI}$ describing intracellular degradation of Epo-bound EpoR, a process, which had the smallest reaction fluxes (Figure 10.11). Kinetic parameter estimates show that EpoR traffic in single cells is a highly dynamic and variable process. Estimates of k_{syn} shows that EpoR is produced at a very high rate of around 4000 proteins per minute, implying its fast turnover, which could be already noticed in photobleaching and CHX experiments. Epo treated cells consumed between 200 and 2000 Epo molecules per minute. From the amount of 2000 to $2 \cdot 10^4$ EpoR at the plasma membrane about one tenth is exchanged per minute with the intracellular pool of EpoR. Correlations between the kinetic model parameters for different cells were in general not significant besides a significant correlation between k_{syn} and k_{deg} (Table B.2). Some insignificant positive correlations could be observed between kinetic parameters describing vesicle transport processes. However, no clear interrelations between the velocities of different model reactions were found.

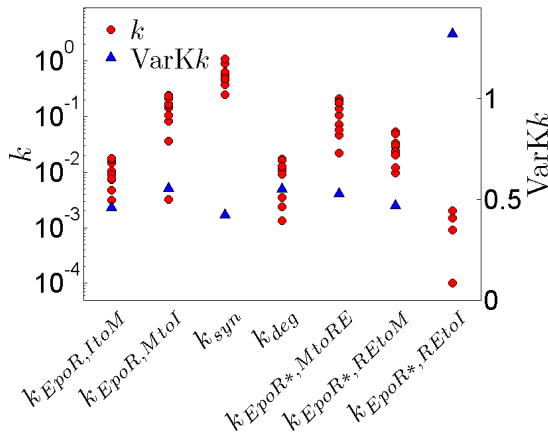


Figure 10.11. Best fit parameters of Epo internalizing model cells and coefficients of variation. VarKs values were around 0.5 for all but the smallest kinetic parameter ($k_{EpoR^*,REtoI}$). The parameter unit for k_{syn} is nM/min and $1/min$ for all other parameters.

Next, it was tested to which extent different receptor traffic processes account for the variable EpoR dynamics. So far, all kinetic parameters besides the parameters $k_{Epo,on}$ and $k_{Epo,off}$ were variable in single cell models of the cell ensemble model. Iteratively, different kinetic parameters were fixed to global values for all included

10.3. Cell-to-cell variability in EpoR traffic

cells while the other parameters were allowed to have individual values. The corrected Akaike information criterion (AIC_{corr}) was used to assess if fixing a certain parameter to a global value for all cells causes significant deterioration of the model. For the model variant 'AD', all possible combinations for fixing kinetic parameters to global values were tested. To account for different initial concentrations of EpoR in cells, the parameter k_{syn} was allowed to be variable for different cells in every case, which leads to 64 different model variants with different possible combinations of global kinetic parameters.

To obtain a 'parameter ranking', Figure 10.12 visualizes differences in AIC_{corr} between the model variant, in which all kinetic parameters besides $k_{Epo,on}$ and $k_{Epo,off}$ were individually estimated in different cells (top) and all other model variants with global kinetic parameters. The ΔAIC_{corr} values for each model variant are shown as colors of squares, and abbreviated names of parameters defined as being equal for all single cell models are listed below squares for each variant, respectively. Starting from the model, in which all parameters besides k_{syn} are equal for all cells (bottom), in each successive row one of the global kinetic parameters is allowed to vary between cells. The path of maximal AIC_{corr} changes, starting for the maximally restricted model version, is indicated by blue lines in Figure 10.12. The sequence, in which the smallest improvements in AIC_{corr} are gained is indicated by red lines. In this sequence, changes in parameter restrictions, which cause the strongest model improvements, occur at the end. This sequence

$$\begin{aligned}
 & k_{EpoR_{RE}^*,deg,REtoI} \rightarrow k_{deg} \rightarrow k_{EpoR,MtoI} \\
 & \rightarrow k_{EpoR,ItoM} \rightarrow k_{EpoR_{RE}^*,REtoM} \rightarrow k_{EpoR_{RE}^*,MtoRE}
 \end{aligned}$$

suggest a ranking of parameters, which have the strongest capacity for explaining cell-to-cell variability. The strongest deteriorations in AIC_{corr} can be observed for fixing the two parameters for internalization of Epo-bound EpoR ($k_{EpoR_m^*,MtoRE}$) and EpoR recycling ($k_{EpoR_{RE}^*,REtoM}$), and for additionally fixing the parameter for transport of free EpoR to the plasma membrane ($k_{EpoR,ItoM}$). This suggests that the processes of $EpoR_m^*$ internalization, EpoR recycling and transport to the plasma membrane have the strongest impact on cell-to-cell variability in EpoR dynamics. Fixing other parameters as k_{deg} or $k_{EpoR,MtoI}$ in the model variant, in which other kinetic parameters were defined as variable, causes weak changes in AIC_{corr} but still slightly deteriorate the model.

In summary, an experimental setup could be developed to quantify EpoR transport in single cells and analyze cellular heterogeneity in Epo consumption, EpoR transport and recycling based on mathematical models. A minimal model variant was selected, which reliably explains the EpoR transport dynamics in a heterogeneous ensemble of cells. Kinetic parameter estimates in different cells showed that processes of EpoR transport, recycling, synthesis and degradation are variable to similar extent, indicated by coefficients of variation around 0.5. The kinetics of

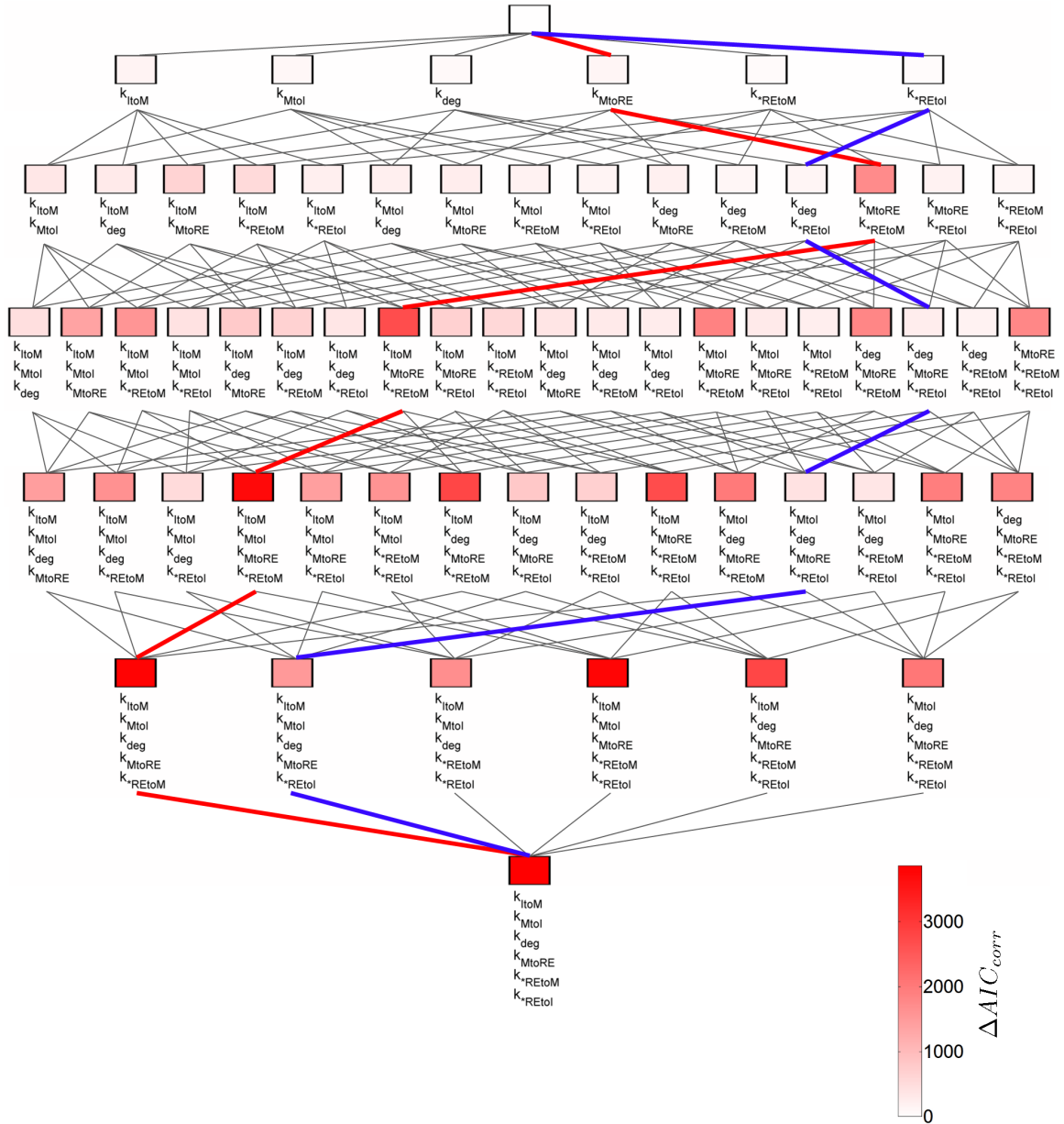


Figure 10.12. Decreases in AIC_{corr} by restricting the variability of kinetic parameters. For model variants, AIC_{corr} differences to the variant, in which all kinetic parameters were variable, are indicated by colors (best fit of $n = 100$ fits per variant), and abbreviated names of parameters defined as being equal for all ensemble model cells are listed below colored boxes, respectively. Links were drawn between variants, in which one additional parameter was defined as equal or variable between cells. Red lines indicate the path of minimal and blue lines for maximal AIC_{corr} changes from the most restricted variant (bottom) to the least restricted variant (top).

10.3. Cell-to-cell variability in *EpoR* traffic

EpoR synthesis and internalization, *Epo* consumption and receptor recycling varied between cells by an order of magnitude. For comparison, the cell ensemble model of caspase-8 activation described in part I could explain the variable behavior of different cells sufficiently well by assuming equal kinetic parameters but individual initial concentrations for all cells. In the caspase-8 activation model, the described biochemical reactions were sufficiently simple, and it can be assumed that all involved signaling species were known and included in the model. Contrarily, in the *EpoR* system, model reactions summarize the kinetics of a complex interplay of several processes, which are involved in vesicle transport and functions of the endocytic recycling compartment. A cell ensemble model consisting of single cell models that were similar to population data based models could explain the variable behavior of a group of cells sufficiently well by assuming variable kinetic parameters. An approach to rank kinetic parameters according to their capacity of explaining cell to cell variability showed that model parameters on *EpoR** internalization, *EpoR* recycling and transport to the plasma membrane explain most of the cell-to-cell variability.

Conclusions

10.3. Cell-to-cell variability in EpoR traffic

This thesis presents a new approach for describing biochemical signal transduction networks in heterogeneous cell populations by cell ensemble models. These models consist of sets of ordinary differential equations for each included cell. Single cell models of the ensemble are linked by boundary conditions that assure compliance with physiological limitations. The approach allows merging experimental data from single cells and population average data to combine information of different qualities. Merging single cell and population data could be shown to facilitate discrimination between different hypotheses on underlying biochemical mechanisms (chapter 7) and increase the accuracy of parameter estimations (chapter 10).

The approach was applied in two biochemical systems, the initiation of extrinsic apoptosis by activation of caspase-8 (part I) and the intracellular transport of erythropoietin receptors (EpoR) (part II). As described in chapter 4 of part I, a new method was developed to quantify protease enzyme activities in single cells based on confocal microscopy of compartmentalized cleavage probes. A large set of single cell data was recorded from two cell lines, HeLa wt and death receptor overexpressing HeLa cells, stimulated with different doses of cell death ligand. The dataset was enriched by population data, using the conventional method of western blots, which was the basis of earlier apoptosis models (chapter 5). An interesting phenomenon was detected with regard to receptor oligomerization: At extremely high ligand concentrations apoptosis was decelerated. This non-intuitive phenomenon could be explained by mathematical models based on ordinary differential equations that could be analytically solved (chapter 6). With regard to the molecular mechanism of caspase-8 activation, complementary hypotheses on the described in the literature were implemented in different kinetic cell ensemble models, and a minimal model variant was selected, which indicated that CD95 receptor clustering is required for the initiation of apoptosis (chapter 7). In particular, the model predicted different cleavage mechanisms of two cleavage sites in procaspase-8, which establish a positive feedback mechanism that contributes to a controlled cell death initiation. While the prodomain cleavage site was cleaved by an intramolecular ('cis') mechanism, an interdimeric ('trans') cleavage mechanism was predicted for cleavage of the enzymatic domain cleavage site in procaspase-8. The model could be experimentally verified by cleavage probes containing prodomain or enzymatic domain cleavage sequences. The identified 'cis/trans' mechanism supports 'pathway branching': at weak ligand concentrations, procaspase-8 is consumed without inducing an effective cleavage activity towards apoptosis inducing substrates, which inhibits apoptosis, while non-apoptotic signaling pathways of death receptors can be sustained. At increasing ligand concentrations, the production of active caspase-8 intermediates is strongly accelerated to initialize cell death. An analogy could be drawn between the activation process of caspase-8 and the related enzyme caspase-9, which is activated at protein complexes denoted as apoptosomes. In both enzymes, the final product, caspase-8/p18 or caspase-9 is short-lived after being separated from the activating protein complex, compared to a more stable intermediate form, which causes most of the integrated cleavage activity of the enzyme. This principle, denoted as 'molecular timer', assures the efficient use of procaspase-8 or procaspase-9 to cleave downstream

signaling proteins and allows rapid termination of the response after removal of the cell death stimulus.

The experimental data was explained by a multivariate log-normal joint distribution of initial protein concentrations and threshold concentrations of the signaling protein tBID, which were sufficient for inducing apoptosis (8). Thereby, functional roles of signaling proteins could be characterized. While signaling proteins upstream of caspase-8 control the timing and the variability of programmed cell death, downstream signaling proteins control the survival of cells. In this context, the model can be used to predict cell death in a heterogeneous population of cells under various experimental conditions. The model might be used to predict the effects of co-drugs for cancer chemotherapy, which impact on the distributions of initial protein concentrations of pro-apoptotic proteins and lower tBID thresholds that are sufficient for apoptosis, in order to quantitatively optimize therapeutic drug concentrations and concentration trajectories.

A second cell ensemble model was formulated to study cell-to-cell variability in intracellular traffic of erythropoietin receptors (EpoR). An experimental setup was developed to quantitatively measure the internalization of fluorescently labeled erythropoietin (Epo) in cell that express EpoR fused to the fluorescent protein GFP. Contrary to the model of apoptosis initiation (part II), initial concentrations of all included model species could be directly determined from experimental data, but model reactions had to be described by variable kinetic parameters. Whereas, in the caspase-8 activation model all signaling species were known and included in the model, intracellular transport reactions in the EpoR model summarized several non-observable processes involved in vesicle traffic. A cell ensemble model, which simultaneously described data from Epo internalizing cells and data from auxiliary experiments on EpoR synthesis and degradation, could explain the heterogeneous kinetics of different cells by variable kinetic parameters. Reaction fluxes showed that EpoR turnover and transport kinetics differed by an order of magnitude between cells. By systematically restricting the degrees of freedom of the model it could be demonstrated that a subset of kinetic parameters, which describe the internalization of Epo-bound EpoR, receptor recycling and transport of free EpoR to the plasma membrane accounts for most of the variability between cells.

In the future, characterizing the variable response kinetics of cells based on model predictions might support the optimization of therapeutically used cytokines as Epo or interferons in targeted cell populations. In the context of cell-to-cell variability of initial protein concentrations and intracellular signaling processes one is reminded of the problem of fractional killing by chemotherapies: while applying a certain chemotherapeutic protocol stimulates apoptosis in a fraction of cancer cells, the surviving fraction will continue dividing. Characterizing the variability of initial protein concentrations in a tumor cell population combined with mathematical modeling might facilitate the eradication of a heterogeneous population of cancer cells.

Appendix

A. Additional material on the cell ensemble model of apoptosis

A.1. Additional figures

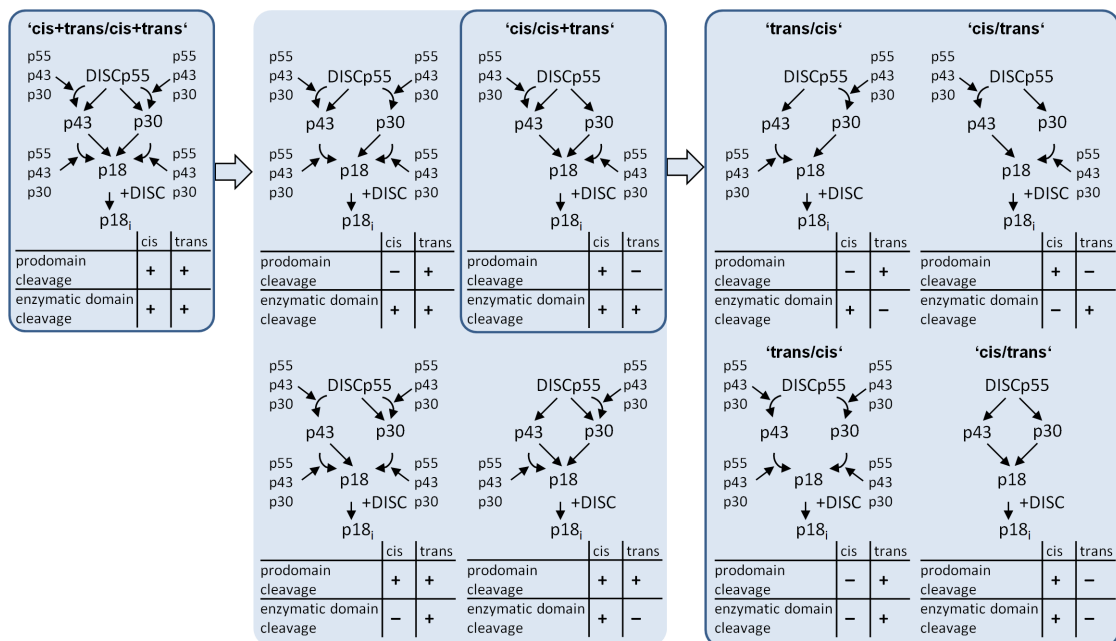


Figure A.1. Schematic representation of model variants. The enzymatic domain sites and the prodomain sites are potentially cleaved in cis, in trans or both in cis and trans leading to nine alternative model topologies. The full topology, in which both sites are cleaved in cis and trans can be iteratively simplified to four minimal topologies, in which only two cleavage modes are possible. The variants surrounded by boxes were fitted to experimental data.

Models with different prodomain site cleavage constants for p55 and p43 have only slight improvements in fit quality In the initial formulation of the 'cis/cis' model variant, a single kinetic constant was assumed for both prodomain cleavage reactions ($p55 \rightarrow p30$ and $p43 \rightarrow p18$) and one for enzymatic domain cleavage reactions ($p55 \rightarrow p43$ and $p30 \rightarrow p18$). The inability of this model to fit the data may be due to an oversimplification: faster cis prodomain cleavage from p43 to p18 than from p55 to p30 may be expected, because the active center of p43 is constantly open after cleavage of the enzymatic domain. Therefore an extended 'cis/cis' variant with two

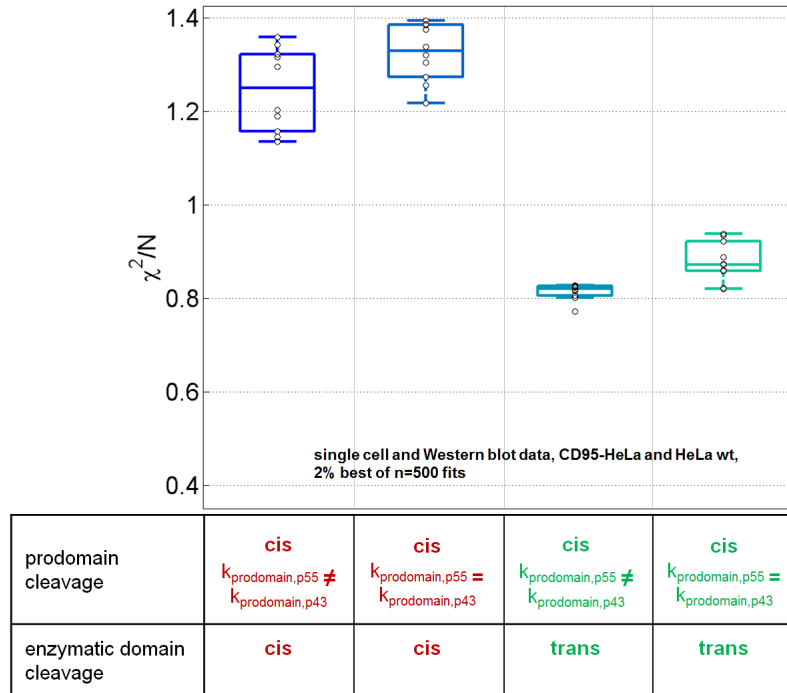


Figure A.2. Fit qualities of extended 'cis/cis' and 'cis/trans' model variants. Cis cleavage of p43 to p18 could be faster than cis cleavage of p55 to p30. Alternatively both reactions could have equal speed as the same site is cleaved. Therefore, cis cleavage of the prodomain site can be described with either different or equal kinetic constants for cleavage reactions from p55 to p30 ($k_{\text{prodomain,p55}}$) and from p43 ($k_{\text{prodomain,p43}}$) to p18. This hypothesis was tested in the rejected 'cis/cis' topology and the 'cis/trans' topology, which was the best fitting smallest model variant. As indicated by χ^2/N values for the best fits models with unequal constants do not improve fit quality substantially compared to models with equal parameters.

different prodomain cleavage parameters for the reactions $p55 \rightarrow p30$ and $p43 \rightarrow p18$ was implemented, and its ability to fit the data was tested. However, this model extension did not improve fit quality (Figure A.2). Therefore, also a pure cis model topology with separate cleavage constants for the two prodomain cleavage reactions is not capable in explaining experimental data and can therefore be ruled out.

Simulations to predict effects of initial concentration changes originating at different ligand concentrations To further illustrate functional roles of signaling protein species at different ligand concentrations, changes in cell death medians and coefficients of variation due to two-fold changes in initial concentrations were calculated, originating at different ligand levels (Figures A.3 and A.4). For this purpose, effects of increases from to times the original initial concentrations were determined. Simulations showed that the cell-to-cell variability and the speed of cell death are strongly dependent on levels of the death ligand, death receptors and

A.1. Additional figures

FADD. Due to inverse bell-shaped active receptor profiles, the influence of cell death ligand and receptor level fold changes on cell death timing and variability can be small or large, dependent on initial ligand levels. It was shown, that overexpression of an apoptotic signaling protein can increase its influence on cell death variability [95]. Here, the contrary phenomenon, that receptor overexpression causes the cell death variability of CD95-HeLa cells to be less sensitive towards CD95R level changes, could be observed.

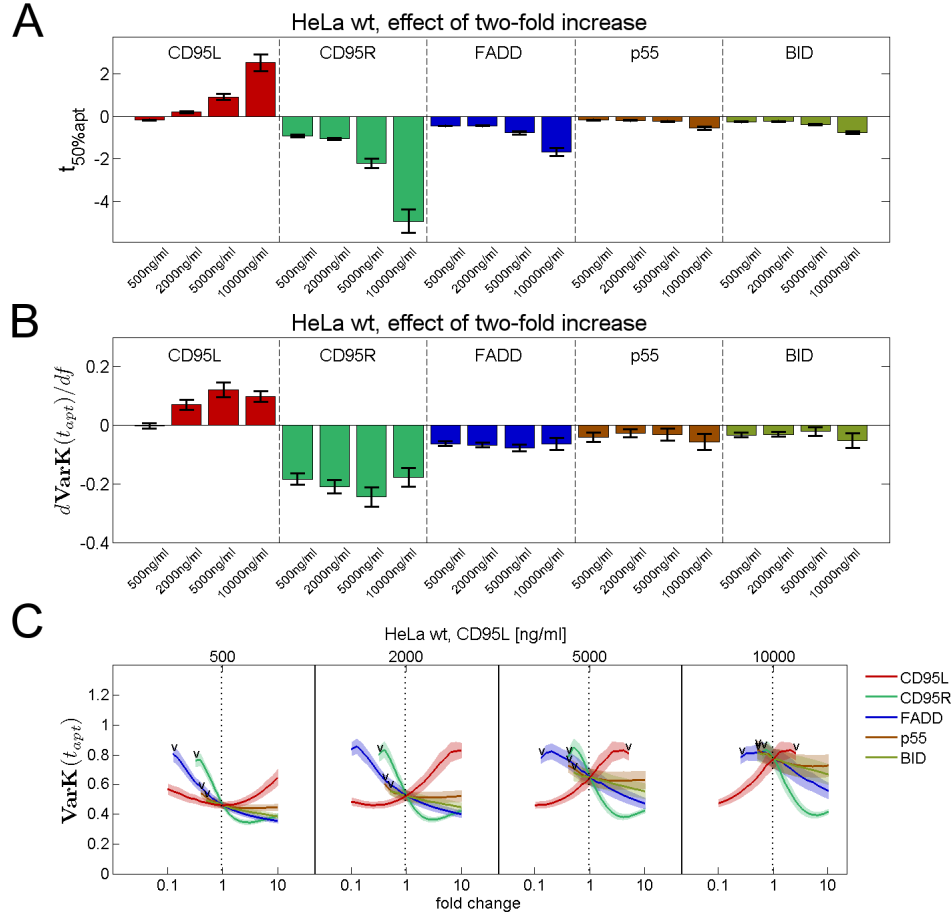


Figure A.3. 'cis/trans' model predictions in HeLa wt cells on effects of fold changes in initial protein concentrations. For estimations from each of the best 1% of $n = 1000$ fits, hundred sets of initial protein concentrations were randomly sampled from multivariate joint distributions of estimated initial levels for CD95 receptors, FADD, p55 and BID, as well as tBID thresholds. (A) Effects in HeLa wt cells of two-fold increases in initial protein concentrations on median cell death times originating from ligand concentrations used in single cell experiments. Bars represent effects of two-fold changes around the origin at one. In HeLa wt cells, amounts of CD95 receptors represent a bottleneck for cell death kinetics as indicated by strong changes of median cell death times dependent on receptor level fold-changes. (B) Effects of two-fold increases in initial protein concentrations on coefficients of variation of cell death times. (C) Predicted fold change trajectories of coefficients of variation of apoptosis times. Effects of fold changes between on tenth and ten times of the initial protein concentrations were simulated. Error bars in panels (A) and (B) and shaded areas in panel (C) show standard deviations from the best 1% of $n = 1000$ fits.

A.1. Additional figures

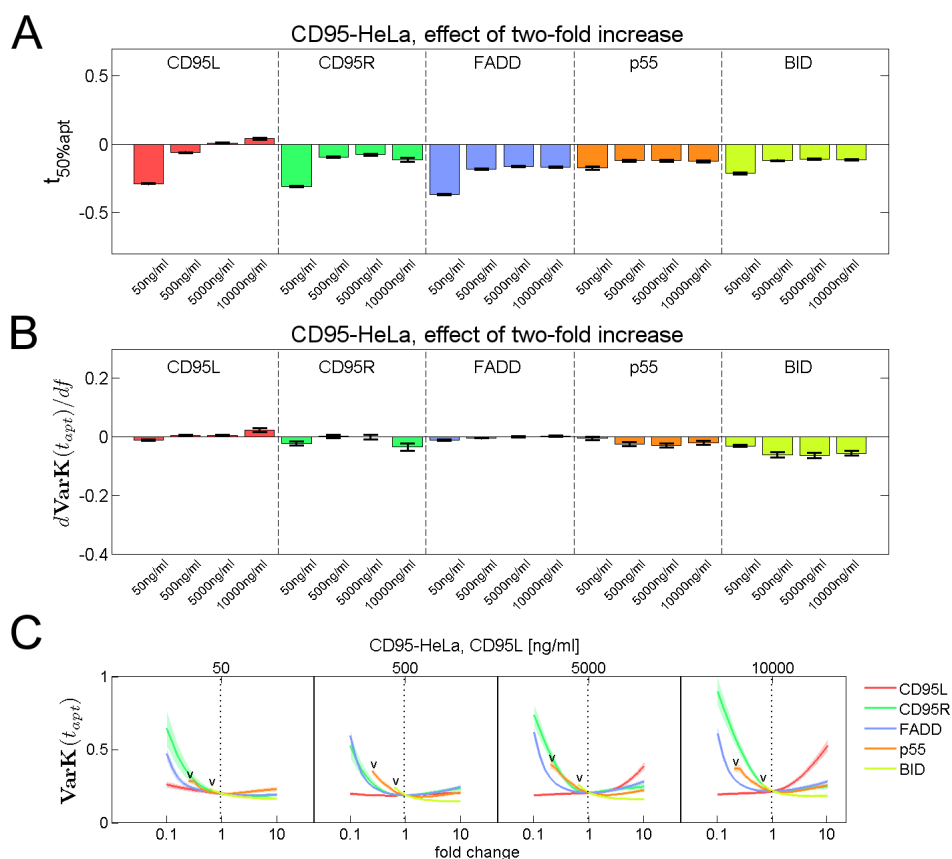


Figure A.4. 'cis/trans' model predictions in CD95-HeLa cells on effects of fold changes in initial protein concentrations as in Figure A.3. (A) Effects of two-fold increases in initial protein concentrations on median cell death times originating from ligand concentrations used in single cell experiments. The strong influence of receptor levels in HeLa wt cells is completely lost in CD95-HeLa cells, in which changes in all involved proteins have similar effects on cell death timing. (B) Effects of two-fold increases in initial protein concentrations on coefficients of variation of cell death times. (C) Predicted fold change trajectories of coefficients of variation of apoptosis times as in Figure A.3.

A.2. Model equations and kinetic parameters

reaction rates	
$v_1 = k_{on,FADD}[CD95_{active}][FADD]$	$v_{11} = k_{cl,D374,trans,p55}[p30]$
$v_2 = k_{off,FADD}[DISC]$	$([DISC_p55] + [p30])$
$v_3 = k_{on,p55}[DISC][p55]$	$v_{12} = k_{cl,D374,trans,p43}[p30][p43]$
$v_4 = k_{cl,D216,cis}[DISC_p55]$	$v_{13} = k_{cl,D216,cis}[p43]$
$v_5 = k_{cl,D216,trans,p55}[DISC_p55]$	$v_{14} = k_{cl,D216,trans,p55}[p43]$
$([DISC_p55] + [p30])$	$([DISC_p55] + [p30])$
$v_6 = k_{cl,D216,trans,p43}[DISC_p55][p43]$	$v_{15} = k_{cl,D216,trans,p43}[p43]^2$
$v_7 = k_{cl,D374,cis}[DISC_p55]$	$v_{16} = k_{p18,inactive}[p18]$
$v_8 = k_{cl,D374,trans,p55}[DISC_p55]$	$v_{17} = k_{cl,BID}[BID]([p43] + [p18])$
$([DISC_p55] + [p30])$	$v_{18} = k_{cl,probe}[Pr_{ER}F_1][p18]$
$v_9 = k_{cl,D374,trans,p43}[DISC_p55][p43]$	$v_{19} = k_{cl,probe}[Pr_{cpl}F_2]([p43] + [p18])$
$v_{10} = k_{cl,D374,cis}[p30]$	

Table A.1. Reaction rates in 'cis+trans/cis+trans' and 'cis/trans' model variants.

differential equations 'cis+trans/cis+trans'		differential equations 'cis/trans'	
$\frac{d[CD95_{active}]}{dt} = -v_1 + v_2$	(1)	$\frac{d[CD95_{active}]}{dt} = -v_1 + v_2$	(1)
$\frac{d[FADD]}{dt} = -v_1 + v_2$	(2)	$\frac{d[FADD]}{dt} = -v_1 + v_2$	(2)
$\frac{d[p55]}{dt} = -v_3$	(3)	$\frac{d[p55]}{dt} = -v_3$	(3)
$\frac{d[DISC]}{dt} = v_1 - v_2 + v_{10} + v_{11}$	(4)	$\frac{d[DISC]}{dt} = v_1 - v_2 + v_{11} + v_{12} + v_{13}$	(4)
$+v_{12} + v_{13} + v_{14} + v_{15}$			
$\frac{d[DISC_p55]}{dt} = v_3 - v_4 - v_5 - v_6$	(5)	$\frac{d[DISC_p55]}{dt} = v_3 - v_4 - v_8 + v_9$	(5)
$-v_7 - v_8 + v_9$			
$\frac{d[p30]}{dt} = v_4 + v_5 + v_6 - v_{10} - v_{11} - v_{12}$	(6)	$\frac{d[p30]}{dt} = v_4 - v_{11} - v_{12}$	(6)
$\frac{d[p43]}{dt} = v_7 + v_8 + v_9 - v_{13} - v_{14} - v_{15}$	(7)	$\frac{d[p43]}{dt} = v_8 + v_9 - v_{13}$	(7)
$\frac{d[p18]}{dt} = v_{10} + v_{11} + v_{12} + v_{13}$	(8)	$\frac{d[p18]}{dt} = v_{11} + v_{12} + v_{13} - v_{16}$	(8)
$+v_{14} + v_{15} - v_{16}$			
$\frac{d[tBID]}{dt} = v_{17}$	(9)	$\frac{d[tBID]}{dt} = v_{17}$	(9)
$\frac{d[Pr_{ER}]}{dt} = v_{18}$	(10)	$\frac{d[Pr_{ER}]}{dt} = v_{18}$	(10)
$\frac{d[Pr_{cpl}]}{dt} = v_{19}$	(11)	$\frac{d[Pr_{cpl}]}{dt} = v_{19}$	(11)

Table A.2. Equations of the model variants 'cis+trans/cis+trans' and 'cis/trans'.

A.2. Model equations and kinetic parameters

parameter	value of best fit	mean $\pm \sigma$
$k_{on,FADD}$ [1/min]	$8.12 \cdot 10^{-4}$	0.00276 ± 0.00175 ($\pm 63.4\%$)
$k_{off,FADD}$ [1/min]	0.00567	0.00940 ± 0.0107 ($\pm 114\%$)
$k_{on,p55}$ [1/min]	$4.92 \cdot 10^{-4}$	$4.04 \cdot 10^{-4} \pm 9.53 \cdot 10^{-5}$ (± 23.6)
$k_{cl,D216}$ (prodomain) [1/min]	0.0114	$0.0110 \pm 8.82 \cdot 10^{-4}$ ($\pm 8.01\%$)
$k_{cl,D374}$ (enc. domain),trans,p55 [nM/min]	$4.47 \cdot 10^{-4}$	$4.39 \cdot 10^{-4} \pm 2.49 \cdot 10^{-4}$ (± 56.7)
$k_{cl,D374}$ (enc. domain),trans,p43 [nM/min]	0.00344	$0.00333 \pm 4.58 \cdot 10^{-4}$ (± 13.7)
$k_{p18,inactive}$ [1/min]	0.0950	0.0943 ± 0.00694 (± 7.36)
$k_{cl,BID}$ [nM/min]	$5.29 \cdot 10^{-4}$	$5.29 \cdot 10^{-4} \pm 6.28 \cdot 10^{-5}$ ($\pm 11.9\%$)
$k_{cl,probe}$ (nM/min)	0.00152	0.00157 ± 0.0147 ($\pm 9.35\%$)
$K_{D,R}$ (nM)	8.98	196 ± 145 (± 73.8)
$K_{D,L}$ [nM]	15.4	55.2 ± 26.1 (± 47.2)
$s_{caspase-8}$ [nM/min]	0.00149	$0.00153 \pm 1.46 \cdot 10^{-4}$ ($\pm 9.51\%$)
$s_{Pr,mCherry}$ [nM]	0.0173	0.0144 ± 0.00212 (± 14.7)
$s_{Pr,mGFP}$ [nM]	0.00350	$0.00350 \pm 4.24 \cdot 10^{-4}$ ($\pm 12.1\%$)

Table A.3. Parameters of the fitted 'cis/trans' model. Values of the 1% best of n=1000 fits to single cell and western blot data (CD95-HeLa and HeLa wt cells) were included for means and standard deviations.

Additional material on the cell ensemble model of apoptosis

A.3. Flux analysis in caspase-8 cleavage model variants

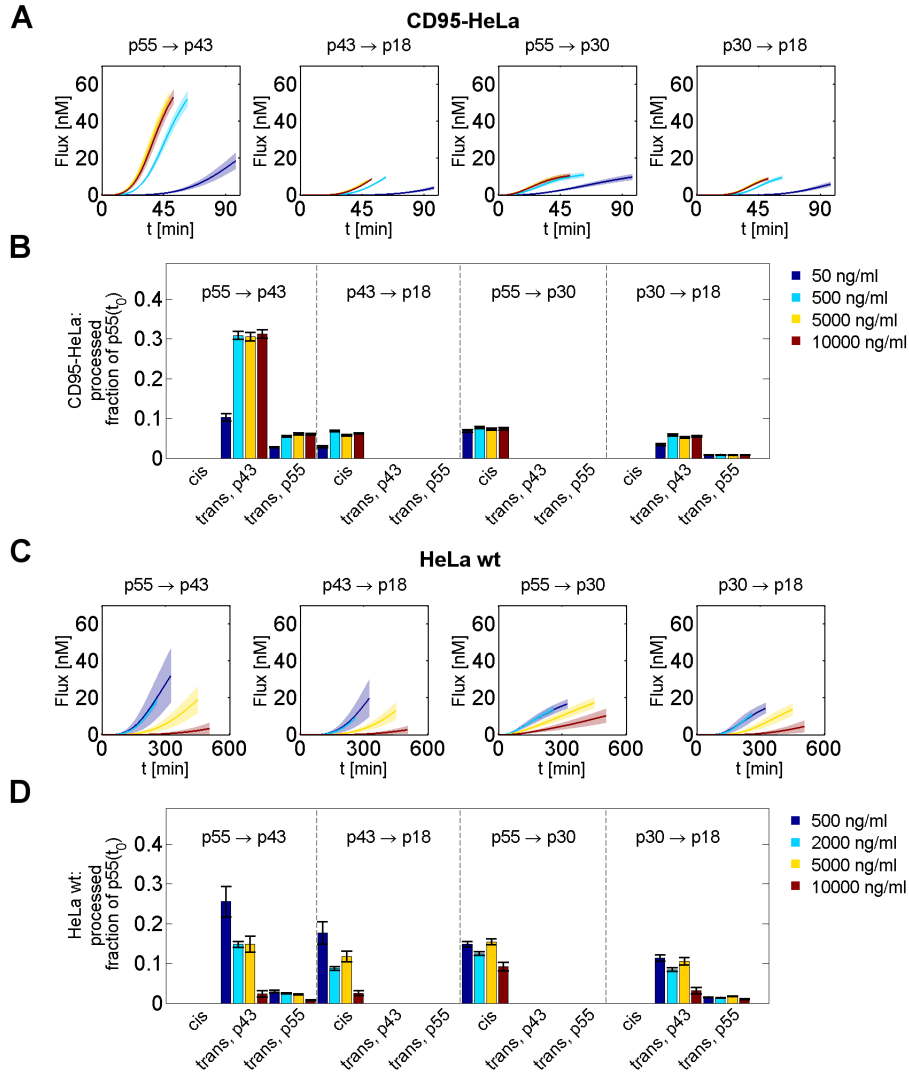


Figure A.5. Reaction fluxes for the ‘cis/trans’ topology (prodomain site cleavage in cis, enzymatic domain cleavage in trans) as in Figure 7.8. Integrated reaction fluxes for procaspase-8 cleavage are shown in panel (A) for CD95-HeLa and in panel (C) for HeLa wt cells. Panels (B) and (D) show fractions of initial p55 levels that are processed within the different cleavage reactions. Similar as in the ‘cis+trans/cis+trans’ variant, trans cleavage of p55 by p43 is the reaction, in which the largest p55 fractions are cleaved. Solid lines in panels (A) and (C) represent mean trajectories from the best 1% of 1000 fits to the complete set of single cell and population data, respectively. Shaded areas (A and C) and error bars (B and D) represent standard deviations of these fits.

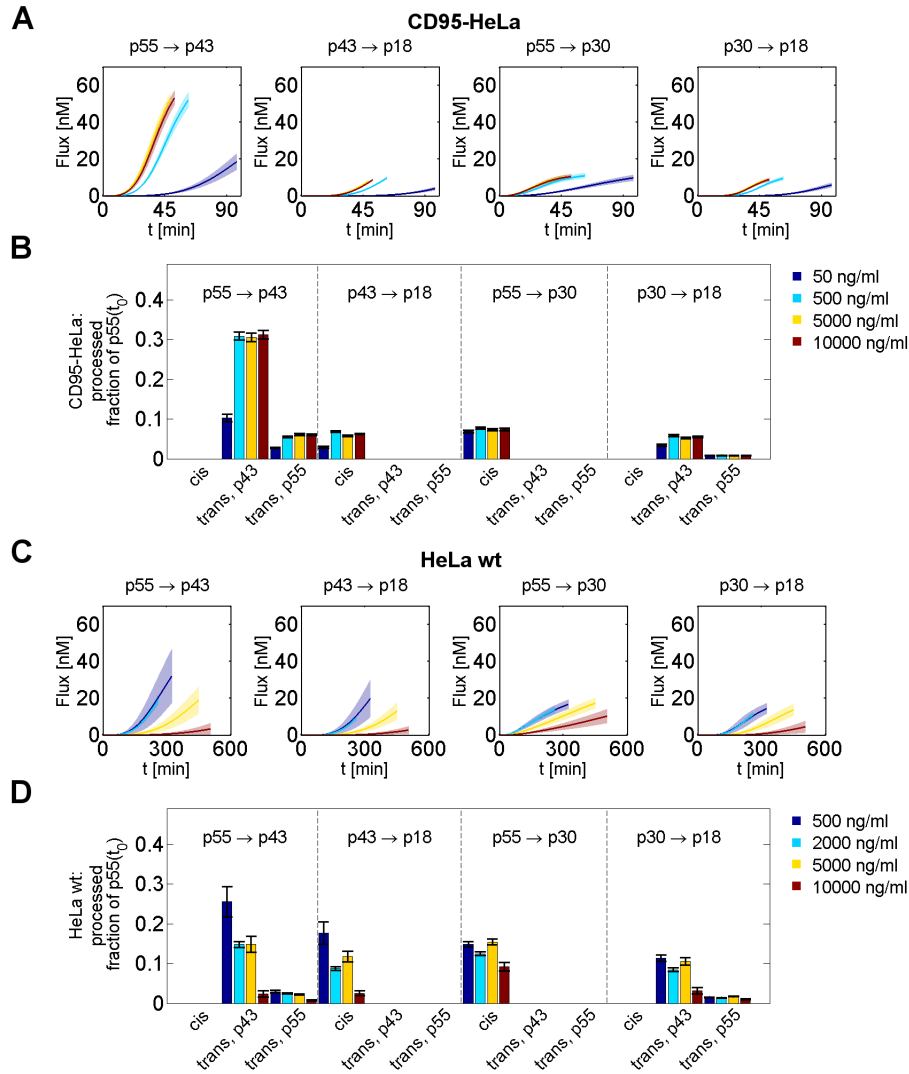


Figure A.6. Reaction fluxes for the ‘trans/trans’ topology (prodomain site and enzymatic domain site cleavages in trans) as in Figure A.5. Integrated reaction fluxes for procaspase-8 cleavage are shown in panel (A) for CD95-HeLa and in panel (C) for HeLa wt cells. Panels (B) and (D) show fractions of initial p55 levels that are processed within the different cleavage reactions.

A.4. Quantification of total signaling protein numbers

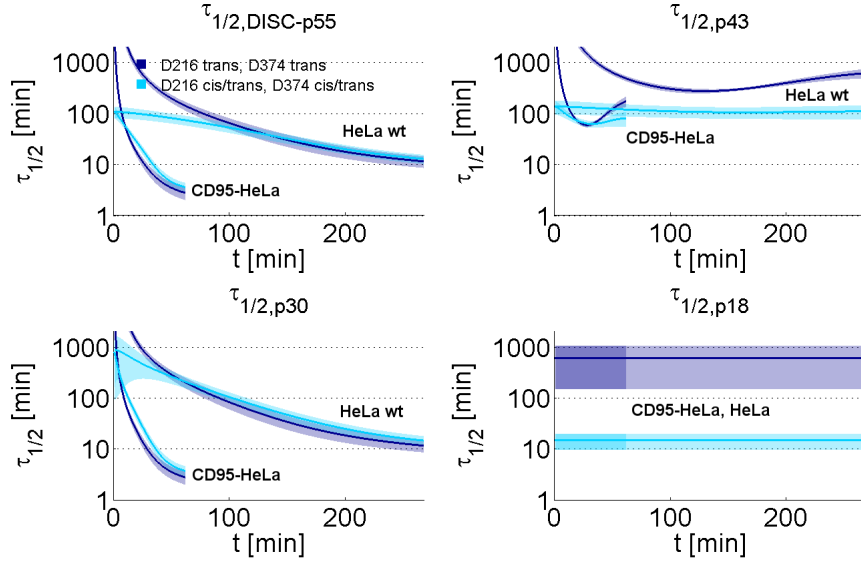


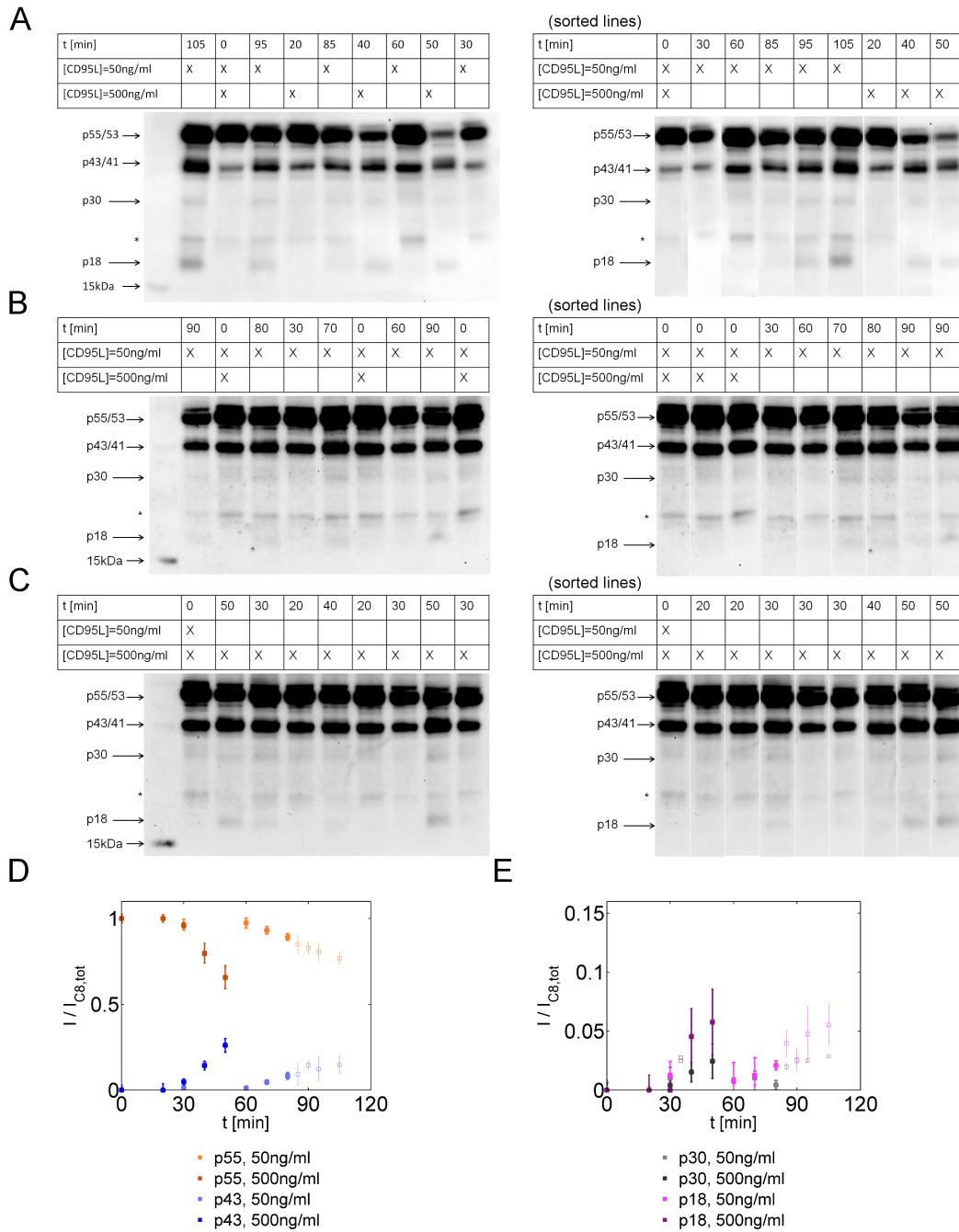
Figure A.7. Comparison between model estimates of protein half-lives $\tau_{1/2}$ between the ‘trans/trans’ and the ‘cis+trans/cis+trans’ model variants for CD95-HeLa and HeLa wt cells as in Figure 7.10. Both variants show very similar half-life estimates for p55 and p30, but differ in predicted half-life times for p43 and p18. Notably, the ‘trans/trans’ variant predicts much larger half-life times for p18, meaning that p18 is rarely inactivated before the time of apoptosis of CD95-HeLa and HeLa wt cells. Solid lines represent mean trajectories and shaded areas represent standard deviations from the best 1% of 1000 fits to the complete set of single cell and population data, respectively.

A.4. Quantification of total signaling protein numbers

Absolute signaling protein concentrations and their variability were determined by quantitative western blotting and flow cytometry based assays in order to further constrain the mathematical model of caspase-8 processing.

Estimates of average protein levels of FADD, procaspase-8 and BID in probe expressing cells were obtained by calibrated western blots (Table 5.1). The order of samples was shuffled to avoid biases from gel and blotting inhomogeneities [170]. Cell lines stably expressing FADD-GFP or p55-GFP were generated from HeLa wt cells. The same cell line was used to transiently express BID-GFP-mCherry. The concentrations of FADD-GFP, p55-GFP and BID-GFP-mCherry in fusion protein lysates were estimated by simultaneously blotting fusion protein lysates together with different doses of recombinant GFP. Endogenous levels of FADD, p55, BID and cytosolic cleavage probes (NES-GIETDS-mCherry) were determined by blotting different doses of fusion protein lysates together with lysates of probe expressing CD95-HeLa and HeLa wt cells (Figures A.10-A.12). For ER probe (Calnexin-GIETDS-mGFP) level estimations, lysates of probe expressing cell lines were blotted together with

recombinant GFP (Figure A.12). Estimates of FADD and p55 had the same order of magnitude as in the study of Fricker et al. [46] ($N_{FADD} \approx 200.000/cell$ compared to $130.000/cell$, and $N_{p55} \approx 320.000/cell$ compared to $250.000/cell$). Here, FADD and p55 levels of similar magnitude in probe expressing CD95-HeLa and HeLa wt cells were measured.



A.4. Quantification of total signaling protein numbers

Figure A.8. Caspase-8 western blot time series were used to generate population observables for model fitting. (A-C) Exemplary western blots from experiments in CD95-HeLa cells at 50ng/ml and 500ng/ml . For each data point included in model fitting three replicates were measured. Intensities of every band were background corrected and normalized to the sum of all caspase-8 bands (p55/53, p43/41, p30 and p18), respectively. Western blots are shown with original orders of lines (left plots) and sorted according to time points and experiments (right plots). An unspecific band is marked by a star. (D) Background corrected and normalized intensities for p55 and p43 were used for model fitting at times before cells started to undergo apoptosis (until $80'$ at $[CD95L] = 50\text{ng/ml}$ and until $50'$ at $[CD95L] = 500\text{ng/ml}$), and if at least three replicates were recorded. Time points included for model fitting are displayed as solid squares and not included time points as empty squares (error bars: standard error of the mean). (E) Background corrected and normalized intensities for p30 and p18 as in (D).

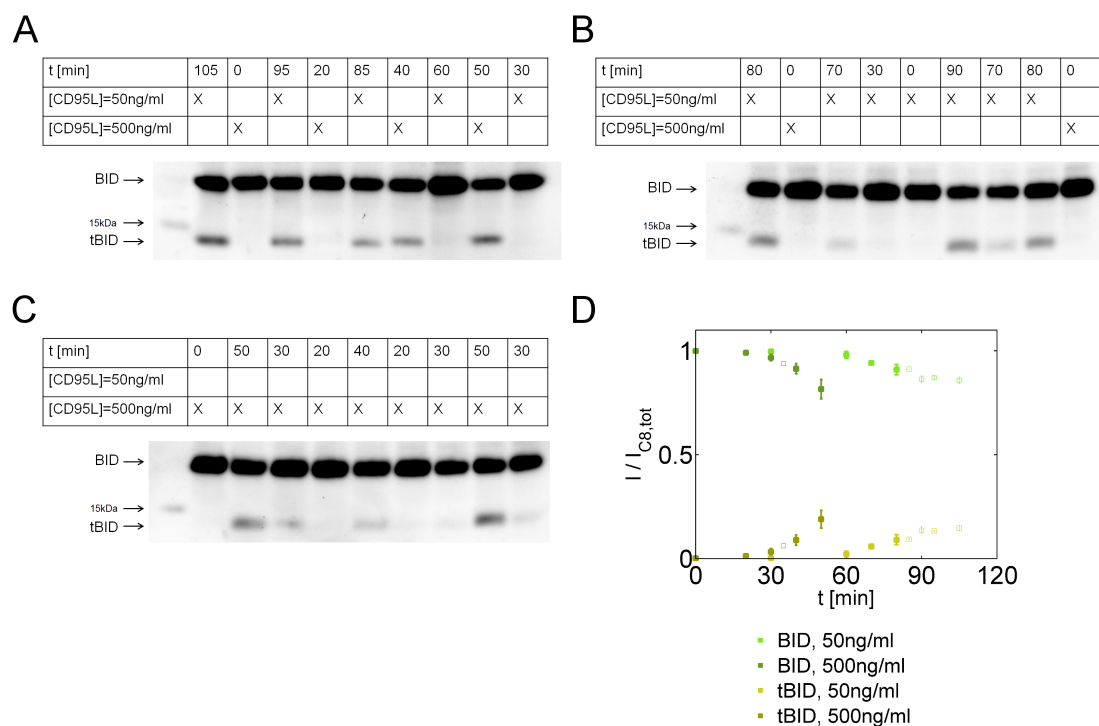
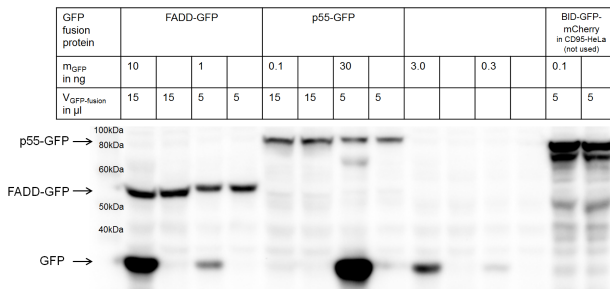


Figure A.9. BID and tBID western blot time series served as population observables for model fitting. (A-C) As for caspase-8, for each time point included in model fitting three replicates were measured in CD95-HeLa cells at 50ng/ml and 500ng/ml . Intensities of every band were background corrected and normalized to the sum of BID and tBID, respectively. (D) As for caspase-8, background subtracted and normalized intensities were used for model fitting before the first cells underwent apoptosis, and if at least three replicates were available to estimate experimental errors (solid squares: time points included for model fitting, empty squares: not included data points).

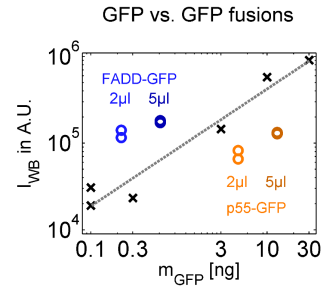
	CD95R-HeLa	HeLa
\hat{V}_{cell} (c. i.) in fl	3585 (3457, 3717)	4236 (3903, 4597)
$c(u_{5\%}, u_{95\%})$	(2554, 5031)	(2751, 6521)
\hat{V}_{cpl} (c. i.) in fl	2515 (2413, 2622)	2980 (2722, 3263)
$c(u_{5\%}, u_{95\%})$	(1705, 3711)	(1845, 4813)
\hat{A}_{cell} (c. i.) in μm^2	1475 (1424, 1527)	1404 (1314, 1501)
$c(u_{5\%}, u_{95\%})$	(1063, 2046)	(988, 1995)
$\hat{I}_0(Pr, cpl)$ (c. i.) in A.U.	54.46 (51.09, 58.05)	61.68 (58.41, 65.15)
$c(u_{5\%}, u_{95\%})$	(29.95, 99.02)	(46.24, 82.29)
$\hat{I}_0(Pr, ER)$ (c. i.) in A.U.	34.88 (33.77, 36.03)	22.21 (19.59, 25.17)
$c(u_{5\%}, u_{95\%})$	(25.77, 47.21)	(11.46, 43.04)

Table A.4. Cellular and cytosolic volumes, cell surface areas and average fluorescence intensities for the cytosolic and the ER-anchored cleavage probes were obtained by segmentation from confocal microscopy image stacks. Median values, confidence intervals for the median estimates, and percentiles of the lognormal distributions are given in brackets.

A GFP fusions vs. GFP
(FADD-GFP and p55-GFP)



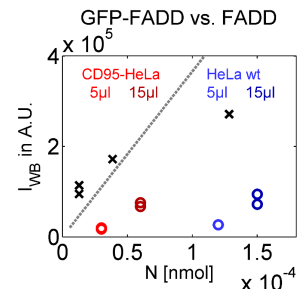
B



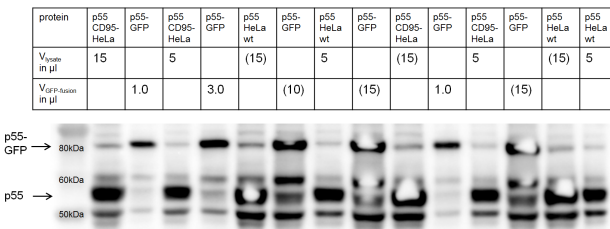
C FADD vs. FADD-GFP



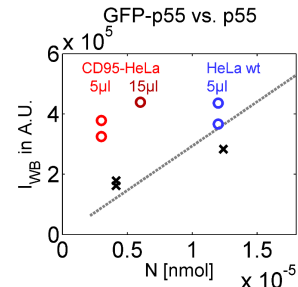
D



E p55 vs. p55-GFP



F



A.4. Quantification of total signaling protein numbers

Figure A.10. Estimation of average FADD and p55 levels in probe expressing CD95-HeLa and HeLa wt cells by calibrated western blot. (A) Blotting FADD-GFP and p55-GFP together with doses of recombinant GFP served to estimate concentrations of FADD and p55 fusions (B). (C, D) To estimate FADD levels, FADD-GFP lysate doses were blotted together with $5\mu\text{l}$ or $15\mu\text{l}$ of lysates from probe expressing CD95-HeLa and HeLa wt cells. In panel (C) a part between 30kDa and 50kDa was cut out. (E, F) p55 levels were estimated by simultaneously blotting p55-GFP with lysates from probe expressing cells. Intensities were background corrected. Values in brackets indicate oversaturated bands that were excluded from evaluations.

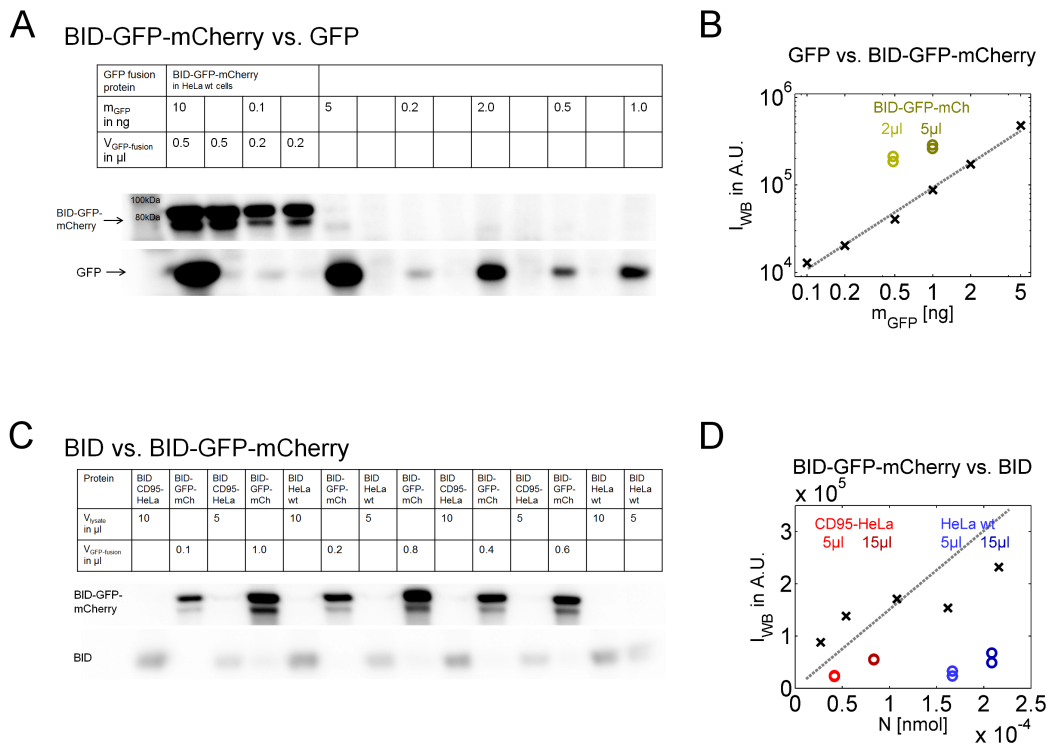


Figure A.11. Estimation of average BID levels in probe expressing CD95-HeLa and HeLa wt cells (A, B) BID-GFP-mCherry levels were calibrated by blotting together with doses of recombinant GFP. (C, D) BID levels in probe expressing CD95-HeLa and HeLa wt cells were estimated by blotting together with FADD-GFP lysates. White lines indicate that intervening lanes were cut out.

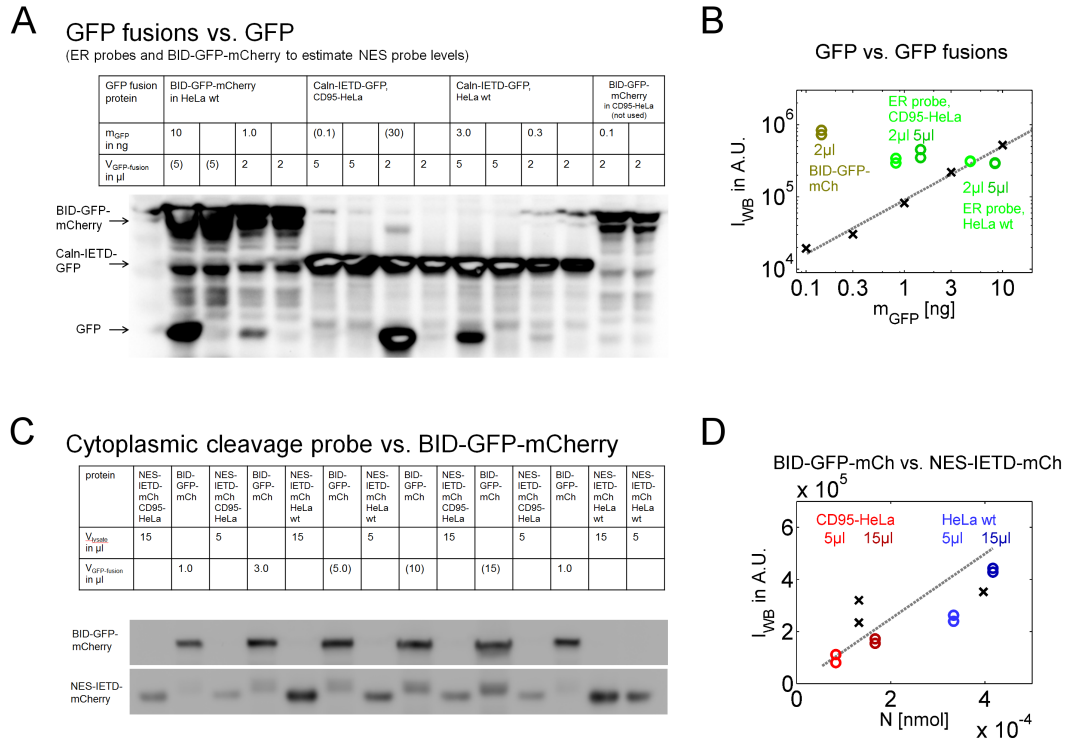


Figure A.12. Estimation of average cleavage probe levels in probe expressing CD95-HeLa and HeLa wt cells. (A, B) Levels of ER anchored probes (Calnexin-GIETDS-GFP) could be directly estimated by blotting together with recombinant GFP (B). BID-GFP-mCherry, expressed in HeLa wt cells, was calibrated with recombinant GFP to estimate cytosolic probe (NES-GIETDS-mCherry) levels (abbreviations: caln - calnexin, mCh - mCherry). Values in brackets indicate oversaturated bands that were excluded from evaluations. Bands for ER probes were evaluated despite signs of oversaturation as it was sufficient to estimate lower boundaries of expression levels ($N_{ERprobes} \geq 8 \cdot 10^6/cell$). (C, D) To estimate cytosolic probe levels, probe expressing cell lysates were blotted together with BID-GFP-mCherry lysate. In panel (C) intervening lanes were spliced out.

A.5. Using flow cytometry to estimate receptor levels and set upper and lower boundaries for initial concentrations

Mean levels of CD95 receptors and variability of CD95 receptors, FADD, p55 and BID were determined in probe expressing or not probe expressing HeLa wt and CD95-HeLa cells by immunostaining followed by flow cytometry (Figures A.13 and A.14). The absolute concentration of CD95 receptors was estimated with help of calibration beads carrying defined epitope numbers for secondary antibodies (Table 5.2, Figure A.13). FACS distributions were used to restrict the variability of initial protein concentrations in the model to physiologically reasonable levels. To measure

A.5. Using flow cytometry to estimate receptor levels and set upper and lower boundaries for initial concentrations

variability of protein levels independent from cell size, FACS events were filtered for cells of similar volumes by gating for narrow front scatter and side scatter intervals. As controls in FACS measurements, cells were treated with secondary but no primary antibodies. To correct intensity measurements for background fluorescence, medians of normal distribution function fits to intensities of control measurements were subtracted. The lognormal distribution parameters μ and σ for initial concentration distributions were determined by fitting to rescaled and background corrected FACS signals. In order to restrict initial protein concentrations in the model, 5% and 95% percentiles were calculated and combined with mean signals from western blots to set lower and upper limit for parameter fitting, respectively (Table 5.3).

Coefficients of variation in the range of $VarK = 0.8 \dots 1.1$ were obtained, which are rather large compared to studies on the variability of protein levels [171, 172], probably due to additional variability from intracellular antibody staining and FACS measurements. For this reason, the obtained 5% percentiles were used as lower and 95% percentiles as upper allowed boundaries for estimations of initial protein concentrations in each cell. Cellular volumes that were used to calculate average protein concentrations from protein numbers per cell as well as surface areas were determined by segmentation from confocal microscopic image stacks (Table A.4).

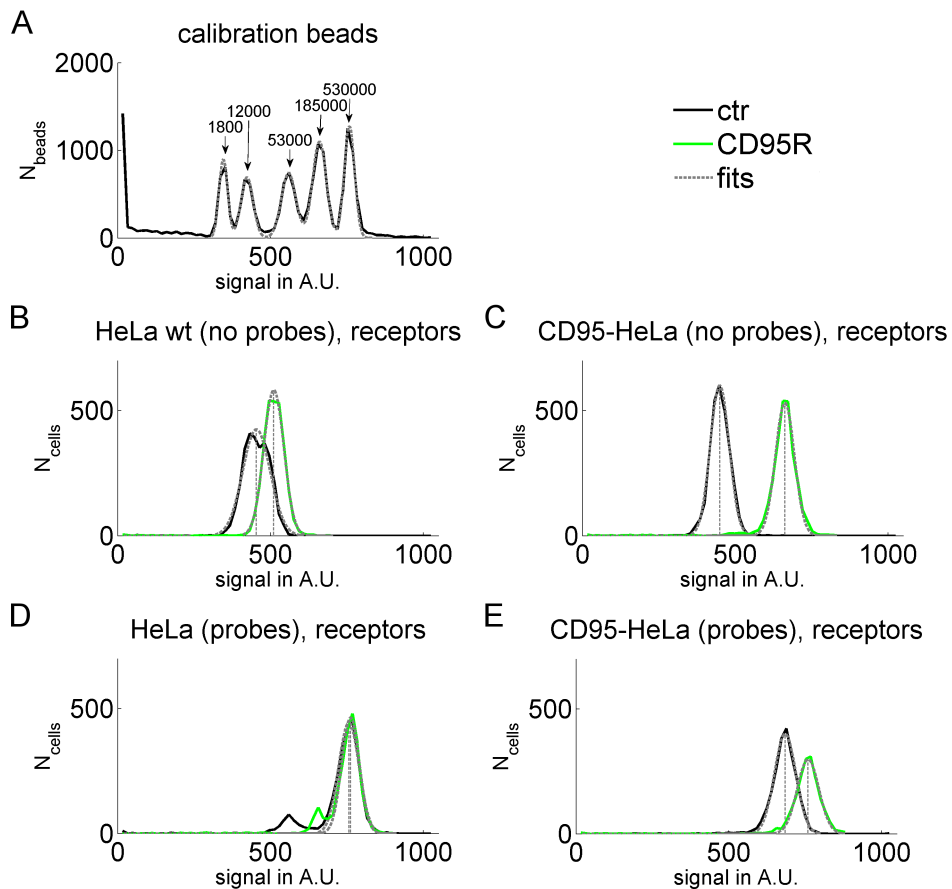


Figure A.13. Flow cytometry of cells immunostained for CD95 receptors. (A) To estimate average levels of membrane bound receptors, beads with five different numbers of epitopes for fluorescence labeled secondary antibodies were used. Thereby, the FACS signal representing the common logarithm of fluorescence intensity plus background was rescaled. In not probe expressing HeLa wt (B) or CD95-HeLa (C), and probe expressing HeLa (D) or CD95-HeLa (E) cells, receptor levels were estimated by fitting normal distribution functions ('fits') and subtracting background signals of control measurements ('ctr').

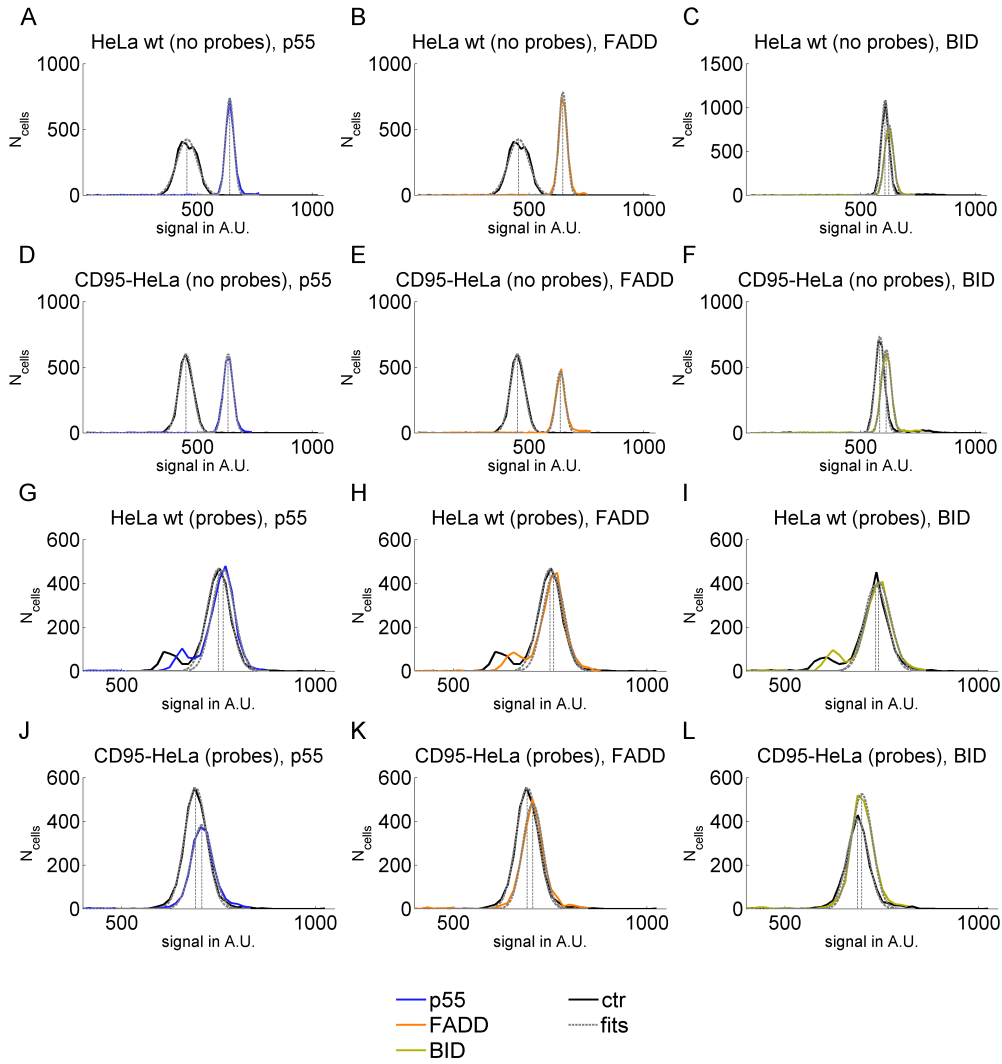


Figure A.14. Flow cytometry of cells immunostained for p55, FADD and BID. Native HeLa wt (A-C) and CD95-HeLa (D-F), as well as probe expressing HeLa (G-I) and CD95-HeLa cells (J-L) were stained for p55 (left column), FADD (central column) and BID (right column). Normal distribution functions were fitted to cells stained with primary antibodies and control measurements.

B. Additional material on the cell ensemble model of Epo receptor traffic

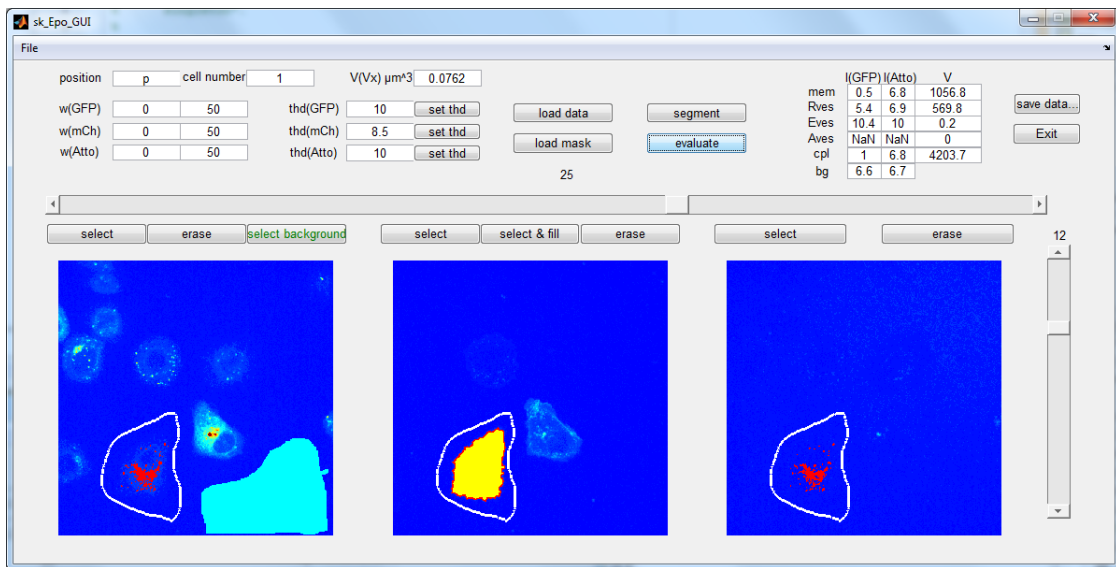


Figure B.1. GUI of the segmentation software. Three windows display EpoR-GFP (left), MyrPalm-mCherry (center) and Epo-Cy5.5 (right) images and segmented ROIs. Inside predefined areas for single cells, membrane and vesicle ROIs (containing EpoR-GFP, Epo-Cy5.5 or EpoR-GFP *and* Epo-Cy5.5) are segmented according to intensity threshold values to determine ROI volumes and mean EpoR-GFP and Epo-Cy5.5 intensities for each time point. ROI borders can be manually corrected. Background ROIs are manually selected to determine background GFP and Cy5.5 intensity values that are subtracted from intensities in cellular ROIs (light blue area in left image window).

reaction rates, auxiliary models	
$v_1 = k_{EpoR,ItoM}[EpoR_i]$	
$v_2 = k_{EpoR,MtoI}[EpoR_m]$	
$v_3 = k_{syn}$	
$v_4 = k_{deg}[EpoR_i]$	
$v_5 = k_{FRAP}([EpoR_m] + [EpoR_i])\theta(t - t_{on})\theta(t_{off} - t)$	

differential equations, auxiliary models	
<i>photobleached cells</i>	<i>CHX treated cells</i>
$\frac{d[EpoR_m]}{dt} = v_1 - v_2 - v_5$	$\frac{d[EpoR_m]}{dt} = v_1 - v_2$
$\frac{d[EpoR_i]}{dt} = -v_1 + v_2 + v_3 - v_4 - v_5$	$\frac{d[EpoR_i]}{dt} = -v_1 + v_2 - v_4$
$\frac{d[EpoR_{deg}]}{dt} = v_4$	$\frac{d[EpoR_{deg}]}{dt} = v_4$

Table B.1. Reaction rates and equations of the auxiliary EpoR traffic model variants. In photobleached cells, a short FRAP pulse was applied to decrease the total amount of GFP fused EpoR, implemented by the kinetic constant k_{FRAP} and Heaviside functions describing the pulse between t_{on} and t_{off} . Auxiliary models of photobleached cells were implemented to independently estimate the variable kinetics of EpoR-GFP synthesis in single cells. In cycloheximide (CHX) treated cells new synthesis of EpoR was inhibited to quantify the variable degradation kinetics in single cells.

	k_{ItoM}	k_{MtoI}	k_{syn}	k_{deg}	k_{*MtoRE}	k_{*REtoM}	k_{*REtoI}
k_{ItoM}		-0,04	0,60	0,05	0,61	0,31	-0,48
k_{MtoI}	-0,04		0,28	0,16	-0,11	0,47	-0,39
k_{syn}	0,60	0,28		0,70	0,60	0,55	-0,46
k_{deg}	0,05	0,16	0,70		0,17	0,16	0,06
k_{*MtoRE}	0,61	-0,11	0,60	0,17		0,22	-0,28
k_{*REtoM}	0,31	0,47	0,55	0,16	0,22		-0,56
k_{*REtoI}	-0,48	-0,39	-0,46	0,06	-0,28	-0,56	

Table B.2. Correlation coefficients for kinetic parameters of Epo internalizing cells. The only significant correlation was the positive correlation between k_{syn} and k_{deg} ($p = 0.024$).

Bibliography

- [1] KALLENBERGER S & LEGEWIE S (2013) Modeling formalisms in systems biology of apoptosis. In: LAVRIK I, ed., *Systems Biology of Apoptosis*, chap. 1, 1–32, Springer, New York, NY, 1st ed.
- [2] KALLENBERGER S, LEGEWIE S, & EILS R (2014) Applications in cancer research: mathematical models of apoptosis. In: EILS R & KRIETE A, eds., *Computational Systems Biology: From Molecular Mechanisms to Disease*, in press, Elsevier Academic Press, Amsterdam; Boston, 2nd ed.
- [3] HANAHAN D & WEINBERG RA (2011) Hallmarks of cancer: the next generation. *Cell*, 144 (5), 646–674.
- [4] LAVRIK I, GOLKS A, & KRAMMER PH (2005) Death receptor signaling. *Journal of cell science*, 118, 265–267.
- [5] MUZIO M, CHINNAIYAN AM, KISCHKEL FC, O’ROURKE K, SHEVCHENKO A, NI J, SCAFFIDI C, ET AL. (1996) FLICE, a novel FADD-homologous ICE/CED-3-like protease, is recruited to the CD95 (Fas/APO-1) death-inducing signaling complex. *Cell*, 85 (6), 817–827.
- [6] KISCHKEL FC, HELLBARDT S, BEHRMANN I, GERMER M, PAWLITA M, KRAMMER PH, & PETER ME (1995) Cytotoxicity-dependent APO-1 (Fas/CD95)-associated proteins form a death-inducing signaling complex (DISC) with the receptor. *The EMBO journal*, 14 (22), 5579–5588.
- [7] MEDEMA JP, SCAFFIDI C, KISCHKEL FC, SHEVCHENKO A, MANN M, KRAMMER PH, & PETER ME (1997) FLICE is activated by association with the CD95 death-inducing signaling complex (DISC). *The EMBO journal*, 16 (10), 2794–2804.
- [8] FUENTES-PRIOR P & SALVESEN GS (2004) The protein structures that shape caspase activity, specificity, activation and inhibition. *The Biochemical journal*, 384 (Pt 2), 201–232.
- [9] DENG Y, LIN Y, & WU X (2002) TRAIL-induced apoptosis requires bax-dependent mitochondrial release of Smac/DIABLO. *Genes & development*, 16 (1), 33–45.
- [10] GARCÍA-SÁEZ AJ (2012) The secrets of the bcl-2 family. *Cell death and differentiation*, 19 (11), 1733–1740.

- [11] VERHAGEN AM, EKERT PG, PAKUSCH M, SILKE J, CONNOLLY LM, REID GE, MORITZ RL, ET AL. (2000) Identification of DIABLO, a mammalian protein that promotes apoptosis by binding to and antagonizing IAP proteins. *Cell*, 102 (1), 43–53.
- [12] DU C, FANG M, LI Y, LI L, & WANG X (2000) Smac, a mitochondrial protein that promotes cytochrome c-dependent caspase activation by eliminating IAP inhibition. *Cell*, 102 (1), 33–42.
- [13] LIU X, KIM CN, YANG J, JEMMERSON R, & WANG X (1996) Induction of apoptotic program in cell-free extracts: requirement for dATP and cytochrome c. *Cell*, 86 (1), 147–157.
- [14] ZHANG XD, ZHANG XY, GRAY CP, NGUYEN T, & HERSEY P (2001) Tumor necrosis factor-related apoptosis-inducing ligand-induced apoptosis of human melanoma is regulated by smac/DIABLO release from mitochondria. *Cancer research*, 61 (19), 7339–7348.
- [15] SUN XM, BRATTON SB, BUTTERWORTH M, MACFARLANE M, & COHEN GM (2002) Bcl-2 and bcl-xL inhibit CD95-mediated apoptosis by preventing mitochondrial release of Smac/DIABLO and subsequent inactivation of x-linked inhibitor-of-apoptosis protein. *The Journal of biological chemistry*, 277 (13), 11345–11351.
- [16] LI S, ZHAO Y, HE X, KIM TH, KUHARSKY DK, RABINOWICH H, CHEN J, ET AL. (2002) Relief of extrinsic pathway inhibition by the bid-dependent mitochondrial release of smac in fas-mediated hepatocyte apoptosis. *The Journal of biological chemistry*, 277 (30), 26912–26920.
- [17] KLUCK RM, BOSSY-WETZEL E, GREEN DR, & NEWMAYER DD (1997) The release of cytochrome c from mitochondria: a primary site for bcl-2 regulation of apoptosis. *Science (New York, NY)*, 275 (5303), 1132–1136.
- [18] SAMEJIMA K & EARNSHAW WC (2005) Trashing the genome: the role of nucleases during apoptosis. *Nature reviews Molecular cell biology*, 6 (9), 677–688.
- [19] ALGECIRAS-SCHIMNICH A, SHEN L, BARNHART BC, MURMANN AE, BURKHARDT JK, & PETER ME (2002) Molecular ordering of the initial signaling events of CD95. *Molecular and cellular biology*, 22 (1), 207–220.
- [20] SCAFFIDI C, FULDA S, SRINIVASAN A, FRIESEN C, LI F, TOMASELLI KJ, DEBATIN KM, ET AL. (1998) Two CD95 (APO-1/Fas) signaling pathways. *The EMBO journal*, 17 (6), 1675–1687.
- [21] DANIAL NN & KORSMEYER SJ (2004) Cell death: Critical control points. *Cell*, 116 (2), 205–219.

Bibliography

- [22] GALLUZZI L, KEPP O, & KROEMER G (2012) Mitochondria: master regulators of danger signalling. *Nature Reviews Molecular Cell Biology*, 13 (12), 780–788.
- [23] NAIR VD, YUEN T, OLANOW CW, & SEALFON SC (2004) Early single cell bifurcation of pro- and antiapoptotic states during oxidative stress. *The Journal of biological chemistry*, 279 (26), 27494–27501.
- [24] JANES KA, ALBECK JG, GAUDET S, SORGER PK, LAUFFENBURGER DA, & YAFFE MB (2005) A systems model of signaling identifies a molecular basis set for cytokine-induced apoptosis. *Science (New York, NY)*, 310 (5754), 1646–1653.
- [25] TENTNER AR, LEE MJ, OSTHEIMER GJ, SAMSON LD, LAUFFENBURGER DA, & YAFFE MB (2012) Combined experimental and computational analysis of DNA damage signaling reveals context-dependent roles for erk in apoptosis and G1/S arrest after genotoxic stress. *Molecular systems biology*, 8, 568.
- [26] CALZONE L, TOURNIER L, FOURQUET S, THIEFFRY D, ZHIVOTOVSKY B, BARILLOT E, & ZINOVYEV A (2010) Mathematical modelling of cell-fate decision in response to death receptor engagement. *PLoS computational biology*, 6 (3), e1000702.
- [27] MAI Z & LIU H (2009) Boolean network-based analysis of the apoptosis network: irreversible apoptosis and stable surviving. *Journal of theoretical biology*, 259 (4), 760–769.
- [28] PHILIPPI N, WALTER D, SCHLATTER R, FERREIRA K, EDERER M, SAWODNY O, TIMMER J, ET AL. (2009) Modeling system states in liver cells: survival, apoptosis and their modifications in response to viral infection. *BMC systems biology*, 3, 97.
- [29] SCHLATTER R, SCHMICH K, AVALOS VIZCARRA I, SCHEURICH P, SAUTER T, BORNER C, EDERER M, ET AL. (2009) ON/OFF and beyond—a boolean model of apoptosis. *PLoS computational biology*, 5 (12), e1000595.
- [30] ZHANG R, SHAH MV, YANG J, NYLAND SB, LIU X, YUN JK, ALBERT R, ET AL. (2008) Network model of survival signaling in large granular lymphocyte leukemia. *Proceedings of the National Academy of Sciences of the United States of America*, 105 (42), 16308–16313.
- [31] SVINGEN PA, LOEGERING D, RODRIQUEZ J, MENG XW, MESNER J PETER W, HOLBECK S, MONKS A, ET AL. (2004) Components of the cell death machine and drug sensitivity of the national cancer institute cell line panel. *Clinical cancer research: an official journal of the American Association for Cancer Research*, 10 (20), 6807–6820.

- [32] REHM M, HUBER HJ, HELLWIG CT, ANGUISSOLA S, DUSSMANN H, & PREHN JHM (2009) Dynamics of outer mitochondrial membrane permeabilization during apoptosis. *Cell death and differentiation*, 16 (4), 613–623.
- [33] CHEN C, CUI J, LU H, WANG R, ZHANG S, & SHEN P (2007) Modeling of the role of a bax-activation switch in the mitochondrial apoptosis decision. *Biophysical journal*, 92 (12), 4304–4315.
- [34] SIEHS C, OBERBAUER R, MAYER G, LUKAS A, & MAYER B (2002) Discrete simulation of regulatory homo- and heterodimerization in the apoptosis effector phase. *Bioinformatics (Oxford, England)*, 18 (1), 67–76.
- [35] DÜSSMANN H, REHM M, CONCANNON CG, ANGUISSOLA S, WÜRSTLE M, KACMAR S, VÖLLER P, ET AL. (2010) Single-cell quantification of bax activation and mathematical modelling suggest pore formation on minimal mitochondrial bax accumulation. *Cell death and differentiation*, 17 (2), 278–290.
- [36] SCHLEICH K, WARNKEN U, FRICKER N, OZTÜRK S, RICHTER P, KAMMERER K, SCHNÖLZER M, ET AL. (2012) Stoichiometry of the CD95 death-inducing signaling complex: Experimental and modeling evidence for a death effector domain chain model. *Molecular cell*, 47 (2), 306–319.
- [37] DUMITRU CA & GULBINS E (2006) TRAIL activates acid sphingomyelinase via a redox mechanism and releases ceramide to trigger apoptosis. *Oncogene*, 25 (41), 5612–5625.
- [38] FUSSENEGGER M, BAILEY JE, & VARNER J (2000) A mathematical model of caspase function in apoptosis. *Nature biotechnology*, 18 (7), 768–774.
- [39] ALBECK JG, BURKE JM, SPENCER SL, LAUFFENBURGER DA, & SORGER PK (2008) Modeling a snap-action, variable-delay switch controlling extrinsic cell death. *PLoS biology*, 6 (12), 2831–2852.
- [40] BAGCI EZ, VODOVOTZ Y, BILLIAR TR, ERMENTROUT GB, & BAHAR I (2006) Bistability in apoptosis: roles of bax, bcl-2, and mitochondrial permeability transition pores. *Biophysical journal*, 90 (5), 1546–1559.
- [41] BENTELE M, LAVRIK I, ULRICH M, STÖSSER S, HEERMANN DW, KALTHOFF H, KRAMMER PH, ET AL. (2004) Mathematical modeling reveals threshold mechanism in CD95-induced apoptosis. *The Journal of cell biology*, 166 (6), 839–851.
- [42] HARRINGTON HA, HO KL, GHOSH S, & TUNG KC (2008) Construction and analysis of a modular model of caspase activation in apoptosis. *Theoretical biology & medical modelling*, 5, 26.

Bibliography

- [43] HUA F, CORNEJO MG, CARDONE MH, STOKES CL, & LAUFFENBURGER DA (2005) Effects of bcl-2 levels on fas signaling-induced caspase-3 activation: molecular genetic tests of computational model predictions. *Journal of immunology*, 175 (2), 985–995.
- [44] OKAZAKI N, ASANO R, KINOSHITA T, & CHUMAN H (2008) Simple computational models of type I/type II cells in fas signaling-induced apoptosis. *Journal of theoretical biology*, 250 (4), 621–633.
- [45] EISSING T, CONZELMANN H, GILLES ED, ALLGÖWER F, BULLINGER E, & SCHEURICH P (2004) Bistability analyses of a caspase activation model for receptor-induced apoptosis. *The Journal of biological chemistry*, 279 (35), 36892–36897.
- [46] FRICKER N, BEAUDOUIN J, RICHTER P, EILS R, KRAMMER PH, & LAVRIK IN (2010) Model-based dissection of CD95 signaling dynamics reveals both a pro- and antiapoptotic role of c-FLIPL. *The Journal of cell biology*, 190 (3), 377–389.
- [47] HO KL & HARRINGTON HA (2010) Bistability in apoptosis by receptor clustering. *PLoS computational biology*, 6 (10), e1000956.
- [48] NEUMANN L, PFORR C, BEAUDOUIN J, PAPP A, FRICKER N, KRAMMER PH, LAVRIK IN, ET AL. (2010) Dynamics within the CD95 death-inducing signaling complex decide life and death of cells. *Molecular systems biology*, 6, 352.
- [49] WÜRSTLE ML, LAUSSMANN MA, & REHM M (2010) The caspase-8 dimerization/dissociation balance is a highly potent regulator of caspase-8, -3, -6 signaling. *The Journal of biological chemistry*, 285 (43), 33209–33218.
- [50] LAUSSMANN MA, PASSANTE E, HELLWIG CT, TOMICZEK B, FLANAGAN L, PREHN JHM, HUBER HJ, ET AL. (2012) Proteasome inhibition can impair caspase-8 activation upon submaximal stimulation of apoptotic tumor necrosis factor-related apoptosis inducing ligand (TRAIL) signaling. *The Journal of biological chemistry*, 287 (18), 14402–14411.
- [51] CHEN C, CUI J, ZHANG W, & SHEN P (2007) Robustness analysis identifies the plausible model of the bcl-2 apoptotic switch. *FEBS letters*, 581 (26), 5143–5150.
- [52] CUI J, CHEN C, LU H, SUN T, & SHEN P (2008) Two independent positive feedbacks and bistability in the bcl-2 apoptotic switch. *PLoS one*, 3 (1), e1469.
- [53] LINDNER AU, CONCANNON CG, BOUKES GJ, CANNON MD, LLAMBI F, RYAN D, BOLAND K, ET AL. (2013) Systems analysis of BCL2 protein family interactions establishes a model to predict responses to chemotherapy. *Cancer Research*, 73 (2), 519–528.

- [54] LEGEWIE S, BLÜTHGEN N, & HERZEL H (2006) Mathematical modeling identifies inhibitors of apoptosis as mediators of positive feedback and bistability. *PLoS computational biology*, 2 (9), e120.
- [55] REHM M, HUBER HJ, DUSSMANN H, & PREHN JHM (2006) Systems analysis of effector caspase activation and its control by x-linked inhibitor of apoptosis protein. *The EMBO journal*, 25 (18), 4338–4349.
- [56] STUCKI JW & SIMON HU (2005) Mathematical modeling of the regulation of caspase-3 activation and degradation. *Journal of theoretical biology*, 234 (1), 123–131.
- [57] ZHANG T, BRAZHNİK P, & TYSON JJ (2009) Computational analysis of dynamical responses to the intrinsic pathway of programmed cell death. *Biophysical journal*, 97 (2), 415–434.
- [58] HUBER HJ, DUSSMANN H, KILBRIDE SM, REHM M, & PREHN JHM (2011) Glucose metabolism determines resistance of cancer cells to bioenergetic crisis after cytochrome-c release. *Molecular systems biology*, 7, 470.
- [59] ZHANG H, XU Q, KRAJEWSKI S, KRAJEWSKA M, XIE Z, FUESS S, KITADA S, ET AL. (2000) BAR: an apoptosis regulator at the intersection of caspases and bcl-2 family proteins. *Proceedings of the National Academy of Sciences of the United States of America*, 97 (6), 2597–2602.
- [60] MCDONALD R E ROBERT & EL-DEIRY WS (2004) Suppression of caspase-8- and -10-associated RING proteins results in sensitization to death ligands and inhibition of tumor cell growth. *Proceedings of the National Academy of Sciences of the United States of America*, 101 (16), 6170–6175.
- [61] SCOTT FL, STEC B, POP C, DOBACZEWSKA MK, LEE JJ, MONOSOV E, ROBINSON H, ET AL. (2009) The fas-FADD death domain complex structure unravels signalling by receptor clustering. *Nature*, 457 (7232), 1019–1022.
- [62] LI B & DOU QP (2000) Bax degradation by the ubiquitin/proteasome-dependent pathway: involvement in tumor survival and progression. *Proceedings of the National Academy of Sciences of the United States of America*, 97 (8), 3850–3855.
- [63] SCHORR K, LI M, KRAJEWSKI S, REED JC, & FURTH PA (1999) Bcl-2 gene family and related proteins in mammary gland involution and breast cancer. *Journal of mammary gland biology and neoplasia*, 4 (2), 153–164.
- [64] REED JC (1999) Dysregulation of apoptosis in cancer. *Journal of clinical oncology: official journal of the American Society of Clinical Oncology*, 17 (9), 2941–2953.

Bibliography

- [65] CERTO M, DEL GAIZO MOORE V, NISHINO M, WEI G, KORSMEYER S, ARMSTRONG SA, & LETAI A (2006) Mitochondria primed by death signals determine cellular addiction to antiapoptotic bcl-2 family members. *Cancer cell*, 9 (5), 351–365.
- [66] DENG J, CARLSON N, TAKEYAMA K, DAL CIN P, SHIPP M, & LETAI A (2007) BH3 profiling identifies three distinct classes of apoptotic blocks to predict response to ABT-737 and conventional chemotherapeutic agents. *Cancer cell*, 12 (2), 171–185.
- [67] BRUNELLE JK & LETAI A (2009) Control of mitochondrial apoptosis by the bcl-2 family. *Journal of cell science*, 122 (Pt 4), 437–441.
- [68] NI CHONGHAILE T & LETAI A (2008) Mimicking the BH3 domain to kill cancer cells. *Oncogene*, 27 Suppl 1, S149–157.
- [69] VO TT & LETAI A (2010) BH3-only proteins and their effects on cancer. *Advances in experimental medicine and biology*, 687, 49–63.
- [70] HECTOR S, REHM M, SCHMID J, KEHOE J, MCCAWLEY N, DICKER P, MURRAY F, ET AL. (2012) Clinical application of a systems model of apoptosis execution for the prediction of colorectal cancer therapy responses and personalisation of therapy. *Gut*, 61 (5), 725–733.
- [71] MURPHY C, WEYHENMEYER B, SCHMID J, KILBRIDE SM, REHM M, HUBER HJ, SENFT C, ET AL. (2013) Activation of executioner caspases is a predictor of progression-free survival in glioblastoma patients: a systems medicine approach. *Cell death & disease*, 4, e629.
- [72] LESSENE G, CZABOTAR PE, & COLMAN PM (2008) BCL-2 family antagonists for cancer therapy. *Nature reviews Drug discovery*, 7 (12), 989–1000.
- [73] GÓMEZ-BENITO M, MARZO I, ANEL A, & NAVAL J (2005) Farnesyltransferase inhibitor BMS-214662 induces apoptosis in myeloma cells through PUMA up-regulation, bax and bak activation, and mcl-1 elimination. *Molecular pharmacology*, 67 (6), 1991–1998.
- [74] WILLIS SN, CHEN L, DEWSON G, WEI A, NAIK E, FLETCHER JI, ADAMS JM, ET AL. (2005) Proapoptotic bak is sequestered by mcl-1 and bcl-xL, but not bcl-2, until displaced by BH3-only proteins. *Genes & development*, 19 (11), 1294–1305.
- [75] FISCHER SF, VIER J, KIRSCHNEK S, KLOS A, HESS S, YING S, & HÄCKER G (2004) Chlamydia inhibit host cell apoptosis by degradation of proapoptotic bh3-only proteins. *J Exp Med*, 200 (7), 905–916.

- [76] FERRELL J J E (1996) Tripping the switch fantastic: how a protein kinase cascade can convert graded inputs into switch-like outputs. *Trends in biochemical sciences*, 21 (12), 460–466.
- [77] TOIVONEN HT, MEINANDER A, ASAOKA T, WESTERLUND M, PETTERSSON F, MIKHAILOV A, ERIKSSON JE, ET AL. (2011) Modeling reveals that dynamic regulation of c-FLIP levels determines cell-to-cell distribution of CD95-mediated apoptosis. *The Journal of biological chemistry*, 286 (21), 18375–18382.
- [78] POP C, FITZGERALD P, GREEN DR, & SALVESEN GS (2007) Role of proteolysis in caspase-8 activation and stabilization. *Biochemistry*, 46 (14), 4398–4407.
- [79] SONG Z, YAO X, & WU M (2003) Direct interaction between survivin and Smac/DIABLO is essential for the anti-apoptotic activity of survivin during taxol-induced apoptosis. *The Journal of biological chemistry*, 278 (25), 23130–23140.
- [80] GOLDSTEIN JC, WATERHOUSE NJ, JUIN P, EVAN GI, & GREEN DR (2000) The coordinate release of cytochrome c during apoptosis is rapid, complete and kinetically invariant. *Nature cell biology*, 2 (3), 156–162.
- [81] REHM M, DUSSMANN H, JANICKE RU, TAVARE JM, KOGEL D, & PREHN JHM (2002) Single-cell fluorescence resonance energy transfer analysis demonstrates that caspase activation during apoptosis is a rapid process. role of caspase-3. *The Journal of biological chemistry*, 277 (27), 24506–24514.
- [82] ALBECK JG, BURKE JM, ALDRIDGE BB, ZHANG M, LAUFFENBURGER DA, & SORGER PK (2008) Quantitative analysis of pathways controlling extrinsic apoptosis in single cells. *Molecular cell*, 30 (1), 11–25.
- [83] REED JC, MIYASHITA T, TAKAYAMA S, WANG HG, SATO T, KRAJEWSKI S, AIMÉ-SEMPÉ C, ET AL. (1996) BCL-2 family proteins: regulators of cell death involved in the pathogenesis of cancer and resistance to therapy. *Journal of cellular biochemistry*, 60 (1), 23–32.
- [84] SCHMID J, DUSSMANN H, BOUKES GJ, FLANAGAN L, LINDNER AU, O’CONNOR CL, REHM M, ET AL. (2012) Systems analysis of cancer cell heterogeneity in caspase-dependent apoptosis subsequent to mitochondrial outer membrane permeabilization. *The Journal of biological chemistry*, 287 (49), 41546–41559.
- [85] TYAS L, BROPHY VA, POPE A, RIVETT AJ, & TAVARÉ JM (2000) Rapid caspase-3 activation during apoptosis revealed using fluorescence-resonance energy transfer. *EMBO reports*, 1 (3), 266–270.

Bibliography

- [86] HOFFMANN JC, PAPP A, KRAMMER PH, & LAVRIK IN (2009) A new c-terminal cleavage product of procaspase-8, p30, defines an alternative pathway of procaspase-8 activation. *Molecular and cellular biology*, 29 (16), 4431–4440.
- [87] HUGHES MA, HARPER N, BUTTERWORTH M, CAIN K, COHEN GM, & MACFARLANE M (2009) Reconstitution of the death-inducing signaling complex reveals a substrate switch that determines CD95-mediated death or survival. *Molecular cell*, 35 (3), 265–279.
- [88] GOLKS A, BRENNER D, FRITSCH C, KRAMMER PH, & LAVRIK IN (2005) c-FLIPR, a new regulator of death receptor-induced apoptosis. *The Journal of biological chemistry*, 280 (15), 14507–14513.
- [89] KRUEGER A, SCHMITZ I, BAUMANN S, KRAMMER PH, & KIRCHHOFF S (2001) Cellular FLICE-inhibitory protein splice variants inhibit different steps of caspase-8 activation at the CD95 death-inducing signaling complex. *The Journal of biological chemistry*, 276 (23), 20633–20640.
- [90] SCAFFIDI C, SCHMITZ I, KRAMMER PH, & PETER ME (1999) The role of c-FLIP in modulation of CD95-induced apoptosis. *The Journal of biological chemistry*, 274 (3), 1541–1548.
- [91] LAVRIK I & KRAMMER PH (2012) Regulation of CD95/Fas signaling at the DISC. *Cell death and differentiation*, 19 (1), 36–41.
- [92] PFEUTY B, DAVID-PFEUTY T, & KANEKO K (2008) Underlying principles of cell fate determination during g1 phase of the mammalian cell cycle. *Cell cycle (Georgetown, Tex)*, 7 (20), 3246–3257.
- [93] BAGCI EZ, VODOVOTZ Y, BILLIAR TR, ERMENTROUT B, & BAHAR I (2008) Computational insights on the competing effects of nitric oxide in regulating apoptosis. *PloS one*, 3 (5), e2249.
- [94] SPENCER SL, GAUDET S, ALBECK JG, BURKE JM, & SORGER PK (2009) Non-genetic origins of cell-to-cell variability in TRAIL-induced apoptosis. *Nature*, 459 (7245), 428–432.
- [95] GAUDET S, SPENCER SL, CHEN WW, & SORGER PK (2012) Exploring the contextual sensitivity of factors that determine cell-to-cell variability in receptor-mediated apoptosis. *PLoS computational biology*, 8 (4), e1002482.
- [96] HASENAUER J, WALDHERR S, DOSZCZAK M, RADDE N, SCHEURICH P, & ALLGÖWER F (2011) Identification of models of heterogeneous cell populations from population snapshot data. *BMC bioinformatics*, 12, 125.
- [97] CHAVES M, EISSING T, & ALLGÖWER F (2008) Bistable biological systems: A characterization through local compact input-to-state stability. *IEEE Transactions on Automatic Control*, 53 (Special Issue), 87–100.

- [98] ALDRIDGE BB, GAUDET S, LAUFFENBURGER DA, & SORGER PK (2011) Lyapunov exponents and phase diagrams reveal multi-factorial control over TRAIL-induced apoptosis. *Molecular systems biology*, 7, 553.
- [99] CHOI AMK, RYTER SW, & LEVINE B (2013) Autophagy in human health and disease. *The New England journal of medicine*, 368 (7), 651–662.
- [100] RUBINSTEIN AD & KIMCHI A (2012) Life in the balance - a mechanistic view of the crosstalk between autophagy and apoptosis. *Journal of cell science*, 125 (Pt 22), 5259–5268.
- [101] WU H, LIU X, JAENISCH R, & LODISH HF (1995) Generation of committed erythroid bfu-e and cfu-e progenitors does not require erythropoietin or the erythropoietin receptor. *Cell*, 83 (1), 59–67.
- [102] OSTER HS, NEUMANN D, HOFFMAN M, & MITTELMAN M (2012) Erythropoietin: the swinging pendulum. *Leuk Res*, 36 (8), 939–944.
- [103] MACDOUGALL IC & ECKARDT KU (2006) Novel strategies for stimulating erythropoiesis and potential new treatments for anaemia. *Lancet*, 368 (9539), 947–953.
- [104] KLINGMÜLLER U, BERGELSON S, HSIAO JG, & LODISH HF (1996) Multiple tyrosine residues in the cytosolic domain of the erythropoietin receptor promote activation of stat5. *Proc Natl Acad Sci U S A*, 93 (16), 8324–8328.
- [105] HORVATH CM (2000) Stat proteins and transcriptional responses to extracellular signals. *Trends Biochem Sci*, 25 (10), 496–502.
- [106] SWAMEYE I, MULLER TG, TIMMER J, SANDRA O, & KLINGMULLER U (2003) Identification of nucleocytoplasmic cycling as a remote sensor in cellular signaling by databased modeling. *Proc Natl Acad Sci U S A*, 100 (3), 1028–1033.
- [107] SOCOLOVSKY M, NAM H, FLEMING MD, HAASE VH, BRUGNARA C, & LODISH HF (2001) Ineffective erythropoiesis in stat5a(-/-)5b(-/-) mice due to decreased survival of early erythroblasts. *Blood*, 98 (12), 3261–3273.
- [108] KOURY MJ & BONDURANT MC (1990) Erythropoietin retards dna breakdown and prevents programmed death in erythroid progenitor cells. *Science*, 248 (4953), 378–381.
- [109] CUI Y, RIEDLINGER G, MIYOSHI K, TANG W, LI C, DENG CX, ROBINSON GW, ET AL. (2004) Inactivation of stat5 in mouse mammary epithelium during pregnancy reveals distinct functions in cell proliferation, survival, and differentiation. *Mol Cell Biol*, 24 (18), 8037–8047.

Bibliography

- [110] TYSON JJ, CHEN KC, & NOVAK B (2003) Sniffers, buzzers, toggles and blinkers: dynamics of regulatory and signaling pathways in the cell. *Curr Opin Cell Biol*, 15 (2), 221–231.
- [111] LEVCHENKO A & IGLESIAS PA (2002) Models of eukaryotic gradient sensing: application to chemotaxis of amoebae and neutrophils. *Biophys J*, 82 (1 Pt 1), 50–63.
- [112] VENKATRAMAN L, CHIA SM, NARMADA BC, WHITE JK, BHOWMICK SS, FORBES DEWEY C JR, SO PT, ET AL. (2012) Plasmin triggers a switch-like decrease in thrombospondin-dependent activation of $\text{tgf-}\beta 1$. *Biophys J*, 113 (5), 1060–1068.
- [113] FERRELL J JR & MACHLEDER EM (1998) The biochemical basis of an all-or-none cell fate switch in xenopus oocytes. *Science*, 280 (5365), 895–898.
- [114] REDDY CC, NIYOGI SK, WELLS A, WILEY HS, & LAUFFENBURGER DA (1996) Engineering epidermal growth factor for enhanced mitogenic potency. *Nat Biotechnol*, 14 (13), 1696–1699.
- [115] RESAT H, EWALD JA, DIXON DA, & WILEY HS (2003) An integrated model of epidermal growth factor receptor trafficking and signal transduction. *Biophys J*, 85 (2), 730–743.
- [116] SCHMIDT-GLENEWINKEL H, REINZ E, EILS R, & BRADY NR (2009) Systems biological analysis of epidermal growth factor receptor internalization dynamics for altered receptor levels. *The Journal of biological chemistry*, 284 (25), 17243–17252.
- [117] SULAHIAN R, CLEAVER O, & HUANG LJS (2009) Ligand-induced epor internalization is mediated by jak2 and p85 and is impaired by mutations responsible for primary familial and congenital polycythemia. *Blood*, 113 (21), 5287–5297.
- [118] BULUT GB, SULAHIAN R, MA Y, CHI NW, & HUANG LJS (2011) Ubiquitination regulates the internalization, endolysosomal sorting, and signaling of the erythropoietin receptor. *J Biol Chem*, 286 (8), 6449–6457.
- [119] GAMBIN A, CHARZYNSKA A, ELLERT-MIKLASZEWSKA A, & RYBINSKI M (2013) Computational models of the jak1/2-stat1 signaling. *JAKSTAT*, 2 (3), e24672.
- [120] VERA J, BACHMANN J, PFEIFER AC, BECKER V, HORMIGA JA, DARIAS NVT, TIMMER J, ET AL. (2008) A systems biology approach to analyse amplification in the jak2-stat5 signalling pathway. *BMC Syst Biol*, 2, 38.
- [121] CAO Y (2013) Erythropoietin in cancer: a dilemma in risk therapy. *Trends Endocrinol Metab*, 24 (4), 190–199.

- [122] BUNN HF (2007) New agents that stimulate erythropoiesis. *Blood*, 109 (3), 868–873.
- [123] GROSS AW & LODISH HF (2006) Cellular trafficking and degradation of erythropoietin and novel erythropoiesis stimulating protein (NESP). *The Journal of biological chemistry*, 281 (4), 2024–2032.
- [124] BECKER V, SCHILLING M, BACHMANN J, BAUMANN U, RAUE A, MAIWALD T, TIMMER J, ET AL. (2010) Covering a broad dynamic range: information processing at the erythropoietin receptor. *Science (New York, NY)*, 328 (5984), 1404–1408.
- [125] BACHMANN J, RAUE A, SCHILLING M, BECKER V, TIMMER J, & KLINGMÜLLER U (2012) Predictive mathematical models of cancer signalling pathways. *Journal of internal medicine*, 271 (2), 155–165.
- [126] KALLENBERGER SM, BEAUDOUIN J, CLAUS J, FISCHER C, SORGER PK, LEGEWIE S, & EILS R Intra- and interdimeric caspase-8 self-cleavage controls strength and timing of cd95 induced apoptosis. *Science Signaling*, submitted.
- [127] NAREDI-RAINER N, PRESCHER J, HARTSCHUH A, & C LD (2013) Confocal microscopy. In: KUBITSCHECK U, ed., *Fluorescence Microscopy: From Principles to Biological Applications*, chap. 5, 175–213, Wiley-VCH Verlag GmbH & Co. KGaA, Weinheim, 1st ed.
- [128] MINSKY M (1961), Microscopic apparatus. us patent 3,013,467.
- [129] DEMTRÖDER W (2002) *Experimentalphysik 2, Elektrizität und Optik*. Springer, Berlin.
- [130] SEMWOGERERE D & WEEKS ER (2005) Confocal microscopy. *Encyclopedia of Biomaterials and Biomedical Engineering G Wnek, and G Bowlin, editors Taylor and Francis, New York*.
- [131] WILHELM S (2008) *Confocal Laser Scanning Microscopy*. Carl Zeiss MicroImaging GmbH, Jena.
- [132] NIPKOW P (1884), Elektrisches teleskop, german patent 30,105.
- [133] TANAAMI T, OTSUKI S, TOMOSADA N, KOSUGI Y, SHIMIZU M, & ISHIDA H (2002) High-speed 1-frame/ms scanning confocal microscope with a microlens and nipkow disks. *Appl Opt*, 41 (22), 4704–4708.
- [134] HEINTZMANN R (2013) Introduction to optics and photophysics. In: KUBITSCHECK U, ed., *Fluorescence Microscopy: From Principles to Biological Applications*, chap. 1, 1–31, Wiley-VCH Verlag GmbH & Co. KGaA, Weinheim, 1st ed.

Bibliography

- [135] PÉDELACQ JD, CABANTOUS S, TRAN T, TERWILLIGER TC, & WALDO GS (2006) Engineering and characterization of a superfolder green fluorescent protein. *Nat Biotechnol*, 24 (1), 79–88.
- [136] BEAUDOUIN J, LIESCHE C, ASCHENBRENNER S, HÖRNER M, & EILS R (2013) Caspase-8 cleaves its substrates from the plasma membrane upon CD95-induced apoptosis. *Cell death and differentiation*.
- [137] SCAFFIDI C, MEDEMA JP, KRAMMER PH, & PETER ME (1997) FLICE is predominantly expressed as two functionally active isoforms, caspase-8/a and caspase-8/b. *The Journal of biological chemistry*, 272 (43), 26953–26958.
- [138] WALCZAK H, MILLER RE, ARIAIL K, GLINIAK B, GRIFFITH TS, KUBIN M, CHIN W, ET AL. (1999) Tumoricidal activity of tumor necrosis factor-related apoptosis-inducing ligand in vivo. *Nature medicine*, 5 (2), 157–163.
- [139] SNAPP EL, HEGDE RS, FRANCOLINI M, LOMBARDO F, COLOMBO S, PEDRAZZINI E, BORGESSE N, ET AL. (2003) Formation of stacked ER cisternae by low affinity protein interactions. *The Journal of cell biology*, 163 (2), 257–269.
- [140] PRESS WH, VETTERLING WT, TEUKOLSKY SA, & P FB (1992) *Numerical recipes in C++*, chap. 15. Modeling of data, 661–711. Cambridge University Press, New York, NY, 2nd ed.
- [141] HENGL S, KREUTZ C, TIMMER J, & MAIWALD T (2007) Data-based identifiability analysis of non-linear dynamical models. *Bioinformatics (Oxford, England)*, 23 (19), 2612–2618.
- [142] RAUE A, KREUTZ C, MAIWALD T, BACHMANN J, SCHILLING M, KLINGMÜLLER U, & TIMMER J (2009) Structural and practical identifiability analysis of partially observed dynamical models by exploiting the profile likelihood. *Bioinformatics (Oxford, England)*, 25 (15), 1923–1929.
- [143] BRONSTEIN IN, SEMENDJAJEW KA, MUSIOL G, & MÜHLIG H (2001) *Taschenbuch der Mathematik*, chap. 18. Optimierung, 870–906. Verlag Harri Deutsch, Frankfurt am Main.
- [144] SORENSEN DC (1982) Newton’s method with a model trust region modification. *SIAM Journal on Numerical Analysis*, 19 (2), 409–426.
- [145] JARRE F & STOER J (2004) *Optimierung*. Springer, Berlin.
- [146] ALDRIDGE BB, HALLER G, SORGER PK, & LAUFFENBURGER DA (2006) Direct lyapunov exponent analysis enables parametric study of transient signalling governing cell behaviour. *Systems biology*, 153 (6), 425–432.
- [147] RAUE A, BECKER V, KLINGMÜLLER U, & TIMMER J (2010) Identifiability and observability analysis for experimental design in nonlinear dynamical models. *Chaos (Woodbury, NY)*, 20 (4), 045105.

- [148] BURNHAM KP & ANDERSON DR (2002) *Model selection and multi-model inference: a practical information-theoretic approach*, chap. 7. Statistical Theory and Numerical Results, 352–436. Springer, New York, NY, 2nd ed.
- [149] AKAIKE H (1973) Information theory and an extension of the maximum likelihood principle. In: PETROV B & F C, eds., *Second international symposium on information theory*, 267–281, Akademinai Kiado, Budapest.
- [150] BURNHAM KP & ANDERSON DR (2004) Multimodel inference understanding aic and bic in model selection. *Sociological methods & research*, 33 (2), 261–304.
- [151] KULLBACK S & LEIBLER RA (1951) On information and sufficiency. *The Annals of Mathematical Statistics*, 22 (1), 79–86.
- [152] HURVICH CM & TSAI CL (1989) Regression and time series model selection in small samples. *Biometrika*, 76 (2), 297–307.
- [153] CLAUS J (2009) *Data-based Modeling of Caspase-8 Activation and Substrate Cleavage*. Master’s thesis, Heidelberg University.
- [154] HELLWIG CT & REHM M (2012) TRAIL signaling and synergy mechanisms used in TRAIL-based combination therapies. *Molecular cancer therapeutics*, 11 (1), 3–13.
- [155] BOLDIN MP, GONCHAROV TM, GOLTSEV YV, & WALLACH D (1996) Involvement of mach, a novel mort1/fadd-interacting protease, in fas/apo-1- and tnf receptor-induced cell death. *Cell*, 85 (6), 803–815.
- [156] CHANG DW, XING Z, CAPACIO VL, PETER ME, & YANG X (2003) Inter-dimer processing mechanism of procaspase-8 activation. *The EMBO journal*, 22 (16), 4132–4142.
- [157] CHANG DW, XING Z, PAN Y, ALGECIRAS-SCHIMNICH A, BARNHART BC, YAISH-OHAD S, PETER ME, ET AL. (2002) c-flip(1) is a dual function regulator for caspase-8 activation and cd95-mediated apoptosis. *The EMBO journal*, 21 (14), 3704–3714.
- [158] MICHEAU O, THOME M, SCHNEIDER P, HOLLER N, TSCHOPP J, NICHOLSON DW, BRIAND C, ET AL. (2002) The long form of FLIP is an activator of caspase-8 at the fas death-inducing signaling complex. *The Journal of biological chemistry*, 277 (47), 45162–45171.
- [159] BOATRIGHT KM, RENATUS M, SCOTT FL, SPERANDIO S, SHIN H, PEDERSEN IM, RICCI JE, ET AL. (2003) A unified model for apical caspase activation. *Molecular cell*, 11 (2), 529–541.

Bibliography

- [160] DONEPUDI M, MAC SWEENEY A, BRIAND C, & GRÜTTER MG (2003) Insights into the regulatory mechanism for caspase-8 activation. *Molecular cell*, 11 (2), 543–549.
- [161] OBERST A, POP C, TREMBLAY AG, BLAIS V, DENAULT JB, SALVESEN GS, & GREEN DR (2010) Inducible dimerization and inducible cleavage reveal a requirement for both processes in caspase-8 activation. *The Journal of biological chemistry*, 285 (22), 16632–16642.
- [162] CHEN M, OROZCO A, SPENCER DM, & WANG J (2002) Activation of initiator caspases through a stable dimeric intermediate. *The Journal of biological chemistry*, 277 (52), 50761–50767.
- [163] KELLER N, MARES J, ZERBE O, & GRÜTTER M (2009) Structural and biochemical studies on procaspase-8: new insights on initiator caspase activation. *Structure (London, England: 1993)*, 17 (3), 438–448.
- [164] KELLER N, GRÜTTER M, & ZERBE O (2010) Studies of the molecular mechanism of caspase-8 activation by solution NMR. *Cell death and differentiation*, 17 (4), 710–718.
- [165] GRANELL S, BALDINI G, MOHAMMAD S, NICOLIN V, NARDUCCI P, STORRIE B, & BALDINI G (2008) Sequestration of mutated alpha1-antitrypsin into inclusion bodies is a cell-protective mechanism to maintain endoplasmic reticulum function. *Mol Biol Cell*, 19 (2), 572–586.
- [166] FISCHER U, HUBER J, BOELENS WC, MATTAJ IW, & LÜHRMANN R (1995) The hiv-1 rev activation domain is a nuclear export signal that accesses an export pathway used by specific cellular rnas. *Cell*, 82 (3), 475–483.
- [167] SPENCER SL & SORGER PK (2011) Measuring and modeling apoptosis in single cells. *Cell*, 144 (6), 926–939.
- [168] FÖRSTER T (1948) Zwischenmolekulare energiewanderung und fluoreszenz. *Annalen der physik*, 437 (1-2), 55–75.
- [169] SAHOO H & SCHWILLE P (2011) FRET and fcs—friends or foes? *Chemphyschem*, 12 (3), 532–541.
- [170] SCHILLING M, MAIWALD T, BOHL S, KOLLMANN M, KREUTZ C, TIMMER J, & KLINGMÜLLER U (2005) Computational processing and error reduction strategies for standardized quantitative data in biological networks. *The FEBS journal*, 272 (24), 6400–6411.
- [171] COHEN-SAIDON C, COHEN AA, SIGAL A, LIRON Y, & ALON U (2009) Dynamics and variability of ERK2 response to EGF in individual living cells. *Molecular cell*, 36 (5), 885–893.

- [172] SIGAL A, MILO R, COHEN A, GEVA-ZATORSKY N, KLEIN Y, LIRON Y, ROSENFELD N, ET AL. (2006) Variability and memory of protein levels in human cells. *Nature*, *444* (7119), 643–646.
- [173] KLEBER S, SANCHO-MARTINEZ I, WIESTLER B, BEISEL A, GIEFFERS C, HILL O, THIEMANN M, ET AL. (2008) Yes and PI3K bind CD95 to signal invasion of glioblastoma. *Cancer cell*, *13* (3), 235–248.
- [174] CHAN FK, CHUN HJ, ZHENG L, SIEGEL RM, BUI KL, & LENARDO MJ (2000) A domain in TNF receptors that mediates ligand-independent receptor assembly and signaling. *Science (New York, NY)*, *288* (5475), 2351–2354.
- [175] PAPOFF G, HAUSLER P, ERAMO A, PAGANO MG, LEVE GD, SIGNORE A, & RUBERTI G (1999) Identification and characterization of a ligand-independent oligomerization domain in the extracellular region of the CD95 death receptor. *Journal of Biological Chemistry*, *274* (53), 38241–38250.
- [176] SIEGEL RM, FREDERIKSEN JK, ZACHARIAS DA, CHAN FKM, JOHNSON M, LYNCH D, TSIEN RY, ET AL. (2000) Fas preassociation required for apoptosis signaling and dominant inhibition by pathogenic mutations. *Science*, *288* (5475), 2354–2357.
- [177] ASHKENAZI A & DIXIT VM (1998) Death receptors: Signaling and modulation. *Science*, *281* (5381), 1305–1308.
- [178] HUANG B, EBERSTADT M, OLEJNICZAK ET, MEADOWS RP, & FESIK SW (1996) NMR structure and mutagenesis of the fas (APO-1/CD95) death domain. *Nature*, *384* (6610), 638–641.
- [179] NAGATA S & GOLSTEIN P (1995) The fas death factor. *Science (New York, NY)*, *267* (5203), 1449–1456.
- [180] SMITH CA, FARRAH T, & GOODWIN RG (1994) The TNF receptor superfamily of cellular and viral proteins: activation, costimulation, and death. *Cell*, *76* (6), 959–962.
- [181] MAIWALD T & TIMMER J (2008) Dynamical modeling and multi-experiment fitting with PottersWheel. *Bioinformatics (Oxford, England)*, *24* (18), 2037–2043.
- [182] BRATTON SB & SALVESEN GS (2010) Regulation of the apaf-1-caspase-9 apoptosome. *Journal of cell science*, *123* (Pt 19), 3209–3214.
- [183] MALLADI S, CHALLA-MALLADI M, FEARNHEAD HO, & BRATTON SB (2009) The apaf-1*procaspase-9 apoptosome complex functions as a proteolytic-based molecular timer. *The EMBO journal*, *28* (13), 1916–1925.

Bibliography

- [184] KOCH AL (1966) The logarithm in biology. 1. mechanisms generating the log-normal distribution exactly. *J Theor Biol*, 12 (2), 276–290.
- [185] LIMPERT E, STAHEL WA, & ABBT M (2001) Log-normal distributions across the sciences: keys and clues. *BioScience*, 51 (5), 341–352.
- [186] BENGTSSON M, STÅHLBERG A, RORSMAN P, & KUBISTA M (2005) Gene expression profiling in single cells from the pancreatic islets of langerhans reveals lognormal distribution of mrna levels. *Genome Res*, 15 (10), 1388–1392.
- [187] KLEIBER C & KOTZ S (2003) *Statistical Size Distributions in Economics and Actuarial Sciences*. John Wiley & Sons, Hoboken, NJ.
- [188] CHEN L, PARK SM, TUMANOV AV, HAU A, SAWADA K, FEIG C, TURNER JR, ET AL. (2010) CD95 promotes tumour growth. *Nature*, 465 (7297), 492–496.
- [189] DICKENS LS, BOYD RS, JUKES-JONES R, HUGHES MA, ROBINSON GL, FAIRALL L, SCHWABE JWR, ET AL. (2012) A death effector domain chain DISC model reveals a crucial role for caspase-8 chain assembly in mediating apoptotic cell death. *Molecular cell*, 47 (2), 291–305.
- [190] SORKIN A & VON ZASTROW M (2009) Endocytosis and signalling: intertwining molecular networks. *Nat Rev Mol Cell Biol*, 10 (9), 609–622.
- [191] SHANKARAN H, RESAT H, & WILEY HS (2007) Cell surface receptors for signal transduction and ligand transport: a design principles study. *PLoS Comput Biol*, 3 (6), e101.
- [192] GRANT BD & DONALDSON JG (2009) Pathways and mechanisms of endocytic recycling. *Nat Rev Mol Cell Biol*, 10 (9), 597–608.
- [193] BAJZER Z, MYERS AC, & VUK-PAVLOVIC S (1989) Binding, internalization, and intracellular processing of proteins interacting with recycling receptors. a kinetic analysis. *J Biol Chem*, 264 (23), 13623–13631.

Acknowledgements

At first I would like to thank Prof. Roland Eils for giving me the opportunity to work on my PhD project in his department and for supervising my PhD studies. In his department I could find a motivating environment, state-of-the-art technical equipment and a variety of contacts to other scientific groups at the BioQuant, DKFZ and Heidelberg University. I acknowledge that I received support for visiting several national and international scientific conferences in Heidelberg and at other places. During my time as PhD student, I really enjoyed taking part in the Eilslabs retreats to the Kleinwalsertal and the DKFZ retreats to Kloster Schöntal.

I would like to thank Prof. Christoph Cremer for scientific discussions and his helpful advice with regard to microscopy techniques, and his group at the Kirchhoff Institute for Physics for comments and ideas.

I am very grateful to Dr. Stefan Legewie, who has introduced me to the field of mathematical models of cellular signaling networks and supervised my PhD project. He set me to work on the apoptosis modeling project and connected me with the group of Prof. Dirk-Peter Herten to work on the Epo modeling project. I thank for helpful and enjoyable discussions at the beginning in Heidelberg and later on the telephone or during visits of his group at the IMB in Mainz. Furthermore I thank him for “bringing me good English writing by”.

I thank Dr. Joel Beaudouin for introducing me to a variety of microscopy and biochemical methods, and for his impressive biochemical knowledge. Joel showed me nearly everything from the scratch, starting from live-cell imaging, cell culture and transfection techniques. Furthermore, I thank Sabine Aschenbrenner for teaching me how to do western blots and DNA preparation.

I thank Anne-Lucia Unger for collaborating on the study on Epo receptor traffic and Prof. Dirk-Peter Herten for supervising the project. Working on models of Epo receptor traffic, I became a member of the LungSys research consortium. I am grateful to the opportunity of giving several presentations on the Epo receptor modeling project at 'LungSys General Meetings' in Heidelberg.

Furthermore, I am grateful to Prof. Peter Sorger (Harvard Medical School, Boston) who invited me after his sabbatical at the Eilslabs for a guest stay in his lab. During my stay in Boston from February to June 2012, which was supported by the German Academic Exchange Service (DAAD), I could work on the project

Acknowledgements

of apoptosis modeling, and enjoyed an inspiring and highly motivating atmosphere.

I further thank Prof. Jens Timmer (Freiburg University) and Prof. Fabian Theis (Helmholtz Center and TU Munich) for inviting me to present my projects at their group seminars and sharing their thoughts and ideas with me.

A special thanks goes to my current and former office mates, Sven Mesecke, Dr. Hannah Schmidt-Glenewinkel, Dr. Matt Rogon, Dr. Charley Choe, Dr. Paula Gonzalez, Dr. Johanna Berndt, Dr. Tobias Ahsendorf and Dr. Lakshmi Venkatraman. I really enjoyed scientific and non-scientific conversations and working together with you. Furthermore I would like to thank present and former the Eilslabs members Dr. Jens Keienburg, Anashua Banerji, Clarissa Liesche, Dr. Barbara Di Ventura, Linda Klauss, Roman Kurilov, Dominik Niopek, Julia Rönsch, Dr. Christian Conrad, Marcel Waschow, Lorenz Maier, Julia Neugebauer, Katharina Jechow, Simon Eck, Marti Bernardo Faura and Yara Reis for a decent atmosphere.

In this place, I would like to thank PD Dr. Hans-Otto Carmesin who introduced me to the field of physics and neurosciences during my time at school, and Prof. Ulrich Eysholdt for his mentoring during my studies of physics and human medicine at Erlangen University.

Last but not least I would like to thank my family, my parents Erika and Hans-Martin, my brother Jochen and my grandmother Elisabeth for their support and encouragement.

Constanze. What would I do or where would I be without you? Words are not enough to thank you.